Macrocyclic Porphyrin Receptors

Mechanisms of Binding, Slippage, Switching & Threading

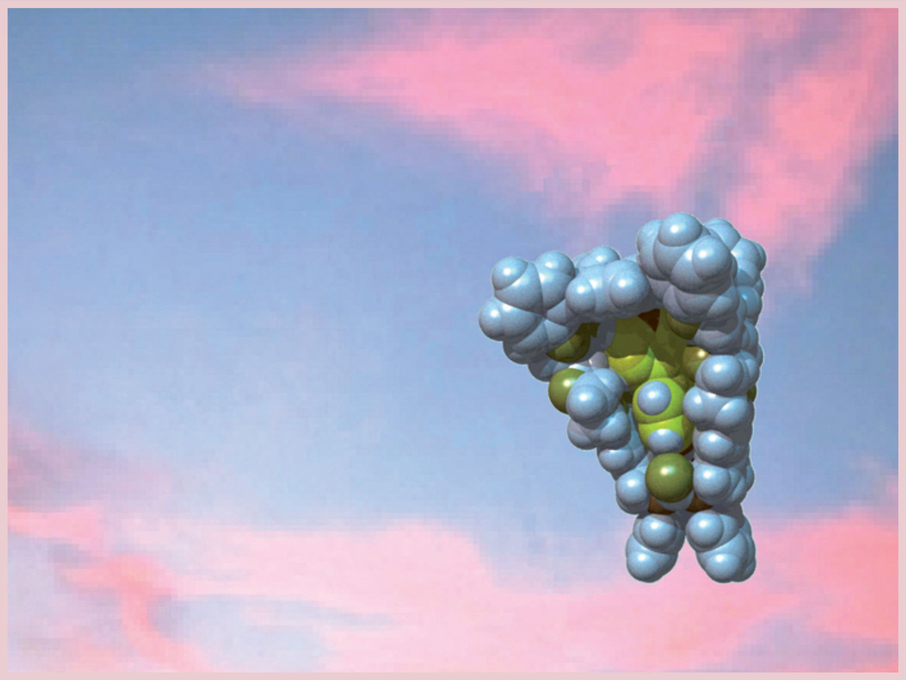

ALEXANDER DEUTMAN

Macrocyclic Porphyrin Receptors

Mechanisms of Binding, Slippage, Switching & Threading

Een wetenschappelijke proeve op het gebied van de
Natuurwetenschappen, Wiskunde en Informatica

Proefschrift

ter verkrijging van de graad van doctor
aan de Radboud Universiteit Nijmegen
op gezag van rector magnificus prof. mr. S.C.J.J. Kortmann,
volgens het besluit van het college van decanen
in het openbaar te verdedigen op vrijdag 26 februari 2010
om 10.30 uur precies

door

Alexander Benjamin Christoffel Deutman

geboren op 9 april 1977
te Nijmegen

Promotores:	Prof. dr. A. E. Rowan
	Prof. dr. R. J. M. Nolte
Copromotor:	Dr. J. A. A. W. Elemans
Manuscriptcommissie:	Prof. dr. J. C. M. van Hest
	Prof. dr. G. Ercolani
	Prof. dr. D. A. Leigh

ISBN: 978-90-9025113-4

‘All Science is either Physics or Stamp Collecting’
Ernest Rutherford (1871-1937)

Contents

1

Introduction and Literature Survey

1. Introduction

Life is conditioned at the molecular level. Large molecules that consist of carbohydrates, lipids, nucleic acids, and amino acids are covalently constructed to form well-known structures such as proteins, phospholipids, and RNA. The three-dimensional structures of these individual molecules and the assembly of these molecules into superstructures, such as the cell membrane, DNA, and protein complexes, is mainly governed by weak and reversible non-covalent bonding interactions. These weak interactions also play key roles in the working mechanism of the impressive molecular machineries that process energy, matter, and information. It is the basis for substrate recognition, protein flexibility, signal transduction, and most other important molecular processes at the heart of life.

The importance of these weak non-covalent binding interactions is by now well recognized and a new area of chemistry that focuses on the nature of these interactions, known as Supramolecular Chemistry, has evolved over the past decades. Through the use of relatively simple (but ever increasing in complexity and functionality) artificial systems a large number of important concepts based on these non-covalent interactions have been demonstrated, such as molecular self assembly, template directed synthesis, supramolecular catalysis, interlocked architectures, polymer threading, and molecular machines. These studies have increased the level of understanding of the natural supramolecular binding interactions and pave the way for novel artificial materials and catalysts.

In this chapter, the supramolecular aspects of the replisome, i.e., the machinery responsible for the replication of DNA, will be presented and the important supramolecular concepts of the replisome will be illustrated with artificial examples from the field of supramolecular chemistry. This will help to provide a good picture of the importance of non-covalent bonding interactions in natural systems and, in the mean time, provide a good overview of the recent advances in the field of supramolecular chemistry.

2. The DNA replication machinery

The transmission of genetic material from one generation to the next is critical for the proliferation of all organisms. The efficient copying of DNA is carried out by a large molecular machine called the replisome, which couples the highly processive unwinding of parental DNA with the synthesis of new daughter strands (Figure 1).[1] Although the replisome differs depending on the organism, the basic mechanisms of replication are alike and highly conserved through evolution.[2] The replisome consists of numerous different proteins that act together to advance a DNA replication

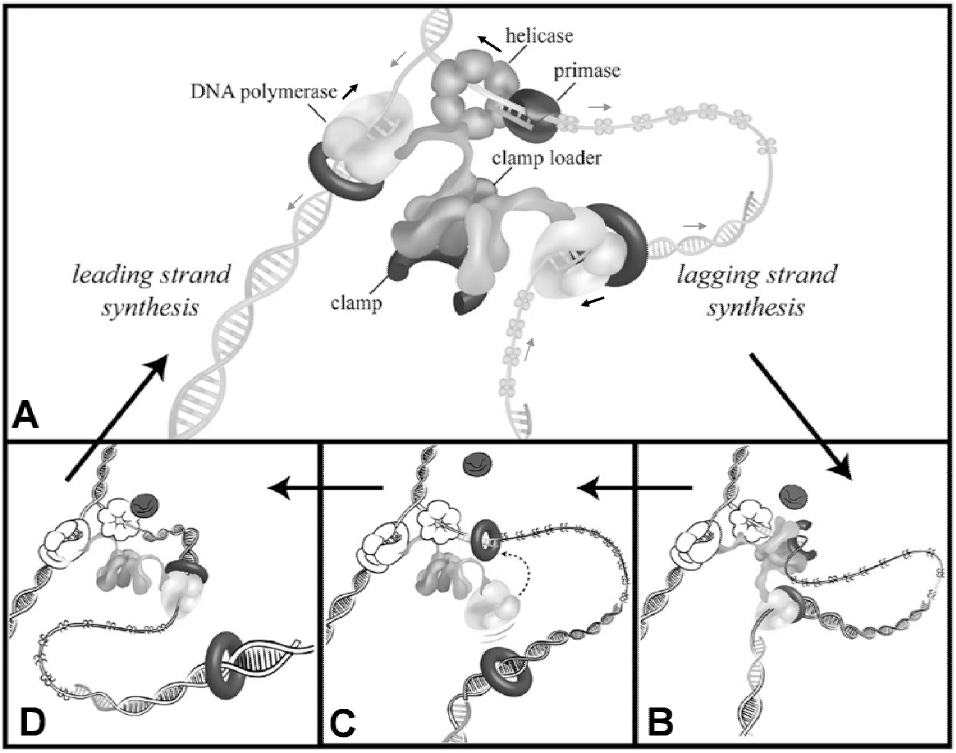

Figure 1. The cycle of lagging strand synthesis in the *E-coli* replisome. (A) As the lagging strand polymerase synthesizes an Okazaki fragment, the clamp loader opens a new clamp and the helicase recruits primase to the replication fork to initiate the next fragment. (B) After synthesis of the RNA primer, the clamp loader displaces the primase and loads the clamp onto the new primer/template junction. (C) Completion of Okazaki fragment synthesis triggers recycling of the lagging strand polymerase to the newly loaded clamp, leaving the old clamp behind. (D) The lagging strand polymerase synthesizes the new Okazaki fragment, completing a full circle. Fork unwinding and leading strand synthesis continue throughout the cycle.

fork.[3] Replisome assembly occurs during a brief window of time, known as initiation, in which a variety of requisite catalytic and scaffolding factors are sequentially recruited to DNA.[4] This initiation begins at defined regions on the DNA, termed origins.[5] Initiator proteins bind to the origins after which protein complexes that load or recruit the replisome recognize the initiator-origin complex.[6,7] The duplex DNA is locally melted[8] to allow access to the information encoded by individual bases in single stranded DNA and the recruitment of the different proteins takes place to form the replisome. The parental DNA duplex is unwound by a multimeric donut shaped helicase,[9] which results in the formation of two single stranded DNA fragments; the leading strand and the lagging strand (Figure 1). The helicase translocates onto the lagging strand in the 5´ to 3´ direction, just ahead of the leading strand polymerase (Figure 1A). This polymerase duplicates the leading strand in a continuous fashion.[10] The polymerase is tethered to the DNA by a circular sliding clamp, which embraces the newly formed duplex DNA and slides freely along it enabling rapid and processive replication.[11] The polymerases cannot initiate synthesis in the absence of a nucleic acid primer, so the first step in DNA synthesis is the formation of a short RNA primer by specialized RNA polymerases known as primases (see Figure 1a).[12] In principle, leading strand synthesis requires only one priming event because the polymerase moves continuously along the single leading strand.

The single strand that leaves the helicase, the lagging strand, is duplicated by another polymerase/sliding clamp complex. Because the lagging strand reads antiparallel to the leading strand and in replication the 5´ to 3´ pattern must be used, the DNA replication occurs in the direction away from the helicase. For this reason, the lagging strand must grow discontinuously. This discontinuous replication results in the production of series of short sections of DNA (<2 kb), called Okazaki fragments.[13] In order to replicate each Ozaki fragment, the polymerase/sliding clamp complex needs to reload in close proximity to the helicase. The replisome makes use of a clamp loader to achieve this with high fidelity.[14] This clamp loader loads a new clamp just behind the replisome, where the primase has synthesized the necessary primer DNA-RNA duplex (Figure 1B).[15] The polymerase that has just completed the replication of the preceding Okazaki fragment is then released from its sliding clamp and reloads onto the newly attached sliding clamp just behind the replisome (Figure 1C) after which it starts replicating the next Okazaki fragment (Figure 1D).

This complicated process occurs with extremely high speed and fidelity. The replisome in *E. coli* moves of about 1 kb per second (~400 nm/s), which is about the length of the Ozaki fragment. *E. coli* is capable of reproducing its 4.6 megabase genome from a single origin of replication with high fidelity in less than 40 minutes. For a nice movie illustration of the working mechanism of this stunning molecular motor system, see:
http://nl.youtube.com/watch?v=nIwu5MevZyg

3. Advances in supramolecular Chemistry

The fascinating mechanism of the replisome is one of the most complex and elegant examples of a natural molecular machine. Each different compartment of the replisome contains specific functionalities required for part of the replication and the cooperative working of these compartments results in the highly processive replication of the DNA. Designing and synthesizing a molecular system as complex and versatile as the replisome is beyond the possibilities of present day chemistry. Nevertheless, a large number of the important concepts that can be observed in the activities of the replisome have already been mimicked by the field of supramolecular chemistry and advanced insights into the working mechanisms have been obtained.

In the following subsections, a number of important noncovalent (supramolecular) features of the replisome will be examined and the concepts will be further illustrated with some artificial examples from the field of supramolecular chemistry.

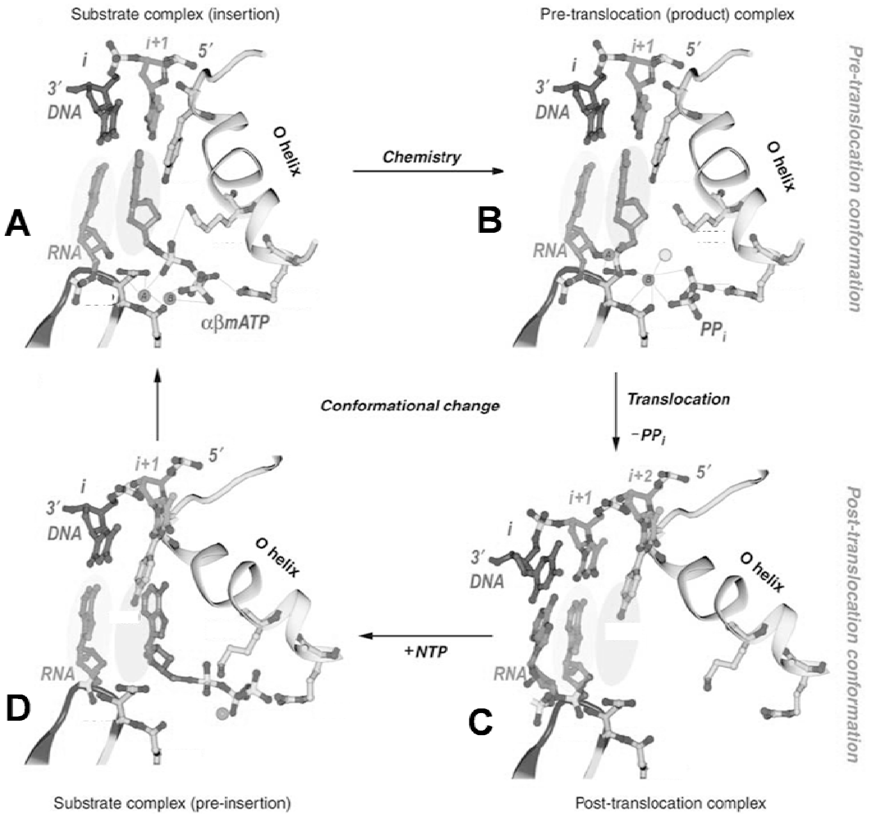

Figure 2. Structural changes at the active site during a single nucleotide addition cycle. (A) The matching nucleotide triphosphate (NTP) is bound noncovalently in position by the complimentairy base pair interactions and ionic croslinking interactions of the triphospate with different domains in the polymerase. (B) The Phosphoryl transfer reaction results in the elongation of the formed DNA with one base and the formation of PP$_i$.(C) Release of the Metal-PP$_i$ results in conformational changes to the system in which the Polymerase translocates and preorganizes for the binding of the next NTP. (D) The next NTP binds to the polymerase through a pre-insertion complex after which, by a final conformational change, the substrate binds and starts a new cycle.

3.1 Supramolecular catalysis

The polymerization of deoxyribonucleotides into single DNA strands, thereby forming a new duplex DNA, is catalyzed by the DNA polymerase.[16] It reads the DNA strand as a template and uses it to synthesize the new strand in which the complimentary deoxiribonucleotides are positioned with amazing accuracy. Like many enzymes, this is achieved by providing the ideal microenvironment for the catalytic conversion. A matching nucleotide triphospate (NTP) is positioned inside this microenvironment and is stabilized by the nucleotide on the single strand DNA. Various other precisely placed interactions provided by the polymerase, such as metal-ligand, dipole-dipole, and π-π interactions also provide stabilization (Figures 2A and 2D). The phosphoryl transfer reaction, in which the newly formed strand is elongated with one nucleotide and pyrophosphate (PP$_i$) is formed, then occurs with high fidelity (Figure 2B). This efficiency is not only the result of the precise pre-organization of the reactive components, which puts the substrate into position (hence a very high effective concentration), but also the result of the various stabilizing interactions between the microenvironment and the reactants in their transition state conformation that lead to rate enhancement. Release of the formed PP_i is accomplished with conformational response of the polymerase (Figure 2C); both the polymerase translocates on the DNA to the next available nucleotide on the single strand and the interior of the polymerase opens to allow the binding of the next complimentary nucleotide triphospate (Figure 2D). Once this is complete, a new cycle is started.

The ability of enzymes like DNA polymerase to catalyze chemical reactions has been a source of inspiration to the field of supramolecular chemistry. A large number of artificial catalysts have been reported in which increased chemical reactivity or selectivity has been observed as a result of supramolecular binding interactions.[17–28] In general, two different approaches have been chosen. In the first, two reacting molecules are brought together as a result of stabilizing interactions inside a binding pocket (Figures 3A–B). In the second, a catalytic center is connected covalently to the molecule in the proximity of a binding pocket that is designed for the specific binding of substrate molecules (Figures 3C–D). Both strategies can result in an increase in the effective concentration of the reactive components and therefore to enhanced reaction rates. In addition to this templating effect, the confined reaction compartment can also influence the regio- and stereoselectivity of the reaction. A third crucial effect is that of transition state stabilization; interactions between the substrate(s) and the microenvironment effectively reduce the reaction barrier and lead to enhanced rates compared to uncatalyzed reactions.

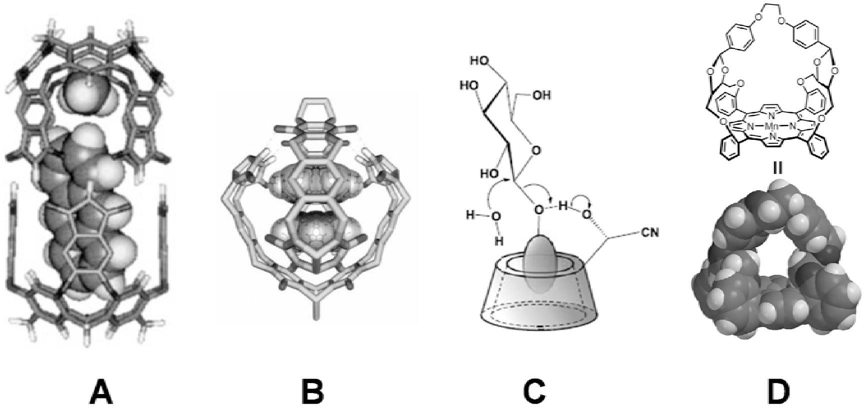

Figure 3. Schematic representations of inclusion complexes. (A) Cylindrical capsule based on a pyrogallolarene dimer in which anthracene and methane are simultaneously encapsulated. (B) Softball dimer based on glycoluril with two molecules of benzene encapsulated. (C) A cyanohydrin cyclodextrin catalyst. (D) A basket-handle porphyrin catalyst.

One of the best, recent examples of transition state stabilization by a catalytically active artificial cavitant has been reported Raymond, Bergman, and coworkers in 2007.[29] They used a highly charged and water soluble, metal-ligand assembly that had a hydrophobic interior cavity to catalyze the normally acidic hydrolysis of orthoformates in basic solution. The nanoreactor cavity has a strong selectivity for protonated substrates, thereby facilitating the protonation of the orthoformate necessary for the hydrolysis, even in a basic environment (Figure 4). Catalytic amounts (1 mol%) of the nanoreactor caused rate accelerations of up to 890-fold. The nanoreactor exhibits substrate size selectivity in which orthoformate substrates that are too large to fit inside the cavity are not readily hydrolyzed. In addition, the catalytic reaction inside the nanoreactor obeys Michaelis–Menten kinetics and exhibits competitive inhibition like many natural enzymatic systems. The enhanced reaction rate is unambiguously the result of transition state stabilization inside the confined microenvironment of the nanoreactor in which the protonated reaction intermediates are shielded from the basic environment.

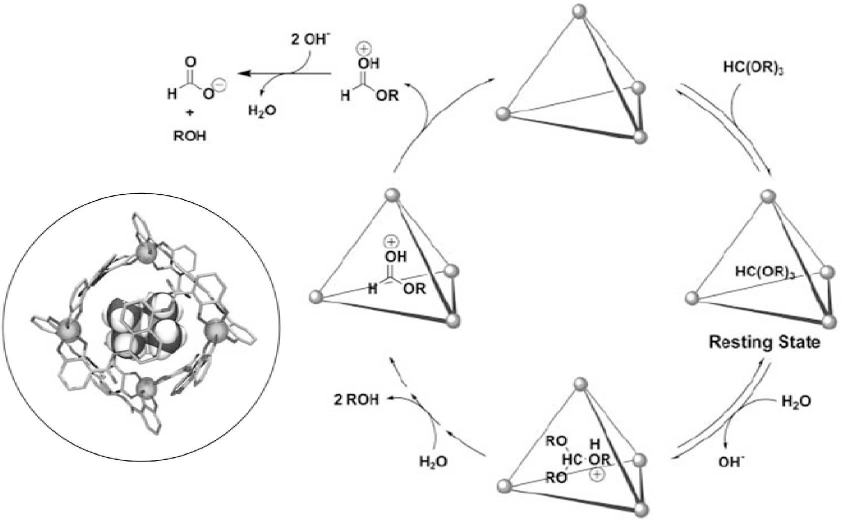

Figure 4. Mechanism for catalytic orthoformate hydrolysis inside the cavity of a highly charged and water-soluble, metal-ligand assembly.

Another clear-cut example of catalysis inside an artificial cavity has been reported by Liu and Wulff.[30] They constructed an artificial mimic of the natural enzyme carboxypeptidase A[31] by molecular imprinting in synthetic polymers. Polymer imprinting is a technique in which a polymer is formed and crosslinked in the presence of a molecule that is afterwards extracted, thus leaving complimentary cavities behind. The authors imprinted polymers containing amidinium moieties and Zn^{2+} or Cu^{2+} centers with substrates that strongly resembled the transition-state conformation of carbonates in the process of hydrolysis (Figure 5). When substrates exhibiting a very similar structure to the template were used, an extremely high (over 10^5-fold) enhancement in the rate of catalyzed to uncatalyzed reaction (k_{cat}/k_{uncat}) was observed. The study strongly suggests that the stabilizing interactions between the microenvironment of the artificial cavity and the reaction transition state result in the accelerated rates of hydrolysis. This artificial catalyst was also found to display size selectivity, Michaelis–Menten kinetics, competitive inhibition, and other properties typical of enzymes.

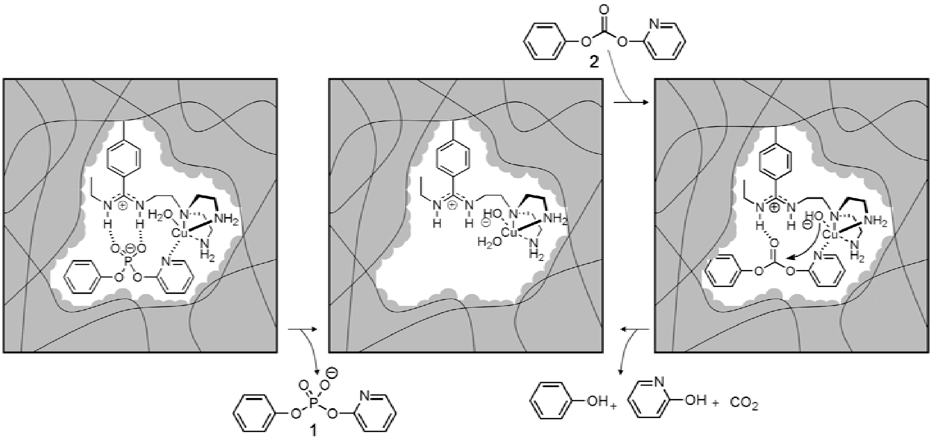

Figure 5. Imprinted polymer and the mimicry of the catalysis of carbopeptidase A. Left side: Imprinting in the presence of **1**, which strongly resembles the transition state conformation of **2**. Middle: The cavity after removal of **1**. Right side: Hydrolysis of carbonate **2** inside the cavity of the imprinted polymer.

Although the artificial catalytic examples are not yet as efficient as the natural enzymatic systems, these studies have clearly proven the principles of rate enhancement by means of transition state stabilization and substrate templation, and of regio- and stereo-selectivity as a result of the confined cavities of the catalysts. Other less beneficial properties of artificial catalysts, such as product inhibition have also been observed.[32–34] In order to further improve artificial systems, the catalysts involved need to be more finely tuned. An ideal catalyst should have a high selectivity and affinity for the substrate(s) thereby templating the reactive groups in the ideal geometries. The catalyst's microenvironment should furthermore provide the ideal stabilizing interactions of the transition state to further reduce the activation energy of the reaction. Finally, the product should be easily released to free the catalysts for a new catalytic cycle. This therefore requires that a catalyst can respond, in a conformational sense, to each fragment of the reaction it catalyses, a feature that has yet to be developed in the catalytically active artificial receptors. Better design of the artificial catalysts based on these principles could well result in proficiencies comparable to the natural enzymatic systems.

3.2 Cooperative binding effects

Cooperativity (or allostery) is a widely used term in the field of biochemistry. It refers to (binding) events in which enzymes or receptors are influenced by binding events at other remote binding sites within the enzyme or receptor.[35–38] Cooperative effects can be positive (the binding enhances the events of a remote site) or negative (the binding obstructs the events of a remote site) and this type of regulation is said to be intrinsic to the control of most metabolic and signal-transduction pathways.[39] One of the most well-known natural examples of cooperativity is the binding of oxygen to hemoglobin;[40] in which the binding of the first molecule of oxygen enhances the binding of the second and so forth. Cooperative binding interactions are, however, observed in a very large number of natural systems.

The replisome can also be seen as a highly cooperative enzymatic system in which interactions between the different subunits strongly affect each others function. For instance, the DNA-polymerase is strongly dependant on the interactions with the sliding clamp, which is illustrated by the observation that in the absence of the sliding clamp the DNA-polymerase can only catalyze the inclusion of a small number of nucleotides to the single DNA strand before dissociating from the strand (in the presence of a sliding-clamp over 50 kb can be included without dissociation).[41] Furthermore, the helicase activity is greatly stimulated by (cooperative) interactions with other subunits of the clamp-loader/polymerase complex.[42] The loading of the polymerase to the DNA primer is also highly cooperative. The polymerase can only load onto the single stranded DNA by replacing a primase, which is in turn recruited by interactions with the helicase.[43] In the lagging strand synthesis there is cooperative signaling, which makes that the DNA-polymerase dissociates from the finished Ozaki fragment and reloads onto a new sliding clamp to start the synthesis of a new Ozaki fragment. Although the exact mechanism is still under debate, it is clear that the clamp loader complex plays a decisive role in the dissociation of the DNA-polymerase from the finished strand, reducing the dissociation half life from 5 minutes to far less than 1 second.[11,44]

Although the field of supramolecular chemistry has not yet been able to reproduce the versatility and efficiency of the cooperative interactions observed in nature, a large number of artificial systems have been reported that at least mimic the principles of cooperativity as observed in enzymes and receptors. In many artificial receptors containing two or more remote binding sites, binding events to one binding site were shown to either positively or negatively influence the binding to remote binding sites.[45–58]

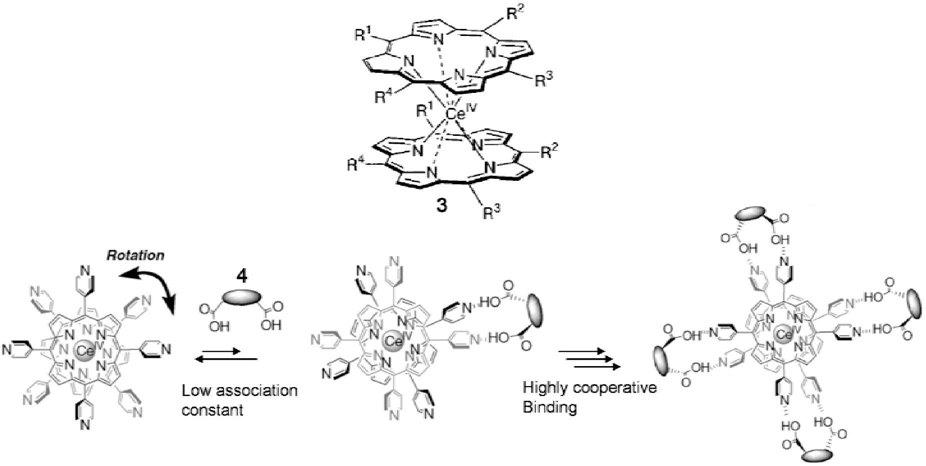

Figure 6. The positive homotropic cooperativity in the binding of dicarboxylic acid guests to a bis[porphyrinato]cerium-(IV) double decker complex.

The group of Shinkai has been especially productive in the development of different artificial systems displaying positive and negative heterotropic and homotropic cooperative binding effects.[59–63] An example of positive homotropic allostery in a bis[porphyrinato]cerium-(IV) double decker complex (**3**)[64–65] is presented in Figure 6. Dicarboxylic acid guests (**4**) were shown to bind to two pyridyl groups of opposing porphyrins by means of hydrogen bonding interactions. It was observed that the binding of the first dicarboxylic acid guest strongly enhances the binding of the second and so forth. This was argued to originate from restriction in the rotation of the porphyrin around the cerium ion. The binding of the first guest suppresses this rotation, after which the subsequent binding of the second, third, and fourth guest can occur cooperatively.

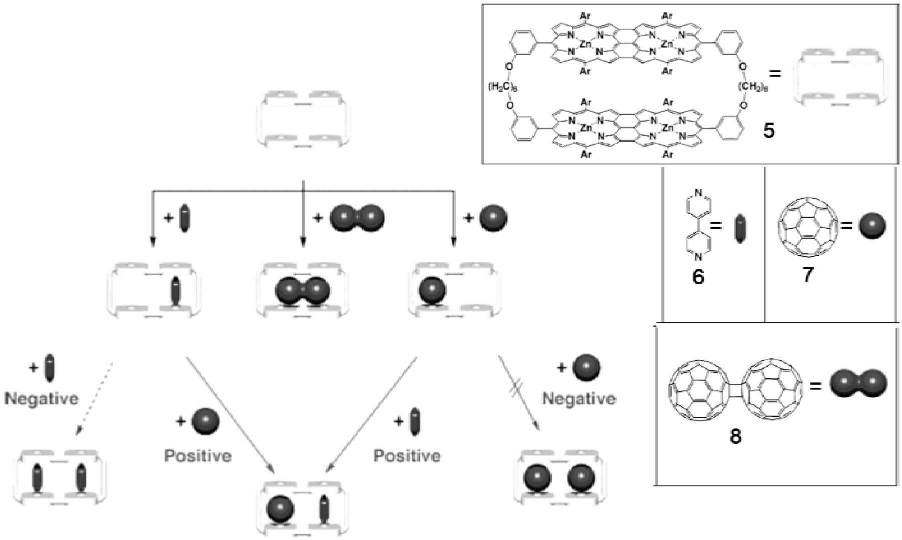

Figure 7. Positive heterotropic and negative homotropic cooperativity in the binding of various functions to a fused zinc porphyrin array.

An interesting highly conjugated artificial receptor displaying both negative homotropic cooperative effects and positive heterotropic effects has been reported by the group of Takuzo Aida (Figure 7).[66] A fused zinc porphyrin array (**5**) was synthesized that is capable of coordinating diamines to the metal ions inside the cavity and can also bind fullerene molecules inside the cavity. A negative cooperative effect was observed for the combined binding of two molecules of bipyridine (bipy; **6**) inside the receptor molecule. This is presumably due to transmission of the first-ligating bipy through the π-conjugation of the receptor to the second binding site, which then has a lower affinity toward the second bipy molecule.[67] Both C_{60} (**7**) and C_{120} (**8**) bind strongly inside the cavity of the receptor (K_{assoc}-$C_{60} \approx 10^4$, K_{assoc}-$C_{120} \approx 10^8$), however, no 2:1 complex formation of C_{60} was ever observed inside the receptor (independent of temperature or concentration). This last observation suggests a very high negative cooperative effect for the binding of the second C_{60} molecule. The combined binding of C_{60} and bipy to the receptor, on the other hand, revealed strong positive cooperative effects. The association constant of C_{60} to the complex between the receptor and bipy was 8.5 times larger than in the absence of bipy. The authors conclude that this effect is the result of electronic communication between C_{60} and diamines through the π-conjugated fused metalloporphyrins, although it takes little imagination to come up with other reasonable explanations.

Cooperativity plays an important role in the self-assembly of many natural superstructures. It is associated with protein folding and cell-membrane formation and can, for instance, be observed in the formation of the rod-like tobacco mosaic virus.[68] DNA duplex formation is also highly cooperative. It is known that a certain number of base pairs are required before double helix assembly occurs.[69] Short oligonucleotides do not form duplex DNA complexes in solution whereas longer chains assemble into the well-known double helix. This is the result of the additive stabilizing interactions of the complimentary base pairs in longer fragments, in addition to other effects, such as π-π stacking between the base pairs, solvent effects, excluded volume effects by helix formation, and others.[70]

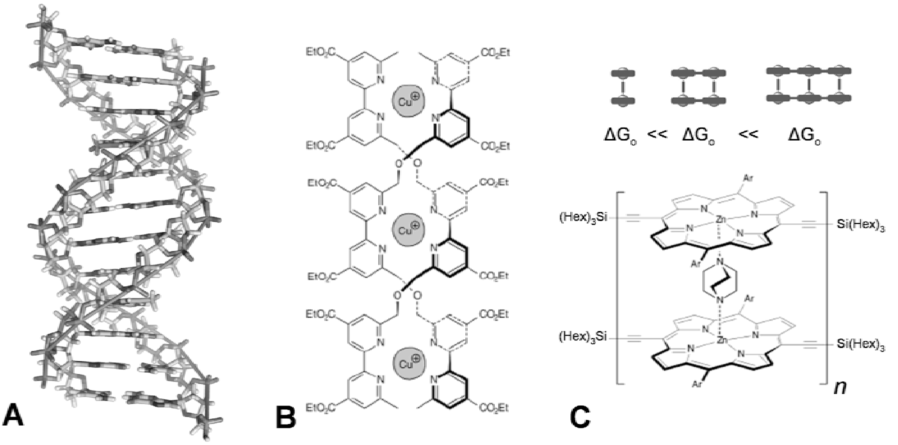

Figure 8. Different supramolecular assemblies that depend upon the cooperative action of multiple binding interactions. (A) duplex DNA. (B) Lehn's Helicates. (C) Porphyrin ladders by Anderson and Tayler

The field of supramolecular chemistry has shown that highly ordered and large artificial molecular assemblies can be obtained with the help of cooperative binding effects. Both the helicates obtained by Lehn and co-workers[71–73] (Figure 8B) and the porphyrin ladders by Anderson and Tayler (Figure 8C) are preeminent examples. Lehn and Pfeil carried out an analysis of the binding of Cu^I ions to a tris-bipyridine ligand and concluded, from the stepwise increase in the complex stability upon increasing numbers of Cu^I ions present, that the assembly of the resulting trihelicate (Figure 8B) is a self-organization process displaying positive cooperativity. Comparable results were obtained by Andersen and Tayler.[74] They developed linear zinc-porphyrin oligomers, and studied the self-assembling properties of these linear molecules with bivalent amines (which are sandwiched in between two porphyrins) into double-stranded 'porphyrin ladders'(Figure 8C). They observed that the stabilities of the ladder complexes increased linearly with the length (number of porphyrins in the system). Moreover, they observed what they called 'narcissistic self-sorting' in which, for instance, a mixture of linear molecules containing two and three porphyrin molecules give only ladders composed of 2/2 and 3/3 in the presence of DABCO (Figure 8C). This last observation nicely reveals how molecules can automatically self assemble into their thermodynamically most favorable conformation, as can be observed in the self-assembly of, for instance, DNA and proteins.

Ercolani illustrated nicely that these examples of increased stabilities can be fully ascribed to the non-cooperative chelate effect[75] and therefore lack the additional cooperative interactions that, for instance, likely operate in the duplex formation of DNA. Nevertheless, these results illustrate that the cooperative acting of multiple recognition sites on a molecular system induce the stabilities of the supramolecular assemblies and thereby facilitate the formation of large defined structures.

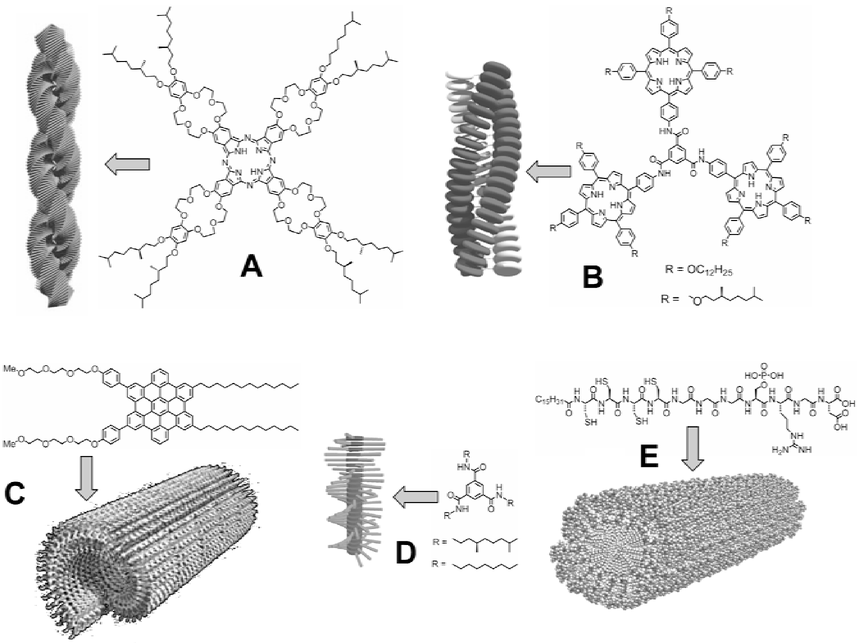

Figure 9. Well defined linear supramolecular assemblies by the group of Nolte (A, B), Aida (C), Meijer (D), and Stupp (E).

Another approach to the formation of well-defined large objects by self-assembly is that of stack formation (Figure 9). Relatively small, amphiphilic molecules containing different functionalities have been shown to organize into well-defined rod like structures simply by stacking on top of each other. These supramolecular nano-rods often adopt helical structures in which the helicity (left- or right handed) can be controlled by a single chiral group in the molecule.[76–83] Intriguing concepts like sergeant and soldiers, the majority rules, and other have been discussed in the literature.[84] These studies have clearly revealed how large and highly ordered structures can be formed by self-assembling processes in which the properties of the molecules determine the formed structure of the supramolecular assembly from a bottom-up approach. Although the mechanism governing the formation of these structures is not completely unraveled yet, it is clear that the same principles that govern the formation of well-defined natural structures operate on these artificial examples.

3.3 Interlocked architectures

The ability of the sliding clamp to keep the DNA polymerase attached to the DNA template for a large number of base insertions originates from its unique structural properties. When the sliding clamp is loaded onto the DNA by the clamp loader complex it adopts a ring-shaped geometry that fully interlocks the DNA inside its cavity (Figure 1). This mechanical interlocking of the DNA prevents the dissociation of the sliding-clamp/polymerase complex from the DNA. In the mean time, the sliding clamp leaves enough space between its cavity and the DNA, which allows for the rapid translocation along the DNA, necessary for the fast replication process.[85] Such interlocked geometries, in which long biopolymers thread through confined pores, channels, and other toroidal structures can be observed in a variety of other natural processes. For instance, in the translocation of DNA and RNA across membranes or in the infection of cells by viruses,[86] and in (post-transcriptional) translocation of proteins through membranes.[87–89]

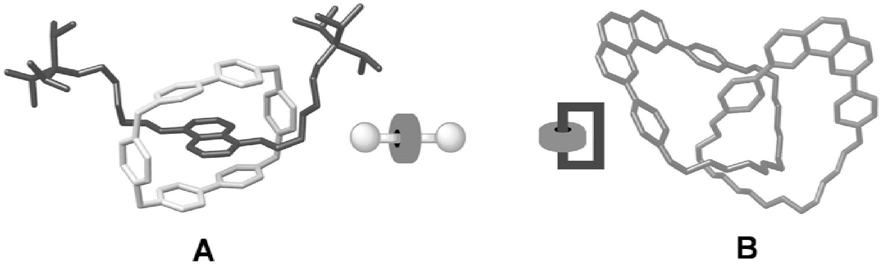

Figure 10. (A) Rotaxane structure. (B) Catenane structure.

The unique properties of such interlocked architectures have been widely explored in the field of supramolecular chemistry. A large number of artificial rotaxane structures [90–92] (in which a molecular rotor is threaded by a linear axle that is blocked at both ends, Figure 10A) and catenane structures[93] (in which two molecular ring-shaped components are mechanically interlocked, Figure 10B) have been developed. The dynamics of such interlocked species have been widely studied and recently a number of interesting applications of such structures in molecular motors, muscles, shuttles, and switches have been reported and will be discussed more thoroughly in the next section.

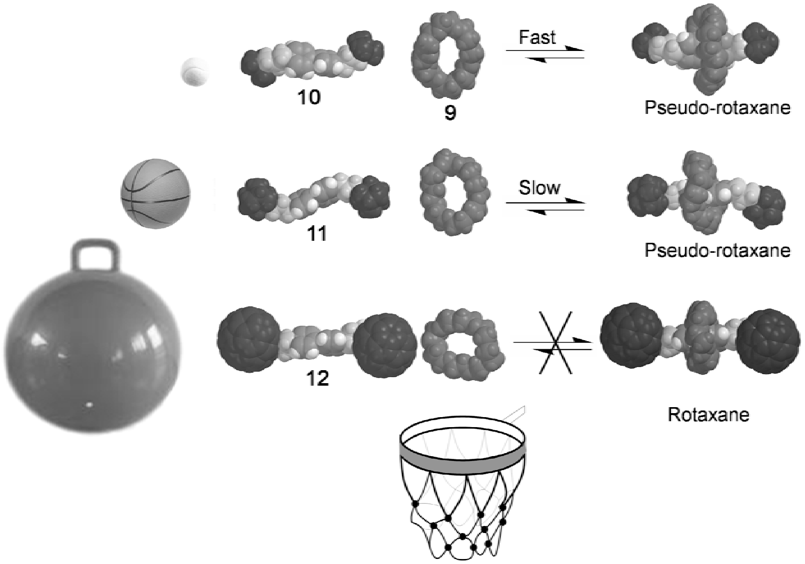

Figure 11. Slippage of a macrocyclic molecule (**9**) will be fast over dumbbells with small stoppers (**10**), slow in the case where the stoppers approach the dimensions of the cavity (**11**), and fully obstructed when the stoppers exceed the dimensions of the macrocyclic ring (**12**).

The reversible formation of many rotaxane structures, so called pseudo-rotaxanes, has added some important insights into the field of supramolecular chemistry. Not only have the effects of supramolecular binding interactions on complex stabilities been widely explored and understood by means of studying the thermodynamics of pseudo-rotaxane formation, but also the kinetics of pseudo-rotaxane formation and dissociation has received serious attention. For instance, in-depth studies of slippage,[94–99] in which the macrocyclic component has to traverse a bulky substituent (Figure 11) have been conducted. In line with intuition, smaller substituents are traversed more easily than larger ones. In addition, all-or-nothing effects have been observed in slippage in which a macrocycle can not traverse a molecule that exceeds the dimensions of the macrocyclic interior. This observation hints towards the mechanisms by which enzymatic systems can differentiate between substrate molecules that vary in size. Moreover, slippage studies in different solvent systems have clearly revealed that solvent interactions play a decisive role in both the thermodynamics and kinetics of pseudo-rotaxane complex formation. An observation that strongly stresses the concept that supramolecular binding does not only involve the interacting molecular systems but is also highly dependant on the interplaying solvent.

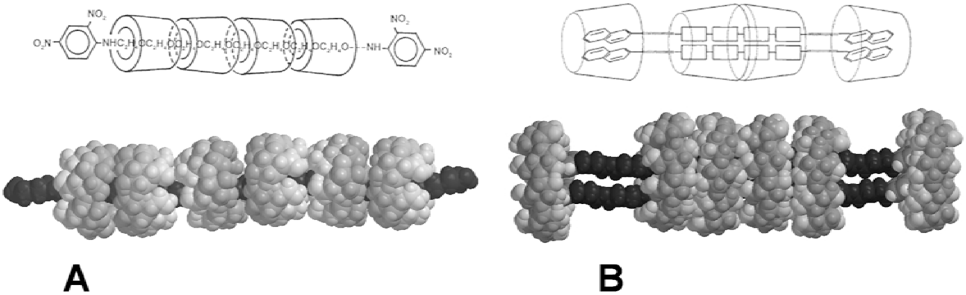

Figure 12. Molecular necklaces of cyclodextrins threaded onto PEG by Harada. (A) A series of α-cyclodextrins on a single PEG chain end capped with bulky end-groups and a space filling representation of such a structure. (B) Inclusion of two PEG chains in a series of γ-cyclodextrins and a space filling representation of the structure.

In addition to the exploration of relatively small interlocked artificial systems, it was soon found that macrocyclic molecules can also thread polymers. The first examples were reported by Harada, who found that polyethylene glycol (PEG) could penetrate the ‘beaker-like tunnel’ of cyclodextrins.[100,101] A so called molecular necklace was synthesized in which several cyclodextrins were threaded onto a PEG chain by self assembly and were trapped by capping the chain with bulky end groups (Figure 12A).[102] In time a large number of such molecular necklaces and related structures involving, amongst others, cyclodextrins, cucurbiturils, and tetracationic cyclophanes as macrocycles have been reported.[103–109] As observed in smaller interlocked structures, the stabilities and the geometries of the formed complexes depend upon the interactions between the macrocycles and the polymer chains. As a result of the reversible character of the supramolecular interactions in time the thermodynamically most favored geometry will be adopted. This has resulted, for instance, in the formation of necklaces in which two polymer chains are double-threaded through a number of macrocycles (Figure 12B).[110]

Both polyrotaxanes (in which the end-groups of the polymers are capped with bulky substituents) and pseudopolyrotaxanes (in which macrocycles can reversibly thread the polymer chain) are of increasing relevance, as they give rise to new polymeric materials with interesting properties in a straightforward and modular way from known building blocks.[111–113] From a bio-mimetic point of view, it is clear that the threading of polymers inside macrocyclic molecules and movement through these cavities can easily occur; this feature is not only restricted to natural processes. In order to further understand the mechanisms that govern the threading of polymers through small macrocycles a number of studies have been carried out that focus on the kinetics of artificial threading processes.

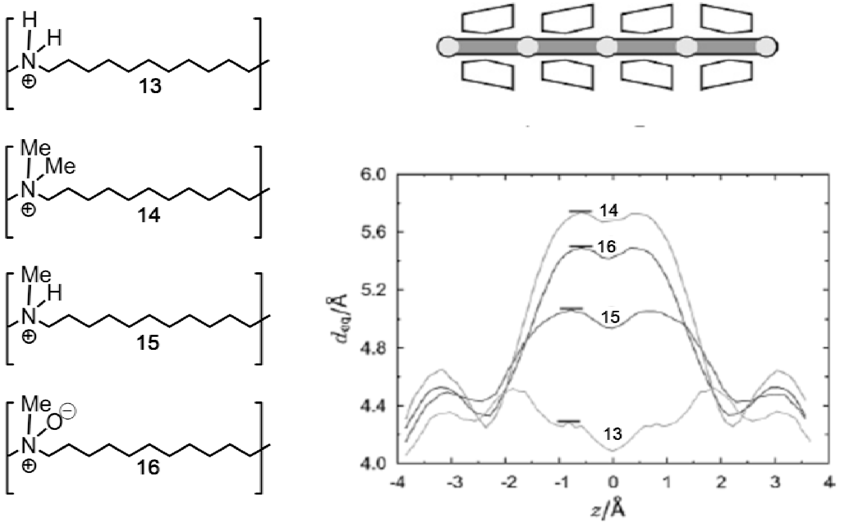

Figure 13. Left: poly-(bola-amphiphile) type polymers. Top: schematic representation of a pseudo-polyrotaxane of α-cyclodextrin rings onto these polymers. Right: Bulkiness of the hydrophilic groups of the different chains.

An elegant study, which clearly revealed that small changes in the polymer can have dramatic effects on the pseudo-polyrotaxane formation was carried out by Wenz.[114] A number of so called poly(bola-amphiphile) type polymers were synthesized that vary only in the substitution pattern on the tertiary amines (Figure 13). Threading kinetics of α-cyclodextrin rings onto these polymers were investigated by ^{1}H NMR spectroscopy. The time t_{90}, necessary to reach 90% completion of the threading process, was taken as a measure of the bulkiness of the hydrophilic groups along the polymer chain. The t_{90} values decreased by more than three orders of magnitude as the diameters of the hydrophilic groups decreased from 5.5 to 4.3 Å (Figure 13). These findings revealed that the threading and translocation speed can be altered dramatically by delicate changes in the polymer chain, an observation that could be explained to be the result of steric hindrance between the macrocycle and the bulkier polymer fragments.

The group of Harada has been working on self-threaded cavities.[115,116] They synthesized a number of poly(ethyleneglycol)-substituted cyclodextrins of different chain lengths, which contain an aromatic moiety on the polymer chain in the proximity of the cyclodextrin (Figure 14). As a result of the high affinity of this aromatic moiety for the interior of the cyclodextrin the molecules adopt self-threaded geometries. The addition of half an equivalent of a guest with a high affinity for the cavity of the cyclodextrin (1-adamantanecarboxylic acid, **17**) competes with the intramolecular self-threaded complex and results in an equilibrium between the de-threaded and self-threaded cyclodextrins (in a 1:1 ratio).[117] The threading/de-threading kinetics of this dynamic competition experiment were studied by means of variable-temperature NMR and 2D EXSY NMR experiments and it was revealed that the conformational exchange rates decreased exponentially with the length of the PEG chain.

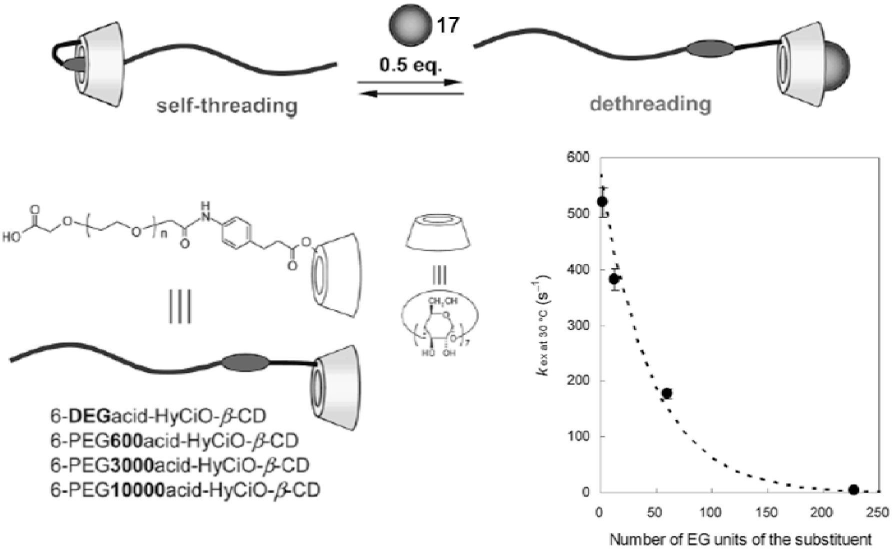

Figure 14. Self threaded β-cyclodextrin equipped polymers. Top: the competition equilibrium in the presence of 1-adamantanecarboxylic acid. Right: length dependency of the threading kinetics.

These threading studies revealed some important aspects about the threading of macrocycles onto polymer chains. Cavity size, chain length, chain functionalities, but also the solvent and temperature affect the threading rates and all can be assumed to also affect the natural polymer translocation systems. From a mechanistic point of view, however, a lot remains to be discovered. The field of supramolecular chemistry should be explicitly suited to uncover mechanistic details of polymer threading and polymer translocation processes.

3.4 Directional motion

Although not as clear as typical protein motors, like kinesin[118] (which move along microtubule cables powered by the hydrolysis of ATP) and myosin[119] (which generate force in skeletal muscle through a power stroke mechanism), the replisome shares the important feature of directional motion. One double-stranded DNA chain enters the protein complex and two daughter double-stranded DNA chains leave it in a highly processive and one-dimensional fashion. The replisome uses the energy stored in the molecular bonds of nucleotide triphosphates (e.g., ATP) for its functions and directionality. The binding of the initiator proteins to the origins,[120,121] the unwinding of the transiently stable duplex DNA by the helicase and its translocation,[122] the loading of the sliding clamps,[15,123–126] and the polymerization reaction of nucleotide insertion by the DNA polymerase and its translocation are all processes that are fueled by the hydrolysis of nucleotide triphosphates (mainly ATP). All these processes drive the DNA through the replisome in one direction only.

Directional motion is of fundamental importance in nature since it lies at the heart of many biological processes in which chemical energy is converted into stepwise, linear, or rotary motion, for instance, in ion or polymer transport across membranes, or in the contraction of muscles. It is therefore of fundamental importance to study the basic concepts that underlie this principle, not only to understand the mechanisms by which natural systems convert chemical energy into directed motion, but also to design artificial molecular motors that can actually perform work.

In the macroscopic world, the first condition to obtain directional motion is to provoke motion in the first place. At the molecular level, however, this is not necessary because of the brownian motion, rotation, and translation intrinsic to molecules. Molecules constantly vibrate and collide as a result of the thermal energy present. Imagine being a molecule of alcohol in a glass of beer for just one second. You will have more than 10^{11} collisions with a neighboring water molecule and in the order of 10^{10} collisions with fellow alcohol molecules. The proton on your oxygen will exchange at least 1000 times (depending on the pH of the beer) with neighboring water or alcohol molecules. In the mean time you will go through billions of conformational changes and you will, on average, travel a distance of one micrometer (over a thousand times your own length), which does not reflect the speed of motion but is the outcome of a completely random path. It is clear that as a molecule of alcohol you are floating in a hurricane. Likewise, proteins should also be seen as 'kicking and screaming stochastic molecules'[127] despite the impression left by the beautiful and elegant static structures that so often decorate the covers of Nature, Science, Proceedings of the National Academy of Science, USA, and many other journals. The thermal noise power reversibly exchanged between the enzymatic motors and its environment is many orders of magnitude greater than the power provided by the chemical fuel to drive directed motion,[128] and achieving directional motion by converting energy into motion therefore seems like swimming in a hurricane. Natural system displaying directional motion circumvent this problem by not using the input of (mostly) chemical energy to work against the brownian motion, but rather use this energy to harness and direct the brownian motion in the wanted direction.

This is, for instance, illustrated by the translocation along the DNA by the DNA-polymerase. After the insertion of a new nucleotide into the newly formed DNA strand, a metal bound-PPi leaves the polymerase (Figure 2). The resulting conformational changes result in a temporary thermodynamically unfavorable situation of the polymerase on the newly formed DNA strand. The translocation to the next free nucleotide is then simply an energetically downhill process. The motion itself is caused by the brownian thermal fluctuations, whereas the directionality is the result of the conformational changes to the system caused by NTP-hydrolysis and the release of the metal-bound PP_i.

Linear unidirectional motion. In the field of supramolecular chemistry, a large number of molecular systems have been described that use an external energy source to achieve directional motion. The most frequently used approach to obtain linear motion is that of rotaxanes in which a macrocyclic component shuttles between two (or more) stations on the thread. In the absence of an external stimulus the average distribution of the macrocycle on the two stations will simply depend on the relative thermodynamic stabilities of the respective stations and the macrocycle, and is purely statistical. The shuttling rate in turn depends on both the thermodynamic stabilities between the stations and macrocycles, in addition to the properties of the linear part connecting the two stations. For instance, a higher affinity between a station and the macrocycle translates into lower dissociation rates of the macrocycle from the station and hence lower shuttling rates. More bulky or longer linear parts will also contribute to lower shuttling rates as observed in polymer threading studies. In the absence of an external stimulus the macrocycle will constantly shuttle as a result of the thermal energy induced brownian motion but the average rotaxane system will remain in equilibrium, which means that there is no net motion or directionality. Directional motion can be provided with the use of an external stimulus, which modifies the macrocycle or station and thereby changes the relative stabilities between the two and hence the energy landscape. As a result of this stimulus, the system will be temporarily out of equilibrium, after which the statistical distribution of macrocycle between the stations will move towards the new equilibrium and thus result in a net motion of macrocycle. It should be noted that such motion is still fully statistical. The macrocyclic component will continue shuttling back and forth between the stations, but as a result of the changed affinity for the stations caused by the external stimulus its residential time on the different stations has changed and therefore so to has the statistical distribution. The efficiency of the switching between the stations simply depends upon the relative thermodynamic stabilities of the respective station/macrocycle complexes before and after the stimulus. A large number of shuttles have been reported that are based on this principle using light,[129–138] heat,[139] electrons,[140–143] chemistry,[144–148] pH,[149–154] and binding[155–157] events as the external stimulus. In the case of reversible processes, the macrocyclic component can be switched back and forth between the different stations.

A nice example of directional motion of a photo-switchable shuttle (**18**) and its mechanisms has been reported recently by Paolo Raiteri,[158] a co-worker of, amongst others, J. Fraser Stoddart and Alberto Credi. This strategy, devised to obtain the photo-induced shuttling movement of a macrocycle between the two stations $A1^{2+}$ and $A2^{2+}$, is based on a "four-stroke" synchronized sequence of electronic and atomic processes (Figure 15A). Excitation of the photoactive unit P^{2+} by light (step 1) is followed by the transfer of an electron from this unit to $A1^{2+}$ (step 2), a process which competes with the intrinsic decay of the P^{2+} excited state (step 3). After the reduction of $A1^{2+}$, with the consequent "deactivation" of this station, the ring moves (step 4) by 1.3 nm towards $A2^{2+}$, a step that is in competition with the back electron transfer from $A1^{+}$ (still encircled) to the oxidized unit P^{3+} (step 5). Eventually, a back electron transfer from the "free" reduced station $A1^{+}$ to the oxidized unit P^{3+} (step 6) restores the electron-acceptor ability to this radical cationic station. As a consequence of this electronic reset, a thermally activated back movement of the ring from $A2^{2+}$ to $A1^{2+}$ takes place (step 7). By using different computational techniques, the authors calculated the free energy of the shuttling process and successfully reproduced the relative stability of the different molecular co/conformation (Figure 15B). These calculations clearly revealed how the energy of light is used to change the energy profile of the rotaxane system after which the brownian motion provokes the shuttling of the macrocycle. The study also revealed that the presence of the counter-ions have a rate-determining influence on the shuttling rate and, in addition, the authors put forward some relevant suggestions to increase the shuttling rates in the next generation of molecular shuttles.

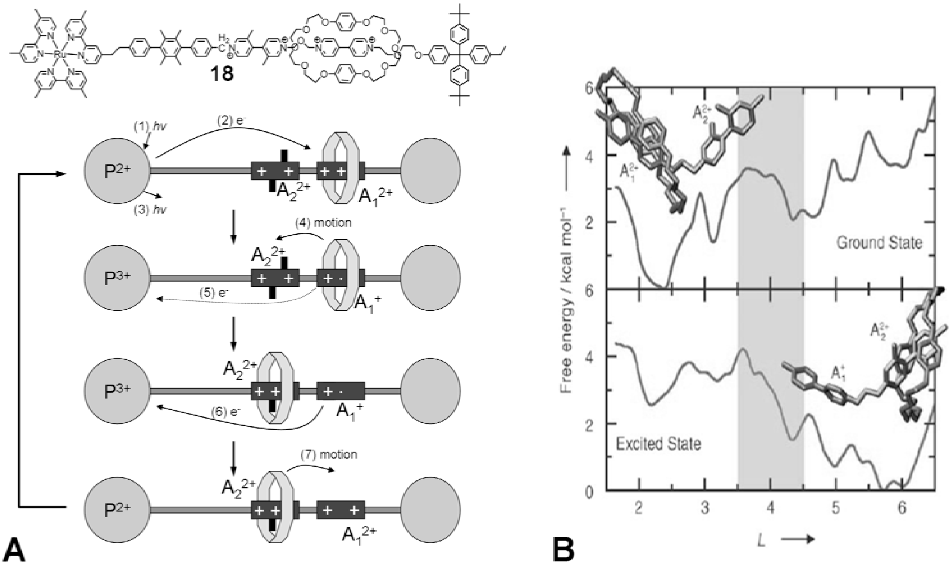

Figure 15. (A) Rotaxane **18**, which can be switched between stations A1 and A2 upon irradiation with light. (B) The energy profile of the system before irradiation (top) and after irradiation (bottom).

Directional rotational motion. Directional rotary molecular motors are another class of artificial molecular systems displaying directional motion.[159] In these systems a sequence of steps result in a full 360° unidirectional movement around a central axis. A number of studies have revealed that such a rotation can be achieved at the molecular level. For instance, by a sequence of chemical modifications that allow the 360° unidirectional rotation around a single bond (Figure 16A).[160] The best molecular examples of unidirectional rotary motion have been provided by Feringa and co-workers in which light is used to isomerise a carbon-carbon double bond from cis to trans. This results in the movement of bulky groups into unstable positions, which then thermally relax to achieve a 180° rotation (Figure 16B).[161] The rotation efficiencies of rotors were further increased and functional groups have been added that allow the integration of theses rotors into more complex systems (Figure 16C).[162–164] It must be noted that these rotary molecular machines do not rely on a supramolecular non-covalent approach, but on a chemical approach.

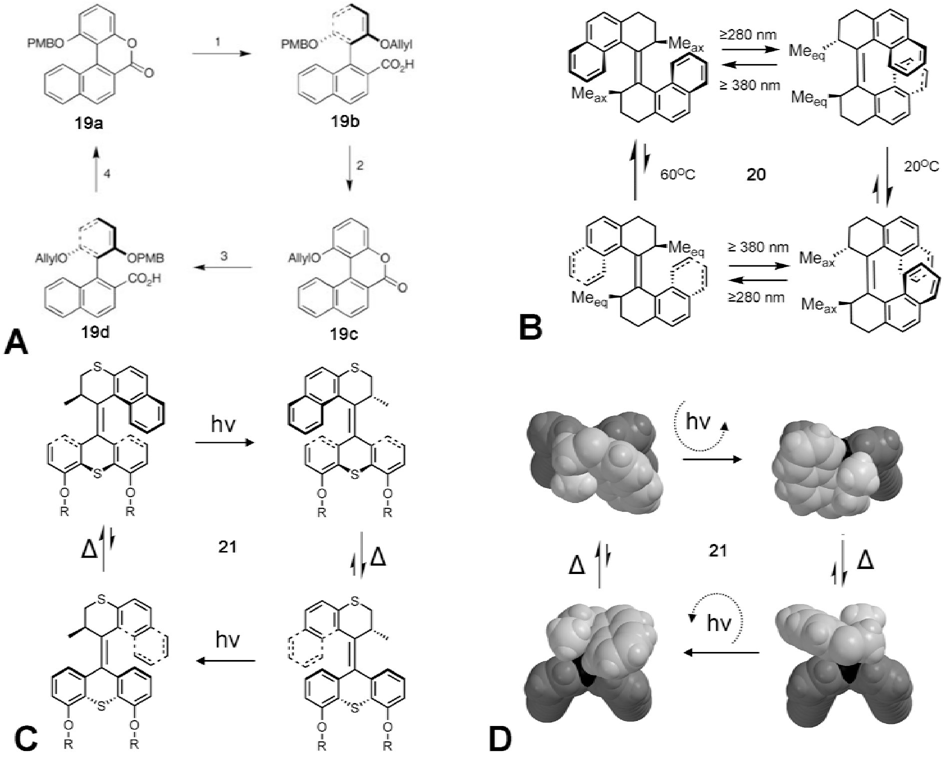

Figure 16. Examples of 360° unidirectional rotation around a single bond. (A) Four consecutive chemical reactions cause a 360° rotation. (B) First generation molecular rotor in which rotation is the result of light induced cis to trans isomerization, followed by thermal relaxation to a thermodynamically more favorable conformation. (C) Second generation molecular rotor based on the same principle as B. (D) Space filling model of C.

A supramolecular catenane system has been used to achieve 360° directional rotation of a macrocyclic ring around a the larger ring (Figure 17A), although chemical reactions (de-/re-silylations and de-/re-tritylations) were also needed to achieve this rotation.[165] As a result of these chemical reactions, the (brownian) motion of the macrocycle in the unwanted direction was mechanically obstructed. Although at first sight this method looks very complex, as multiple reaction and separation steps (with far from excellent yields) are needed to obtain the 360° rotation, nature presumably uses comparable principles in which temporary covalent bonds are utilized to restrict the motion of enzymatic systems in unwanted directions. Another delicate supramolecular example of a directional rotary machine is the multicomponent [3]catenane-based system (Figure 17B) in which unidirectional movement of the small rings along the larger ring can be achieved by applying light, chemical stimuli, or heat. In this process the backward brownian movement is prevented by the presence of the second ring.[166]

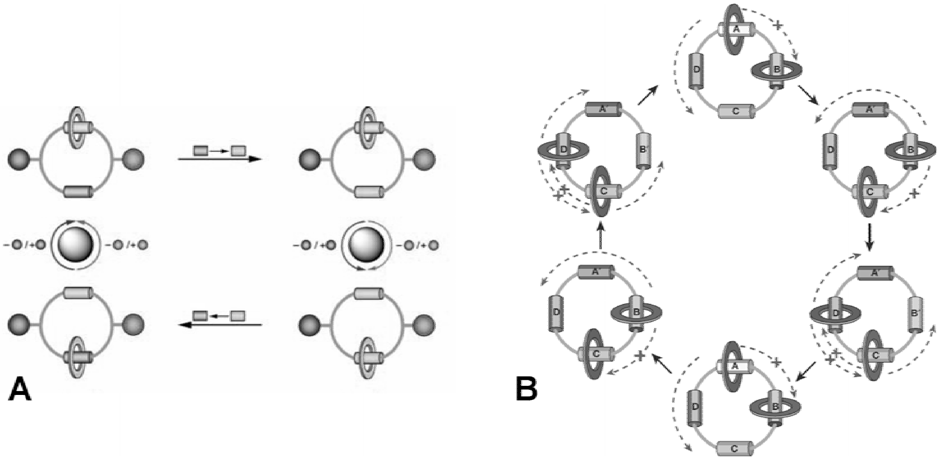

Figure 17. Cartoon representations of catenane systems capable of unidirectional 360° rotation.

Ratcheting. Many of the reported molecular motors (both artificial and natural) have been described as molecular ratchets. For instance brownian ratchets, information ratchets, Feynman ratchets, flashing ratchets, tilting ratchets, and rocking ratchets.[167–173] The term ratcheting originates from a well-known 'gedankenexperiment' published in 1912 by Smoluchowski,[174] which was reformulated and elucidated in the early 1960s by Richard Feynman in his famous "Lecture of Physics".[175] The idea was to use a ratchet/pawl mechanism from the macroscopic scale to direct the random thermal brownian motion in one direction. The machine consists of an axle with vanes at one of its ends and a ratchet at the other. The first impression is that the axle may only turn in one direction because of the pawl mechanism and a directed motion is generated by means of the thermal fluctuations. This would result in free perpetual motion, obviously violating the second law of thermodynamics. The paradox was explained by Feynman: Every single part of the device is subjected to the never-ending bombardments of equal intensity in all directions. It is therefore possible that, due to the brownian motion, the pawl would rise above the ratchet's teeth and cause turns in both directions with the same probability (the principle of microscopic reversibility). The net motion is then obviously zero. The devise as described could only work in the case of temperature differences between the compartments (the ratchet and the vanes) in which energy is obviously extracted from the temperature gradient in agreement with the second law. Other variants can also be imagined in which reversible chemical modifications to the ratchet's teeth next to the pawl temporarily restrict the motion in that direction. This would leave the ratchet no option but to rotate in the wanted direction. Although in this case the motion itself is the result of the thermal brownian fluctuations, the input of chemical energy is needed to harness the motion.

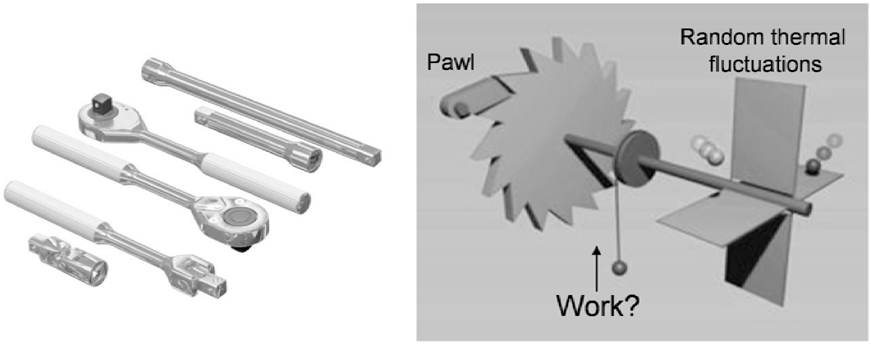

Figure 18. Brownian ratchet ‘gedankenexperiment’.

This thus implies that an external energy source is always needed to convert the thermal brownian energy into directed motion. One might argue that such mechanisms therefore have little similarities with macroscopic ratchets because the system needs to be constantly changed, and temporarily directed out of equilibrium, by the input of energy. The usage of the term brownian ratchet (or related terminologies, such as ratcheting) should therefore be seen in the light of this historic ‘gedankenexperiment’ and basically means nothing more than ‘harnessing the brownian motion in a wanted direction with the help of an external energy source’. This is furthermore demonstrated by the fact that in all the literature examples that explain directional motion with the use of such ratcheting mechanisms (both natural and artificial), external energy sources are applied to achieve this directional motion and the second law of thermodynamics is always obeyed. Also in the recent, intriguing articles by Dave Leigh and co-workers they present work in which they claim to be ratcheting particles energetically uphill,[176–177] the ‘particles’, however, always move toward equilibrium and not away from it.

Although it might have contributed to a better insight of the mechanisms responsible for directional motion, the term ratcheting may also cause some confusion. It is covered with a haze of ‘making the impossible possible’, which may give some the impression that (biological) molecular systems can do work for free.

In the light of the above it is worthwhile to discuss another intriguing approach to achieve unidirectional motion as reported recently by Harada and co-workers.[178–179] They observed that in the slippage of α-cyclodextrins (**23**) over a 2-methylpyridinium group in **22** the geometry of the formed pseudo-rotaxane was kinetically controlled (Figure 19A). Initially, the cyclodextrin preferentially adopted the **prA** orientation on the thread in which the smaller face of the cone shaped cyclodextrin faces the 2-methyl-pyridinium groups. This is the result of faster slippage over the 2-methylpyridinium group in that specific orientation (in which the wider part of the cyclodextrin slips first over the bulky group) compared to the other possible orientation (**prB**). The slippage in the opposite orientation (in which first the narrow part of the cyclodextrin slips over the bulky group) is considerably slower. Although the authors do not discuss the cause of this observation, this selectivity is most likely the result of more slippage transition state stabilizing interactions in one orientation compared to the other (hence a higher slippage rate).

Thermodynamically, both orientations of the formed pseudo-rotaxane are about equally as stable since, in time, both conformations become present in equal amounts when the system approaches equilibrium as can be seen in Figure 19B.

This study nicely shows how the specific orientations of blocking groups can kinetically control the geometry of the formed rotaxane and thereby the directionality of the formed complex. In their conclusion, the authors go even one step further and state: 'The controlling face of the ring component is expected to be efficient enough to realize the unidirectional movement in the rotaxane due to its non-symmetric structure. We are now studying the dynamics of α-CD (α-cyclodextrins) on the axle compounds with multi-stations in detail'.

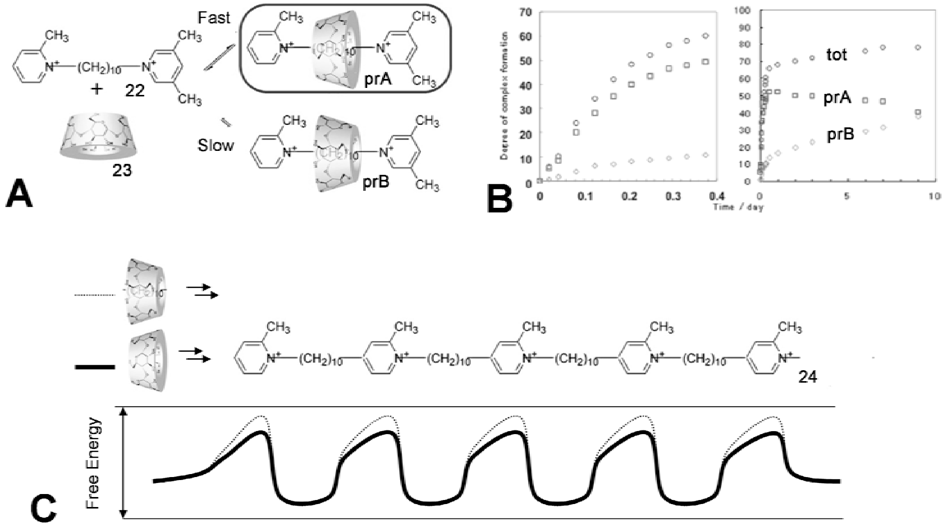

Figure 19. (A) Slippage of α-cyclodextrin (**23**) over the 2-methylpyridinium stopper of dumbbell-shaped **22** in two possible orientations. (B) Plot of pseudo-rotaxane formation in time in which the different pseudo-rotaxane isomers **prA** and **prB** and the total pseudo-rotaxane (**tot**) ratio are plotted over time. (C) Hypothetical molecule **24** and the energy-diagrams of slippage of the α-cyclodextrin in two different orientations.

In other words, the authors hoped to achieve unidirectional motion on the rotaxane by synthesizing a sequence of blocking groups as presented in Figure 19C. This last perspective is worthwhile discussing in detail because such unidirectional motion would imply the working of a real macroscopic like-'ratcheting' mechanism that does not need an external energy source. It is tempting to picture such a mechanism. Consider for instance that cyclodextrin **23** is made of a soft and flexible rubber and the bulky 2-methyl-pyridinium groups are rock-solid. At the macroscopic scale a lot more force would be needed to move the flexible rubber to the left than to the right, when in the **prA** orientation, on the multi-station molecule **24**. Unfortunately, such a mechanism would at the microscopic scale violate the principle of microscopic reversibility.

If we look at the simple energy diagram that can be drawn for the movement of a cyclodextrin over the multi station axle (Figure 19C), it immediately becomes clear that there is no ground for unidirectional motion since there is no downhill reaction coordinate. The slippage rate over the blocking groups can be faster depending on the orientation of the cyclodextrin but the movement will be faster in both directions. If the macrocycle does specifically move in one direction in the example presented in Figure 19C this would imply that the macrocycle moves energetically uphill, which violates the second law of thermodynamics and the principle of microscopic reversibility. It is therefore highly unlikely that the movement of cyclodextrins on the multi-station molecule will occur in one direction.

Likewise, directional rotation can not be obtained by attaching one or more chiral groups to a randomly rotating system in the hope that the chirality will provoke rotation in one direction only (a trick that might work in macroscopic machines). In order to obtain (uni)directional motion, an external energy source is always needed or the system has to be out of equilibrium at the start of the experiment.

3.5 Applications

The possibility to direct the motion of molecular shuttles and rotors has opened a new area of research where macroscopic movement can be achieved with the use of a bottom-up approach in which directional motion at the molecular level causes work on the macroscopic scale.

By attaching rotors and shuttles to surfaces and by controlling the movement of these stations it has been demonstrated that macroscopic objects can indeed be moved as a result of the directional motion on the molecular level.

A famous example is presented in Figure 20 in which liquids are being transported up a slope with a 12° incline.[180] This is the result of light induced switching of a surface-bound synthetic molecular rotaxane. Irradiation of the rotaxane moves the ring onto a fluoroalkane component, which concomitantly changes the surface energy and attracts the liquid. As a result, the droplet starts moving (in this case up a slope) in the direction where the surface is irradiated.

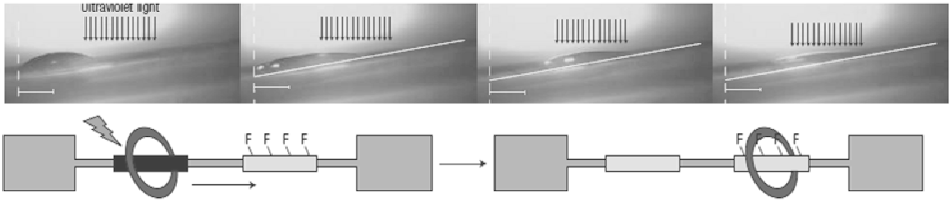

Figure 20. Transport of liquids up a slope (with a 12° incline) as a result of light induced shuttling of a surface-attached rotaxane, which changes the polarity of the surface in the irradiated zone.

Another elegant study revealed that a bistable [3]rotaxane structure can be employed as a molecular muscle (Figure 21A).[181] The surface of a cantilever beam was covered with rotaxanes, which were connected to the surface through the two macrocyclic parts. Oxidation of the redox-active stations of the rotaxane forced the rings to move to the inner neutral stations and resulted in contraction of the rotaxane, thereby bending the beam.

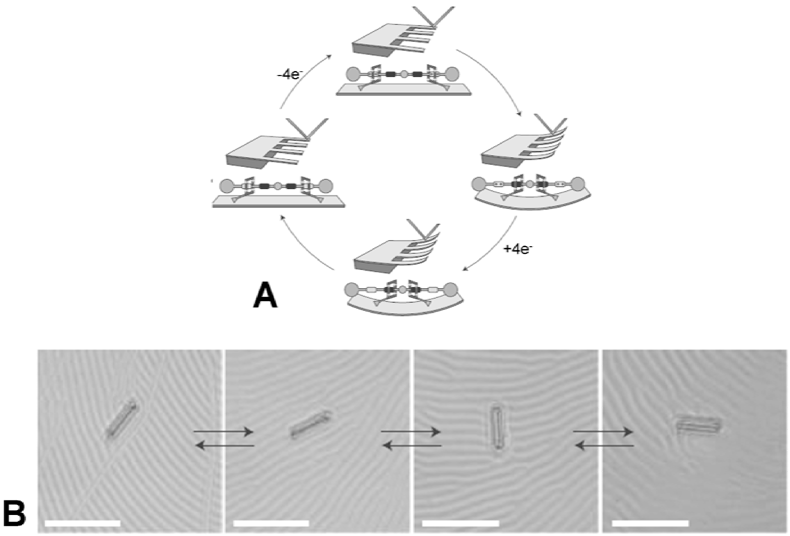

Figure 21. (A) Molecular muscle capable of bending cantilever beams by the cooperative action of linear rotaxane motors. (B) Glass rod rotating on a liquid crystal that is doped with a second-generation light-driven molecular motor during irradiation with ultraviolet light.

Feringa and co-workers showed that second generation light-driven molecular motors, which are attached to a surface, can rotate microscopic objects that exceed the nanometer in size by a factor of 10,000 with directional control (Figure 21B).[182] The rotation of surface textures and microscale objects was achieved by embedding the rotors in a liquid-crystal film. The energy provided by light changes the chirality of the motor, which is amplified through the liquid-crystalline host matrix.

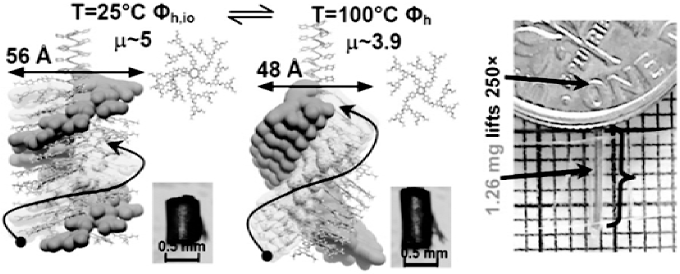

Figure 22. Helical dendronized cis-polyphenylacetylenes that undergo thermally induced cisoid-to-transoid conformational isomerisation, which can be used to obtain macroscopic motion.

The dendronized cis-polyphenylacetylenes (Cis-PPAs) reported by Percec and co-workers[183] are another approach to obtain macroscopic work from a bottom-up approach. These helical polymers undergo thermally induced cisoid-to-transoid conformational isomerism in bulk (Figure 22). Upon heating this material (so called ‘nanomechanical actuators’) a US dime could be lifted to illustrate that the properties of this material can be used to do work.

In addition to these, examples in which macroscopic motion is accomplished by the directional motion at the molecular level, other applications of directional artificial molecular systems are finding their way into the literature. For instance in molecular electronic memory devices,[184–186] but also in systems in which the pH induced switching of rotaxanes is used for controlled release of active molecules.[187]

4. Conclusion

The replisome can be seen as one of the most elegant natural enzymatic systems that features most of the aspects that dominate the field of supramolecular chemistry today. It is a molecular machine that does not only utilize many important concepts, such as supramolecular catalysis, cooperative binding interactions, translocation along polymers, and directional movement, but it moreover combines these different concepts to achieve replication of DNA with puzzling accuracy and speed. It is clear that the field of supramolecular chemistry is far from developing artificial systems as versatile as the replisome. One can not expect that artificial systems will ever display the replisome's proficiency, however, the field of supramolecular chemistry is still relatively young and has already made dramatic contributions to our understanding of supramolecar interactions in molecular systems. This is also due to the fact that most artificial systems are relatively simple compared to their complex natural counterparts, which allows the controlled studying of specific supramolecular interactions without getting lost in the complexity of the system.

From the large number of artificial systems displaying supramolecular catalytic activity, it has been demonstrated how nature uses the interiors of enzymes to provide the ideal microenvironment in terms of geometry and functionality to catalyze chemical reactions. The many examples of cooperative binding interactions observed in artificial systems have helped us in better understanding how binding events can both influence thermodynamic and kinetic events at remote sites. Many threaded artificial systems have been reported, and some have even been utilized to obtain directional motion.

It has thus become clear that specific aspects of biological systems can be, and have been, mimicked by relatively simple artificial systems and many concepts of the working mechanisms of the natural examples have been demonstrated and approved through these systems.

Ahead lays a fascinating path in which, with the use of artificial systems, many more relevant supramolecular mechanisms operating in nature will be unraveled. Moreover, new materials, catalysts, medicine, and other relevant molecular systems will be developed that rely on the supramolecular principles we have uncovered and are still uncovering today.

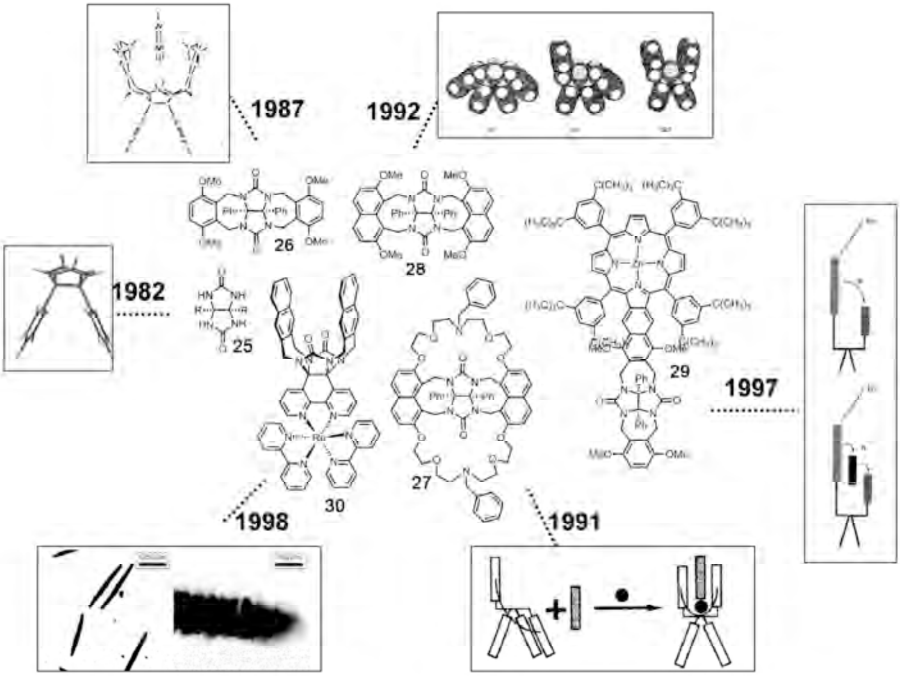

Figure 23. Evolution of molecules based on glycoluril developed in the Nolte group.

5. Scope of this thesis

To keep up with, and stay ahead, of the developments in the field of supramolecular chemistry the Nolte group has been working on a number of different synthetic and bio-hybrid research areas. One area that has been an important research subject through the history of the group focuses on supramolecular binding interactions to artificial molecular clips based on glycoluril. In time, the design and synthesis of these clips has had a gradual evolution, resulting in a large number of receptors and catalysts based on the binding pockets of phenyl substituted glycolurils displaying a variety of different supramolecular properties (Figure 23).[188–194] One specific type, the so-called porphyrin-clips (**31**), are macrocyclic molecules consisting of biphenyl-substituted glycolurils, which are covalently capped with a porphyrin through four oxyethylene spacers (Figure 24A).[195–196] These porphyrin-clips have been a very fruitful research subject covering a number of different subjects that are relevant to the field of supramolecular chemistry. The electron rich cavities of these molecules have been shown to be excellent receptors for a variety of aromatic substrates.[195] The presence of the porphyrin not only allows for the straightforward measuring of binding events (even at sub-micromolar concentrations) as a result of the strong UV-Vis and fluorescence properties of the porphyrin, it also allows the insertion of different metal ions. By inserting a zinc ion into the porphyrin surface, the porpyrin-clip can coordinate electron-donating ligands to the zinc (Figure 24C). It was shown that different pyridine derivatives can coordinate strongly to the zinc on the inside of the cavity, or weakly to the outside depending on the bulkiness of the pyridine derivatives and the stabilizing interactions on the macrocycle's interior. Moreover, strong positive cooperative binding effects have been observed for the combined binding of dimethylviologen and *tert*-butylpyridine with **Zn-31** (Figure 24D),[197] a feature that will be further investigated in this thesis.

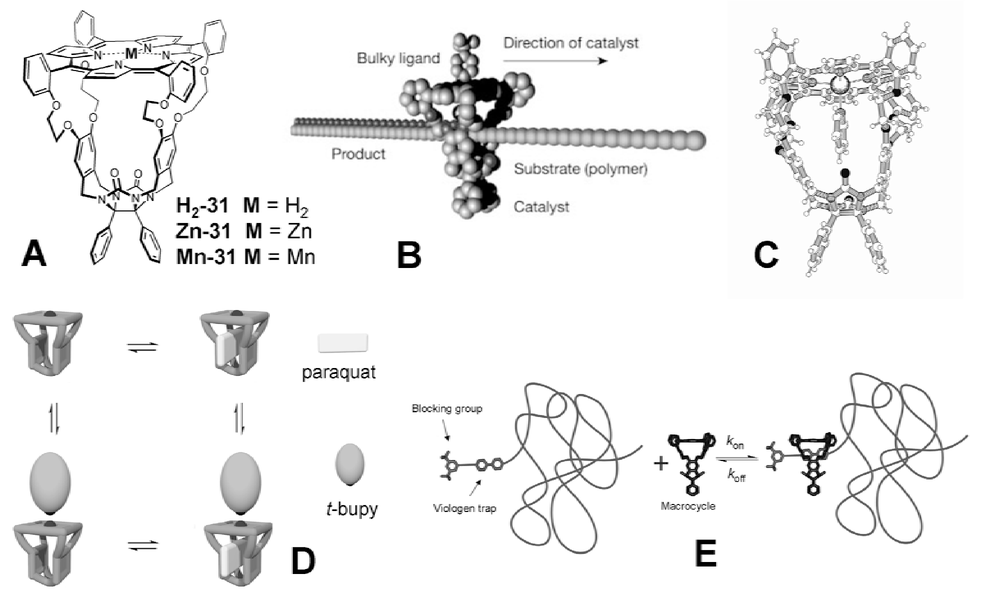

Figure 24. (A) Molecular structure of porphyrin clips. (B) **Mn-31** as an epoxidation catalyst. (C) X-ray structure of **Zn-31** in which a pyridine molecule is coordinated. (D) Cooperative binding of *t*-bupy and methyl-viologen (paraquat) to **Zn-31**. (E) Approach used to study the kinetics for threading polymers on **H$_2$-31** and **Zn-31**.

Insertion of a manganese ion into the porphyrin ring converts the porphyrin clip into a catalyst (**Mn-31**) that can perform epoxidation reactions on a variety of olefin substrates. It was shown that the conversion of cis-stilbene and trans-stilbene could be directed to the inside or the outside of the cavity by the use of coordinating pyridines (that also enhances the activity of the catalyst), which resulted in a different catalytic turnover frequency and (cis/trans) configuration of the formed epoxides.[198,199] Moreover, this same trick could be used on a polymer (polybutadiene) substrate. By shielding the outside of the catalyst **Mn-31** with bulky *tert*-butylpyridine the oxidation of the double bonds of the polymer occurred apparently on the inside of the cavity, as was suggested by careful analysis of the cis/trans ratios and turnover frequencies (Figure 24B).[200] This thus indicated that the porphyrin-clip can thread onto and move along polymeric substrates while performing catalytic action, thereby mimicking some of the important features of the replisome. To further investigate this threading of the porphyrin clip, a supramolecular approach was developed to allow the accurate measuring of this threading on different polymer substrates (Figure 24E). By end-capping polymers with viologen derivatives that have a bulky blocking group at the end, polymer substrates were obtained that contained a recognition site to which the porphyrin clips can bind only after threading onto and translocation along the polymer chain. It was demonstrated that the porphyrin-clips indeed traverse different (i.e., PolyTHF and polybutadiene) polymer derivatives and form pseudo-rotaxane complexes in which the porphyrin clip embraces the viologen recognition site simply by self assembly.[201] Careful kinetic measurements of the threading and de-threading properties moreover revealed a clear polymer length dependency in which the traversing of longer polymers cost extra entropy of activation ($\Delta S^{\neq}$). Later, the presence of outside- or inside-coordinating pyridine ligands was shown to have a critical influence on the threading kinetics of **Zn-31**.[202]

In this thesis some supramolecular aspects of porphyrin-clips, in particular cooperative binding, slippage, and threading, will be further investigated. A number of novel porphyrin-clips bearing extended spacers have been synthesized and will be discussed in Chapters 2 and 3. The binding properties of these more flexible receptors towards ligands and guests varying in size were evaluated and compared with the previously reported smaller and more rigid cavity. In addition, the cooperative binding effects of pyridines and viologen derivatives to these novel porphyrin-clips were investigated. Chapter 3, firstly, focuses on the accurate interpretation of such multi-component cooperative binding schemes and describes a method to obtain accurate values of cooperative effects. In addition, from a comparison between the different porphyrin-clips, the mechanisms of the cooperative binding effects could be identified. Chapter 4 describes the kinetics of the slippage of these novel porphyrin-clips over bulky substituents and the cooperative effects of the presence of pyridine ligands on these slippage-rates, which moreover provides useful information about the mechanisms governing the cooperative binding processes. In Chapter 5, investigations are described that concern the possibility of the small and rigid macrocycle to move over a folded polymer chain. In Chapter 6, a mechanism is proposed (a modified consecutive hopping model) that successfully describes the (previously reported and new) experimental threading results. The threading of one of the novel flexible porphyrin-clips is described in Chapter 7. The presented results clearly reveal that the nature of the macrocycle strongly influences the threading process and demonstrates that the motion of the larger but more flexible macrocycle along the polymer chain is slower than that of the smaller but more rigid cavity. Chapter 8 focuses on the surprising observation that chains of intermediate lengths (8−22 atoms) are traversed as fast as, or faster than, chains of smaller lengths. The experimental observations could be explained with the help of an 'intramolecular looping' mechanism. In Chapter 9, the results of a side-project focused on the guest induced switching between basket-handle porphyrin isomers are presented.

6. References

1. Langston, L. D.; O'Donnell, M. *Molecular Cell* **2006**, *23*, 155−160 and references therein.
2. Broyde, S.; Wang, L.; Rechkoblit, O.; Geacintov, N. E.; Patel, D. J. *Trends in Biochemical Sciences* **2008**, *33*, 209−219 and references therein.
3. Hamdan, S. M.; Joseph J. Loparo, J. J.; Takahashi, M.; Richardson, C. C.; Oijen, A. M. *Nature* **2009**, *457*, 336−340 and references therein.
4. Kornberg, A.; Baker, T. DNA Replication **1992** (New York: W.H. Freeman & Company).
5. Sclafani, R. A.; Holzen, T. M. *Annu. Rev. Genet.* **2007**, *41*, 237−280.
6. O'Donnell, M.; Kuriyan, J. *Curr. Opin. Struct. Biol.* **2006**, *16*, 35–41.
7. Duderstadt, K. E.; Berger, J. M. *Critical Reviews in Biochemistry and Molecular Biology* **2008**, 43, 163−187 and references therein.
8. Li, D.; Zhao, R.; Lilyestrom, W.; Gai, D.; Zhang, R.; Decaprio, J.A.; Fanning, E.; Jochimiak, A.; Szakonyi, G.; Chen, X. S. *Nature* **2003**, *423*, 512–518.
9. Tuteja, N.; Tuteja, R. *Eur. J. Biochem.* **2004**, *271*, 1849–1863.

10. Rothwell, P. J.; Waksman, G. *Advances in protein chemistry* **2005**, *71*, 401−440.
11. Johnson, A.; O'Donnell, M. *Annu. Rev. Biochem.* **2005**, *74*, 283–315.
12. Frick, D. N.; Richardson, C. C. *Annu. Rev. Biochem.* **2001**, *70*, 39−80.
13. Ogawa, T. ; Okazaki, T. ; *Annu. Rev. Biochem.* **1980**, *49*, 421−457.
14. Indiani, C.; O'Donnell, M. *Nature Reviews* **2006**, *7*, 751−761 and references therein.
15. Ason, B.; Handayani, R.; Williams, C. R.; Bertram, J. G.; Hingorani, M. M.; O'Donnell, M.; Goodman, M. F.; Bloom, L. B. *J. Biol. Chem.* **2003**, *278*, 10033−10040.
16. Steitz, T. A. *The EMBO Journal* **2006**, *25*, 3458–3468 and references therein.
17. Yoshizawa, M.; Tamura, M.; Fujita, M. *Science* **2006**, *312*, 251−254.
18. Vriezema, D. M.; Aragones, M. C.; Elemans, J. A. A. W.; Cornelissen, J. J. L. M.; Rowan, A. E.; Nolte, R. J. M. *Chem. Rev.* **2005**, *105*, 1445−1489 and references therein.
19. Machut, C.; Patrigeon, J.; Tilloy, S.; Bricout, H.; Hapiot, F.; Monflier, E. *Angew. Chem. Int. Ed.* **2007**, *46*, 3040−3042.
20. Yamaguchi, T.; Fujita, M. *Angew. Chem. Int. Ed.* **2008**, *47*, 2067−2069.
21. Bjerre, J.; Rousseau, C.; Marinescu, L.; Bols, M. *Appl. Microbiol. Biotechnol.* **2008**, *81*, 1−11 and references therein.
22. Slagt, V. F; Kaiser, P.; Berkessel, A.; Kuil, M.; Kluwer, A. M.; van Leeuwen, P. W. N. M.; Reek, J. N. H. *Eur. J. Inorg. Chem.* **2007**, 4653–4662 and references therein.
23. Fiedler, D.; van Halbeek, H.; Bergman, R. G.; Raymond K. N. *J. Am. Chem. Soc.* **2006**, *128*, 10240−10252.
24. Yang, C.; Mori, T.; Origane, Y.; Ko, Y. H.; Selvapalam, N.; Kim, K.; Inoue, Y. *J. Am. Chem. Soc.* **2008**, *130*, 8574−8575.
25. Pluth, M. D.; Bergman, R. G.; Raymond K. N.; *Angew. Chem. Int. Ed.* **2007**, *46*, 8587−8589.
26. Rebek, J. Jr. *Angew. Chem. Int. Ed.* **2005**, *44*, 2068−2078 and references therein.
27. Koblenz, T. S.; Wassenaar, J.; Reek, J. N. H. *Chem. Soc. Rev.* **2008**, *37*, 247–262 and references therein.
28. Rocha Gonsalves, A. M. A.; Pereira, M. M. *J. Mol. Cat. A Chem.* **1996**, *113*, 209−221.
29. Pluth, M. D.; Bergman, R. G.; Raymond, K. N. *Science* **2007**, *316*, 85−88.
30. Liu, J.-Q.; Wulff, G. *J. Am. Chem. Soc.* **2008**, *130*, 8044-8054.
31. Breslow, R.; Wernick, D. L. *Proc. Nat. Acad. Sci. USA* **1977**, *74*, 1303−1307.
32. Fiedler, D.; Leung, D. H.; Bergman, R. G.; Raymond, K. N. *Acc. Chem. Res.* **2005**, *38*, 351−360 and references therein.
33. Leung, D. H.; Bergman R. G.; Raymond, K. N. *J. Am. Chem. Soc.* **2006**, *128*, 9781−9797 and references therein.
34. Kang, J.; Santamaria, J.; Hilmersson, G.; Rebek, J. Jr. *J. Am. Chem. Soc.* **1998**, *120*, 7389−7390.
35. Changeux, J-.P.; Edelstein, S. J. *Science* **2005**, *308*, 1424−1428.
36. Williams, D. H.; Stephens, E.; O'Brien, D. P.; Zhou, M. *Angew. Chem. Int. Ed.* **2004**, *43*, 6596−6616.
37. Liu, Y.; Chen, Y. *Acc. Chem. Res.* **2006**, *39*, 681−691.
38. Garcés, J. L.; Acerenza, L.; Mizraji, E.; Mas, F. *J. Biol. Phys.* **2008**, *34*, 213–235.
39. Ricard, J.; Cornish-Bowden, A. *Eur. J. Biochem.* **1987**, *166*, 255−272.
40. Perutz, M. F.; Fermi, G.; Luisi, B.; Shaanan, B.; Liddington, R. C *Acc. Chem. Res.*, **1987**, *20*, 309−321.
41. Bloom, L. B. *Critical Reviews in Biochemistry and Molecular Biology* **2006**, *41*, 179−208.
42. Anand, S. P.; Khan, S. A. *Nucleic Acids Res.* **2004**, *32*, 3190−3197.
43. Cavanaugh, N. A.; Kuchta, R. D. *J. Biol. Chem.* **2009**, *284*, 1523−1532.
44. Leu, F.P.; Georgescu, R.; O'Donnell, M. *Mol. Cell* **2003**, *11*, 315–327.

45. Traylor, T. G.; Mitchell, M. J.; Ciconene, J. P.; Nelson, S. *J. Am. Chem. Soc.* **1982**, *104*, 4986–4989.
46. Tabushi, I.; Sasaki, T. *J. Am. Chem. Soc.* **1983**, *105*, 2901-2902.
47. Rebek, J., Jr.; Costello, T.; Marshall, L.; Wattley, R.; Gadwood, R. C.; Onan, K. *J. Am. Chem. Soc.***1985**, *107*, 7481–7487.
48. Ayabe, M.; Ikeda, A.; Kubo, Y.; Takeuchi, M.; Shinkai, S. *Angew. Chem. Int. Ed.* **2002**, *41*, 2790–2792.
49. Thordarson, P.; Bijsterveld, E. J. A.; Elemans, J. A. A. W.; Kasak, P.; Nolte, R. J. M.; Rowan. A. E. *J. Am. Chem. Soc.* **2003**, *125*, 1186–1187.
50. Rebek, J., Jr.; Wattley, R. V. *J. Am. Chem. Soc.* **1980**, *102*, 4853–4854.
51. Kobuke, Y.; Satoh, Y. *J. Am. Chem. Soc.* **1992**, *114*, 789–790.
52. Schneider, H.-J.; Ref, D. *Angew. Chem. Int. Ed.* **1990**, *29*, 1159–1160.
53. Baldes, R.; Schneider, H.-J. *Angew. Chem. Int. Ed.* **1995**, *34*, 321–323.
54. Heo, J.; Mirkin, C. A. *Angew. Chem. Int. Ed.* **2006**, *45*, 941–944.
55. Darbost, U.; Seneque, O.; Li, Y.; Bertho, G.; Marrot, J.; Rager, M.-N.; Reinaud, O.; Jabin, I. *Chem. Eur. J.* **2007**, *13*, 2078–2088.
56. Deng, D.; James, T. D.; Shinkai, S. *J. Am. Chem. Soc.* **1994**, *116*, 4567–4572.
57. Al-Sayah, M. H.; Branda, N. R. *Angew. Chem. Int. Ed.* **2000**, *39*, 945–947.
58. Tobey, S. L.; Anslyn, E. V. *J. Am. Chem. Soc.* **2003**, *125*, 10963–10970.
59. Takeuchi, M.; Ikeda, M.; Sugasaki, A.; Shinkai, S. *Acc. Chem. Res.* **2001,** *34*, 865–873 and references therein.
60. Ikeda, M.; Hasegawa, T.; Numata, M.; Sugikawa, K.; Sakurai, K.; Fujiki, M.; Shinkai, S. *J. Am. Chem. Soc.* **2007**, *129*, 3979–3988.
61. Wakabayashi, R.; Kubo, Y.; Hirata, O.; Takeuchi, M.; Shinkai, S. *Chem. Commun.* **2005**, *46*, 5742–5744.
62. Hirata, O.; Takeuchi, M.; Shinkai, S. *Chem. Commun.* **2005**, *30*, 3805–3807.
63. Ikeda, M.; Takeuchi, M.; Shinkai, S.; Tani, F.; Naruta, Y.; Sakamoto, S.; Yamaguchi, K. *Chemistry-A European Journal* **2002**, *8*, 5541–5550.
64. Takeuchi, M.; Imada, T.; Shinkai, S. *J. Am. Chem. Soc.* **1996**, *118*, 10658–10659.
65. Takeuchi, M.; Imada, T.; Shinkai, S. *Bull. Chem. Soc. Jpn.* **1998**, *71*, 1117–1123.
66. Sato, H.; Tashiro, K.; Shinmori, H.; Osuka, A.; Murata, Y.; Komatsu, K.; Aida, T. *J. Am. Chem. Soc.,* **2005**, *127*, 13086–13087.
67. Sato, H.; Tashiro, K.; Shinmori, H.; Osuka, A.; Aida, T. *Chem. Commun.*, **2005**, 2324–2326.
68. Lindsey, J. S. *New Journal of Chemistry* **1991**, *15*, 153–180.
69. Carrillo-Nava, E.; Mejia-Radillo, Y.; Hinz, H.-J. *Biochemistry* **2008**, *47,* 13153–13157.
70. Snir, Y.; Kamien, R. D. *Science* **2005**, *307*, 1067.
71. Lehn, J.-M. Supramolecular Chemistry: Concepts and Perspectives; VCH Publishers: Weinheim, **1995**.
72. Constable, E. In *Comprehensive Supramolecular Chemistry*; Atwood, J. L., Davies, J. E. D.; MacNicol, D. D.; Vogtle F.; Sauvage, J.-P.; Hosseini, M. W.; Eds.; Pergamon: Oxford, **1996**; Vol. 9, pp 213–252.
73. Pfeil, A.; Lehn, J.-M. *J. Chem. Soc., Chem. Commun.* **1992**, 838–840.
74. Taylor, P. N.; Anderson, H. L. *J. Am. Chem. Soc.* **1999**, *121*, 11538–11545.
75. Ercolani, G. *J. Am. Chem. Soc.* **2003**, *125*, 16097–16103.
76. Engelkamp, H.; Middelbeek, S.; Nolte R.J. M. *Science* **1999**, *284*, 785–788.
77. Van Hameren, R.; Schön, P.; van Buul, A.; Hoogboom, J.; Lazarenko, S. V.; Gerritsen, J. W.; Engelkamp, H.; Christianen, P. N, C.; Heus, H. A.; Maan, J. C.; Rasing, Th.; Speller, S.; Rowan, A. E.; Nolte, R. J. M.; Elemans, J. A. A. W. *Science* **2006**, *314*, 1433–1436.

78. Hirschberg, J. H.; Brunsveld, L.; Ramzi, A.; Vekemans, J. A. J. M.; Sijbesma, R. P.; E.W. Meijer, E. W. *Nature* **2000**, *407*, 167–170.
79. Messmore, B. W.; Sukerkar, P. A.; Stupp, S. I. *J. Am. Chem. Soc.* **2005**, *127*, 7992–7993.
80. George, S. J.; Tomovic, Z.; Smulders, M. M. J.; de Greef, T. F. A.; Leclere, P. E. L. G.; Meijer, E. W.; Schenning, A. P. H. J. *Angew. Chem. Int. Ed.* **2007**, *46*, 8206 –8211.
81. Yamamoto, Y.; Fukushima, T.; Suna, Y.; Ishii, N.; Saeki, A.; Seki, S.; Tagawa, S.; Taniguchi, M.; Kawai, T.; Aida, T. *Science* **2006**, *314*, 1761–1764.
82. Percec, V.; Gloddle, M.; Bera, T. K.; Miura, Y.; Shivanovskaya, I.; Singer, K. D.; Balagurusamy, V. S. K.; Heiney, P. A.; Schnell, I.; Rapp, A.; Spiess, H.-W.; Hudson, S. D.; Duan, H. *Nature*, **2002**, *419*, 384–387.
83. Stupp, S. I.; LeBonheur, V.; Walker, K.; Li, L. S.; Huggins, M.; Keser, M.; Arnstutz, A. *Science*, **1997**, 276, 384–389.
84. Smulders, M. M. J.; Schenning, A. P. H. J.; Meijer, E. W. *J Am. Chem. Soc.* **2008**, *130*, 606–611.
85. Hingorani, M. M.; O'Donnell, M. *Curr. Biol.* **2000**, *10*, R25–R29.
86. Mancini, E. J.; Kainov, D. E.; Grimes, J. M.; Tuma, R.; Bamford, D. H.; Stuart, D. I. *Cell* **2004**, *118*, 743–755.
87. Wickner, W.; Schekman, R. *Science* **2005**, *310*, 1452–1456.
88. Blobel, G. *ChemBioChem* **2000**, *1*, 86–102.
89. Rapoport, T. A. *Nature* **2007**, *450*, 663–669.
90. Aricó, F.; Badjic, J. D.; Cantrill, S. J.; Flood, A. H.; Leung, K. C.-F.; Liu, Y.; Stoddart J. F. *Topics in Current Chemistry* **2005**, *249*, 203–259 and references therein.
91. Dichtel, W. R.; Miljanic, O. S.; Zhang, W.; Spruell, J. M.; Patel, K.; Aprahamian, I.; Heath, J. R.; Stoddart, J. F. *Acc. Chem. Res.* **2008**, *41*, 1750–1761 and references therein.
92. Sauvage, J.P.; *Acc. Chem. Res.*, **1998**, *31*, 611–619 and references therein.
93. Safarowsky, O.; Windisch, B.; Mohry, A.; Vögtle. F. *Journal für praktische Chemie*, **2000**, *342*, 437–444 and references therein.
94. Ashton, P. R.; Bělohradsky, M.; Philp, D.; Stoddart, J. F. *J. Chem. Soc,.Chem. Commun.* **1993**, *16*, 1269–1274.
95. Ashton, P. R.; Bělohradsky, M.; Philp, D.; Spencer, N.; Stoddart, J. F. *J. Chem. Soc., Chem. Commun.* **1993**, *16*, 1274–1277.
96. Amabilino, D. B.; Ashton, P. R.; Bělohradsky, M.; Raymo, F. M.; Stoddart, J. F. *J. Chem. Soc., Chem. Commun.* **1995**, *7*, 751–753.
97. Bělohradsky, M.; Philp, D.; Raymo, F. M.; Stoddart, J. F. In *Organic Reactivity: Physical and Biological Aspects*; Golding, B. T.; Griffin, R. J.; Maskill, H.; Eds.; RSC Special Publication No. 148: Cambridge, **1995**; pp 387–398.
98. Ashton, P. R.; Ballardini, R.; Balzani, V.; Bělohradsky, M.; Gandolfi, M. T.; Philp, D.; Prodi, L.; Raymo, F. M.; Reddington, M. V.; Spencer, N.; Stoddart, J. F.; Venturi, M.; Williams, D. J. *J. Am. Chem. Soc.* **1996**, *118*, 4931–4951.
99. Ashton, P. R.; Baxter, I.; Fyfe, M. C. T.; Raymo, F. M.; Spencer, N.; Stoddart, J. F.; White, A. J. P.; Williams, D. J. *J. Am. Chem. Soc.* **1998**, *120*, 2297–2307.
100. Harada, A.; Kamachi, M. *Macromolecules* **1990**, *23*, 2821–2823.
101. Harada, A.; Kamachi, M. *J. Chem. Soc., Chem. Commun.* **1990**, 1322–1323.
102. Harada, A.; Li, J.; Kamachi, M. *Nature* **1992**, *356*, 325–327.
103. Gong C. G.; Gibson, H. W. *Curr. Opin. Solid State Mater. Sci.* **1997**, *2*, 647–652.
104. Wenz, G.; Steinbrunn M. B.; Landfester, K. *Tetrahedron* **1997**, *53*, 15575–15592.
105. Wenz, G. *Angew. Chem. Int. Ed. Engl.* **1994**, *33*, 803–822.
106. Nepogodiev S. A.; Stoddart, J. F. *Chem. Rev.* **1998**, *98*, 1959–1976.
107. Whang, D.; Kim, K. *J. Am. Chem. Soc.* **1997**, *119*, 451–452.

108. Bilig, T.; Oku, T.; Furusho, Y.; Koyama, Y.; Asai, S.; Takata, T. *Macromolecules* **2008**, *41*, 8496−8503.
109. Zhang, W. Y.; Dichtel, W. R.; Stieg, A. Z.; Benitez, D.; Gimzewski, J. K.; Heath, J. R.; Stoddart, J. F. *Proc. Nat. Acad. Sci.* **2008**, *105*, 6514−6519.
110. Harada, A.; Li, J.; Kamachi, M. *Nature* **1994**, *370*, 126−128.
111. Batten, S. R.; Dietrich-Buchecker, C.; Flapan, E.; Fujita, M.; Geerts, Y.; Gibson, H. W.; Gong, C.; Heim, C.; Kahn, O.; Mark, J. E.; Mathonière, C.; Ouahab, L.; Rapenne, G.; Raymo, F. M.; Robson, R.; Sauvage, J.-P.; Seeman, N. C.; Stoddart, J. F.; Stumpf, H. O.; Udelhofen, D.; Vögtle, F.; Wasserman, E. *Molecular Catenanes, Rotaxanes and Knots* Sauvage, J.-P.; Dietrich-Buchecker, C.; Eds.; Wiley-VCH: New York, **1999**.
112. Hubin, T. J.; Kolchinski, A. G.; Vance, A. L.; Busch, D. H. *Adv. Supramol. Chem.* **1999**, *5*, 237−357.
113. Raymo, F. M.; Stoddart, J. F. *Chem. Rev.* **1999**, *99*, 1643−1663 and references therein.
114. Wenz, G.; Gruber, C.; Keller, B.; Schilli, C.; Albuzat, T.; Muller, A. *Macromolecules* **2006,** *39,* 8021−8026.
115. Inoue, Y.; Miyauchi, M.; Nakajima, H.; Takashima, Y.; Yamaguchi, H.; Harada, A. *J. Am. Chem. Soc.* **2006**, *128*, 8994−8995.
116. Inoue, Y.; Kuad, P.; Okumura, Y.; Takashima, Y.; Yamaguchi, H.; Harada, A. *J. Am. Chem. Soc.* **2007**, *129*, 6396−6397.
117. Inoue, Y.; Miyauchi, M.; Nakajima, H.; Takashima, Y.; Yamaguchi, H.; Harada A. *Macromolecules* **2007**, *40*, 3256−3262.
118. Hirokawa, N. *Science* **1998**, *279*, 519-526.
119. Finer, J. T.; Simmons, R. M.; Spudich, J. A. *Nature* **1994**, *368*, 113−119.
120. Stenlund, A. *Nature Reviews* **2003**, *4*, 777−785.
121. Yu, J.; Ha, T.; Schulten, K. *Biophys. J.* **2007**, *93*, 3783−3797.
122. Tuteja, N.; Tuteja, R. *Eur. J. Biochem.* **2004**, *271*, 1849−1863.
123. Naktinis, V.; Onrust, R.; Fang, L. O'Donnell, M. *J. Biol. Chem.* **1995**, *270*, 13358−13365.
124. Bertram, J. G.; Hingorani, M. M.; Beechem, J. M.; O'Donnell, M.; Goodman, M. F.; Bloom, L.B. *J. Biol. Chem.* **2000**, *275*, 28413−28420.
125. Ason, B.; Bertram, J. G.; Hingorani, M. M.; Beechem, J. M.; O'Donnel, M.; Goodman, M. F.; Bloom, L. B. *J. Biol. Chem.* **2000**, *275*, 3006−3015.
126. Pietroni, P.; von Hippel, P. H. *J. Biol.Chem.* **2008**, *283*, 28338−28353.
127. Weber, G. *Adv. Protein Chem.* **1975**, *29*, 1–83.
128. Astumian, R. D. *Phys. Chem. Chem. Phys.* **2007**, *9*, 5067–5083.
129. Benniston, A. C.; Harriman, A. *Angew. Chem. Int. Ed. Engl.* **1993**, *32*, 1459−1461.
130. Benniston, A. C.; Harriman, A.; Lynch, V. M. *J. Am. Chem. Soc.* **1995**, *117*, 5275−5291.
131. Murakami, H.; Kawabuchi, A.; Kotoo, K.; Kunitake, M.; Nakashima, N. *J. Am. Chem. Soc.* **1997**, *119*, 7605−7606.
132. Armaroli, N.; Balzani, V.; Collin, J.-P.; Gaviňa, P.; Sauvage, J.-P.; Ventura, B. *J. Am. Chem. Soc*. **1999**, *121*, 4397−4408.
133. Wurpel, G. W. H.; Brouwer, A. M.; van Stokkum, I. H. M.; Farran, A.; Leigh, D. A. *J. Am. Chem. Soc*. **2001**, *123*, 11327−11328.
134. Brouwer, A. M.; Frochot, C.; Gatti, F. G.; Leigh, D. A.; Mottier, L.; Paolucci, F.; Roffia, S.; Wurpel, G. W. H. *Science* **2001**, *291*, 2124−2128.
135. Stanier, C. A.; Alderman, S. J.; Claridge, T. D. W.; Anderson, H. L. *Angew. Chem., Int. Ed.* **2002**, *41*, 1769−1772.
136. Altieri, A.; Bottari, G.; Dehez, F.; Leigh, D. A.; Wong, J. K. Y.; Zerbetto, F. *Angew. Chem. Int. Ed.* **2003**, *42*, 2296−2300.
137. Murakami, H.; Kawabuchi, A.; Matsumoto, R.; Ido, T.; Nakashima, N. *J. Am. Chem. Soc.* **2005**, *127*, 15891−15899.

138. Balzani, V.; Clemente-León, M.; Credi, A.; Ferrer, B.; Venturi, M.; Flood, A. H.; Stoddart, J. F. *Proc. Natl. Acad. Sci. U.S.A.* **2006**, *103*, 1178–1183.
139. Bottari, G.; Dehez, F.; Leigh, D. A.; Nash, P. J.; Pérez, E. M.; Wong, J. K. Y.; Zerbetto, F. *Angew. Chem. Int. Ed.* **2003**, *42*, 5886–5889.
140. Bissell, R. A.; Córdova, E.; Kaifer, A. E.; Stoddart, J. F. *Nature* **1994**, *369*, 133–136.
141. Altieri, A.; Gatti, F. G.; Kay, E. R.; Leigh, D. A.; Martel, D.; Paolucci, F.; Slawin, A. M. Z.; Wong, J. K. Y. *J. Am. Chem. Soc.* **2003**, *125*, 8644–8654.
142. Long, B.; Nikitin, K.; Fitzmaurice, D. *J. Am. Chem. Soc.* **2003**, *125*, 15490–15498.
143. Steuerman, D. W.; Tseng, H.-R.; Peters, A. J.; Flood, A. H.; Jeppesen, J. O.; Nielsen, K. A.; Stoddart, J. F.; Heath, J. R. *Angew. Chem. Int. Ed.* **2004**, *43*, 6486–6491.
144. Gong, C.; Gibson, H. W. *Angew. Chem. Int. Ed. Engl.* **1997**, *36*, 2331–2333.
145. Jiménez, M. C.; Dietrich-Buchecker, C.; Sauvage, J.-P *Angew. Chem., Int. Ed.* **2000**, *39*, 3284–3287.
146. Tseng, H.- R.; Vignon, S. A.; Stoddart, J. F. *Angew. Chem. Int. Ed.* **2003**, *42*, 1491–1495.
147. Nørgaard, K.; Laursen, B. W.; Nygaard, S.; Kjaer, K.; Tseng, H.-R.; Flood, A. H.; Stoddart, J. F.; Bjørnholm, T. *Angew. Chem. Int. Ed.* **2005**, *44*, 7035–7039.
148. Barrell, M. J.; Leigh, D. A.; Lusby, P. J.; Slawin A. M. Z. *Angew. Chem. Int. Ed.* **2008**, *47*, 8036–8039.
149. Martínez-Díaz, M.-V.; Spencer, N.; Stoddart, J. F. *Angew. Chem. Int. Ed. Engl.* **1997**, *36*, 1904–1907.
150. Marlin, D. S.; González Carbrera, D.; Leigh, D. A.; Slawin, A. M. Z. *Angew. Chem. Int. Ed.* **2006**, *45*, 77–83.
151. Badjic, J. D.; Balzani, V.; Credi, A.; Silvi, S.; Stoddart, J. F. *Science* **2004**, *303*, 1845–1849.
152. Keaveney, C. M.; Leigh, D. A. *Angew. Chem. Int. Ed.* **2004**, *43*, 1222–1224.
153. Badjic, J. D.; Ronconi, C. M.; Stoddart, J. F.; Balzani, V.; Silvi, S.; Credi, A. *J. Am. Chem. Soc.* **2006**, *128*, 1489–1499.
154. Crowley, J. D.; Leigh, D. A.; Lusby, P. J.; McBurney, R. T.; Perret-Aebi, L.-E.; Petzold, C.; Slawin, A. M. Z.; Symes, M. D. *J. Am. Chem. Soc.* **2007**, *129*, 15085–15090.
155. Vignon, S. A.; Jarrosson, T.; Iijima, T.; Tseng, H.-R.; Sanders, J. K. M.; Stoddart, J. F. *J. Am. Chem. Soc.* **2004**, *126*, 9884–9885.
156. Marlin, D. S.; González Carbrera, D.; Leigh, D. A.; Slawin, A. M. Z. *Angew. Chem. Int. Ed.* **2006**, *45*, 77–83.
157. Marlin, D. S.; González Carbrera, D.; Leigh, D. A.; Slawin, A. M. Z. *Angew. Chem. Int. Ed.* **2006**, *45*, 1385–1390.
158. Raiteri, P.; Bussi, G.; Cucinotta, C. S.; Credi, A.; Stoddart, J. F.; Parrinello, M. *Angew. Chem. Int. Ed.* **2008**, *47*, 3536–3539.
159. Ross Kelly, T.; De Silva, H.; Silva, R. A. *Nature* **1999**, *401*, 150–152.
160. Fletcher, S. P.; Dumur, F.; Pollard, M. M.; Feringa, B. L. *Science* **2005**, *310*, 80–82.
161. Koumura, N.; Zijlstra, R. W. J.; van Delden R. A.; Harada, N.; Feringa, B. L. *Nature* **1999**, *401*, 152–155.
162. Feringa, B. L.; van Delden, R. A.; ter Wiel, M. K. J. *Pure Appl. Chem.* **2003**, *75*, 563–575.
163. Koumura, N.; Geertsema, E. M.; van Gelder, M. B.; Meetsma, A.; Feringa, B, L. *J. Am. Chem. Soc.* **2002**, *124*, 5037–5051.
164. van Delden, R. A.; ter Wiel, M. K. J.; Pollard, M. M.; Vicario, J.;. Koumura, N.; Feringa, B. L. *Nature* **2005**, *437*, 1337–1340.
165. Hernandez, J. V.; Kay, E. R.; Leigh, D. A. *Science* **2004**, *306*, 1532–1537.
166. Leigh, D. A.; Wong, J. K. Y.; Dehez, F.; Zerbetto, F. *Nature* **2003**, *424*, 174–179.
167. Astumian, R. D. *Science* **1997**, *276*, 917–922.
168. Jülicher, F.; Ajdari, A.; Prost, J. *Rev. Mod. Phys.* **1997**, *69*, 1269–1281.

169. Reimann, P. *Phys. Rep.* **2002**, *361*, 57–265.
170. Reimann, P.; Hänggi, P. *Appl. Phys. A* **2002**, *75*, 169–178.
171. Parrondo, J. M. R.; De Cisneros, B. J. *Appl. Phys. A* **2002**, *75*, 179–191.
172. Gabrys, B. J.; Pesz, K.; Bartkiewicz, S. J. *Physica A* **2004**, *336*, 112–122.
173. Linke, H.; Downton, M. T.; Zuckermann, M. J. *Chaos* **2005**, *15*, 026111.
174. Smoluchowski. M. *Physik. Zeitschr.* **1912**, *13*, 1069.
175. Feynman, R. P.; Leighton, R. B.; Sands. M. *The Feynman Lectures Of Physics*, volume 1. Addison Wesley, Reading, MA, **1963**.
176. Chatterjee, M. N.; Kay, E. R.; Leigh, D. A. *J. Am. Chem. Soc.* **2006**, *128*, 4058–4073.
177. Alvarez-Prez, M.; Goldup, S. M.; Leigh, D. A.; Slawin, A. M. Z. *J. Am. Chem. Soc.* **2008**, *138*, 1836–1838.
178. Yamaguchi, H.; Oshikiri, T.; Harada, A. *J. Phys. Condens. Matter* **2006**, *18*, S1809–S1816.
179. Oshikiri, T.; Takashima, Y.; Yamaguchi, H.; Harada, A. *J. Am. Chem. Soc.* **2005**, *127*, 12186–12187.
180. Berna, J.; Leigh, M.; Lubomska, M.; Mendoza, S. M.; Perez, E. M.; Rudolf. P.; Teoberto, G.; Zerbetto, F. *Nature Mater.* **2005**, *4*, 704–710.
181. Liu, Y.; Flood, A. H.; Bonvallet, P. A.; Vignon, S. A.; Northrop, B. H.; Tseng, H. R.; Jeppesen, J. O.; Huang, T. J.; Brough, B.; Baller, M.; Magonov, S.; Solares, S. D.; Goddard, W. A.; Ho, C. M.; Stoddart, J. F. *J. Am. Chem. Soc.* **2005**, *127*, 9745–9759.
182. Eelkema, R.; Pollard, M. M.; Vicario, J.; Katsonis, N. H.; Serrano-Ramon, B.; Baaistiansen, C. W. M.; Broer, D.; Feringa, B. L. *Nature* **2006**, *440*, 163.
183. Rudick, J. G.; Percec, V. Macromol. Chem. Phys. **2008**, *209*, 1759–1768.
184. Steuerman, D. W.; Tseng, H.-R.; Peters, A. J.; Flood, A. H.; Jeppesen, J. O.; Nielsen, K. A.; Stoddart, J. F.; Heath, J. R. *Angew. Chem. Int. Ed.* **2004**, *43*, 6486–6491.
185. Flood, A. H.; Stoddart, J. F.; Steuerman, D. W.; Heath, J. R. *Science* **2004**, *306*, 2055–2056.
186. Green, J. E. et al. *Nature* **2007**, *445*, 414–417.
187. Angelos, S.; Yang, Y.-W.; Patel, K.; Stoddart, J. F.; Zink, J. I. *Angew. Chem. Int. Ed.* **2008**, *47*, 2222–2226.
188. Sijbesma, R. P.; Nolte, R. J. M. *J. Am. Chem. Soc.* **1991**, *113*, 6695–6696.
189. Sijbesma, R. P.; Nolte, R. J. M. *Recl. Trav. Chim. Pays-Bas* **1993**, *112*, 643–647.
190. Rowan, A. E.; Elemans, J. A. A. W.; Nolte, R. J. M. *Acc. Chem. Res.* **1999**, *32*, 995–1006.
191. Reek, J. N. H.; Rowan, A. E.; de Gelder, R.; Beurskens, P. T.; Crossley, M. J.; de Feyter, S.; de Schryver, F.; Nolte R. J. M. *Angew. Chem., Int. Ed. Engl.* **1997**, *36*, 361–363.
192. Schenning, A. P. H. J.; de Bruin, B.; Feiters, M. C.; Nolte, R. J. M. *Angew. Chem., Int. Ed. Engl.* **1994**, *33*, 1662–1663.
193. Van Nunen, J. L. M.; Folmer, B. F. B.; Nolte R. J. M. *J. Am. Chem. Soc.* **1997**, *119*, 283–284.
194. Van Nunen, J. L. M.; Stevens, R. S. A.; Picken, S. J.; Nolte R. J. M. *J. Am. Chem. Soc.* **1994**, *116*, 8825–8826.
195. Elemans, J. A. A. W.; Claase, M. B.; Aarts, P. P. M.; Rowan, A. E.; Schenning, A. P. H. J.; Nolte, R. J. M. *J. Org. Chem.* **1999**, *64*, 7009–7016.
196. Rowan, A. E.; Aarts, P. P. M.; Koutstaal, K. W. M. *Chem. Commun.* **1998**, 611–612.
197. Thordarson, P.; Coumans, R. G. E.; Elemans, J. A. A. W.; Thomassen, P. J.; Visser, J.; Rowan, A. E.; Nolte, R. J. M. *Angew. Chem. Int. Ed.* **2004**, *43*, 4755–4759.
198. Elemans, J. A. A. W.; Bijsterveld, E. J. A.; Rowan, A. E.; Nolte. R. J. M. *Eur. J. Org. Chem.* **2007**, 751–757.
199. Elemans, J. A. A. W.; Bijsterveld, E. J. A.; Rowan, A. E.; Nolte, R. J. M. *Chem. Commun.* **2000**, 2443–2444.

200. Thordarson, P.; Bijsterveld, E. J. A.; Rowan, A. E.; Nolte, R. J. M. *Nature* **2003**, *424*, 915−918.
201. Coumans, R. G. E.; Elemans, J. A. A. W.; Nolte, R. J. M.; Rowan, A. E. *Proc. Natl. Acad. Sci.* **2006**, *103*, 19647−19651.
202. Hidalgo Ramos, P. ; Coumans, R. G. E.; Deutman, A. B. C.; Smits, Jan. M. M.; de Gelder, R.; Elemans, J. A. A. W.; Nolte, R. J. M.; Rowan, A. E. *J. Am. Chem. Soc.* **2007**, *129*, 5699−5702.

2

Flexible Porphyrin Receptors derived from Diphenylglycoluril. Synthesis, Conformational analysis, and Binding properties

1. Introduction

In search for new synthetic catalysts that function according to the principles of enzymes, a number of catalytically active receptor molecules have been developed and described in the literature,[1] many of which consist of metal porphyrins that are covalently connected to a substrate recognizing cavity.[2–12] Previously, the so-called porphyrin clips have been described as cavity molecules based on diphenylglycoluril capped with a porphyrin roof (**$H_2$2**, **$H_2$3**, Chart 1).[13] Insertion of a manganese ion into the porphyrin plane of **$H_2$2** to give **Mn2** turned the receptor molecule into a catalyst for the epoxidation of alkenes. The catalysis reaction was forced to take place inside the cavity of the catalyst when the outside was shielded by coordinating a bulky axial ligand to the manganese center.[14,15] Using this approach, processive enzymes that facilitate the manipulation of the biopolymers DNA and RNA, such as λ-exonuclease, have been mimicked.[16] It was shown that receptor **Mn2** was capable of oxidizing the double bonds of a polybutadiene strand while the polymer was in the process of threading through the cavity of the catalyst.[17] Unlike many of the natural processive catalysts that operate in a sequential fashion, the oxidation of polybutadiene by **Mn2** seemed to be a random process since the rate of movement over the polymer was several orders of magnitude larger than the turnover rate of the catalytic reaction.[18]

With the aim to further control the threading of the catalysts by means of implying a more induced fit-like binding of the receptor during the process of catalysis, a new flexible porphyrin clip molecule **1** (Chart 1) was designed, which has a larger and more flexible cavity than that of receptor **2**. By studying **1** and its catalytically active manganese derivative it is expected that new insights into the working mechanisms of the threading and catalysis will be obtained. In this chapter, the synthesis, conformational analysis, and binding properties of this new, flexible porphyrin clip molecule will be described.

Chart 1

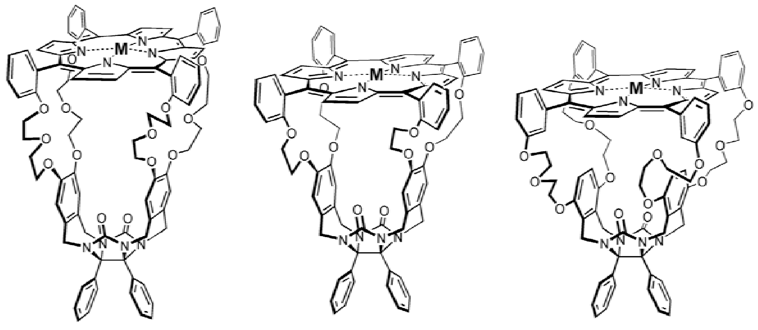

$H_2$1 M = H_2
Zn1 M = Zn
Mn1 M = Mn

$H_2$2 M = H_2
Zn2 M = Zn
Mn2 M = Mn

$H_2$3 M = H_2
Zn3 M = Zn

2. Results and discussion

2.1 Design

A catalyst ideally consists of a substrate-recognizing binding region that is located in the proximity of a catalytically active site. Interactions between the substrate(s) and the binding region during the process of catalysis might result in regio- or stereoselectivity. This concept has been shown to work in many examples of supramolecular catalysts[19–23] and templating capsules.[24–27] In our group it has been shown that the cis/trans ratio of the formed epoxides in the oxidation of olefins by **Mn2** can be influenced by directing the catalysis towards the inside or the outside of its cavity.[14,17] In natural enzymatic systems, the mechanisms of substrate recognition, catalysis, and product release are explained in terms of 'lock-and-key',[28,29] induced-fit,[30] and conformational selection,[31,32] or a combination of all three. The crucial steps in enzymatic catalysis are high selectivity for the substrate, the ability to lower the activation energy of the transition state of the reaction compared to an uncatalyzed reaction, and little affinity of the catalyst for the product, thereby promoting product release. Whereas the induced-fit theory is most frequently used to explain the working mechanisms of many natural enzymatic systems, so far most synthetic supramolecular catalysts function according to a 'lock-and-key' mechanism in which the preorganization of a rigid molecular receptor determines the binding of substrate molecules and only little conformational changes are possible during the process of catalysis. **Mn2** is a very rigid cavity molecule and therefore operates in a lock-and-key fashion. Sanders has suggested[33] that the rigidity of most synthetic supramolecular catalysts is a drawback and that more flexible systems might well improve the catalytic performance because they allow a conformational response to catalytic processes, comparable to enzymes in nature. In the Nolte group a porphyrin receptor **3** (Chart 1), which has larger and more flexible spacers connected to the meta-positions of the porphyrin phenyl groups and to the *o*-xylylene positions of the cavity side-walls, has been synthesized.[13] It shows a high degree of induced-fit behavior for the binding of guest molecules,[13] but the association constants for a large number of derivatives are significantly lower than those observed for the binding of guests in rigid receptor **2** because the cavity of **3** is too wide to provide ideal stabilizing interactions to the guest molecules. To obtain a catalyst that still binds guests strongly to the inside of its cavity while applying an induced fit-mechanism, receptor **1** was designed. It has extended crown ether spacers connected to the ortho-phenyl positions of the porphyrin. The molecule is expected to have a larger, but narrower cavity than receptor **3**, which will be better suited for the complexation of guest molecules. The extra oxyethylene unit in the spacer will provide the molecule with the flexibility needed for induced-fit binding.

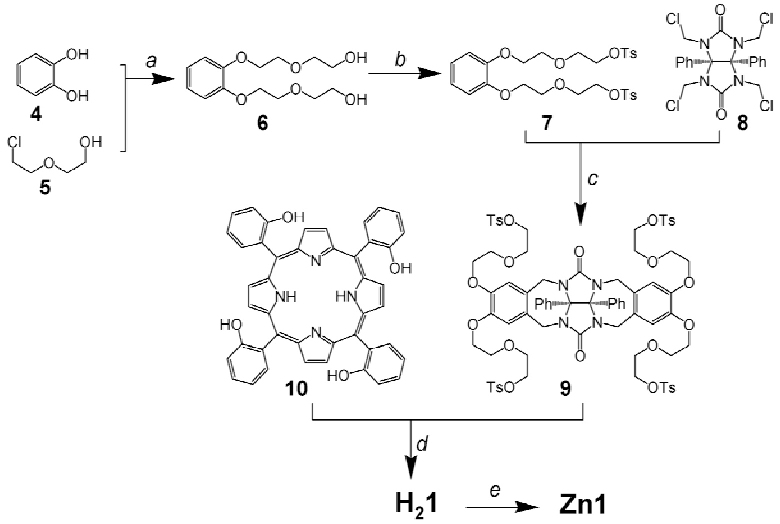

Scheme 1 Synthesis of **$H_2$1** and **Zn1**. Reagents and conditions: a) K_2CO_3 , DMF, 100 °C, 12 h, 98%; b) TosCl, pyridine, 2 h, 62%; c) $SnCl_4$, 1,2-dichloroethane, reflux, 16 h, 23%; d) K_2CO_3, DMF, 110 °C 10–15%; e) $Zn(OAc)_2\cdot 2H_2O$, MeOH/DCM 1:1 (v/v) 96%.

2.2 Synthesis

The synthesis of **$H_2$1** (Scheme 1) involved the alkylation of catechol (**4**) with 2-(2-chloroethoxy)-ethanol (**5**) in the presence of K_2CO_3 in DMF to form diol **6**[34] in nearly quantitative yield. Diol **6** was treated with *p*-toluenesulfonyl chloride in pyridine to give the ditosylate **7** in a yield of 62%.[35] A Friedel Crafts alkylation between tetrakis(chloromethyl) diphenylglycoluril **8**[36] and ditosylate **7** in 1,2-dichloroethane, using tin tetrachloride as a Lewis acid catalyst, gave the tetratosylated clip **9** in a moderate 23% yield. In addition to **9**, a mono-walled compound and a mixture of isomers of **9** were obtained in which the aromatic side-walls were not connected by the 4,5-positions but by the 3,4-positions. The different products could be separated and purified by column chromatography followed by precipitation in *n*-hexane. Tetratosylate **9** was reacted with 5,10,15,20-tetrakis(*meso-o*-hydroxyphenyl)porphyrin **10** in DMF under basic conditions to give the free base porphyrin clip **$H_2$1** in a 10–15% yield after purification by column chromatography, preparative TLC, and precipitation in *n*-pentane. **$H_2$1** was nearly quantitatively converted to its corresponding zinc derivative **Zn1** by the reaction with an excess of zinc acetate dihydrate in a 1:1 (v/v) mixture of dichloromethane and methanol.

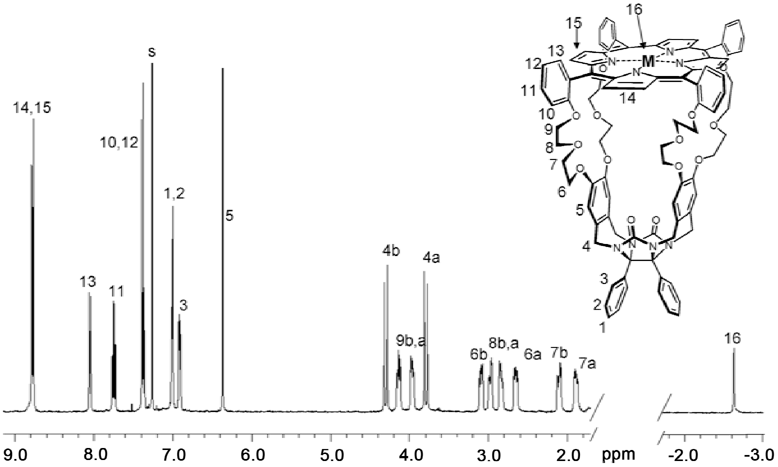

Figure 1. Proton assignment in the 400 MHz ^{1}H-NMR spectrum of **$H_2$1** in $CDCl_3$.

2.3 Structural analysis

The structure of **$H_2$1** was elucidated with ^{1}H-NMR spectroscopy. All proton resonances could be assigned with the help of COSY and 2D-ROESY techniques. The ^{1}H-NMR spectrum of **$H_2$1** in $CDCl_3$ at room temperature (Figure 1) reveals C_{2v} symmetry of the compound. For all eight oxyethylene protons in the spacer region separate signals could be observed. Compared to the oxyethylene proton signals of ditosylate **7**, the proton signals of H-6, H-7, and H-8 exhibit a large upfield shift of 1 to 2 ppm, which can be ascribed to the shielding effect of the porphyrin ring current, suggesting that these protons are all in the direct proximity of the porphyrin surface. Molecular modeling calculations of **$H_2$1** based on the NOE constraints observed in the 2D-ROESY spectrum predicted an average non-symmetric conformation for the molecule, in which the clip framework is arranged in a twisted fashion underneath the porphyrin roof with the crown ether spacers filling the space between these two moieties (Figure 2). This non-symmetry is not observed in the ^{1}H-NMR spectrum at room temperature because the exchange of the different conformations is fast on the NMR timescale. Variable temperature NMR experiments in $CDCl_3$ demonstrated that it is possible to freeze out non-symmetrical conformations of the molecule. In the 500 MHz ^{1}H-NMR spectrum in $CDCl_3$ at 218 K, a doubling of the shifts was observed for protons throughout the molecule (Figure 3b). The downfield shifted resonances of the spacer protons (most clearly those of H-7a and H-7b, which are in closest proximity to the porphyrin) suggested that, at a lower temperature, they are further away from the porphyrin plane, which indicated that the molecule has adopted a more open conformation.

The insertion of a zinc ion into the porphyrin to give **Zn1** causes a broadening of signals over the entire range of the ^{1}H-NMR spectrum in $CDCl_3$, most dramatically for the signals of the side-wall protons H-5, the phenyl proton H-3, and the benzylic protons H-4a and H-4b (Figure 3). These signals are shifted upfield compared to the signals of **$H_2$1**, which indicated that in **Zn1** the clip moiety is located closer to the porphyrin roof. This effect is proposed to be the result of intramolecular coordination between one of the crown ether oxygen atoms of the spacer and the zinc ion in the porphyrin. A 2D ROESY NMR measurement showed NOE contacts between many of the crown ether protons and the porphyrin β-pyrrole protons (H-14, H-15), which confirms the proposed closed conformation of the molecule. Further evidence for the intramolecular coordination was obtained from the UV-Vis spectrum of **Zn1** in $CHCl_3$ (Figure 4), in which the porphyrin Soret and Q bands were redshifted by 7 and 13 nm, respectively, compared to these bands in the UV-Vis spectrum of **Zn2** where such an interaction is absent. These redshifts are typically observed when oxygen atoms (from molecules such as [1,4]dioxane, tetrahydrofuran, and diethylether) are coordinated to the zinc center in porphyrins.[37] The very broad appearance of the Soret band of **Zn1** compared to reference zinc porphyrins indicated that the molecules are present as a mixture of conformers in which either the intramolecular coordination is absent (absorption maximum at 419 nm) or it is present and the molecule adopts a closed conformation (absorption maximum at 429 nm). The two conformers are present in a roughly 1:2 ratio as could be determined by deconvolution (Figure 4). In order to rule out that the observed spectral properties are a result of coordination of water molecules to the zinc ion on the inside of the cavity (which has been observed in crystal structures of some crown ether functionalized porphyrins[38]), a ^{1}H-NMR titration was performed in $CDCl_3$ of **Zn1** with water. Although the titration revealed a weak coordination of this ligand ($K_a = 30$ M^{-1}) to the inside of the cavity, it induced an opening of the cavity rather than a closing, as can be concluded from the downfield shift of the resonances of H-3, H-4, and H-5 (Figure 3c, d). These observations indicated that water coordination does not account for the observed closed conformation of **Zn1**.

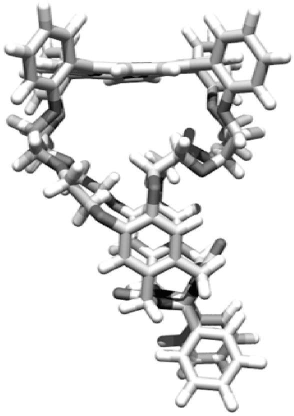

Figure 2. Computer-modeled structure of **$H_2$1** in $CDCl_3$ at room temperature, based on the ^{1}H-NMR, COSY, and 2D ROESY spectra.

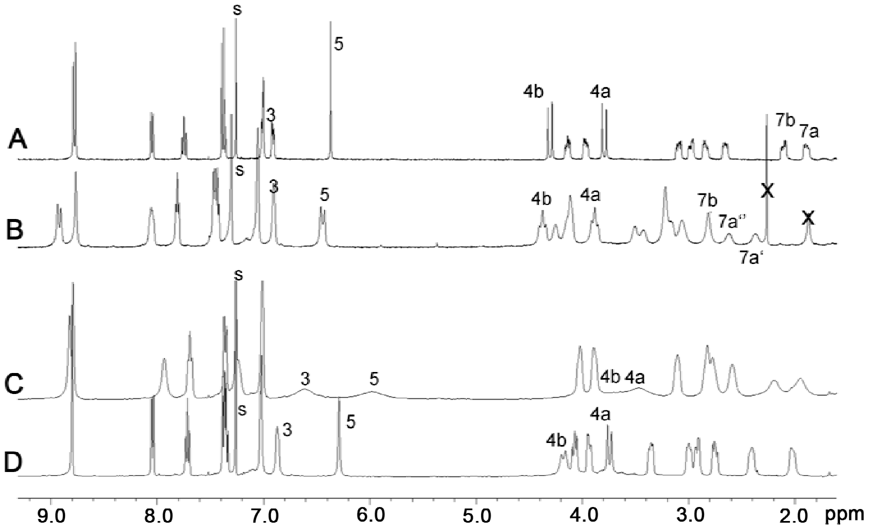

Figure 3. 400 MHz (A, C, and D) and 500 MHz (B) ^{1}H-NMR spectra of **$H_2$1** at (A) 298K and (B) 218K in $CDCl_3$, and of **Zn1** (C) in the presence of 0.7 equivalents of water in $CDCl_3$ and (D) in $CDCl_3$ saturated with water. For proton numbering scheme see Figure 1.

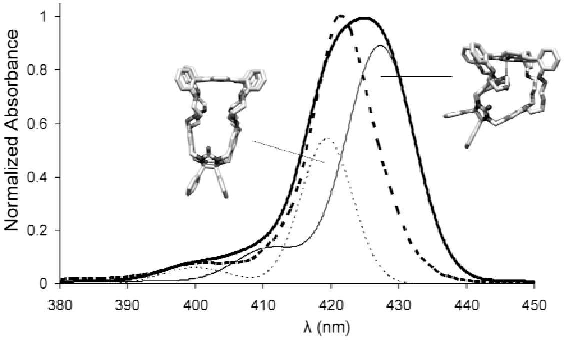

Figure 4. Selection of normalized UV-Vis spectra in chloroform of **Zn1** (—), **Zn2** (- - -), and the contributions, calculated by deconvolution, of the intramolecular zinc-oxygen coordinated (——) versus the non-coordinated (- - -) conformers of **Zn1** to the total spectrum.

2.4 Binding properties

Cavity-containing porphyrin receptor molecules based on diphenylglycoluril are known to be capable of binding small aromatic guest molecules by a variety of interactions, viz., by hydrogen bonding, π-π interactions,[39] van der Waals interactions, dipole interactions, and in the case when a zinc ion is present in the porphyrin, by complexation of ligands to the metal centre. Herein, the complexation behavior of pyridine and viologen guest molecules to receptors **H$_2$1** and **Zn1** will be investigated.

Chart 2

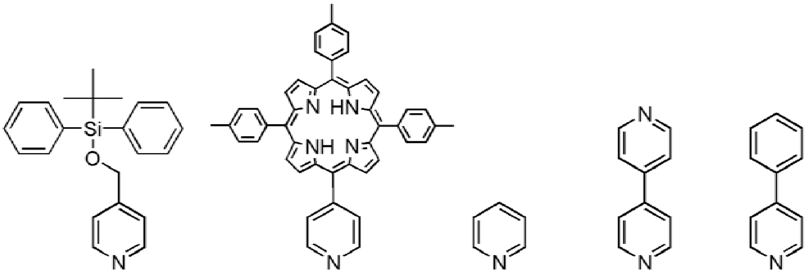

P1 **P2** **P3** **P4** **P5**

Binding of pyridine derivatives. A number of ^{1}H-NMR and UV-Vis titrations were carried out in $CDCl_3/CD_3CN$ 1:1 (v/v) and $CHCl_3/CH_3CN$ 1:1 (v/v), respectively, to investigate the binding of pyridine-containing substrates **P1–P5** (Chart 2) to receptor **Zn1**. Upon coordination of all the pyridine ligands, the UV-Vis spectra showed very similar 3-4 nm red-shifts of the porphyrin Soret band. In addition, the presence of several isosbestic points indicated the formation of well-defined receptor-guest complexes. Upon the addition of each of the ligands, the broad signals in the ^{1}H-NMR spectrum of **Zn1** sharpened, which indicated that the proposed intramolecular zinc-oxygen coordination is replaced by the coordination of the pyridine ligands. The bulky pyridines **P1** and **P2** are too large to fit inside the cavity and as a result they can only coordinate to the zinc ion from the outside. Coordination of these ligands to **Zn1** induced, in both cases, identical shifts in the ^{1}H-NMR spectra, which indicates that similar binding geometries occur. The downfield shifts of the signals of protons H-3, H-4, and H-5 indicate that the cavity adopts a more open conformation, very similar to that observed for **H$_2$1**, which is confirmed by the nearly identical resonances observed for **Zn1** in the ^{1}H-NMR spectrum (Table 2). The calculated association constants for **P1** and **P2** with **Zn1** are relatively low (K_a for **P1** = 550 M^{-1}, K_a for **P2** = 350 M^{-1}), which is due to the absence of additional stabilizing interactions by the cavity and also to the competition of the intramolecular zinc-oxygen coordination with the coordination of the ligands. Pyridine (**P3**) coordinates predominantly on the inside of the cavity. In the ^{1}H-NMR spectrum of the complex, the signals of the oxyethylene protons H-6 and H-7 have shifted downfield, which indicates that their position in close proximity to the porphyrin has been occupied by the ligand (Table 2). The association constant (K_a = 3200 M^{-1}) is of the same order of magnitude as other pyridine to zinc-porphyrin association constants in this solvent mixture,[40] which suggests that **P3** only experiences small extra stabilizing interactions despite its position inside the cavity of **Zn1**. As opposed to the complexes of **P3** with **Zn2** and **Zn3**, which are further stabilized by favorable π-π interactions leading to high association constants (typically K_a **Zn2**-**P3** ($CHCl_3$) = 1.1 x 10^5 M^{-1} , K_a **Zn2**-**P3** ($CHCl_3/CH_3CN$ 1:1 (v/v)) = 7.5 x 10^4 M^{-1}, and K_a **Zn3**-**P3** ($CHCl_3$) = 1.4 x 10^4 M^{-1}),[13] the **Zn1/P3** complex apparently does not experience these extra stabilizing interactions, probably because the complex cannot adopt a geometry in which the pyridine ring sits in between the cavity side-walls due to the longer crown ether spacers. Molecular modeling indicated that Bipy (**P4**) and Phepy (**P5**) are large enough to be accommodated with an ideal fit inside the cavity of **Zn1**. The addition of **P4** or **P5** to **Zn1** resulted in complexes in which the ^{1}H-NMR spectra revealed dramatic conformational changes of the receptor molecule (Table 2), which suggests a strong induced-fit binding mechanism. In the 2D ROESY spectrum, NOE contacts between the protons of the guests and of the cavity proved their coordination inside the cavity. Despite the occurrence of large geometrical rearrangements, the measured association constants are high (K_a for **P4** = 3.1×10^4 M^{-1}, K_a for **P5** = 2.8×10^4 M^{-1}). The crystal structures of both complexes could be determined and these demonstrated the nearly perfect fit of the guests inside the cavity of **Zn1** (Figure 5). In both complexes, **Zn1** has adopted a stretched conformation and the lower aromatic rings of the guests are located in between the cavity side-walls; the average distances between the aromatic rings is 3.26 Å in the complex of **Zn1** with **P4** and 3.39 Å in the complex with **P5**. In accordance with literature examples of complexes between Zn(II)porphyrins and pyridine-based ligands,[41–43] the zinc ion is tilted out of the porphyrin surface towards the pyridine ligand (in both cases by 0.29 Å) and the pyridine nitrogen–zinc bond distance is uniformly 2.1 Å. The stretched conformation of **Zn1** in the X-ray structures of the complexes is in agreement with the downfield-shifted resonances in the NMR spectra of protons H-3 and H-4, which are pushed away from the porphyrin upon the binding of **P4** and **P5**. The resonances of H-8 and H-9 displayed upfield shifts, whereas the signals of H-6 and H-7 shifted downfield (Table 2). These shifts are clearly the result of **Zn1** adopting a stretched conformation upon the binding of **P4** and **P5**, which brings protons H-8 and H-9 closer to the shielding porphyrin than H-6 and H-7, whereas in unoccupied **Zn1**, H-6 and H-7 are located much closer to the porphyrin. The cavity of **Zn1** in the complex with **P5** is slightly more stretched (0.25 Å) than in the complex with **P4**, which is the result of the difference in size between these guests. A careful look at Table 2 revealed that this more stretched conformation of the complex with **P5**, compared to the complex with **P4**, is also apparent from the different complexation induced shift values (the resonances of H-3, H-4, and H-5 are located more downfield in the complex with **P5**), which indicates that the complexation geometry in solution is similar to that in the crystal.

Table 1. Association constants (K_a) and binding free energies (ΔG^o) between **Zn1** and pyridine ligands **P1**–**P5**

Guest	K_a (M^{-1})	ΔG^o (kJ mol^{-1})
P1[a,b]	$(5.5 \pm 0.3) \times 10^2$	−15.6
P2[a]	$(3.5 \pm 0.7) \times 10^2$	−14.5
P3[a,b]	$(3.2 \pm 0.8) \times 10^3$	−20.0
P4[b,c]	$(3.1 \pm 1.0) \times 10^4$	−25.6
P5[b]	$(2.8 \pm 0.5) \times 10^4$	−25.4

[a] Determined by a ^{1}H-NMR titration in $CDCl_3/CD_3CN$ 1:1 (v/v). [b] Determined by a UV-Vis titration in $CHCl_3/CH_3CN$ 1:1 (v/v). [c] The bivalent character of **P4** was taken into account by dividing the experimentally obtained value of the association constant by a factor 2.[44]

Table 2. Selected ^{1}H-NMR resonances for the protons of **$H_2$1**, **Zn1** and **Zn1** receptor-guest complexes between **Zn1** and **P1**, **P3**, **P4**, and **P5**.[a,b]

Proton	**$H_2$1**	**Zn1**	**Zn1+P1**	**Zn1+P3**	**Zn1+P4**	**Zn1+P5**
H-3	6.95	6.52	6.95	6.98	7.02	7.07
H-4a	5.76	3.37	5.75	5.82	5.88	5.95
H-4b	6.48	3.44	6.46	6.51	6.66	6.72
H-5	6.39	5.84	6.38	6.44	6.15	6.28
H-6a	2.87	2.80	2.83	3.32	3.09	3.01
H-6b	3.26	3.22	3.25	3.42	3.27	3.17
H-7a	2.28	2.42	2.27	3.06	3.08	3.01
H-7b	2.49	2.58	2.46	3.06	3.17	3.13
H-8a	2.91	2.83	2.86	3.02	2.52	2.47
H-8b	3.01	2.92	2.97	3.02	2.70	2.65
H-9a	4.02	3.90	3.97	3.90	3.69	3.62
H-9b	4.14	4.03	4.09	4.01	3.75	3.68

[a] Determined by ^{1}H-NMR experiments in $CDCl_3/CD_3CN$ 1:1 (v/v) solution. For the proton numbering scheme see Figure 1. [b] Shifts of the complexes upon full binding of the ligand.

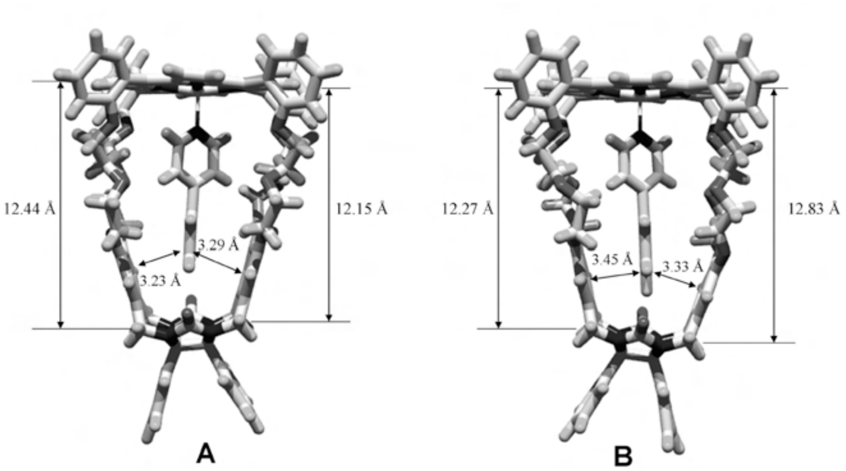

Figure 5. Crystal structures of the complexes between (A) **Zn1** and **P4**, and (B) **Zn1** and **P5**. The dimensions of the cavity and distances between the side-walls and the guests are indicated in the images.

Binding of viologen derivatives. In addition to the binding of pyridine ligands to **Zn1**, the binding of viologen molecules **V1–V5** in the cavity of **$H_2$1** was also investigated (Chart 3). In all cases, NMR and UV-Vis binding experiments revealed the formation of 1:1 complexes. Upon binding of the guests, large downfield shifts were observed for the crown ether spacer proton resonances (H-6, H-7, H-8, and H-9) in the ^{1}H-NMR spectra, indicating that these protons move away from the

Chart 3

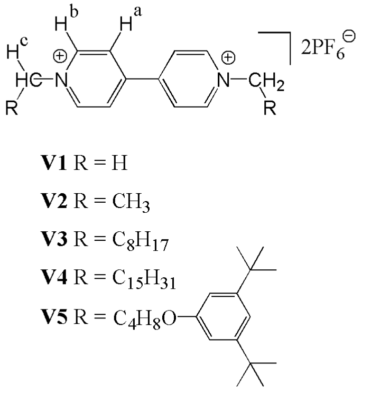

V1 $R = H$

V2 $R = CH_3$

V3 $R = C_8H_{17}$

V4 $R = C_{15}H_{31}$

V5 $R = C_4H_8O$–

porphyrin plane. Simultaneously, large upfield shifts (0.97–1.08 ppm) were observed for the pyrrole NH resonances as a result of shielding by the aromatic surfaces of the guests, which are therefore proposed to bind parallel, and in close proximity, to the porphyrin surface (Figure 6).[45] The large changes in the NMR spectra of **$H_2$1** upon the binding of the viologen guests strongly indicates the occurrence of induced-fit binding mechanisms. The calculated association constants are high (Table 3) and in the same order of magnitude as the binding of **V1** to **$H_2$2** ($K_a = 6.0 \times 10^5$ M^{-1}). Clearly, the binding geometry of **V1** in **$H_2$1** is different than that of **V2**–**V4** in this receptor, which can be concluded from the completely different complexation induced shift (CIS) values that are observed for the complexes (Table 4) and from the significantly higher association constant for the complex between **$H_2$1** and **V1** (Table 3). The flexible, electron rich crown ether spacers play a crucial role in the accommodation of the electron deficient viologen guests. Molecular modeling indicates that two binding geometries of a viologen guest in **$H_2$1**, in which it is oriented parallel to the porphyrin plane, are possible (Figure 6). In the “rotaxane geometry” the crown ether oxygen atoms are facing the inside of the cavity thereby stabilizing the positive charges of the viologen. In the "suit(2)ane geometry",[46] the positive charges of the viologen guest are located in between the two crown ether rings between the cavity side-walls and the porphyrin. In order to force viologen complexation in the rotaxane geometry, **V5** was added to **$H_2$1**. The bulky blocking groups of this guest can only be traversed by the full dimension of the cavity and the geometry of the resulting receptor-guest complex can therefore only be rotaxane-like, as in Figure 6a. The formation of the complex of **$H_2$1** with **V5** was found to occur through a so called ‘slippage’ mechanism; in order to bind the guest, **$H_2$1** first needs to slip over one of the two blocking groups thereby overcoming a high activation barrier.[47–51] At NMR concentrations ($\approx 10^{-3}$ M), it takes several days before the components reach complexation equilibrium.[52] The ^{1}H-NMR and 2D ROESY spectra of the complex are strikingly similar to the spectra of the complexes between **$H_2$1** and **V2**-**V4** (Table 4), which therefore indicates that all these derivatives have pseudo-rotaxane complexation geometries. The complex between **$H_2$1** and **V1** was found to have a suitane geometry (Figure 6b). NOE contacts are observed between the receptor protons H-14 and H-9a/H-9b (see Figure 1), and between H-15 of the receptor and H^c of **V1** (see Chart 3), whereas in the complexes of **$H_2$1** with **V2**–**V5**, H-15 has NOE contacts with H-9b and H-14 with H^c of **V3**–**V5**. The crown ether proton signals furthermore appeared to be very diagnostic for identifying either a rotaxane or a suitane geometry (Figure 7). For instance, in the suitane geometry H-9a experiences more shielding from the porphyrin plane than H-9b, whereas in the rotaxane complexes H-9b is more shielded than H-9a. An attempt was undertaken to convert a complex with rotaxane geometry into a complex with suitane geometry. To achieve this, **V1** was titrated into a solution containing a 1:1 complex between **$H_2$1** and **V2** (Figure 7c). The observed changes in the NMR spectra indeed indicated the formation of the suitane complex between **$H_2$1** and **V1** at the expense of the rotaxane complex between **$H_2$1** and **V2**, confirming the above described interpretations of the NMR data. In addition, the competition experiment revealed that **V1** binds five times stronger to **$H_2$1** than **V2**, in line with the obtained values for the association constants (Table 3).

Table 3. Association constants (K_a) and binding free energies (ΔG^o) of complexes between **$H_2$1** and viologen derivatives **V1**–**V5**.

Guest	K_a (M^{-1})	ΔG^o (kJ mol^{-1})
V1[a,b]	(6.4 ± 0.8) x 10^5	–33.1
V2[a]	(1.2 ± 0.2) x 10^5	–29.0
V3[a]	(1.0 ± 0.2) x 10^5	–28.5
V4[a]	(1.1 ± 0.2) x 10^5	–28.8
V5[c]	(1.0 ± 0.5) x 10^5	–28.5

[a] Determined by UV-Vis titrations in $CHCl_3/CH_3CN$ 1:1 (v/v). [b] Determined by fluorescence titrations in $CHCl_3/CH_3CN$ 1:1 (v/v). [c] Determined by ^{1}H-NMR experiments in $CDCl_3/CD_3CN$ 1:1 (v/v) and based on the integrated values of the free components and the complex at T = 298 K.

Table 4. Selected calculated complexation induced shift (CIS) values (Δδ; ppm) of receptor and guest proton signals upon the binding of viologens **V1**–**V5** in receptor **$H_2$1**.[a]

Proton	Guest				
	V1	**V2**	**V3**	**V4**	**V5**
H-6a	+0.89	+0.35	+0.34	+0.35	+0.35
H-6b	+0.24	+0.35	+0.35	+0.34	+0.35
H-7a	+1.26	+1.35	+1.35	+1.34	+1.36
H-7b	+1.30	+0.95	+0.94	+0.95	+0.95
H-8a	+0.89	+0.88	+0.88	+0.88	+0.88
H-8b	+0.95	+0.64	+0.64	+0.63	+0.63
H-9a	+0.49	+0.77	+0.78	+0.77	+0.79
H-9b	+0.63	+0.21	+0.18	+0.19	+0.18
H-13	–0.45	–0.18	-0.16	–0.17	–0.18
H-16	–1.08	–1.00	-0.98	–0.98	–0.97
H^a	–3.80	–2.98	–2.85	–2.86	–2.89
H^b	–1.16	–1.74	–1.88	–1.89	–1.86
H^c	–0.56	[b]	–1.33	–1.32	–1.28

[a] Determined by ^{1}H-NMR experiments in $CDCl_3/CD_3CN$ 1/1 (v/v). For the proton numbering scheme see Figure 1 and Chart 3. [b] CIS value could not be determined because the signal was obscured by other proton resonances.

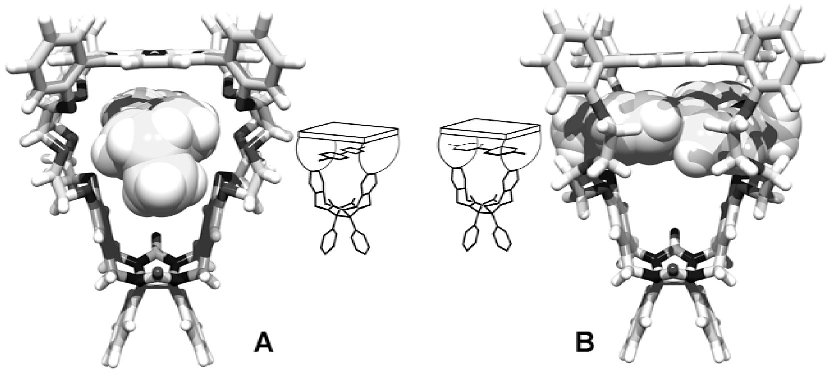

Figure 6. Computer-modeled structures and cartoons of (A) the “rotaxane geometry” of the complex between $\mathbf{H_21}$ and **V2** and (B) the “suit(2)ane geometry” of the complex between $\mathbf{H_21}$ and **V1**, based on the ^{1}H-NMR, COSY, and 2D ROESY spectra.

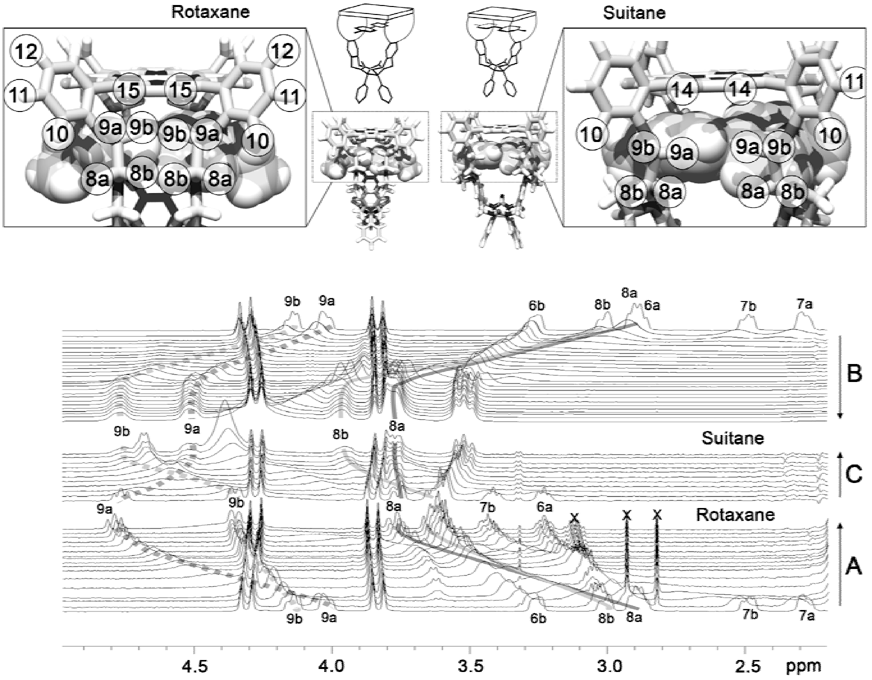

Figure 7. ^{1}H-NMR spectra of $\mathbf{H_21}$ with various amounts of guests **V1** and **V2** in $CDCl_3/CD_3CN$ 1/1 (v/v). (A) From bottom to top increasing amounts of **V2**, (B) from top to bottom increasing amounts of **V1**, (C) from bottom to top increasing amounts of **V1** to a mixture of $\mathbf{H_21}$ and **V2**. The exchanging signals of most of the proton resonances can be followed (lines are added as a guide to the eye).

2.5 Comparison of the complexes

Binding of pyridine and viologen guests in receptor **1** occurs by induced-fit mechanisms similar to those observed for the binding of these guests in flexible receptor **3**. Although the flexible receptor **1** lacks the preorganization of rigid receptor **2**, the association constants obtained for different guests are similar for both receptors, which is somewhat surprising because binding inside the cavity of **1** is accompanied by severe conformational changes. It can therefore be concluded that the binding strength mainly depends on the possibility of **1** to provide the guests with extra stabilizing interactions. Pyridine (**P3**) coordinates strongly on the inside of receptors **Zn2** ($K_a = 1.1 \times 10^5$ M^{-1}) and **Zn3** ($K_a = 1.4 \times 10^4$ M^{-1}) as a result of highly favorable π-π interactions between the cavity side-walls and the aromatic surface of the guest, in addition to the zinc-nitrogen coordination. Although **P3** coordinates on the inside of the cavity of **Zn1**, this receptor cannot provide the guest with such stabilizing π-π interactions, which results in a significantly lower association constant. In contrast, guests **P4** and **P5** completely fill the cavity of **Zn1** and experience, in addition to ideal van der Waals interactions, strong π-π interactions with the cavity side-walls, which results in stronger binding. The association constants between **V1** and **$H_2$1** ($K_a = 6.4 \times 10^5$ M^{-1}) and **V1** and **$H_2$2** ($K_a = 6.0 \times 10^5$ M^{-1}) are several orders of magnitude larger than that observed for the binding of this guest to **$H_2$3** ($K_a = 1100$ M^{-1}). In the complexes with **$H_2$1** and **$H_2$2**, **V1** is bound in a very tight geometry. **$H_2$1** accommodates the positive charges of **V1** between the two crown ether rings and the complex is further stabilized by additional π-π interactions between the porphyrin and the guest. In **$H_2$2**, **V1** is clamped between the cavity side-walls, which provide stabilizing π-π interactions in addition to electrostatic interactions between the crown ether oxygen atoms and the positive charges of the guest. The crown ethers of receptor **$H_2$3** are too widely oriented to favorably wrap themselves around **V1**, which results in a weaker binding strength. The differences in binding strength between the complexes of the different viologen guests with receptor **$H_2$1** (Table 2) can also be explained in this way. In the suitane geometry of the complex between **V1** and **$H_2$1**, the guest is bound more tightly when compared to the more loosely bound guests **V2**–**V5** in the rotaxane geometry, resulting in a higher association constant observed for **V1**.

3. Conclusion

The flexibility of the new porphyrin receptors **$H_2$1** and **Zn1** is expressed in their complex conformational behavior upon the binding of guests. Insertion of a zinc ion into the porphyrin causes a structural change in the cavity, which is attributed to an intramolecular coordination between the zinc ion and the oxygen atoms in the crown ether spacers. The binding of guests on the inside of the cavities induces large conformational changes throughout the receptors. Despite the binding of guests through induced-fit mechanisms, in many cases high association constants are still obtained, which shows that not only 'lock-and-key', but also 'induced-fit' binding can lead to the formation of strong complexes. In following chapters the focus will be on the threading these new flexible receptors over polymers and the slippage over bulky stoppers in order to get better insight in the influences of conformational flexibility and induced-fit binding mechanisms on these processes.

4. Experimental Section

Materials and methods. All syntheses were carried out under an inert nitrogen or argon atmosphere. Chloroform and acetonitrile used in titration experiments were distilled from $CaCl_2$. Dichloromethane, 1,2-dichloroethane, and methanol were distilled from CaH_2. Pyrrole was purified over a plug of alumina prior to use. Salicylic aldehyde was distilled under vacuum. Catechol was recrystallized from dichloromethane prior to use. $MgSO_4$ and K_2CO_3 were dried in an oven (150 ^{o}C). All other solvents and chemicals were commercial materials and used as received. Merck silica gel (60 H) was used for column chromatography and Merck silica gel F254 plates were used for thin layer chromatography (TLC) and preparative TLC. Molecular modeling calculations were performed with the use of Spartan. Fluorescence experiments were performed on a Perkin-Elmer LS50B luminescent spectrometer equipped with a thermostatted cuvette holder. UV-Vis spectra were recorded on a Cary 100 Conc (Varian, Middelburg) UV-Vis spectrometer. Maldi-TOF mass spectrometry was performed on a Bruker Biflex III spectrometer. NMR spectra were taken on a Varian Inova 400 (400 MHz, ^{1}H and 2D spectra) or on a Bruker DMX300 (75 MHz, ^{13}C spectra) and calibrated to an internal standard of tetramethylsilane. Abbreviations used are s, singlet; d, doublet; t, triplet; dd, double doublet; m, multiplet. Ditosylate **7**,[34–35] tetrakis(chloromethyl) diphenylglycoluril **8**,[36] methyl viologen **V1**, and double blocked viologen **V5**,[18] were synthesized according to literature procedures.

Tetra tosyl clip molecule (9)

Compounds **7** (4.5 g, 7.6 mmol) and **8** (1.8 g, 3.8 mmol) were dissolved in freshly distilled 1,2-dichloroethane (300 mL). $SnCl_4$ (4 mL, 32 mmol) was added and the mixture was refluxed under argon for 16 h. After cooling, aqueous 6n HCl (10 mL) was added and the mixture was refluxed for another 30 min. After cooling CH_2Cl_2 (100 mL) was added and the organic layer was washed with aqueous 1n HCl (3x 100 mL) and water and evaporated to dryness. After purification by column chromatography (50% to 70% EtOAc in toluene) and crystallization from nitromethane, compound **9** was obtained as a white solid (1.37 g, 23%):

^{1}H-NMR ($CDCl_3$, 400 MHz): δ 7.76 (d, 8H, J = 8.3 Hz), 7.24 (d, 8H, J = 8.2 Hz), 7.17–7.10 (m, 10H), 6.76 (s, 4H), 4.69 (d, 4H, J = 15.9 Hz), 4.20-4.10 (m, 12H), 3.88–3.83 (m, 8H), 3.69–3.66 (m, 8H), 3.65–3.61 (m 8H), 2.24 (s, 12H) ppm.

^{13}C-NMR ($CDCl_3$, 75 MHz): δ 157.27, 146.88, 144.38, 133.17, 132.42, 130.03, 129.65, 129.31, 128.36, 128.22, 127.78, 127.47, 115.77, 84.94, 69.21, 68.98, 68.28, 44.44, 20.93 ppm.

Free base porphyrin clip ($H_2$1)

A suspension of **9** (120 mg, 0.078 mmol), 5,10,15,20-tetrakis(*meso*-*p*-hydroxyphenyl)porphyrin **10** (53 mg, 0.078 mmol) and K_2CO_3 (100 mg, 0.72 mmol) in DMF (250 mL) was reacted for 16 h under argon atmosphere at 110 ^{o}C. After cooling, filtration of the salts, and evaporation of the solvent, the product was purified by column chromatography (3% MeOH in $CHCl_3$ (v/v)) followed by preparative TLC (eluent 7/7/1 toluene/EtOAc/MeOH (v/v/v)). The product was dissolved in a minimal amount of $CHCl_3$ and to this solution *n*-hexane was added. A precipitate formed, which was

collected by centrifugation and dried under vacuum yielding 16 mg (13%) of $\mathbf{H_21}$ as a purple solid:
^{1}H-NMR ($CDCl_3$, 400 MHz): δ 8.79 (s, 4H), 8.77 (s, 4H), 8.05 (d, 4H, J = 7.1 Hz), 7.75 (t, 4H, J = 7.7 Hz), 7.40–7.35 (m, 8H), 7.03–6.96 (m, 6H), 6.93–6.90 (m, 4H), 6.37 (s, 4H), 4.30 (d, 4H, J = 15.6 Hz), 4.17–4.11 (m, 4H), 4.00–3.94 (m, 4H), 3.79 (d, 4H, J = 15.5 Hz), 3.12–3.06 (m, 4H), 3.01–2.95 (m, 4H), 2.87–2.81 (m, 4H), 2.69–2.64 (m, 4H), 2.14–2.08 (m, 4H), 1.92–1.86 (m, 4H), –2.62 (s, 2H) ppm.
^{13}C-NMR ($CDCl_3$, 75 MHz): δ 159.23, 157.36, 146.50, 135.42, 133.99, 131.71, 130.25, 129.80, 128.69, 128.50, 127.96, 119.93, 118.75, 115.61, 113.20, 85.30, 70.05, 69.32, 68.43, 68.33, 44.30 ppm.
Maldi-TOF MS (*m*/*z*): 1521.90 $(M)^+$.

Zinc porphyrin clip (Zn1)

$\mathbf{H_21}$ (10 mg, 6.6 μmol) and zinc acetate dihydrate (50 mg, 0.23 mmol) were dissolved in a 1/1 (v/v) mixture of MeOH and CH_2Cl_2 (5 mL). The mixture was stirred at room temperature for 1 h. The solvents were evaporated and the salts were removed by chromatography over a plug of silica (eluent MeOH/$CHCl_3$ 1/10 (v/v)). After precipitation in *n*-hexane, 10 mg (96%) of **Zn1** was obtained as a purple solid:
^{1}H-NMR ($CDCl_3$, 400 MHz): δ 8.83 (s, 4H), 8.79 (s, 4H), 7.93 (br s), 7.69 (t, 4H, J = 7.2 Hz), 7.36 (d, 4H, J = 8.1), 7.24 (br s, 4H) 7.05–6.99 (m, 6H), 6.61 (br s, 4H), 6.98 (br s, 4H), 4.02 (br s, 4H), 3.89 (br s, 4H), 3.67 (br s, 4H), 3.47 (br s, 4H), 3.11 (br s, 4H), 2.82 (br s, 4H), 2.78 (br s, 4H), 2.59 (br s, 4H), 2.20 (br s, 4H), 1.95 (br s, 4H) ppm.
^{13}C-NMR (DMSO D_6, 75 MHz): δ 158.78, 156.55, 149.25, 149.14, 146.58, 135.72, 133.29, 132.28, 130.99, 130.43, 129.50, 128.56, 128.48, 127.74, 119.69, 116.99, 115.81, 113.81, 84.49, 69.04, 68.89, 68.57, 68.45, 43.83 ppm.
Maldi-TOF MS (*m*/*z*): 1585.0 $(M)^+$.

4-(tert-Butyl-diphenyl-silanyloxymethyl)-pyridine (P1)

4-Pyridylcarbinol (1.0 g, 9.2 mmol) and imidazole (1.0 g, 14.7 mmol), were dissolved in CH_2Cl_2 (50 ml) and to this solution was slowly added tert-butyl-chloro-diphenyl-silane (3.0 g, 11 mmol). The mixture was stirred at room temperature for 4 h, washed with water, the organic layer was concentrated and the product was purified by column chromatography (50% EtOAc/CH_2Cl_2). Crystallization from nitromethane yielded 2.1 g (6.04 mmol, 66%) of **P1** as a colourless solid:
^{1}H-NMR ($CDCl_3$, 400 mHz): δ 8.56 (d, 2H, J = 5.2 Hz), 7.67 (d, 4H, J = 7.2 Hz), 7.35–7.47 (m, 6H), 7.28 (d, 2H, J = 5.2 Hz), 4.76 (s, 2H), 1.12 (s, 9H) ppm.
^{13}C-NMR ($CDCl_3$, 75 mHz): δ 150.0, 149.7, 135.5, 132.9, 129.9, 127.8, 120.6, 64.1, 26.8, 19.3 ppm.
HR-ESI-MS calcd for $C_{22}H_{26}NOSi^+$: 348.17837. Found: 348.17888 (1.48 ppm).

(*N*,*N*')-Diethyl-4,4'-bipyridinium dihexafluorophosphate (V2)

4,4'-Bipyridine (0.5 g, 6.4 mmol) and iodo-ethane (1 mL, excess) were stirred for 24 h in DMF (20 mL). Diethyl ether (50 mL) was added, the resulting precipitate was filtered off, washed with diethyl

ether, and dried under vacuum. The product was dissolved in a minimal amount of water, and this solution was then added to a saturated aqueous NH_4PF_6 solution to yield, after filtration, washing with water, and drying under vacuum, 1.1 g (68%) of **V2** as a white solid:
^{1}H-NMR (1/1 $CDCl_3/CD_3CN$ (v/v), 400 MHz): δ 8.94 (d, 4H, J = 6.9 Hz), 8.41 (d, 4H, J = 6.3 Hz), 4.70 (q, 4H, J = 7.4 Hz), 1.69 (t, 6H, J = 7.3 Hz) ppm.

(*N,N*')-Dinonyl-4,4'-bipyridinium dihexafluorophosphate (V3).
4,4'-Bipyridine (300 mg, 1.92 mmol) and 2-bromononane (2.0 g, 9.7 mmol) were refluxed in CH_3CN (20 mL) for 24 h. After cooling, the formed precipitate was removed by fitration, washed with diethyl ether, and dried under vacuum. The product was dissolved in a minimal amount of water and this solution was then added to a saturated aqueous NH_4PF_6 solution to yield, after filtration and drying under vacuum, 310 mg (23%) of **G2** as a white solid:
^{1}H-NMR (1/1 $CDCl_3/CD_3CN$ (v/v), 400 MHz): δ 8.93 (d, 4H, J = 6.8 Hz), 8.42 (d, 4H, J = 6.5 Hz), 4.62 (t, 4H, J = 7.6 Hz), 2.00–2.06 (m, 4H), 1.35–1.42 (m, 8H), 1.25–1.35 (m, 16H), 0.89 (t, 6H, J = 6.8 Hz) ppm.
Maldi-TOF MS (*m*/*z*) 410.79 (M-2PF_6^-).

(*N,N*')-Dipentadecyl-4,4'-bipyridinium dihexafluorophosphate (V4)
4,4'-Bipyridine (300 mg, 1.92 mmol) and 2-bromopentadecane (3.0 g, 10.3 mmol) were refluxed in CH_3CN (15 mL) for 24 h. After cooling, the formed precipitate was filtered off, washed with diethyl ether, and dried under vacuum. The product was dissolved in a minimal amount of water, and this solution was then added to a saturated aqueous NH_4PF_6 solution to yield, after filtration and drying under vacuum, 467 mg (28%) of **G2** as a white solid:
^{1}H-NMR ($CDCl_3/CD_3CN$ 1/1 (v/v), 400 MHz): δ 8.91 (d, 4H, J = 7.0 Hz), 8.41 (d, 4H, J = 6.7 Hz), 4.62 (t, 4H, J = 7.6 Hz), 2.00–2.05 (m, 4H), 1.36–1.42 (m, 8H), 1.22–1.33 (m, 44H), 0.88 (t, 6H, J = 6.9 Hz) ppm.

X-Ray structures

Table 5. Crystal data and structure refinement for the complex between **Zn1** and **P4** (Figure 5A).

Identification code	CLIP08
Crystal colour	translucent purple
Crystal shape	triangular regular thick platelet
Crystal size	0.28 x 0.22 x 0.08 mm
Empirical formula	C102 H86 N10 O14 Zn
Formula weight	1741.18
Temperature	293(2) K
Radiation / Wavelength	MoKa (graphite mon.) / 0.71073 A
Crystal system, space group	Orthorhombic, Pc21n
Unit cell dimensions	a, alp= 14.000(3) A, 90 deg.
73269 reflections	b, bet= 19.402(2) A, 90 deg.
2.220 < theta < 27.510)	c, gam= 31.190(7) A, 90 deg.
Volume	8473(3) A^3

Z, Calculated density	4, 1.365 Mg/m^3
Absorption coefficient	0.365 mm^-1
Diffractometer / scan	Nonius KappaCCD with area detector phi and omega scan
F(000)	3640
Theta range for data collection	2.22 to 27.51 deg.
Index ranges	-17<=h<=16, -25<=k<=16, -40<=l<=40
Reflections collected / unique	73269 / 15072 [R(int) = 0.1312]
Reflections observed	6745 ([Io>2sigma(Io)])
Completeness to 2theta = 25.00	93.8%
Absorption correction	SADABS multiscan correction(Sheldrick, 1996)
Refinement method	Full-matrix least-squares on F^2
Computing	SHELXL-97 (Sheldrick, 1997)
Data / restraints / parameters	15072 / 2242 / 1144
Goodness-of-fit on F^2	1.175
SHELXL-97 weight parameters	0.200000 0.000000
Final R indices [I>2sigma(I)]	R1 = 0.1390, wR2 = 0.3369
R indices (all data)	R1 = 0.2520, wR2 = 0.4044
Largest diff. peak and hole	2.064 and -0.708 e.A^-3

Table 6. Crystal data and structure refinement for the complex between **Zn1** and **P5** (Figure 5B).

Identification code	CLP11A
Crystal colour	translucent dark red
Crystal shape	rather regular fragment
Crystal size	0.21 x 0.15 x 0.13 mm
Empirical formula	C103 H86 N9 O14 Zn
Formula weight	1739.18
Temperature	208(2) K
Radiation / Wavelength	MoKalpha (graphite mon.) / 0.71073 A
Crystal system, space group	Orthorhombic, Pc21n
Unit cell dimensions	a, alp= 13.7962(11) A, 90 deg.
94074 reflections	b, bet= 19.645(2) A, 90 deg.
2.210 < theta < 27.500)	c, gam= 32.029(3) A, 90 deg.
Volume	8680.6(14) A^3
Z, Calculated density	4, 1.331 Mg/m^3
Absorption coefficient	0.356 mm^-1
Diffractometer / scan	Nonius KappaCCD with area detector phi and omega scan
F(000)	3636
Theta range for data collection	2.21 to 27.50 deg.
Index ranges	-17<=h<=17, -25<=k<=25, -41<=l<=41
Reflections collected / unique	94074 / 19306 [R(int) = 0.0548]
Reflections observed	10734 ([Io>2sigma(Io)])
Completeness to 2theta = 25.00	99.9%
Absorption correction	SADABS multiscan correction (Sheldrick,1996)
Refinement method	Full-matrix least-squares on F^2
Computing	SHELXL-97 (Sheldrick, 1997)
Data / restraints / parameters	19306 / 1 / 1144

```
Goodness-of-fit on F^2            1.347
SHELXL-97 weight parameters       0.099400   11.042700
Final R indices [I>2sigma(I)]     R1 = 0.1049, wR2 = 0.2561
R indices (all data)              R1 = 0.1770, wR2 = 0.2912
Largest diff. peak and hole       2.351 and -0.420 e.A^-3
```

Determination of association constants.

Solutions of various guest concentrations were added to solutions with known concentrations of **$H_2$1** or **Zn1** by microsyringe (at 298 K). The spectral changes were recorded by ^{1}H-NMR, UV-Vis or Fluorescence spectroscopes and the association constant (K_{assoc}) were determined by non-linear curvefitting using Grafit or Excel according to the formula:

$$\delta_{\mathrm{obs}} = \frac{(\delta_{\mathrm{HG}} - \delta_{\mathrm{H}})}{2 \cdot [\mathrm{H}]_{\mathrm{o}}} \cdot \left([\mathrm{H}]_{\mathrm{o}} + [\mathrm{G}]_{\mathrm{o}} + \frac{1}{K_{\mathrm{assoc}}} - \sqrt{\left([H]_o + [G]_o + \frac{1}{K_{\mathrm{assoc}}} \right)^2 - 4 \cdot [\mathrm{H}]_{\mathrm{o}} [\mathrm{G}]_{\mathrm{o}}} \right) + \delta_{\mathrm{H}}$$

where $[\mathrm{H}]_{\mathrm{o}}$ and $[\mathrm{G}]_{\mathrm{o}}$ are the known concentrations of receptor and guest, respectively, δ_{obs} is the observed signal (chemical shift of a proton, absorbance at a fixed wavelength, or emission at a fixed wavelength) of the receptor upon addition of guest, δ_{H} is the signal of the receptor in the absence of guest, and δ_{HG} is the signal of the receptor upon full occupation of the guest (which is obtained in addition to the value of K_{assoc} by curve-fitting).

^{1}H-NMR competition experiment for binding inside $H_2$1 by V1 and V2.

A solution (0.5 mL 1/1 (v/v) $CDCl_3/CD_3CN$) was prepared containing **V2** (1.0 mM) and **$H_2$1** (0.67 mM). To this solution were added small portions of solutions containing **V1** up to a total of 5.5 mM of **V1**. The ^{1}H-NMR spectra were recorded and from the shifts the approximate ratio of HV2/HV1 could be determined (in which HV2 is the complex between **$H_2$1** and **V2** and HV1 the complex between **$H_2$1** and **V1**). A plot of HV2/HV1 versus ratio of $[\mathrm{V1}]_{\mathrm{o}}/[\mathrm{V2}]_{\mathrm{o}}$ gave a straight line with a slope equal to $K_{\mathrm{assocV1}}/K_{\mathrm{assocV2}}$.

5. References

1. Supramolecular Catalysis. Edited by P. W. N. M. van Leeuwen **2008** WILEY-VCH Verlag GmbH & Co. KGaA, Weinheim ISBN: 978-3-527-32191-9.
2. Kuroda, Y.; Hiroshige, T.; Sera, T.; Shiroiwa, Y.; Tanaka, H.; Ogoshi, H. *J. Am. Chem. Soc.* **1989**, *111*, 1912–1913.
3. Kuroda, Y.; Ito, M.; Sera, T.; Ogoshi, H. *J. Am. Chem. Soc.* **1993**, *115*, 7003–7004.
4. Bonar-Law, R. P.; Sanders, J. K. M. *J. Am. Chem. Soc.* **1995**, *117*, 259–271.
5. Bonar-Law, R. P.; Sanders, J. K. M. *J. Chem. Soc., Perkin Trans. 1* **1995**, 3085–3096.
6. Rudkevich, D. M.; Verboom, W.; Reinhoudt, D. N. *Tetrahedron Lett.* **1994**, *35*, 7131–7134.
7. Rudkevich, D. M.; Verboom, W.; Reinhoudt, D. N. *J. Org. Chem.* **1995**, *60*, 6585–6587.

8. Nagasaki, T.; Fujishima, H.; Takeuchi, M.; Shinkai, S. *J. Chem. Soc., Perkin Trans. 1* **1995**, 1883–1888.
9. Reek, J. N. H.; Rowan, A. E.; Crossley, M. J.; Nolte, R. J. M. *J. Org. Chem.* **1999**, *64*, 6653–6663.
10. Benson, D. R.; Valentekovich, R.; Knobler, C. B.; Diederich, F. *Tetrahedron* **1991**, *47*, 2401–2422.
11. Anderson, S.; Anderson, H. L.; Bashall, A.; McPartlin, M.; Sanders, J. K. M. *Angew. Chem. Int. Ed. Engl.* **1995**, *34*, 1096–1099.
12. Collman, J. P.; Zhang, X.; Hembre, R. T.; Brauman, J. I. *J. Am. Chem. Soc.* **1990**, *112*, 5357–5359.
13. Elemans, J. A. A. W.; Claase, M. B.; Aarts, P. P. M.; Rowan, A. E.; Schenning, A. P. H. J.; Nolte, R. J. M. *J. Org. Chem.* **1999**, *64*, 7009–7016.
14. Elemans, J. A. A. W.; Bijsterveld, E. J. A.; Rowan, A. E.; Nolte. R. J. M. *Eur. J. Org. Chem.* **2007**, 751–757.
15. Elemans, J. A. A. W.; Bijsterveld, E. J. A.; Rowan, A. E.; Nolte, R. J. M. *Chem. Commun.* **2000**, 2443–2444.
16. Trakselis, M. A.; Alley, S. C.; Abel-Santos, E.; Benkovic, S. J. *Proc. Natl Acad. Sci. USA* **2001**, *98*, 8368–8375; Kovall, R.; Matthews, B. W. *Science* **1997**, *277*, 1824–1827.
17. Thordarson, P.; Bijsterveld, E. J. A.; Rowan, A. E.; Nolte, R. J. M. *Nature* **2003**, *424*, 915–918.
18. Coumans, R. G. E.; Elemans, J. A. A. W.; Nolte, R J. M.; Rowan, A E. *Proc. Natl. Acad. Sci.* **2006**, *103*, 19647–19651.
19. Dalla Cort, A.; Mandolini, L.; Schiaffino, L. *Chem. Commun* **2005**, 3867–3869.
20. Zhang, B. L.; Breslow, R. *J. Am. Chem. Soc.* **1997**, *119*, 1676–1681.
21. Mattei, P.; Diederich, F. *Helv. Chim. Acta* **1997**, *80*, 1555–1588.
22. Diederich, F.; Lutter, H. D. *J. Am. Chem. Soc.* **1989**, *111* , 8438–8446.
23. Ortega-Caballero, F.; Rousseau, C.; Christensen, B.; Ellebæk Petersen, T.; Bols, M. *J. Am. Chem. Soc.* **2005**, *127*, 3238–3239.
24. Yoshizawa, M.; Tamura, M.; Fujita, M. *Science,* **2006**, *312*, 251–254.
25. Hooley, R. J.; Biros, S. M.; Rebek, J. Jr. *Angew. Chem. Int. Ed.* **2006**, *45*, 3517–3519.
26. Fiedler, D.; Bergman, R. G.; Raymond, K. N. *Angew. Chem. Int. Ed.* **2004**, *43*, 6748–6751.
27. Fiedler, D.; van Halbeek, H.; Bergman, R. G.; Raymond, K. N. *J. Am. Chem. Soc.* **2006**, *128*, 10240–10252.
28. Fischer, E.; *Ber. Dtsch. Chem. Ges.* **1894**, *27*, 2984–2993.
29. Pauling, L. *Chem. Eng. News* **1946**, *24***,** 1375–1377.
30. Koshland, D. E. *Proc. Natl. Acad. Sci. USA* **1958**, *44*, 98–104.
31. Berger, C.; Weber-Bornhauser, S.; Eggenberger, J.; Hanes, J.; Plückthun, A.; Bosshard, H. R. *FEBS Lett.* **1999**, *450*, 149–153.
32. Bosshard, H. R.; *News Physiol. Sci.* **2001**, *16*, 171–173.
33. Sanders, J. K. M. *Chem. Eur. J.* **1998**, *4*, 1378–1383.
34. Wright, K.; Melandri, F.; Cannizzo, C.; Wakselman, M.; Mazaleyrat, J. P. *Tetrahedron* **2002**, *58*, 5811–5820.
35. Weber, E. *Liebigs Annalen der Chemie* **1983**, *5*, 770–801.
36. Sijbesma, R. P.; Nolte, R. J. M. *Recl. Trav. Chim. Pays-Bas* **1993**, *112*, 643–647.
37. Absorbance maxima and association constants of dioxane, THF, Et_2O, acetone and ring-ether compound 8b,8c-diphenylperhydro-2,6-dioxa-3a,4a,7a,8a-tetraazacyclopenta[*def*]fluorene-

4,8-dione (**11**) to reference zinc porphyrins 5,10,15,20-tetrakis-(2-methoxy-phenyl)-Zn-porphyrin (**Zn4**) and 5,10,15,20-tetrakis-(3-methoxy-phenyl)-Zn-porphyrin (**Zn5**) in chloroform.

Zn4 chloroform	(Soret: 420 nm, Q-bands: 548, 585 nm)
Zn4 + THF $K_a = 12\ M^{-1}$,	(Soret: 425 nm, Q-bands: 556, 594 nm)
Zn4 + dioxane $K_a = 63\ M^{-1}$,	(Soret: 424 nm, Q-bands: 553, 591 nm)
Zn4 + acetone	(Soret: 422 nm, Q-bands: 552, 592 nm)
Zn4 + ringether **11**, $K_a = 9.0\ M^{-1}$,	(Soret: 426 nm, Q-bands: 554, 596 nm)
Zn5 + chloroform	(Soret: 420 nm, Q-bands: 546, 585 nm)
Zn5 + THF $K_a = 20\ M^{-1}$,	(Soret: 425 nm, Q-bands: 556, 596 nm)
Zn5 + dioxane $K_a = 32\ M^{-1}$,	(Soret: 424 nm, Q-bands: 552, 593 nm)
Zn5 + ether $K_a = 0.7\ M^{-1}$,	(Soret: 423 nm, Q-bands: 553, 593 nm)
Zn5 + acetone $K_a = 0.4\ M^{-1}$,	(Soret: 423 nm, Q-bands: 553, 592 nm)

38. Michaudet, L.; Philippe Richard, P.; Boitrel, B. *Tetrahedron. Lett.* **2000**, *41*, 8289–8292.
39. Hunter, C. A.; Sanders, J. K. M. *J. Am. Chem. Soc.* **1990**, *112*, 5525–5534.
40. Calculated association constants of pyridine with 5,10,15,20-tetrakis-(2-methoxy-phenyl)-Zn-porphyrin and 5,10,15,20-tetrakis-(3-methoxy-phenyl)-Zn-porphyrin in acetonitrile/chloroform 1/1 (v/v) are $K_a = 1.4 \times 10^3\ M^{-1}$ and $K_a = 1.0 \times 10^3\ M^{-1}$ respectively.
41. Muniappan, S.; Liptsman, S.; Goldberg. I. *Acta Cryst.* **2006**, *C62*, m140-m143.
42. Shukla, A. D.; Dave, P. C.; Suresh, E.; Das, A. Dastidar, P. *J. Chem. Soc. Dalton Trans.*, **2000**, 4459–4463.
43. Litvinov, A. L.; Konarev, D. V.; Kovalevsky, A. Y.; Neretin, I. S.; Coppens, P.; Lyubovskaya, R. N. *Crystal Growth & Design* **2005**, *5(5),* 1807–1819.
44. Ercolani, G.; Piquet, C.; Borkovec, M.; Hamacek, J, *J. Phys. Chem. B* **2007**, *111*, 12195–12203.
45. For a good comparison of viologen binding to porphyrin receptors: Gunter, M. J.; Jeynes, T. P.; Johnston, M. R.; Turner, P.; Chen, Z. *J. Chem. Soc., Perkin Trans. 1,* **1998**, 1945–1957.
46. Williams, A.R.; Northrop, B. H.; Chang, T.; Stoddart, J. F.; White, A. J. P.; Williams, D. J. *Angew. Chem. Int. Ed.* **2006**, *40*, 6665–6669.
47. Ashton, P. R.; Bělohradsky, M.; Philp, D.; Stoddart, J. F. *J. Chem. Soc., Chem. Commun.* **1993**, *16*, 1269–1274.
48. Ashton, P. R.; Bělohradsky, M.; Philp, D.; Spencer, N.; Stoddart, J. F. *J. Chem. Soc., Chem. Commun.* **1993**, *16*, 1274–1277.
49. Amabilino, D. B.; Ashton, P. R.; Bělohradsky, M.; Raymo, F. M.; Stoddart, J. F. *J. Chem. Soc., Chem. Commun.* **1995**, *7*, 751–753.
50. Bělohradsky, M.; Philp, D.; Raymo, F. M.; Stoddart, J. F. In *Organic Reactivity: Physical and Biological Aspects*; Golding, B. T.; Griffin, R. J.; Maskill, H.; Eds.; RSC Special Publication No. 148: Cambridge, **1995**; pp 387–398.
51. Ashton, P. R.; Ballardini, R.; Balzani, V.; Bělohradsky, M.; Gandolfi, M. T.; Philp, D.; Prodi, L.; Raymo, F. M.; Reddington, M. V.; Spencer, N.; Stoddart, J. F.; Venturi, M.; Williams, D. J. *J. Am. Chem. Soc.* **1996**, *118*, 4931–4951.
52. Slippage of this receptor over blocking groups will be described thoroughly in Chapter 4.

3

Squaring Cooperative Binding Circles. (I) Thermodynamic aspects

1. Introduction

Cooperative binding interactions play an overwhelming role in numerous natural processes. They are utilized to construct discrete assemblies in nature, but also play crucial roles in information transfer[1] at the cellular level. The formation of the rod-like tobacco mosaic virus as a result of cooperative binding interactions between the coat proteins,[2] and the strong cooperative binding of cyclic AMP upon the binding of the gene transcription-regulating cAMP receptor protein to DNA[3] are two examples from nature that are closely related to the research conducted in the Nolte/Rowan group. The most famous example of cooperative binding is, without doubt, the binding of oxygen to hemoglobin.[4–7] Cooperative binding effects can be either positive or negative and are homotropic when multiple identical guest molecules bind to a receptor and heterotropic when they involve the combined binding of different guests to a receptor.[8]

One of the challenges in the field of supramolecular chemistry is to design artificial systems that display cooperative binding effects, not only to better understand the mechanisms involved in the natural processes, but also to obtain functional materials that benefit from the cooperative binding interactions. Over the years a large number of simple artificial receptors have been developed that display positive[9–12] and negative[13–15] homotropic, and positive[16–24] and negative[25–27] heterotropic cooperative binding effects. Although most of these examples convincingly revealed the approximate origin of the observed cooperative binding effects, there are no studies that have focused on the detailed mapping of mechanisms involved in heterotropic cooperative binding events. This is rather surprising since the relatively simple artificial systems that display cooperative binding are explicitly suited to gain a better understanding of the variety of interactions that are involved in cooperative binding effects in the natural systems.

In this chapter the positive heterotropic cooperative binding studies of viologen derivatives and coordinating pyridine ligands to a number of different zinc porphyrin macrocycles based on glycoluril (Figure 1) are presented. Section 2 describes the theoretical evaluations of multicomponent (cooperative) binding models and stresses the importance of fractional saturation on the obtained apparent association constants. Each theoretical assumption is illustrated with an experimental example that reveals the accuracy of the methods used to determine the cooperative binding effects. In section 3, the combined binding of a variety of viologen derivatives and pyridine ligands to the library of macrocyclic porphyrin receptors is evaluated and compared experimentally. From this series of experiments, it will become clear that the observed cooperative effects arise from a number of different additional contributions, which vary depending on the receptor. Solvent inhibition, intramolecular coordination interactions, structural changes of the receptor, and electronic interactions are all factors that can play a role in causing significant cooperative binding effects.

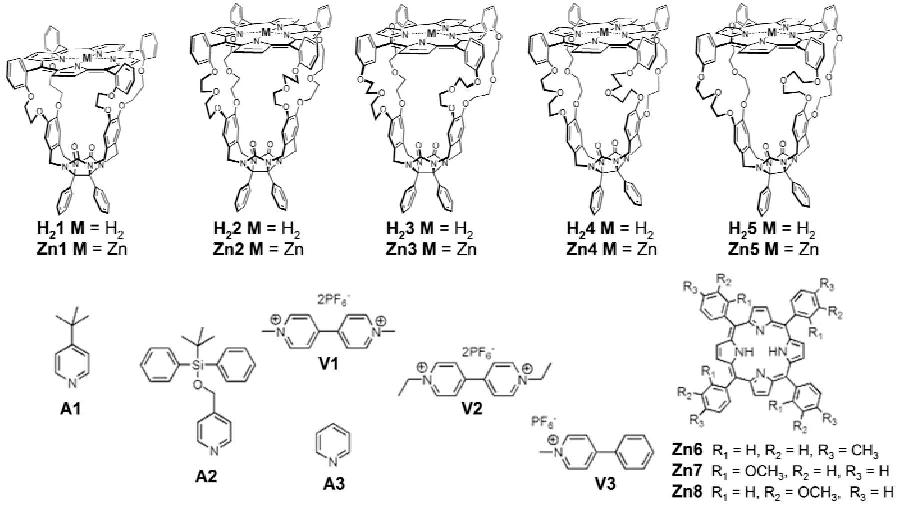

Figure 1. Molecules used in this chapter.

2. How to square a cooperative binding circle

2.1 Introduction

Binding events between a receptor and a guest to form a receptor-guest complex are in general measured by monitoring the changes in complex formation as a result of changes in the concentration of receptor and/or guest. From these data, an association constant can be calculated which is defined: K_{assoc} = [Complex]/{[Receptor][Guest]}. Only the concentrations of receptor, guest, and complex are taken into account in the fitting procedure and the medium in which the experiment is carried out is not. At first sight, this may seem surprising since it is general knowledge that binding events are highly dependant on the medium the measurement was carried out, such as the used solvent, salt concentration, pH, or other factors of which the magnitude of interactions with the receptor and/or guests are unknown to the experimenter. Hence, even though the interactions between the medium and the receptor, the guest, and formed complex, are determining the outcome of a binding experiment, these interactions are simply ignored in the fitting process. This is a reminder that the calculated value of a binding constant is always context dependant and per definition apparent.[28] One may wonder why it is possible to accurately fit a binding event as a simple 1:1 binding process while it is known that a number of other (binding) interactions with the measurement medium are contributing to the obtained binding curve and in fact a multiple binding interaction system is studied. The answer to this is that in the course of the titration experiment the medium remains relatively unaffected (as a result of its molar excess compared to the receptor and guests) and the interactions between the receptor, the guest and the complex with the medium therefore remain constant. As a result, the titration data evolve as a perfect apparent 1:1 binding process that can be treated with a simple 1:1 binding isotherm to give an apparent binding constant that depends on the measured medium.

The above is crucial in the here-developed method to accurately determine heterotropic cooperative binding events. It is possible to treat multiple component interactions with simple 1:1 binding isotherms as long as one obeys that the medium remains relatively unaffected in the course of the titration experiment. The calculated apparent association constants can be treated theoretically to obtain accurate values for the observed heterotropic cooperative binding effects as will become clear in the following sections.

2.2 Squaring a cooperative binding circle

The best way to determine a heterotropic cooperative binding effect is to measure the association constant ${}^{G2}K_{G1}$ of a guest (G1) to the receptor (R) in the presence of a second guest (G2), and then compare the value of the association constant to the one obtained from a titration of guest to the receptor in the absence of the other guest (K_{G1}). The cooperative effect (Ce = ${}^{G2}K_{G1}/K_{G1}$) can simply be calculated. It should be noted, however, that the measured cooperative effect depends strongly on the used experimental conditions. One is dealing with apparent values, which might deviate significantly from the actual cooperative effect of the system. To illustrate this, the three-component binding scheme in Figure 2 is considered.

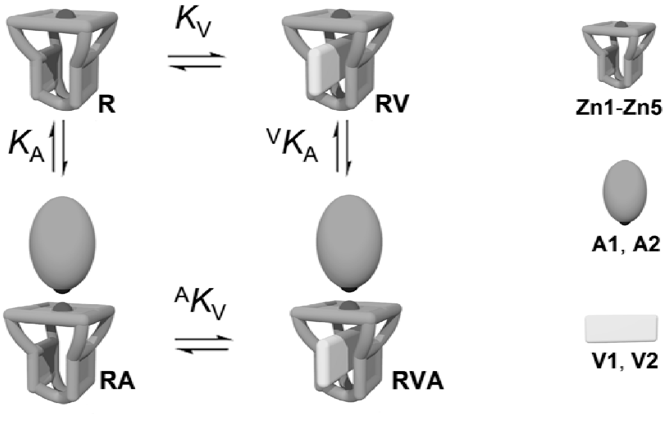

Figure 2. Schematic representation of a three-component binding model involving the combined binding of a bulky pyridine (**A1** or **A2**) and a viologen derivative (**V1** or **V2**) to a porphyrin receptor (**Zn1**–**Zn5**), see Figure 1 for the molecular structures.

The scheme represents the combined binding of a bulky pyridine ligand (A) and a viologen derivative (V) to a zinc porphyrin macrocycle. As a result of its bulkiness, the pyridine ligand can only coordinate to the zinc ion on the outside of the receptor cavity. The electron-deficient viologen derivative has a strong affinity for the inside of the electron-rich cavity of the receptor. In the absence of the other, the axial ligand (A) and the viologen (V) will bind with association constants K_A and K_V, respectively. The cooperative binding effect can simply be measured by the titration of one guest (G1) into a solution of the receptor in the presence of the second guest (G2); the changes to the receptor ($\mathrm{R} + \mathrm{R_{G2}}$) are monitored.

$$\mathrm{R} + \mathrm{R_{G2}} \xrightleftharpoons{\mathrm{G1}} {}_{\mathrm{G1}}\mathrm{R} + {}_{\mathrm{G1}}\mathrm{R_{G2}}$$

It is only necessary that the ratios of $[\mathrm{R}]/[\mathrm{R_{G2}}]$ and $[{}_{\mathrm{G1}}\mathrm{R}]/[{}_{\mathrm{G1}}\mathrm{R_{G2}}]$ remain constant during the titration experiment to be able to obtain the (apparent) association constant with the help of simple 1:1 binding isotherms. This can, in general, be achieved by the addition of an excess (> 20 equiv.) of the second guest G2 with respect to the receptor (R). The obtained association constant will, however, have an apparent value, that depends directly on the association constant and the concentration of the second guest present in solution. This can be seen in Equations 1 and 2, which represent the formulas to calculate the apparent association constant of A to the receptor in the presence of V (${}^\mathrm{V}K_\mathrm{A}$-app) and that of V in the presence of A (${}^\mathrm{A}K_\mathrm{V}$-app).

$$ {}^\mathrm{A}K_\mathrm{V}\text{-app} = \frac{K_\mathrm{V} + [\mathrm{A}]\cdot K_\mathrm{A}\cdot {}^\mathrm{A}K_\mathrm{V}}{1+[\mathrm{A}]\cdot K_\mathrm{A}} \quad (1), \qquad {}^\mathrm{V}K_\mathrm{A}\text{-app} = \frac{K_\mathrm{A} + [\mathrm{V}]\cdot K_\mathrm{V}\cdot {}^\mathrm{V}K_\mathrm{A}}{1+[\mathrm{V}]\cdot K_\mathrm{V}} \quad (2)$$

In determining the magnitude of the cooperative effect ($Ce = {}^\mathrm{A}K_\mathrm{V}/K_\mathrm{V} = {}^\mathrm{V}K_\mathrm{A}/K_\mathrm{A}$), the concentration of the second guest and its association constant with the receptor should be taken into account. Moreover, the magnitude of the observed cooperative effect is linearly dependent on the fractional saturation $y_\mathrm{R\text{–}G}$ (Equation 3) of the receptor with the second guest, which is defined as the fraction of the total number of receptor molecules that are occupied by a particular guest.[29]

$$y_\mathrm{R-G} = \frac{K_\mathrm{G}[\mathrm{G}]}{1+K_\mathrm{G}[\mathrm{G}]} = \frac{[\mathrm{HG}]}{[\mathrm{H}]+[\mathrm{HG}]} \qquad (3)$$

This linear relationship becomes clear when equation 3 is substituted into Equations 1 and 2, to give Equations 4 and 5, respectively.

$$ {}^\mathrm{G2}K_\mathrm{G1}\text{-app} = K_\mathrm{G1}\cdot\{1+y_\mathrm{R\text{-}G2}\cdot(Ce-1)\} \qquad (4)$$

$$Ce\text{-app} = 1 + y_\mathrm{R\text{-}G2}\cdot(Ce-1) \qquad (5)$$

The above indicates that when, for instance, 50% of the receptors is occupied by the second guest (hence $y_\mathrm{R\text{–}G2} = 0.5$), the experimentally obtained association constant of the receptor with the second guest will be exactly halfway between the values of the association constant in the absence (K_G1) and in the presence (${}^\mathrm{G2}K_\mathrm{G1}$) of this second guest. In order to experimentally observe the full cooperative effect when performing the titration of a guest in the presence of a second guest, one has to ensure that the receptor is fully (> 98%) occupied by the second guest. This is especially important when dealing with relatively low association constants ($< 1 \times 10^3\ \mathrm{M}^{-1}$) and polar guest molecules, which could lead to experimental errors caused by severe changes in solvent polarity due to the presence of large concentrations of guest. This problem can be circumvented by performing a series of experiments in the presence of various (low) concentrations of the second guest, from which the magnitude of the cooperative effect can be calculated indirectly with use of any of Equations 1, 2, 4, or 5.

To illustrate that these theoretical assumptions can also be supported experimentally, the combined binding of 4-*tert*-butylpyridine (**A1**) and methyl viologen (**V1**) to the porphyrin receptor **Zn1** (see Figure 1) will be evaluated. The association constant of **A1** to **Zn1** was determined with the help of ^{1}H-NMR and UV-Vis titrations (K_{A1} = 225 M^{-1}, Table 1). ^{1}H-NMR and fluorescence titrations revealed that **V1** binds strongly on the inside of the cavity of **Zn1** (K_{V1} = 8.7 x 10^5 M^{-1}). The influence of the presence of **V1** on the affinity of **A1** for **H$_2$1** was determined by performing a ^{1}H-NMR titration of **A1** in the presence of a slight excess (1.1 equiv.) of **V1** with respect to **H$_2$1**. The titration revealed a strong positive cooperative effect for the binding of **A1** to **Zn1** in the presence of **V1** ($^{\mathrm{V1}}K_{\mathrm{A1}}$-app = 1.1 x 10^4 M^{-1}). As a result of the high association constant of **V1** to **Zn1**, the value of the molar saturation $y_{\mathrm{H-V1}}$ in the experiment was ≈ 1 and the observed cooperative effect therefore practically equals the actual cooperative effect, i.e., *Ce* = 49 (Table 1). In addition, the influence of the presence of **A1** on the binding of **V1** to **Zn1** was studied. The low concentration (≈ µM) fluorescence titrations of **V1** to **Zn1** were performed in the presence of different amounts of **A1**. The formation of the complex between **Zn1** and **V1** resulted in the full quenching of the porphyrin fluorescence emission. Clearly, each increase in the concentration of **A1** resulted in stronger binding of **V1**, as can be seen in Table 1 and Figures 3A and 3B. The plot of the apparent association constant $^{\mathrm{A1}}K_{\mathrm{V1}}$-app against concentration could be fitted using Equation 1. Apart from revealing a *Ce* of 53, (which is nearly identical to the observed *Ce* in the NMR titrations, hence $^{\mathrm{V1}}K_{\mathrm{A1}}/K_{\mathrm{A1}} = {}^{\mathrm{A1}}K_{\mathrm{V1}}/K_{\mathrm{V1}}$, thus obeying Hess's law), the value of K_{A1} was indirectly calculated to be 224 M^{-1}, which is essentially identical to the value calculated from the direct titration experiments of **Zn1** with **A1**. As a result, also the predicted linear relation of a plot of apparent association constant ($^{\mathrm{A1}}K_{\mathrm{V1}}$-app) against fractional saturation ($y_{\mathrm{R-A1}}$) was observed, as can be seen in Figure 3C.

Table 1. Association constants (K_{G1}) and the (apparent) cooperative effects (*Ce*) for the binding of **A1** and **V1** to **Zn1** at 298 K.

G1	G2	K_{G1}	*Ce* (apparent)
A1	-	2.3 x 10^2 M$^{-1\ a,d}$	
A1	**V1** (1 mM)	1.1 x 10^4 M$^{-1\ a,d}$	49
V1	-	8.7 x 10^5 M$^{-1\ b,d}$	
V1	**A1** (0.17 mM)	2.2 x 10^6 M$^{-1\ b,e}$	2.5
V1	**A1** (0.41 mM)	4.6 x 10^6 M$^{-1\ b,e}$	5.3
V1	**A1** (0.81 mM)	9.0 x 10^6 M$^{-1\ b,e}$	10
V1	**A1** (1.55 mM)	1.2 x 10^7 M$^{-1\ b,e}$	14
V1	**A1** (2.84 mM)	2.0 x 10^7 M$^{-1\ b,e}$	23
V1	**A1** (5.69 mM)	2.7 x 10^7 M$^{-1\ b,e}$	31
V1	**A1** (∞ mM)	4.8 x 10^7 M$^{-1\ c,e}$	53

[a] Determined from ^{1}H-NMR titrations in $CDCl_3/CD_3CN$ 1/1 (v/v). [b] Determined from fluorescence titrations in $CHCl_3/CH_3CN$ 1/1 (v/v). [c] Determined by nonlinear curve-fitting of the data with the use of Equation 1. [d] Estimated error 10%. [e] Estimated error 30%.

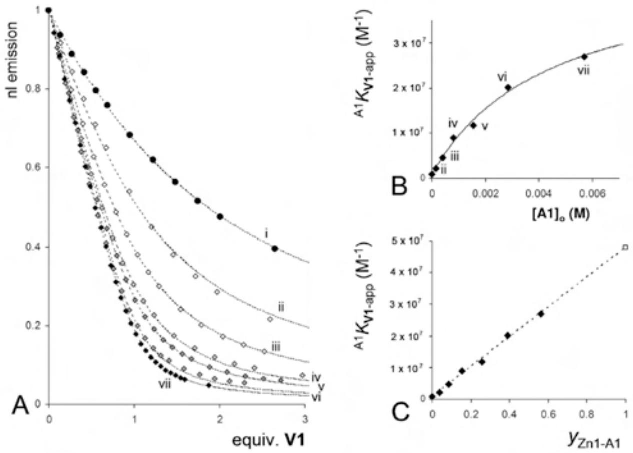

Figure 3. (A) Normalized fluorescence emission of **Zn1** upon the addition of increasing amounts of **V1** in the presence of different amounts of **A1** and the fits obtained with the use of simple 1:1 receptor-guest binding isotherms. (B) Calculated apparent association constants of **V1** with **Zn1** plotted against the concentration of **A1** (M) and the fit obtained when Equation 1 is used. (C) Calculated apparent association constants of **V1** with **Zn1** plotted against the fractional saturation of **Zn1** with **A1** (y_{Zn1-A1}) showing the linear trend, and assuming that $K_{A1} = 225$ M^{-1}.

2.3 Effects of competition

The results described above show that, in a simple three-component receptor-guest system, a thermodynamic circle can be perfectly balanced with the use of 1:1 binding isotherms only. Unambiguously, the binding of either of the used guests to **Zn1** is enhanced by approximately a factor of 50 when **Zn1** is bound to the other guest. This might well be a genuine cooperative effect, for instance, as a result of an electronic interplay between the electron-deficient viologen and the porphyrin and the electron donating pyridine, and/or as a result of steric changes in the complex of the receptor with the first guest that facilitates the binding of the second guest. It should be noted, however, that the balancing of the thermodynamic circle does not provide information about the causes of the observed cooperative effects or whether there might be another pathway that could cause an apparent cooperative effect. A Devil's advocate might, quite fairly, argue that the observed cooperative effect totally originates from ordinary solvent competition, in which a solvent molecule coordinates to the zinc ion on the inside of the cavity of **Zn1**, thereby obstructing both the binding of **A1** and **V1**. The addition of either of these guests removes the solvent molecule from the inside of the cavity and thereby facilitates the binding of the second guest, causing a fully apparent cooperative effect.

To illustrate the consequences of such solvent competition, which might in general be underappreciated in the field of supramolecular chemistry, a simple competitive binding mechanism in which a guest (G) is titrated into a solution containing a receptor (R), of which the binding site is occupied by a solvent molecule (X), is considered.[30]

$$\mathrm{RX} \overset{K_X}{\rightleftharpoons} \mathrm{R} + \mathrm{X} + \mathrm{G} \overset{K_G}{\rightleftharpoons} \mathrm{RG}$$

When performing this titration, an apparent association constant K_G-app is obtained that depends on the concentration of X and the association constant of X with the receptor (K_X), as can be seen in Equation 6.

$$K_G\text{-app} = \frac{K_G}{1 + K_X \cdot [\mathrm{X}]} \tag{6}$$

Also here, the observed association constants depend linearly on the fractional saturation of the receptor with the solvent molecules ($y_{R\text{–}X}$) according to Equation 7.

$$K_G\text{-app} = K_G - y_{R\text{-}X} \cdot K_G \tag{7}$$

The implication of this is that an interaction of the receptor with a (solvent) molecule with a magnitude unknown to the experimenter can severely influence the experimental outcome of a receptor-guest association constant. Consider, for instance, a solvent with a molarity of 55 M and an association constant for the binding site of the receptor of only 0.5 M^{-1}, a value which is generally considered to be random association and therefore of doubtful significance.[31] Under such conditions, however, the measured association constant K_G-app will have a value that is 28.5 times lower than the actual value K_G. Switching to a solvent with comparable polarity, but no affinity for the binding site might therefore result in an increase in the association constant of a factor 28.5 ($\Delta\Delta G$ = 8.3 kJ.mol^{-1}!). So clearly, already the 'random' competitive association of solvent molecules can dramatically influence experimental observations. This competitive solvent binding is an effect that should be taken into account in addition to other known solvent effects such as solvation. In studies that involve coordination to metal ions in different solvents or involve different experimental salt concentrations, this effect can give a better understanding in the experimental binding parameters.

To illustrate that the above described competition effects are indeed observed experimentally, the competitive binding of two guests in **Zn1** will be discussed. Pyridine (**A3**) binds strongly on the inside of the cavity of **Zn1** (K_{A3} = 7.5 x 10^4 M^{-1}, determined by a UV-Vis titration in MeCN/$CHCl_3$ 1/1 (v/v)) and is therefore expected to effectively compete with the binding of **V1**. Fluorescence titrations of **Zn1** with **V1** indeed clearly revealed a weaker binding of **V1** upon increasing the concentration of **A3** (Figures 4A and 4B). The observed value of $^{A3}K_{V1}$-app depends linearly on the fractional saturation of **Zn1** with **A3** ($y_{Zn1\text{–}A3}$), as predicted by Equation 7.

Although this example nicely shows the coherence between theory and experiment, the actual binding model of the combined binding of **A3** and **V1** to **Zn1** is more complicated. Apart from coordinating inside the cavity of **Zn1**, **A3** can also bind to the outside of the cavity and in that way cause a positive cooperative effect (Figure 5). It is clear that this is actually the case, since, as the value of the fractional saturation of **Zn1** with **A3** tends towards 1, the value of $^{A3}K_{V1}$-app does not become zero (which would be expected according to Equation 7) but is $^{A3}K_{V1}$-app = 3.0 x 10^4

M^{-1}. Assuming the binding scheme shown in Figure 5, the apparent association constant for the binding of **V1** in the presence of **A3** will evolve according to Equation 8, in which $K_{\text{A3–total}}$ is the sum of the association constants of the binding of **A3** to the outside ($K_{\text{A3–out}}$) and the inside ($K_{\text{A3–in}}$) of the cavity of **Zn1** respectively ($K_{\text{A3–total}} = K_{\text{A3–in}} + K_{\text{A3–out}}$). Although upon plotting ${}^{\text{A3}}K_{\text{V1}}$-app against $y_{\text{Zn1–A3}}$ the linear relation is still observed (Equation 9), full saturation of **Zn1** with **A3** ($y_{\text{Zn1–A3}} = 1$) leads to a value of ${}^{\text{A3}}K_{\text{V1}}\text{-app} = {}^{\text{A3}}K_{\text{V1}} \cdot (K_{\text{A3–out}}/K_{\text{A3–total}})$.

$$
{}^{\text{A3}}K_{\text{V}}\text{-app} = \frac{K_{\text{V}} + [\text{A3}] \cdot K_{\text{A3–out}} \cdot {}^{\text{A3}}K_{\text{V}}}{1 + [\text{A3}] \cdot K_{\text{A3–total}}} \tag{8}
$$

$$
{}^{\text{A3}}K_{\text{V}}\text{-app} = K_{\text{V}} + y_{\text{Zn1–A3}} \cdot \left(\frac{K_{\text{A3–out}} \cdot {}^{\text{A3}}K_{\text{V1}}}{K_{\text{A3–total}}} - K_{\text{V1}} \right) \tag{9}
$$

Equation 8 thus allows us the indirect calculation of the magnitude of the cooperative effect for the combined binding of **A3** to the outside and **V1** to the inside of **Zn1**. Assuming that the association constant of **A3** to the outside of the cavity of **Zn1** is $K_{\text{A3–out}} = 85\ M^{-1}$,[32] it can be easily calculated that ${}^{\text{A3}}K_{\text{V1}} = 2.6 \times 10^{7}\ M^{-1}$, suggesting a positive cooperative effect for the combined binding of **V1** and **A3** to **Zn1** (${}^{\text{A3}}K_{\text{V1}}/K_{\text{V1}}$) of a factor of 30.[33] These results are fully in line with the binding scheme in Figure 5 and reveal that, even though an apparent negative cooperative effect is observed due to blocking of the cavity by **A3**, this ligand actually strongly enhances the binding of **V1** when it is bound to the outside of the cavity.

Table 2. Apparent association constants (${}^{\text{A3}}K_{\text{V1}}$-app) for the binding of **V1** to **Zn1** in the presence of different amounts of pyridine (**A3**) at 298 K in $CHCl_3/CH_3CN$ 1/1 (v/v) as determined by fluorescence titrations.

[A3]₀ (μM)	${}^{\text{A3}}K_{\text{V1}}$-app
0	$8.7 \times 10^{5}\ M^{-1}$
9.0	$5.3 \times 10^{5}\ M^{-1}$
17.9	$3.9 \times 10^{5}\ M^{-1}$
44.4	$2.1 \times 10^{5}\ M^{-1}$
87.7	$1.4 \times 10^{5}\ M^{-1}$
171	$9.3 \times 10^{4}\ M^{-1}$
400	$5.6 \times 10^{4}\ M^{-1}$
719	$5.0 \times 10^{4}\ M^{-1}$

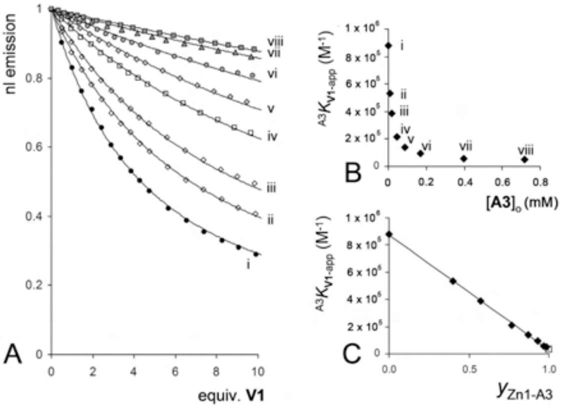

Figure 4. (A) Normalized fluorescence emission of **Zn1** (data points) upon the addition of **V1** in the presence of varying amounts of (increasing from i to viii) the competing guest **A3**, and fits of the curves using a simple 1:1 binding model. (B) Calculated apparent association constants ${}^{\text{A3}}K_{\text{V1}}$-app of **V1** with **Zn1** plotted against the concentration of **A3**. (C) Calculated apparent association constants ${}^{\text{A3}}K_{\text{V1}}$-app of **V1** with **Zn1** plotted against the occupation ratio of **Zn1** by **A3** ($K_{\text{A3}} = 7.5 \times 10^{4}\ M^{-1}$).

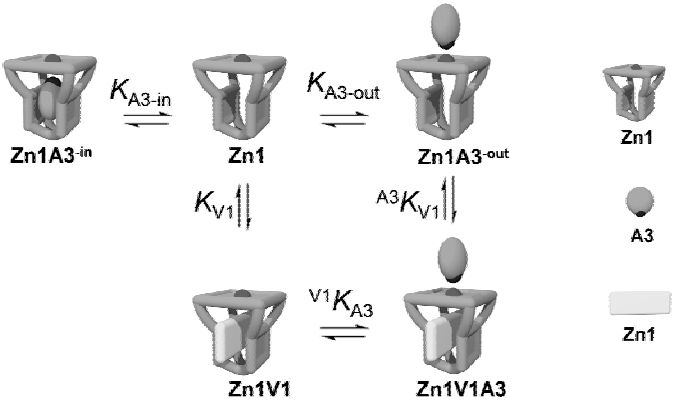

Figure 5. Schematic representation of the binding model between guests **A3** and **V1** and receptor **Zn1**.

The two experimental examples described here demonstrate that the thermodynamic circles balance, and that cooperative effects can be measured accurately. They also shed a light on the apparent character of association constants, since in all the performed titrations apparent 1:1 binding behavior was observed, whereas the binding schemes involved the combined interactions of various guests. Of crucial importance in the determination of the values of the apparent association constants is the fractional saturation of receptors with the interacting guest (or solvent) molecules.

These methods do not just concern the binding of multiple guests to porphyrin macrocycles but can in general be used for receptor-guest systems. To illustrate this, a recent literature example concerning the effect of salts on the apparent stability of cucurbit[7]uril-methyl viologen complexes will be discussed.[34] In the report, the association constants of **V1** with cucurbit[7]uril in water, in the presence of varying concentrations of Na^+ and Ca^{2+} ions, were measured (Figure 6). Increasing salt concentrations resulted in lower apparent association constants for the binding of **V1** to cucurbit[7]uril. The authors concluded that this was the effect of competitive binding of the Na^+ and Ca^{2+} ions inside the openings of the cavity of the receptor, in line with their previous observations of crystal structures of related compounds in which ions were bound inside these openings.[35] The data in the paper were used to derive quantitative values for the binding of Ca^{2+} ions by using a similar competitive binding model as described above. The competitive binding process most likely occurs according to the scheme presented in Figure 6. The two electron-rich openings of the cavity can each accommodate one Ca^{2+} ion, whereas **V1** was shown to form only a 1:1 complex with cucurbit[7]uril. Two models were compared; the first one assumes only 1:1 binding of Ca^{2+} with cucurbit[7]uril (Equation 10), whereas the second model takes a cooperative 2:1 binding of Ca^{2+} with the receptor into account (Equation 11).

$$^{\mathrm{Ca^{2+}}}K_{\mathrm{V1}}\text{-app} = \frac{K_{\mathrm{V1}}}{1 + K_1 \cdot [\mathrm{Ca^{2+}}]} \tag{10}$$

$$^{\mathrm{Ca^{2+}}}K_{\mathrm{V1}}\text{-app} = \frac{K_{\mathrm{V1}}}{1 + K_1 \cdot [\mathrm{Ca^{2+}}] \cdot \{1 + K_2 \cdot [\mathrm{Ca^{2+}}]\}} \tag{11}$$

Analysis of the experimental data with equation 10 revealed that according to the 1:1 binding model, Ca^{2+} binds to the receptor with an association constant of $K = 96$ M^{-1}. A far better fit was, however, obtained with the 2:1 cooperative binding model (Equation 11), as can be seen in Figure 7A. The calculated values were $K_1 = 59$ M^{-1} for the binding of the first Ca^{2+} ion and $K_2 = 9.5$ M^{-1} for the binding of the second ion. The statistical factor of four in such 2:1 binding systems ($K_1 = 4 \cdot K_2$),[36] suggests a small negative cooperative effect for the binding of the second molecule of Ca^{2+} of a factor of 1.5 ($\Delta\Delta G = 1$ kJ·mol^{-1}). Thus, these results do not only demonstrate that the observed lower association constants of **V1** are indeed a result of competition by Ca^{2+} ions, but they furthermore quantify the binding of Ca^{2+} and suggest the formation of 2:1 complexes of Ca^{2+} with cucurbit[7]uril in solution; a small negative cooperative effect is seen for the binding of the second ion. Also in this example, the observed cooperative effect is linearly dependant on the fractional saturation of the receptor (i.e., the relative concentration of receptor that is free in solution determines the magnitude of the apparent association constant of a titrated guest). In the 2:1 binding model the fractional saturation of cucurbit[7]uril with Ca^{2+} ($y_{\mathrm{R\text{-}Ca^{2+}}}$) is defined according to Equation 12, whereas Equation 3 can be used to determine this value assuming a 1:1 binding ratio.

$$y_{\mathrm{H\text{-}Ca^{2+}}} = \frac{K_1 \cdot [\mathrm{Ca^{2+}}] \cdot \{1 + K_2 \cdot [\mathrm{Ca^{2+}}]\}}{1 + K_1 \cdot [\mathrm{Ca^{2+}}] \cdot \{1 + K_2 \cdot [\mathrm{Ca^{2+}}]\}} \tag{12}$$

Substitution of $y_{\mathrm{H\text{-}Ca^{2+}}}$ into Equations 10 (assuming 1:1 binding) or 11 (assuming 2:1 binding) gives Equation 13:

$$^{\mathrm{Ca^{2+}}}K_{\mathrm{V1}}\text{-app} = K_{\mathrm{V1}} - y_{\mathrm{R\text{-}Ca^{2+}}} \cdot K_{\mathrm{V1}} \tag{13}$$

The linear dependency is clearly expressed in Figure 7B, which also shows the better fit of the 2:1 binding mechanism compared to the 1:1 binding model.

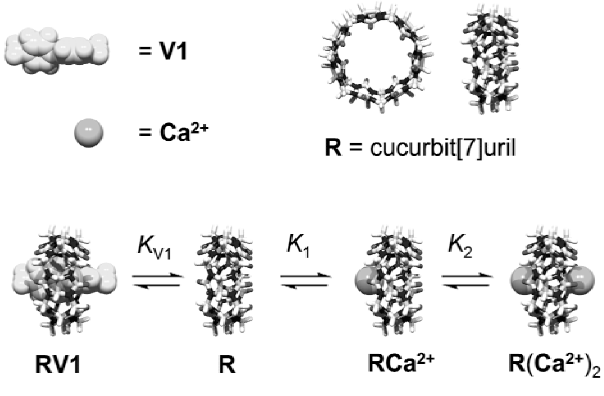

Figure 6. Binding scheme for the competitive binding between **V1** and Ca^{2+} with cucurbit[7]uril.

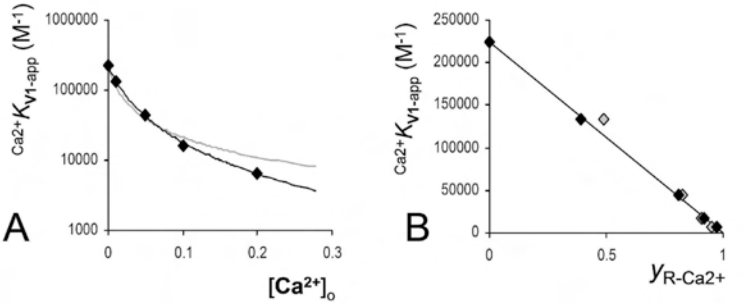

Figure 7. (A) Apparent association constant of the binding of **V1** with cucurbit[7]uril ($^{Ca2+}K_{V1}$–app) plotted against concentration of Ca^{2+} (M) present in solution, with the fits as obtained by equation 10 (—) and equation 11 (—). (B) Association constants ($^{Ca2+}K_{V1}$–app) plotted against molar saturation of cucurbit[7]uril according to the 1:1 binding model (◇) and the 2:1 binding model (◆).

2.4 Conclusion

The theory and experiments presented above have demonstrated that, at least in relatively simple receptor-guest binding studies, the experimental observations are beautifully in line with theory. Cooperative circles for the binding of multiple guests to receptors balance, and can be determined with the use of simple 1:1 binding isotherms only. Clearly, the experimental data often contain more information than is apparent to the experimenter. Of crucial importance to the observed cooperative effects is the fractional saturation of a receptor by a guest that is present in solution. Since in most cases association constants of solvent or salt molecules with receptors, and hence also the fractional saturation of the receptor by these possible inhibitors, are unknown, these molecules are likely to significantly influence the apparent values of association constants with titrated guests. Especially in studies in which different solvent systems and high salt concentrations are used, these competitive interactions inevitably have a considerable influence (even when caused by 'random' binding) and therefore should be taken into account, in addition to other solvent effects such as solvation. Despite the many reports that deal with cooperative effects in artificial receptor-guest systems, the studies described here are the first that map the complete thermodynamic evolution of such systems. It is clear that the squaring of cooperative circles by itself does not contain any information about the possible causes of the cooperative effects. In order to gain detailed information about the mechanisms governing such cooperative effects, it is not only crucial to obtain the accurate values, but also to derive quantitative values of all the interactions that interplay and that could possibly contribute to the observed effects. This, of course, requires a study of as many as possible model systems, the comparison of these studies, and finally, the drawing of general conclusions by deduction.

3. Investigations in the cooperative binding effects to porphyrin macrocycles

3.1 Introduction

As illustrated in Section 2, cooperative binding effects of two guests with a bivalent receptor could be caused by a large number of different factors. Independent of the chosen conditions, a measured association constant is always an apparent one. Although the thermodynamic circles must always balance, it is simply not possible to derive the exact causes of the observed cooperative effects directly. The only means of determining these causes is by studying and comparing as many as possible of the individual parameters that could account for the observed effects. To evaluate the causes of the observed positive cooperativity in the binding of viologens and pyridines with porphyrin macrocycles, it was decided to study the influence of the structure of the receptor by using a library of porphyrin macrocycles based on glycoluril (**Zn1**–**Zn5**, see Figure 1). Aside from 'mapping' the cooperative circles as good as possible by carrying out a series of UV-Vis and NMR titrations, additional studies were performed concerning solvent effects and complex formation of related compounds.

3.2 Synthesis of new porphyrin receptors

Recently, some new members have been added to the family of porphyrin receptors based on glycoluril (Figure 1 and Scheme 1). During the synthesis of previously reported tetratosylate **11a** (see Chapter 2), a significant amount of isomer **11b**, in which one of the aromatic side-walls is not connected by the 4,5-positions but by the 3,4-positions, was also formed. Both isomers **11a** and **11b** were reacted with tetrakis-ortho-hydroxy substituted porphyrin **12** and tetrakis-meta-hydroxy substituted porphyrin **13**, respectively, in DMF and in the presence of a base to give the corresponding products **$H_2$2**–**$H_2$5** in moderate yields (5−15%). The free base porphyrins could be converted to their corresponding zinc derivative (**Zn2**–**Zn5**) by the reaction with an excess of zinc acetate dihydrate in a 1:1 mixture of dichloromethane and methanol.

Compared to **1**, receptors **$H_2$2**–**$H_2$5** (and their corresponding zinc derivatives) have extended ethylene glycol spacers, which give these molecules a larger and more flexible cavity. In receptors **2** and **4** the spacers are connected to the porphyrin ortho-phenyl positions, whereas receptors **3** and **5** have them connected to the meta-phenyl positions. Receptors **4** and **5** both have twisted asymmetric glycoluril units in which two spacers are connected to one side-wall by the 4,5-positions and the two other spacers by the 3,4-positions of the opposing side-wall. Receptor **4** and **5** therefore both consist of two enantiomers. The enantiomers could, unfortunately, not be separated despite several attempts including chiral HPLC. The ^{1}H-NMR spectra of **$H_2$2** and **$H_2$3** revealed an apparent C_{2v} symmetry in which each set of four mirror protons appears as one resonance in the spectrum (Figures 12B and 13B). The ^{1}H- and ^{13}C-NMR spectra of twisted receptors **$H_2$4** and **$H_2$5** showed separate resonances for each individual proton (Figures 14B and

15B) and carbon atom, which highlights the high level of asymmetry in these two receptors. Although it was impossible to assign each individual resonance in the spectra of **$H_2$4** and **$H_2$5**, even with the help of 2D NMR techniques, all the key resonances could be identified.

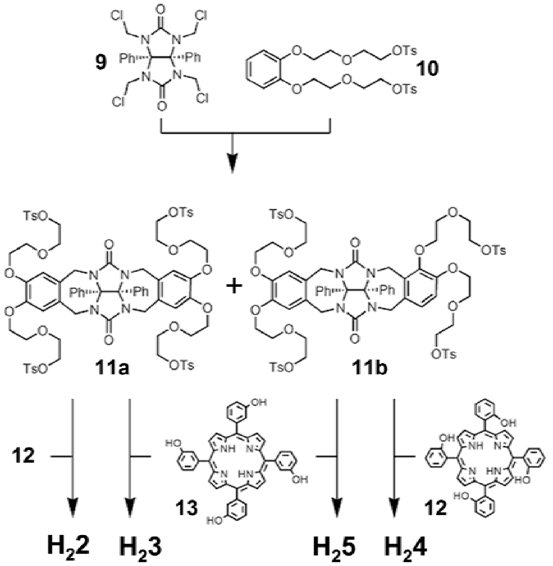

Scheme 1. Syntheses of porphyrin receptor molecules **$H_2$2**-**$H_2$5**.

3.3 Cooperative binding effects

Like receptor **1**, receptors **2**–**5** can bind viologen derivatives inside their cavities with high association constants (Table 3). The receptors that have a wider cavity (**3** and **5**) have a lower affinity for the viologens than the receptors that have a narrower cavity (**1**, **2**, and **4**), which is in line with the observations described in Chapter 2. Unlike **A1**, pyridine **A2** (Figure 1), which contains a bulky protecting group, was found to coordinate exclusively to the outside of all zinc porphyrin receptors **Zn1**–**Zn5**.

Table 3. Association constants ($K_{assoc.}$) of viologens **V1** and **V2** (Figure 1) with porphyrin receptors **$H_2$1**–**$H_2$5** and **Zn1**–**Zn5** at 298 K.

Receptor	Guest	$K_{assoc.}$
$H_2$1	**V1** [b,c]	6.0 x 10^5 M^{-1} [d]
Zn1	**V1** [b,c]	8.7 x 10^5 M^{-1} [d]
Zn1	**V2**	1.2 x 10^6 M^{-1} [d]
Zn1	**V3** [b]	2.6 x 10^4 M^{-1} [e]
$H_2$2	**V1** [b,c]	6.4 x 10^5 M^{-1} [d]
$H_2$2	**V2** [c]	1.2 x 10^5 M^{-1} [d]
Zn2	**V1** [b,c]	1.8 x 10^6 M^{-1} [e]
Zn2	**V2** [b,c]	2.0 x 10^5 M^{-1} [e]
$H_2$3	**V1** [a]	1.2 x 10^3 M^{-1} [e]
Zn3	**V1** [a,c]	4.2 x 10^2 M^{-1} [e]
Zn4	**V1** [c]	9.8 x 10^4 M^{-1} [e]
$H_2$5	**V1** [a]	1.0 x 10^3 M^{-1} [e]
Zn5	**V1** [a,c]	2.6 x 10^2 M^{-1} [e]

[a] Determined by ^{1}H-NMR titrations in $CDCl_3/CD_3CN$ 1/1 (v/v). [b] Determined by UV-Vis titrations in $CHCl_3/CH_3CN$ 1:1 (v/v). [c] Determined by fluorescence titrations in $CHCl_3/CH_3CN$ 1/1 (v/v). [d] Estimated error 10%. [e] Estimated error 30%.

The cooperative binding of **A2** and **V1** with all receptors was studied in detail. To this end, a serie of UV-Vis titrations were performed in which all the cooperative effects could be determined accurately by using the method discussed in Part 1 (Figures 11E, 11G, 12E, 12G, 13D, 13F, 14D, 14F, 15D, and 15F). In addition, ^{1}H-NMR titration experiments were performed (Figures 11B, 11C, 12B, 12C, 13B, 13C, 14B, 14C, 15B, and 15C) providing valuable information about the geometries of the receptors and the formed complexes, as well as duplicate values for the association constants obtained by the UV-Vis titrations. In all cases, the independently calculated association constants obtained by the NMR experiments at millimolar concentration were in very good agreement with the UV-Vis experiments at micromolar concentration (with discrepancies of at most 30% in the calculated binding constant value, but most often within 10% accuracy). The UV-Vis titration spectra of one guest in the presence of an excess of the second guest showed isosbestic points in all cases, which indicated an apparent 1:1 binding behavior.[37] Of course the linear relations in association constant with one guest when plotted versus the fractional saturation of the receptor with the second guest could be observed in all cases (Figures 11F, 11H, 12F, 12H, 12I, 13E, 13G, 14E, 14G, 15E, and 15G). Evaluation of the titration data revealed that all the receptors showed a strong positive cooperativity for the combined binding of **V1** and **A2**, with *Ce* factors ranging from 10 to 131 (Table 4). In the thermodynamic circles of **Zn1**, **Zn2**, **Zn3**, and **Zn4**, the cooperative effects for both directions of the circle were equal within experimental error. The measurements that involved receptor **Zn5** revealed a slight discrepancy between the two directions of the circle ($\Delta\Delta G^o = 0.8$ kJ·mol^{-1}, Table 4), which was most likely caused by changes in the solvent polarity as a result of the large concentrations of **A2** that were required to drive the fractional saturation of **Zn5** with **A2** to significant values. From the series of titration experiments with one guest in the presence of varying concentrations of the second guest, the association constant of the second guest could be calculated with the use of Equations 1, 2, 4, or 5, providing values that were, within error (35%), identical to those obtained by direct titration experiments.

Table 4. Association constants and cooperative effects of the combined binding of **A2** and viologens **V1** and **V2** to receptors **Zn1**–**Zn5** at 298 K. Within brackets the free energy gain for the cooperative effect (kJ·mol^{-1}) is given.

Receptor	G1	G2	K_{G1} [d]	$^{G2}K_{G1}$ [e]	Ce [f]	($\Delta\Delta G^o$)
Zn1	**A2**	**V1**	1.3 x 10^2 M^{-1} [a,b]	9.0 x 10^3 M^{-1} [a,c]	72x	(–10.6)
	V1	**A2**	8.7 x 10^5 M^{-1} [b]	5.3 x 10^7 M^{-1} [c]	61x	(–10.2)
	A2	**V2**	1.3 x 10^2 M^{-1} [a,b]	8.3 x 10^3 M^{-1} [c]	67x	(–10.4)
	V2	**A2**	1.2 x 10^6 M^{-1} [b]	[g]		
	A2	**V3**	1.3 x 10^2 M^{-1} [a,b]	7.5 x 10^3 M^{-1}	60x	(–10.1)
	V3	**A2**	2.6 x 10^4 M^{-1} [b]	[g]		
Zn2	**A2**	**V1**	5.5 x 10^2 M^{-1} [a,b]	8.0 x 10^3 M^{-1} [a,c]	15x	(–6.6)
	V1	**A2**	1.8 x 10^6 M^{-1} [b]	2.8 x 10^7 M^{-1} [c]	15x	(–6.8)
	A2	**V2**	5.5 x 10^2 M^{-1} [a,b]	6.7 x 10^3 M^{-1} [a,c]	12x	(–6.2)
	V2	**A2**	2.0 x 10^5 M^{-1} [b]	2.5 x 10^6 M^{-1} [c]	13x	(–6.3)
Zn3	**A2**	**V1**	4.1 x 10^2 M^{-1} [a,b]	5.5 x 10^3 M^{-1} [c]	12x	(–6.4)
	V1	**A2**	4.2 x 10^2 M^{-1} [a,b]	4.6 x 10^3 M^{-1} [c]	13x	(–6.7)
Zn4	**A2**	**V1**	7.3 x 10^2 M^{-1} [a,b]	7.3 x 10^3 M^{-1} [a,c]	10x	(–5.7)
	V1	**A2**	9.8 x 10^4 M^{-1} [b]	1.0 x 10^6 M^{-1} [c]	10x	(–5.8)
Zn5	**A2**	**V1**	3.2 x 10^1 M^{-1} [a,b]	3.0 x 10^3 M^{-1} [c]	94x	(–11.3)
	V1	**A2**	2.6 x 10^2 M^{-1} [a,b]	3.4 x 10^4 M^{-1} [c]	131x	(–12.1)

[a] Determined by ^{1}H-NMR titrations in $CDCl_3/CD_3CN$ 1/1 (v/v). [b] Determined by UV-Vis titrations in $CHCl_3/CH_3CN$ 1/1 (v/v). [c] Determined by nonlinear curve-fitting of the UV-Vis titration data by using Equation 1. [d] Estimated error 10%. [e] Estimated error 30%. [f] cooperative effect: $Ce = {}^{G2}K_{G1}/K_{G1}$, binding free energy gain for the cooperative effect $\Delta\Delta G^o = -RT \ln({}^{G2}K_{G1}/K_{G1})$, in which R is the gas constant. [g] Not determined.

3.4 Binding of pyridine derivatives to reference porphyrins

In order to appreciate the magnitude of the zinc-nitrogen binding interaction in the used solvent mixture (1/1 (v/v) acetonitrile/chloroform), the binding of **A2** to the reference porphyrins **Zn6**–**Zn8** (see Figure 1) was studied. The association constants of **A2** to **Zn6**–**Zn8** are all of the same order of magnitude ($K_{A2} \approx 2 \text{ x } 10^3$ M^{-1}, Table 5), which indicates that the substitution pattern of the porphyrin *meso*-phenyl groups has little influence on the binding strength of the ligand. The binding of **A2** with receptors **Zn1**–**Zn5**, to which it can only coordinate to the outside of the cavity, is in all cases, significantly lower than the binding of **A2** with **Zn6**–**Zn8** (Table 5). The association constants of **A2** with the porphyrin receptors in the presence of **V1** ($^{V1}K_{A2}$) are, however, uniformly larger than the association constants of **A2** with the reference compounds (see Table 4). This therefore indicated that two general effects are contributing to the observed heterotropic cooperativity. Competing interactions obstruct the binding of axial ligands to zinc on the outside of the cavities compared to non-functionalized porphyrins. The presence of viologen derivatives on the inside of the cavities results in axial ligand binding strengths stronger than those of the reference porphyrins. Addition of **V1** therefore not only undoes the competing interactions present inside the macrocycles, but it furthermore enhances the zinc-pyridine binding strength. Both the possible contributions to the binding constants of competition and enhanced binding in the presence of viologens will be discussed in the following sections.

Table 5. Association constants of **A2** to porphyrins **Zn1**–**Zn8** in 1/1 (v/v) mixtures of chloroform and acetonitrile ($K_{A2}^{(1/1\ CHCl_3/CH_3CN)}$) and in chloroform ($K_{A2}^{(CHCl_3)}$) and the association constants of acetonitrile to porphyrins **Zn1**–**Zn8** in chloroform (K_{CH_3CN}).

Receptor	K_{A2} (1:1 $CHCl_3$:CH_3CN) [a,b,c]	K_{A2} ($CHCl_3$) [b,e]	K_{CH_3CN} [b,f]
Zn1	$1.3 \times 10^2\ M^{-1}$	$2.8 \times 10^2\ M^{-1}$	$0.29\ M^{-1}$
Zn2	$5.5 \times 10^2\ M^{-1}$	$8.1 \times 10^2\ M^{-1}$	$0.15\ M^{-1}$
Zn3	$4.1 \times 10^2\ M^{-1}$	$4.2 \times 10^2\ M^{-1}$	$0.16\ M^{-1}$
Zn4	$7.3 \times 10^2\ M^{-1}$	$1.3 \times 10^3\ M^{-1}$	$0.13\ M^{-1}$
Zn5	$3.2 \times 10^1\ M^{-1}$	$6.6 \times 10^1\ M^{-1}$	$0.07\ M^{-1}$
Zn6 [f]	$2.1 \times 10^3\ M^{-1}$	$1.8 \times 10^3\ M^{-1}$	$0.12\ M^{-1}$
Zn7 [f]	$2.1 \times 10^3\ M^{-1}$	$1.2 \times 10^3\ M^{-1}$	$0.04\ M^{-1}$
Zn8 [f]	$1.8 \times 10^3\ M^{-1}$	$2.2 \times 10^3\ M^{-1}$	$0.11\ M^{-1}$

[a] Determined by ^1H-NMR titrations in $CDCl_3/CD_3CN$ 1:1 (v/v). [b] Determined by UV-Vis titrations, [c] Estimated error 10%. [d] Estimated error 30%. [e] Estimated error 50%. [f] Experimental values were divided by a factor of two to correct for their bivalent character as a result of the two fold symmetry axis.

3.5 The effects of acetonitrile and water

The binding experiments of **A2** clearly suggested that competing interactions played a role in the cavity-containing porphyrins which result in lower association constants compared to non-functionalized porphyrins. It was shown in Section 2 that weak competing interactions can potentially lead to severe changes in observed association constants (larger than the observed cooperative effects), especially where the solvent is concerned. Solvent molecules that inhibit the receptors by coordinating the zinc ion from the inside of the cavity will obstruct the binding of both **V1** and **A2**, thereby causing an apparent cooperative effect for the combined binding of the two guests. Since the fractional saturation of a receptor by a competing (solvent) molecule is linearly related to the observed association constants in the titration experiments of guests, an association constant of $K_a = 1.5\ M^{-1}$ for the binding of acetonitrile on the inside of a cavity would already cause an apparent cooperative effect of a factor 15 (given that the experimental concentration of acetonitrile is 9.5 M). Both water and acetonitrile are known to be capable of coordinating to zinc porphyrins, since formation of such complexes has been observed in a number of X-ray structures[38] and binding studies.[39] It was therefore decided to study the binding properties of these possible inhibitors with the different porphyrins.

The small difference between the association constants of **A2** with the porphyrins in chloroform compared to those values in 1/1 chloroform/acetonitrile (v/v), as presented in Table 5, revealed immediately that the competing effect of acetonitrile is not very large. Both in chloroform and in chloroform/acetonitrile 1/1 (v/v) the binding of **A2** with porphyrin receptors **Zn1**–**Zn5** is significantly lower than with the reference compounds **Zn6**–**Zn8**, which indicated that the coordination of acetonitrile can not be fully responsible for these differences. Other competing interactions must therefore be more dominant contributors to the observed cooperative effects.

Nevertheless, to establish the precise binding strength of the solvent, and hence obtain an idea of the possible magnitude of the competition by acetonitrile, UV-Vis titration experiments were performed in which acetonitrile was added to solutions of the porphyrins in chloroform. The addition of high concentrations of acetonitrile resulted in a red shift of the porphyrin Soret bands, which is typically observed upon the coordination of electron donating ligands to zinc porphyrins. The observation that such shifts were absent upon the titration of acetonitrile to free base porphyrins confirms that the red shifts are caused by coordination of the acetonitrile nitrogen atom to the zinc ion of the porphyrin. The evolution of the spectra was non-isosbestic, which is presumably caused by a gradual change in solvent polarity as a result of the increasing acetonitrile concentration. As a result, only rough values for the binding constants could be determined (Table 5). In the case of all measured porphyrins, **Zn1** clearly has the highest affinity for acetonitrile. This suggests that acetonitrile is coordinated to the zinc ion on the inside of the cavity of **Zn1**. With the help of Equations 3 and 7, it can be calculated that acetonitrile could cause an apparent cooperative effect for the combined binding of **V1** and **A2** (or other combinations of viologens and pyridines) to **Zn1** of a factor of 3.8. Although this value is seemingly irrelevant when compared to the total cooperative effect (a factor of approximately 65), it does contribute roughly 3.3 kJ·mol^{-1} to the total effect of 10.4 kJ·mol^{-1} (almost one third).

The binding of water to the different receptors was evaluated by the use of UV-Vis and ^{1}H-NMR experiments. Titration experiments revealed that water does not bind to receptors **Zn1**, **Zn3**, and **Zn5** and therefore can not inhibit these receptors for the binding of another guest. This could also be demonstrated experimentally since, in both water-saturated and in a 1/1 (v/v) mixture of freshly distilled chloroform and acetonitrile, equal association constants were obtained for the binding of **V1** with **Zn1**. Coordination of water was only observed to *ortho*-extended receptors **Zn2** and **Zn4**; concluded from the appearance of isosbestic points and red shifts of the Soret bands in the UV-Vis spectra and shifts of the cavity- and water proton resonances in the ^{1}H-NMR spectra. The association constants are relatively low (**Zn2**: $K_{\text{water in CHCl}_3} \approx 30\ \text{M}^{-1}$, $K_{\text{water (1/1 CHCl}_3\text{/CH}_3\text{CN)}} \approx 12\ \text{M}^{-1}$, **Zn4**: $K_{\text{water CHCl}_3} \approx 10\ \text{M}^{-1}$). Considering the low concentration of water present (the utmost care was taken to avoid its presence), these values are by no means large enough to cause significant competition. For instance, assuming a water concentration of 10 mM, a competitive effect of only a factor 1.1 (0.2 kJ·mol^{-1}) could be expected for the binding of axial ligands and viologens to **Zn2**.

3.6 Intramolecular coordination

Investigation of the structural properties of the receptors revealed that between the free base and zinc derivatives of porphyrin receptors **2**, **3**, and **5** large differences were observed. Whereas the ^{1}H-NMR spectra of **H$_2$1** and **Zn1**, and **H$_2$4** and **Zn4**, respectively, showed nearly identical values for the resonances of the cavity protons, suggesting very similar geometries (Figures 11B and 14B), in the cases of **Zn2**, **Zn3**, and **Zn5** these resonances had shifted strongly upfield compared to those of their free base derivatives (Figures 12B, 13B, and 15B) both in $CDCl_3$ and in 1:1 mixtures of chloroform and acetonitrile. The signals of the glycoluril backbone protons H-3 and H-4 (Figure

8) showed especially large shifts (Table 7, Figures 12B, 13B, and 15B), which clearly indicates that, in the zinc derivatives, the clip region is located closer to the shielding porphyrin than in the free base compounds. Addition of the bulky ligand **A2**, which coordinates to the zinc ion on the outside of all of the cavities of **Zn1**–**Zn5**, caused, in all cases, the proton resonances to shift downfield to positions similar to those observed for the free base derivatives (Table 7 and Figures 11B−15B). This strongly suggests that an intramolecular coordination of the zinc ion, most probably to one of the cavity oxygen atoms, is responsible for the observed difference in geometries. Such an interaction 'locks' the molecules in a closed geometry. The UV-Vis spectra of the receptors in chloroform indeed confirmed the presence of such an intramolecular coordination in **Zn2**, **Zn3**, and **Zn5**. The Soret bands of **Zn1** and **Zn4** (receptors that do not have a closed geometry as a result of intramolecular coordination) appeared at comparable wavelengths to those of the reference zinc compounds **Zn6**–**Zn8**, whereas the Soret bands of **Zn2**, **Zn3**, and **Zn5** had shifted to larger wavelengths (Table 6). There is clearly coherence between the UV-Vis and ^{1}H-NMR spectroscopic data. When the porphyrin Soret bands appear rather broad, as a result of the presence of molecules in both their locked and unlocked conformation (mostly in **Zn2** and **Zn3**; Figures 12A and B for **Zn2** and Figures 13A and B for **Zn3**), a similar broadening of proton resonances is observed in the ^{1}H-NMR spectra. This broadening is the result of a relatively slow exchange between locked and unlocked geometries of the receptors on the NMR timescale. The relative ratios of locked:unlocked receptor conformation ($K_{\mathrm{L:U}}$) in chloroform could be determined by deconvolution of the UV-Vis spectra. Approximate values of $K_{\mathrm{L:U-}\mathbf{Zn2}} = 2$, $K_{\mathrm{L:U-}\mathbf{Zn3}} = 5$, $K_{\mathrm{L:U-}\mathbf{Zn4}} < 0.2$, and $K_{\mathrm{L:U-}\mathbf{Zn5}} > 10$ were calculated, which indicated that the degree of intramolecular coordination increases with the series **Zn4** < **Zn2** < **Zn3** < **Zn5**. In **Zn5** the intramolecular coordination plays a very dominant role. The ^{1}H-NMR spectrum of **Zn5** shows sharp peaks, many of which have shifted dramatically compared to their positions in the spectrum of **H$_2$5**, because it exists mainly in its locked conformation (also in the presence of acetonitrile). The strong zinc-oxygen interaction competes heavily with the binding of **A2** and explains the very low association constant observed for the binding of this guest ($K_{\mathrm{A2}} = 32$ M^{-1}). The binding of the viologen derivatives in the cavity of **Zn5** is similarly hampered by this intramolecular locking. The addition of either of these guests removes the intramolecular locking and facilitates the binding of the other guest, which results in the observed, very strong, cooperative binding effect in the case of **Zn5**, and to a lesser extent in the cases of **Zn2**, **Zn3**, and **Zn4**.

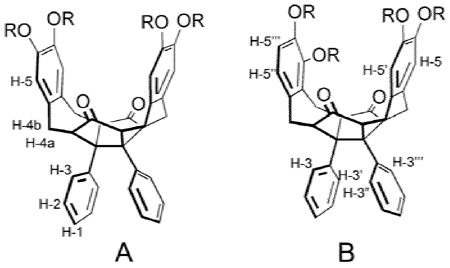

Figure 8. Diphenylglycoluril backbone with proton numbering of (A) porphyrin receptors **1**, **2**, and **3**, (B) receptors **4** and **5**.

3.7 Non-coordinating competitive interactions

The intramolecular zinc-oxygen coordination and/or the inside-coordinating acetonitrile interactions are possible reasons for the observed lower affinity between porphyrin receptors **Zn2**-**Zn5** and **A2**. In **Zn1**, however, the (intramolecular or solvent) zinc coordinating interactions are by no means large enough to account for this effect. This is unambiguously illustrated by the fact that in chloroform the association constant between **A2** and **Zn1** is also significantly lower than those between **A2** and the reference compounds (Table 5). In the mean time, unlike **Zn2**, **Zn3**, and **Zn5** the Soret band of **Zn1** shows a maximum value at 421 nm (like reference compounds **Zn6**–**Zn8**), which indicates that there is no electron donating ligand coordinated to the zinc ion in chloroform. The weak binding between **Zn1** and **A2** must therefore have a non-coordinating competitive source. A number of causes can be postulated for these observations. Such causes could be a distortion of the porphyrin surface as a result of the rigid cavity (which could be unfavorable for zinc-nitrogen coordination on the outside of the cavity), or distant non-coordinating electronic interactions between the zinc and the spacer crown ethers. Unfortunately, it is not possible to determine the exact ground for this additional competition from the available data. A crystal structure of **Zn1**, in which no axial ligand is coordinated, should provide more insights into the possible causes of this competition.

3.8 Effects in the proximity of the viologen to the porphyrin

The observation that the association constants of **A2** with the different viologen-bound-receptors are considerably higher than those of **A2** with the reference porphyrins is clear evidence that the presence of viologens strengthens the zinc-nitrogen coordination bond. In order to determine whether any trends can be observed with respect to the binding geometries and cooperative effects, the structures of the different complexes will be evaluated.

Firstly, the different receptor-viologen complexes will be considered. Interpretation of the ^{1}H-NMR spectra of the receptors with **V1** allowed the prediction of the approximate geometries of the complexes. In the case of receptors **1**–**4**, the ^{1}H-NMR spectra of the complexes of both the zinc and the free base derivatives with **V1** showed similar values for the cavity proton resonances, suggesting similar geometries of the complexes (Table 7 and the NMR spectra in Figures 11−15). In contrast, the spectrum of the complex between **Zn5** and **V1** was significantly different from that of the complex between **$H_2$5** and the same guest. This is most likely a result of some remaining intramolecular coordination between the zinc ion and one of the oxygen atoms inside the cavity in the complex between **Zn5** and **V1**, which was concluded from the observation that the addition of the bulky ligand **A2** caused the cavity proton resonances to shift to values similar to those of the complex between **$H_2$5** and **V1**.[40] Two main overall geometries can be observed for the different receptor-viologen complexes. In the first one, **V1** is clamped in between the two cavity side-walls with the viologen oriented in an edge-to-face manner with respect to the porphyrin; in the second **V1** lies flat under the porphyrin in a face-to-face geometry (Figure 9).[41−42] The first geometry causes the signal of the side-wall protons H-5 (Figure 8) to shift upfield in the ^{1}H-NMR spectra as a result of shielding by the aromatic rings of the guest, whereas the signal of the porphyrin pyrrole NH protons remains relatively unchanged. In case of the latter complex geometry, the signal of the pyrrole NH protons shifts dramatically upfield because of the same shielding interactions. The data in Table 7 reveal that the complexes of receptors **1**, **3**, and **5** with **V1** have an edge-to-face geometry, whereas the complexes of receptors **2** and **4** with **V1** have a face-to-face geometry. These conclusions are confirmed by the observed shifts of the porphyrin Soret bands in the UV-Vis spectra upon complex formation. The edge-to-face complexes of **V1** with the receptors appear at 427 nm, whereas the face-to-face complexes appear at 430 nm (Table 6). Molecular modeling based on this information suggests that **V1** binds closer to the porphyrin in the complex with receptor **1** than in the complexes with receptors **3** and **5** (the last two have longer spacers). The shifts in the ^{1}H-NMR spectra of the pyrrole NH protons furthermore suggest that **V1** binds closer to the porphyrin in the complex with **$H_2$2** than in the complex with **$H_2$4** (Table 7). A look at the association constants of **A2** with the complexes of the different receptors with **V1** ($^{V1}K_{A2}$; Table 4) reveals a clear trend between the proximity of **V1** to the porphyrin and the binding strength of **A2** with these complexes: $^{V1}K_{A2}$ becomes higher in the series of receptors **Zn5** < **Zn3** < **Zn1** and in the series **Zn4** < **Zn2**, an observation that is in line with the proposed influence of the distance of **V1** to the porphyrins.

It was observed in Chapter 2 that ethyl viologen (**V2**) binds to receptors **$H_2$2** and **Zn2** in a completely different geometry than methyl viologen (**V1**). Although the aromatic surfaces of both viologens bind in a face-to-face geometry with respect to the porphyrin plane, **V1** binds in a so called suit(2)ane geometry in which it accommodates the positive charges in between the crown ether rings of **2**. **V2** can not accommodate its positive charges in such a way and adopts a pseudo-rotaxane geometry in the complex with **2** (Figure 9). As a result of these different binding geometries, **V1** binds closer to the porphyrin than **V2** (or at least is tighter inside the receptor). In order to directly study the effects of different binding geometries of viologens with a single receptor, the cooperativity of the combined binding of **A2** and **V2** with **Zn2** were evaluated. Both the ^{1}H-NMR and UV-Vis titration experiments revealed that $^{V1}K_{A2}$ is higher (by a factor 1.19) than $^{V2}K_{A2}$ ($^{V1}K_{A2} = 8.0 \times 10^3\ M^{-1}$, $^{V2}K_{A2} = 6.7 \times 10^3\ M^{-1}$; Table 4). Control experiments with **V2**, **A2**, and **Zn1** (the complexes between **Zn1** and **V1**, and **Zn1** and **V2** have approximately the same rotaxane geometry) showed that the difference between the values ${}^{V1}K_{A2}$ and ${}^{V2}K_{A2}$ for receptor **Zn1** is less pronounced (a factor 1.08; Table 4).

Although the differences are very marginal, the above results suggest that electronic interactions might, at least partially, be responsible for the enhanced zinc-pyridine binding strengths in the presence of viologens. These observations could also be due to steric factors in which the viologens effectively push the zinc out of the porphyrin plane and hence facilitate the axial ligand coordination. In order to further investigate which of the two mechanisms is responsible, it was of interest to study the effect of the mono-substituted viologen guest **V3**. The presence of only one positive charge in **V3** has a large influence on the association constant with **Zn1** ($K_{V3} = 2.6 \times 10^4$ M^{-1}, 34 times lower than that of **Zn1** with **V1**) This indicates that, in the case of the doubly charged guests, both positive charges contribute to the stability of the complex with **Zn1**. The cooperative effect for the binding of **A2** to **Zn1** in the presence of **V3** (*Ce* = 60), on the other hand, is nearly as large as that in the presence of **V1** (*Ce* = 67). These results suggest that either only one of the two positive charges of **V1** and **V2** contributes to the observed cooperative effects, or that other (presumably steric) interactions also contribute to the cooperative effect. For now, this issue will remain unclear. Ideally, in future experiments the cooperative effect of a neutral guest that binds inside the cavity of **Zn1** (or other receptors) could provide the answer.

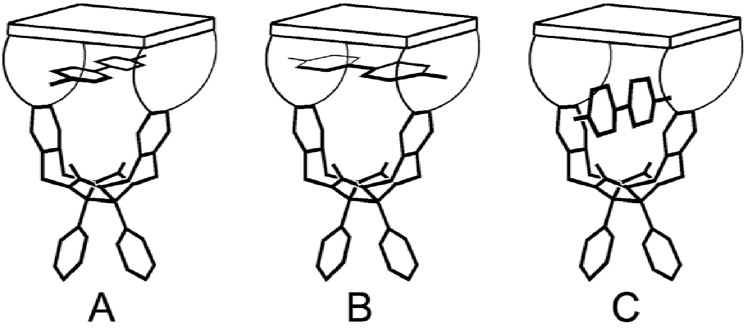

Figure 9. Schematic structures that explain the geometry of the complexes between porphyrin receptors and viologens. (A) Face-to-face rotaxane, (B) Face-to-face suit(2)ane, (C) Edge-to-face rotaxane.

Table 6. Position of the Soret band (nm) of porphyrins **Zn1**–**Zn8**

Receptor	$CHCl_3$ [a]	1/1 $CHCl_3/CH_3CN$ (v/v) [a]	**RA2** [b]	**RV2** [b]	**RV2A2** [b]
Zn1	421	425.5	430	427	429
Zn2	425.5	425.5	429.5	430	434.5
Zn3	430	427.5	427	427	429.5
Zn4	422	425.5	529	430	433
Zn5	428.5	427.5	427	428	431
Zn6	420.5	424	428		
Zn7	421	422	427		
Zn8	421	424	427.5		

[a] Directly measured. [b] Derived from the UV-Vis titration experiments.

Table 7. ^{1}H-NMR spectroscopic data of the different receptors and complexes. Between brackets the shifts Δδ compared to the free base derivative are given.[a]

Receptor (complex)	Proton		
	NH (Δδ)	H-5 (Δδ)	H-3 (Δδ)
H$_2$1	−2.79	6.18	6.87
Zn1		6.22 (+0.04)	6.88 (+0.01)
Zn1+**A2**		6.19 (+0.01)	6.87 (0)
H$_2$1+**V1**	−2.96 (−0.17)	6.02 (−0.16)	6.96 (+0.09)
Zn1 +**V1**		5.98 (−0.20)	6.98 (+0.11)
Zn1+**V1**+**A2**		6.00 (−0.18)	6.99 (+0.12)
H$_2$2	−2.71	6.39	6.96
Zn2		6.02 (−0.37)	6.66 (−0.30)
Zn2+**A2**		6.38 (−0.01)	6.96 (0)
H$_2$2+**V1**	−3.79 (−1.08)	6.30 (−0.09)	6.91 (−0.05)
Zn2 +**V1**		6.29 (−0.10)	6.89 (−0.07)
Zn2+**V1**+**A2**		6.30 (−0.09)	6.91 (−0.05)
H$_2$3	−2.87	6.37	6.88
Zn3		5.92 (−0.45)	6.12 (−0.76)
Zn3+**A2**		6.38 (+0.01)	6.89 (+0.01)
H$_2$3+**V1**	−2.83 (+0.04)	6.15 (−0.22)	6.88 (0)
Zn3 +**V1**		6.11 (−0.26)	6.82 (−0.06)
Zn3+**V1**+**A2**		6.07 (−0.30)	6.87 (−0.01)
H$_2$4	−2.69	6.47	6.93
Zn4		6.34 (−0.13)	6.84 (−0.09)
Zn4+**A2**		6.48 (+0.01)	6.92 (0)
H$_2$4+**V1**	−3.58 (−0.89)	6.32 (−0.15)	6.86 (−0.06)
Zn4 +**V1**		6.30 (−0.17)	6.83 (−0.09)
Zn4+**V1**+**A2**		6.38 (+0.09)	6.89 (+0.04)
H$_2$5	−2.80	6.31	6.82
Zn5		6.26 (−0.04)	5.43 (−1.39)
Zn5+**A2**		6.36 (+0.06)	6.87 (+0.05)
H$_2$5+**V1**	−2.79 (+0.01)	6.04 (−0.27)	6.86 (+0.04)
Zn5 +**V1**		6.15 (−0.16)	6.01 (−0.81)
Zn5+**V1**+**A2**		6.08 (−0.23)	6.84 (−0.01)

[a] Values of resonances belonging to H-5 and H-3 of twisted receptors **4** and **5** were averaged for clarity.

4. Conclusion

Strong positive cooperative effects were observed for the combined binding of viologen derivatives and pyridine ligands to all porphyrin receptors. The fact that the thermodynamic circles balance is not surprising from a theoretical point of view, but stresses the accuracy of the used methods. Moreover, it allowed the accurate determination of cooperative effects. It is clear that the cooperative effects can not be attributed to a single cause but to a number of small, additive contributions. In the different receptors, the contributions to the total effect are distributed differently, but both competitive and enhancing causes can be observed in all cases. The competitive interactions, e.g., solvent molecules binding to the receptor, intramolecular locking, and other presumably electronic or steric interactions obstruct the binding of both viologen and pyridine guests. Addition of the first guest removes the obstructing interaction and so facilitates the binding of the second guest. The enhancing interactions are a result of direct interplay between the two guests and the receptor, and cause stronger binding between the pyridine and the zinc ion compared to unfunctionalized porphyrin molecules. An effort was made to determine all the individual contributions involved, which are summarized below.

(1) *Competitive coordination of acetonitrile to the zinc ion on the inside of the cavity of the receptors obstructs the binding of both viologens and axial ligands.* This 'blocking' of the cavity was observed most strongly for **Zn1** and plays a minor role in **Zn2**–**Zn4**. The weakest binding of acetonitrile was observed with **Zn5**. Although water was shown to bind inside the cavities of receptors **Zn2** and **Zn4**, its affinity is too low to contribute significantly to the observed cooperative effects.

(2) *Intramolecular coordination of one of the cavity oxygen atoms to the zinc ion in the porphyrin.* This interaction locks the receptors in a closed geometry and thereby obstructs the binding of both types of guests. In the case of **Zn5** this locking of the cavity plays a very dominant role, but it also clearly observed in **Zn2** and **Zn3**. Addition of bulky pyridine ligands unlocks the cavities and so facilitates the binding of viologens, whereas the addition of the viologen breaks the intramolecular coordination bond and so facilitates the binding of bulky pyridines.

(3) *The locking and blocking effects do not add up to explain the total of competitive causes.* In the case of **Zn1** there must be additional competing interactions that are responsible for the low association constants with bulky pyridines. These are presumably non-coordinating electronic interactions between the zinc ion and the electron-rich cavity and are most probably associated with some structural changes in the receptor, which need to be overcome upon binding of either of the guests.

(4) *Bond enhancing interplay between viologen, pyridine, and porphyrin.* The observation that the proximity of the viologen to the porphyrin has an effect on the observed association constant of the bulky axial ligand with the zinc porphyrin receptors strongly suggests an (Lewis acid-base-like) electronic interplay between the electron deficient viologen, the porphyrin, and the electron-donating pyridine ligand. Also the observation that the association constants of the bulky axial ligands with viologen bound prorphyrin receptors are higher than those with the reference-unfunctionalized porphyrins suggests such an interplay.

(5) *Structural changes in the receptor upon binding of the guests might also contribute to the stronger binding observed compared to the reference porphyrins.* These changes can, for instance, involve the position of the zinc ion in the porphyrin ring, which is known to be pulled out of the porphyrin plane by coordinating pyridines. The viologen might contribute to this effect by either sterically or electronically pushing the zinc ion out of the porphyrin plane and so assist the pyridine coordination.

Taking all these contributions into account, it is clear that the binding scheme, as presented in Figure 2, is just an apparent one, and that the actual binding scheme is at least as complicated as that in Figure 10A. It is simply impossible to derive all the individual values accurately since, independent of the used experimental conditions, apparent association constants are measured that depend on all the intertwining interactions. Roughly, the individual contributions add up as presented in Figure 10B. Although the observed cooperative effects are in the same order of magnitude for **Zn1** and **Zn5**, the mechanisms that are responsible for them are completely different. In **Zn1**, the competition with acetonitrile on the inside of the rigid cavity contributes to approximately a third to the total observed cooperative effect and the rest is presumably, mainly, a result of electronic interactions (both intramolecular and between the guests and the receptor). In **Zn5**, the intramolecular coordination between the zinc ion in the porphyrin and one of the spacer oxygen atoms, which results in a fully locked conformation, is responsible for the vast majority of the observed cooperative effect. The cooperative binding effects observed for the other receptors (**Zn2**–**Zn4**) are caused by various interactions that all partially contribute to the overall observed effect.

The interactions responsible for the cooperative effects observed in these artificial receptors are also observed in natural systems. Inhibition, activation, induced-fit, lock-and-key, electronic interactions, and allosteric binding are all terms that can be applied to these synthetic receptors.

In the next chapter it will be shown that these cooperative circles also balance when complex formation between the receptors and blocked viologen derivatives, involved in slippage reactions, is considered. The outcome of these kinetic studies strongly support the conclusions of the here presented thermodynamic studies.

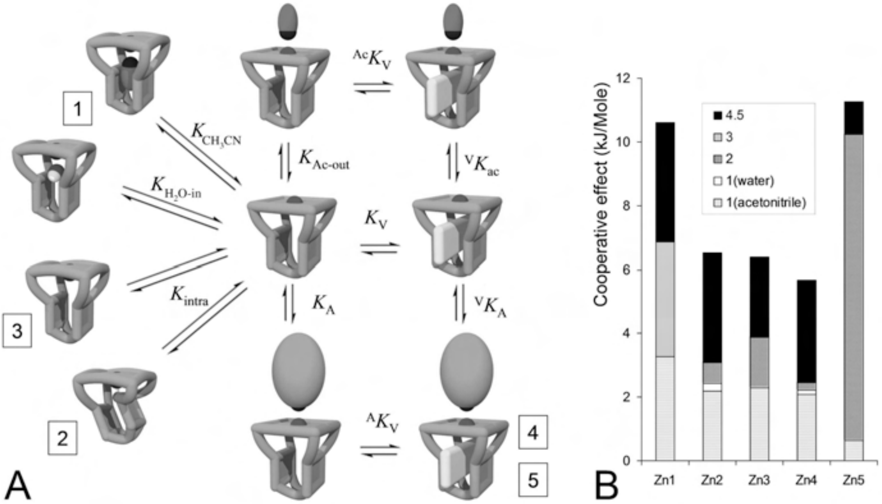

Figure 10. (A) Binding scheme of all interactions that are responsible for the observed cooperative effects. [1] Blocking of the cavity by acetonitrile and water. [2] Intramolecular locking of the cavity as a result of coordination between the zinc and a crown ether oxygen atom in the spacer. [3] Electronic pinning of the cavity as a result of distant interactions between the zinc and the electron-rich interior of the cavity. [4] Electronic interplay between viologen, pyridine, and zinc porphyrin, which genuinely strengthens the stability of the complex. [5] Steric interactions enhancing the combined binding of viologen and pyridine to the zinc-porphyrin. (B) Different contributions (kJ·mol^{-1}) which are responsible for the observed cooperative binding effects per receptor (for explanation see (A) and the text).

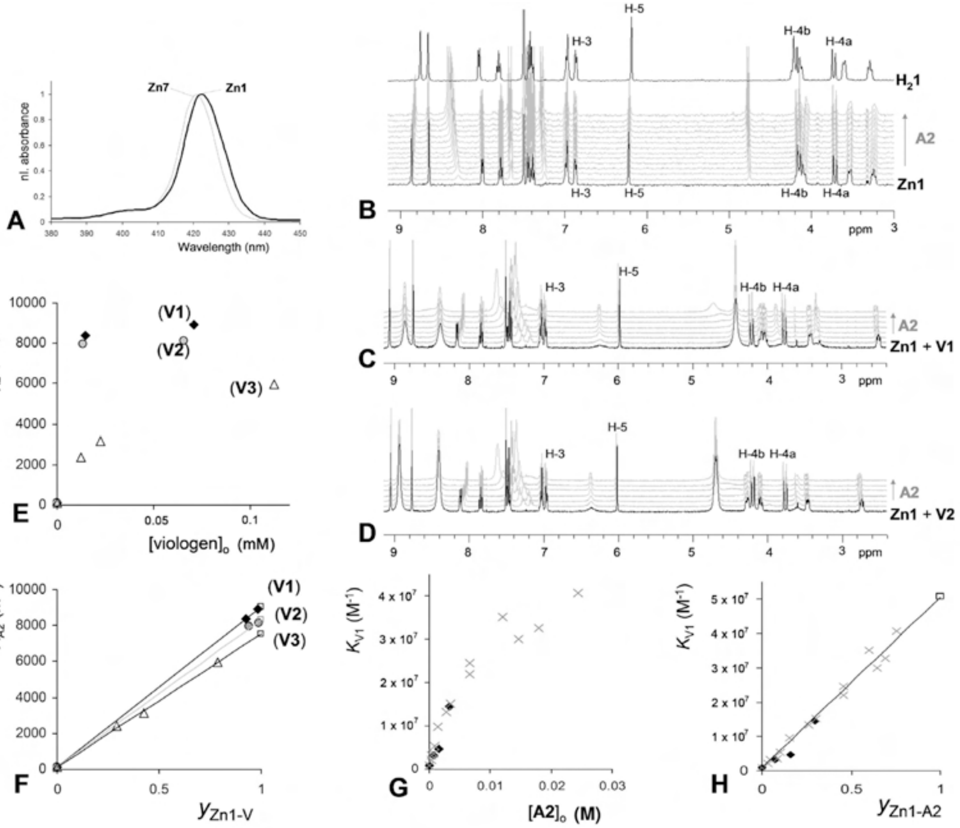

Figure 11. Selection of data concerning the cooperative binding effects involved with **Zn1**. (A) UV-Vis spectra of the Soret bands of **Zn1** and **Zn7** in chloroform, which reveal no significant shifts and hence no intramolecular coordination in **Zn1**. (B) ^{1}H-NMR spectra of **H$_2$1** and a titration of **A2** to **Zn1**, revealing that no significant changes occur in the geometry of the rigid cavity upon insertion of a zinc ion and the subsequent addition of bulky **A2**. (C) ^{1}H-NMR spectra of the titration of **A2** to the complex of **Zn1** with **V1**. (D) ^{1}H-NMR spectra of the titration of **A2** to the complex of **Zn1** with **V2**. (E) Association constants of **A2** with **Zn1**, as obtained by UV-Vis titration experiments, plotted *vs*. the concentration of viologen derivatives **V1**, **V2**, and **V3**. (F) Association constants of **A2** with **Zn1** plotted against the fractional saturation of **Zn1** with the respective viologen derivatives, which clearly reveal the linear relationship and the marginal difference in cooperative effect. (G) Association constants for the binding of **V1** with **Zn1** plotted versus the concentration of **A2** from various UV-Vis and fluorescence titration experiments (the high association constants are difficult to determine accurately at the used experimental concentrations). (H) Association constants for the binding of **V1** with **Zn1** plotted versus the fractional saturation of **Zn1** with **A2**.

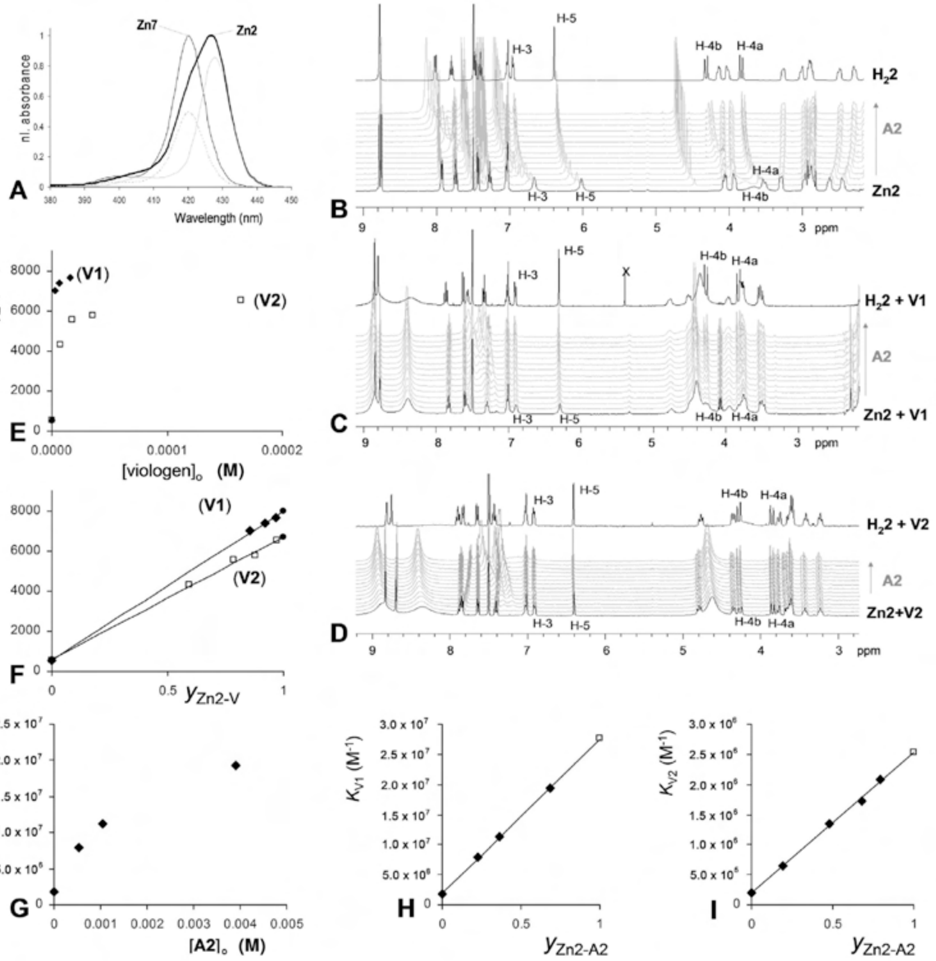

Figure 12. Selection of data concerning the cooperative binding effects involving **Zn2**. (A) UV-Vis spectra of the Soret bands of **Zn2** and **Zn7** in chloroform, revealing a clear red shift as a result of the intramolecular coordination of **Zn2**. (B) ^{1}H-NMR spectra of **$H_2$2** and a titration of **A2** to **Zn2**, revealing the significant changes in the geometry of the flexible cavity upon insertion of a zinc ion as a result of the intramolecular coordination, and the removal of this intramolecular coordination as a result of the addition of **A2**. (C) ^{1}H-NMR spectra of **$H_2$2** with **V1** and a titration of **A2** to the complex of **Zn2** with **V1**, which reveal that, independent of the presence or absence of a zinc ion, the geometries of the formed pseudo-rotaxane complexes are identical. (D) ^{1}H-NMR spectra of **$H_2$2** with **V2** and a titration of **A2** to the complex of **Zn2** with **V2**. (E) Association constants of **A2** with **Zn2** as obtained by UV-Vis titration experiments plotted versus concentration of viologen derivatives **V1** and **V2**. (F) Association constants of **A2** with **Zn2** when plotted against the fractional saturation of **Zn2** with the respective viologen derivatives (**V1** and **V2**), which clearly reveal the linear relation and the marginal difference in cooperative effect. (G) Association constants between **V1** and **Zn2** when plotted against the concentration of **A2** and against (H) the fractional saturation of **Zn2** with **A2** ($y_{Zn1\text{-}A2}$). (I) Association constants between **V2** and **Zn2** when plotted against the fractional saturation of **Zn2** with **A2**.

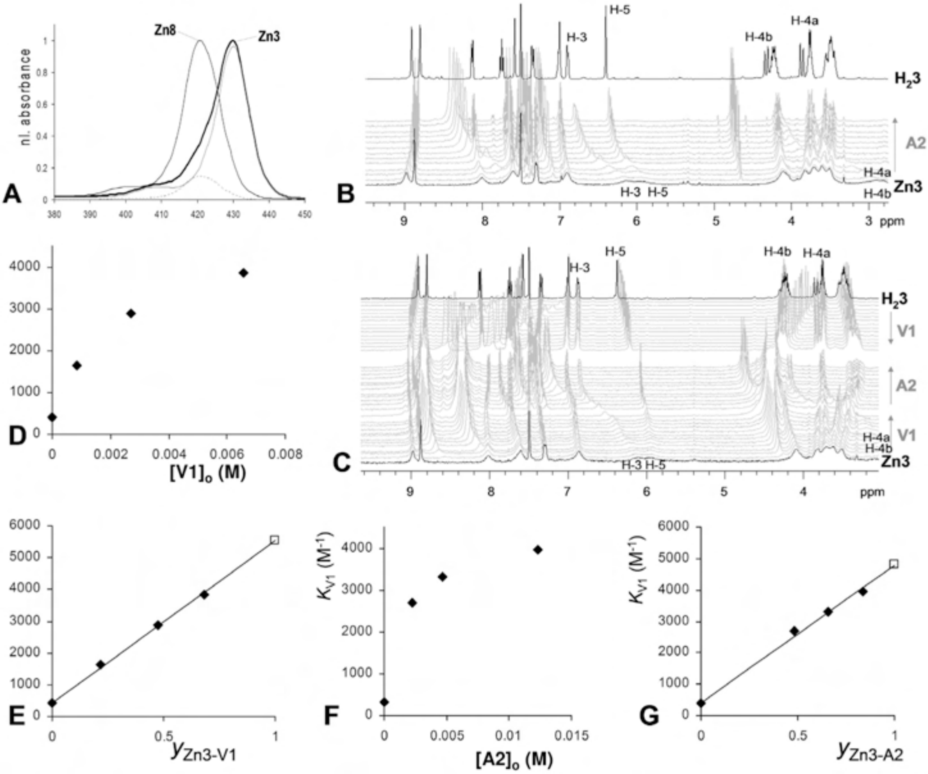

Figure 13. Selection of data concerning the cooperative binding effects involved with **Zn3**. (A) UV-Vis spectra of the Soret bands of **Zn3** and **Zn8** in chloroform, revealing a clear red shift as a result of the intramolecular coordination of **Zn3**. (B) ^{1}H-NMR spectra of **$H_2$2** and a titration of **A2** to **Zn2**, which reveal the significant changes in geometry of the flexible cavity upon insertion of a zinc ion as a result of the intramolecular coordination, and the removal of this intramolecular coordination as a result of the addition of **A2**. (C) ^{1}H-NMR spectra of titrations of **$H_2$3** with **V1** (from top down), and of **Zn3** and **V1** (from bottom up), followed by a titration of **A2**. (D) Association constants of **A2** with **Zn3** as obtained by UV-Vis titration experiments, plotted versus concentration of **V1**. (E) Association constants of **A2** with **Zn3** plotted versus fractional saturation of **Zn3** with **V1**. (F) Association constants of **V1** with **Zn3** as obtained by UV-Vis titration experiments, plotted versus concentration of **A2**. (G) Association constants of **V1** with **Zn3** plotted versus fractional saturation of **Zn3** with **A2**.

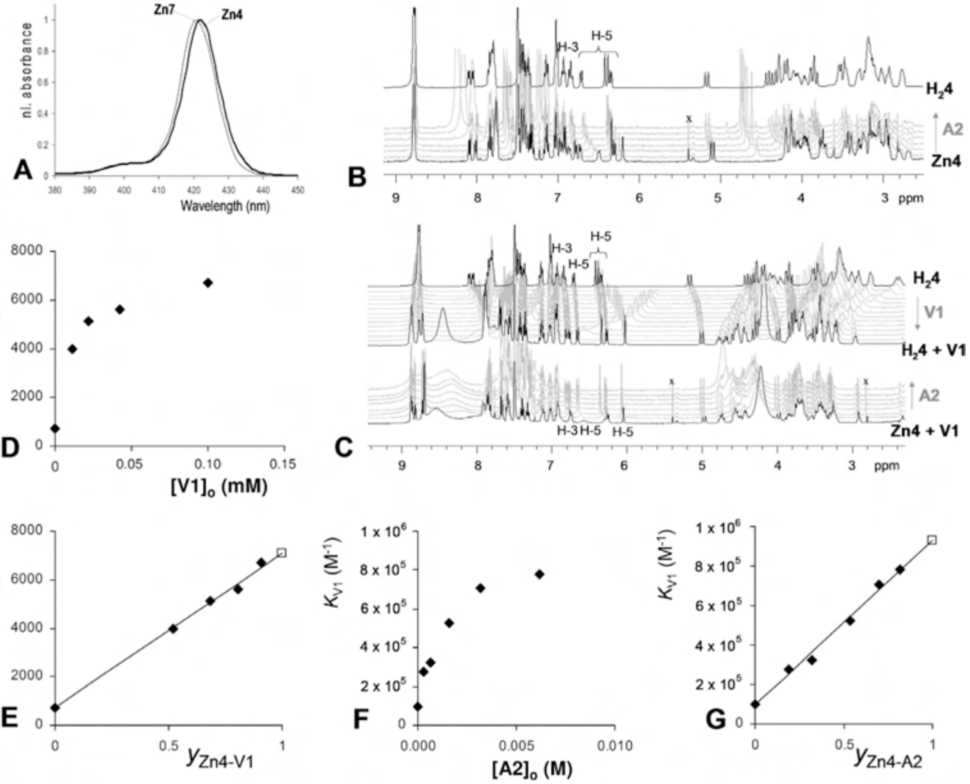

Figure 14. Selection of data concerning the cooperative binding effects involved with **Zn4**. (A) UV-Vis spectra of the Soret bands of **Zn4** and **Zn7** in chloroform, which reveal no significant shifts and hence no intramolecular coordination in **Zn4**. (B) ^{1}H-NMR spectra of **$H_2$4** and a titration of **A2** to **Zn4**, which reveal only little changes in the geometry of the rigid cavity upon insertion of a zinc ion and the subsequent addition of bulky **A2**. (C) ^{1}H-NMR spectra of titrations of the addition of **V1** to **$H_2$4** and of the addition of **A2** to a mixture of **Zn4** and **V1** which indicates that the geometries of the formed receptor-viologen complex is independent of the presence or absence of a zinc ion in the porphyrin or the subsequent coordination of a bulky pyridine. (D) Association constants of **A2** with **Zn4** as obtained by UV-Vis titration experiments plotted versus concentration of **V1**. (E) Association constants of **A2** with **Zn4** plotted versus fractional saturation of **Zn4** with **V1**. (F) Association constants of **V1** with **Zn4** as obtained by UV-Vis titration experiments plotted versus concentration of **A2**. (G) Association constants of **V1** with **Zn4** plotted versus fractional saturation of **Zn4** with **A2**.

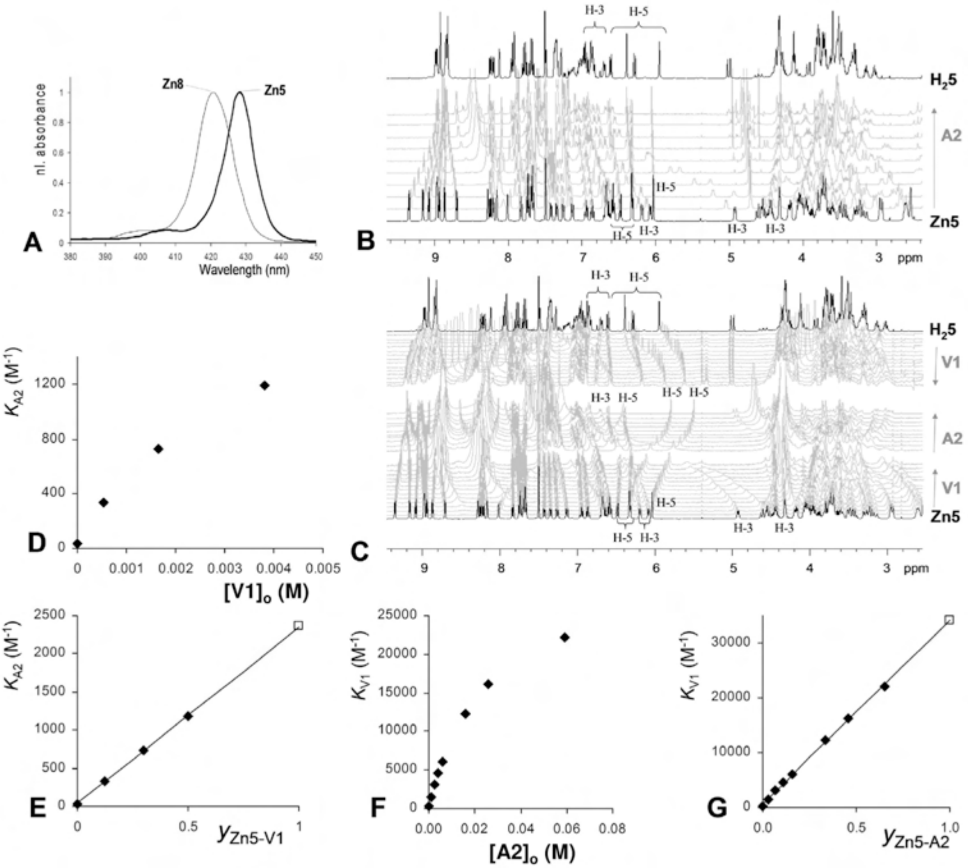

Figure 15. Selection of data concerning the cooperative binding effects involved with **Zn5**. (A) UV-Vis spectra of the Soret bands of **Zn5** and **Zn8** in chloroform, revealing a clear red shift as a result of the intramolecular coordination of **Zn5**. (B) ^{1}H-NMR spectra of **$H_2$5** and a titration of **A2** to **Zn5**, revealing the significant changes in geometry of the flexible cavity upon insertion of a zinc ion as a result of the intramolecular coordination, and the removal of this intramolecular coordination as a result of the addition of **A2**. (C) ^{1}H-NMR spectra of titrations of **$H_2$5** with **V1** (from top down) and of **Zn5** with **V1**, (bottom up) followed by the addition of **A2**. (D) Association constants of **A2** with **Zn5** as obtained by UV-Vis titration experiments plotted versus concentration of **V1**. (E) Association constants of **A2** with **Zn5** plotted versus fractional saturation of **Zn5** with **V1**. (F) Association constants of **V1** with **Zn5** as obtained by UV-Vis titration experiments plotted versus concentration of **A2**. (G) Association constants of **V1** with **Zn5** plotted versus fractional saturation of **Zn5** with **A2**.

5. Experimental

Materials and methods. Chloroform and acetonitrile used in titration experiments were distilled from $CaCl_2$. K_2CO_3 was dried in an oven (150 °C). All other solvents and chemicals were commercial materials and used as received. Merck silica gel (60H) was used for column chromatography and Merck silica gel F254 plates were used for thin layer chromatography (TLC) and preparative TLC. Molecular modeling calculations were performed using the Spartan software. Fluorescence experiments were performed on a Perkin-Elmer LS50B luminescence spectrometer equipped with a thermostatted cuvette holder. UV-Vis spectra were recorded on a Cary 100 Conc (Varian, Middelburg) UV-Vis spectrometer. Maldi-TOF MS was performed on a Bruker Biflex III spectrometer. NMR spectra were taken on a Varian Inova 400 (400 MHz, ^{1}H- and 2D-spectra) or on a Bruker DMX300 (75 MHz, ^{13}C spectra) and calibrated to an internal standard of tetramethylsilane. Abbreviations used are s, singlet; d, doublet; t, triplet; dd, double doublet; m, multiplet. The syntheses of ditosylate **10**, tetrakis(chloromethyl) diphenylglycoluril **9**, tetratosylate **11a**, dimethyl viologen **V1**, diethyl viologen **V2**, silylether protected pyridine **A2**, $\mathbf{H_22}$, and **Zn2** are described in Chapter 2. The syntheses of $\mathbf{H_21}$, **Zn1**, **Zn6**, **Zn7**, and **Zn8** were performed according to literature procedures.[42]

Tetra tosyl clip (11b)

Ditosylate **10** (4.5 g, 7.6 mmol) and **9** (1.8 g, 3.8 mmol) were dissolved in freshly distilled 1,2-dichloroethane (300 mL). $SnCl_4$ (4 mL, 32 mmol) was added and the mixture was stirred under reflux in an argon atmosphere for 16 h. After cooling, aqueous 6n HCl (10 mL) was added and the mixture was refluxed for another 30 min. After cooling, CH_2Cl_2 (100 mL) was added and the organic layer was washed with aqueous 1N HCl (3x 100 mL) and water and evaporated to dryness. After purification by column chromatography (30% to 50% EtOAc in toluene) and crystallization from nitromethane, **11b** was obtained as a white solid (1.02 g, 20%):

^{1}H-NMR ($CDCl_3$, 400 MHz): δ 7.80 (d, 2H, J = 8.2 Hz), 7.77 (d, 2H, J = 8.3 Hz), 7.74 (d, 2H, J = 8.3 Hz), 7.80 (d, 2H, J = 8.3 Hz), 7.32–7.21 (m, 8H, J = 8.2 Hz), 7.15–7.08 (m, 10H), 6.93–6.40 (m, 4H), 5.54 (d, 1H, J = 16.0 Hz), 4.77-4.63 (m, 4H), 4.23–3.57 (m, 40H), 2.40 (s, 3H), 2.29 (s, 3H), 2.27 (s, 3H), 2.12 (s, 3H) ppm.

Free base meta porphyrin clip (H_23)

A suspension of **11a** (120 mg, 0.078 mmol), 5,10,15,20-tetrakis(*meso*-*m*-hydroxyphenyl)porphyrin **13** (53 mg, 0.078 mmol), and K_2CO_3 (100 mg, 0.72 mmol) in DMF (250 mL) was stirred for 16 h under an argon atmosphere at 110 °C. After filtration of the salts and evaporation of the solvents the product was purified by column chromatography (3% MeOH in $CHCl_3$), followed by preparative TLC (1/1 toluene/EtOAc (v/v)). The product was dissolved in a minimal amount of $CHCl_3$ and to this solution *n*-hexane was added. A precipitate was formed, which was collected by centrifugation and dried under vacuum yielding 16 mg (13%) of $\mathbf{H_23}$ as a purple solid:

^{1}**H-NMR** ($CDCl_3/CD_3CN$ 1/1 (v/v) 400 mHz): δ 8.91 (s, 4H), 8.80 (s, 4H), 8.12 (d, 4H, J = 7.3 Hz), 7.74 (t, 4H, J = 7.9 Hz), 7.57 (s, 4H), 7.34 (d, 4H, J = 8.4 Hz), 7.02−6.98 (m, 6H), 6.90−6.85 (m, 4H), 6.37 (s, 4H), 4.32−4.26 (m, 12H), 3.84 (d, 4H, J = 15.8 Hz), 3.79−3.72 (m, 8H), 3.57−3.42 (m, 16H), −2.87 (s, 2H) ppm.
^{13}**C-NMR** ($CDCl_3$, 75 MHz): δ 162.48, 157.59, 156.53, 156.38, 146.75, 143.73, 133.38, 129.60, 128.52, 128.42, 128.06, 127.62, 125.93, 121.03, 119.77, 116.38, 114.88, 85.01, 69.15, 68.64, 67.51, 67.00, 44.83 ppm.
Maldi-TOF MS: (*m*/*z*) 1521.75 $(M)^+$.

Zinc meta porphyrin clip (Zn3)
$\mathbf{H_2 3}$ and an excess of zinc acetate dihydrate were dissolved in a 1:1 (v/v) mixture of methanol and dichloromethane. The mixture was stirred at room temperature for 5 min. The solvents were evaporated and the salts were removed by chromatography over a plug of silica (10% MeOH in $CHCl_3$). After precipitation in *n*-hexane, **Zn3** was obtained as a purple solid:
^{1}**H NMR** (DMSO-D_6, 400 mHz): δ 8.81 (s, 4H), 8.72 (s, 4H), 8.09 (d, 4H, J = 7.3), 7.75 (t, 4H, J = 7.9 Hz), 7.51 (s, 4H), 7.34 (d, 4H, J = 8.2 Hz), 7.07−6.98 (m, 6H), 6.79 (d, 4H, J = 7.0 Hz), 6.47 (s, 4H), 4.31(d, 4H, J = 16.2 Hz), 4.28−4.21 (m, 4H), 4.11−4.04 (m, 4H), 3.78 (d, 4H, J = 16.6 Hz), 3.76−3.70 (m, 8H), 3.56−3.50 (m, 12H), 3.47−3.41 (m, 4H) ppm.
^{13}**C NMR** (DMSO-D_6, 75 MHz): δ 165.49, 156.06, 149.51, 149.13, 145.80, 144.33, 131.54, 129.63, 128.63, 128.39, 127.70, 127.47, 125.55, 119.90, 115.76, 114.52, 79.08, 68.37, 67.93, 67.04, 66.84, 44.02 ppm.
Maldi-TOF MS: (*m*/*z*) 1585.0 $(M)^+$.

Free base twisted ortho porphyrin clip ($\mathbf{H_2 4}$)
A suspension of **11b** (240 mg, 0.16 mmol), 5,10,15,20-tetrakis(*meso-o*-hydroxyphenyl)porphyrin **12** (106 mg, 0.16 mmol), and K_2CO_3 (100 mg, 0.72 mmol) in DMF (500 mL) was stirred for 16 h under an argon atmosphere at 110 °C. After filtration of the salts and evaporation of the solvents the product was purified by column chromatography (3% MeOH in $CHCl_3$ (v/v)) followed by preparative TLC (7/7/1 toluene/EtOAc/MeOH (v/v/v)). The product was dissolved in a minimal amount of $CHCl_3$ and to this solution *n*-hexane was added. A precipitate was formed, which was collected by centrifugation and dried under vacuum yielding 32 mg (13%) of $\mathbf{H_2 4}$ as a purple solid:
^{1}**H-NMR** ($CDCl_3/CD_3CN$ 1/1 (v/v), 400 MHz): δ 8.77 (s, 4H), 8.76 (s, 4H), 8.09 (d, 1H, J = 7.2 Hz), 8.05 (d, 1H, J = 7.2 Hz), 7.86−7.76 (m, 6H), 7.47−7.33 (m, 6H), 7.14 (t, 2H, J = 7.5 Hz), 7.05−7.00 (m, 4H), 6.93 (t, 2H, J = 7.4 Hz), 6.84 (t, 2H, J = 7.4 Hz), 6.71 (d, 1H, J = 8.4 Hz), 6.42 (s, 1H), 6.38 (s, 1H), 6.34 (d, 1H, J = 8.4 Hz), 5.17 (d 1H, J = 15.1 Hz), 4.42 (d 1H, J = 15.8 Hz), 4.34 (d, 1H, J = 16.1 Hz), 4.19 (d, 1H, J = 15.0 Hz), 4.30−3.80 (m, 12H), 3.57−3.42 (m, 5H), 3.32−2.90 (m, 15H), 2.79−2.73 (m, 2H), 2.46−2.34 (m, 2H), −2.69 (s, 2H) ppm.
Maldi-TOF MS: (*m*/*z*) 1521.96 $(M)^+$.

Zinc twisted ortho porphyrin clip (Zn4)

H$_2$4 and an excess of zinc acetate dihydrate were dissolved in a 1:1 mixture of methanol and dichloromethane. The mixture was stirred at room temperature 5 min. The solvents were evaporated and the salts were removed by chromatography over a plug of silica (10% MeOH in CHCl$_3$). After precipitation in *n*-hexane, **Zn4** was obtained as a purple solid in a nearly quantitative yield:

^{1}H NMR (CDCl$_3$/CD$_3$CN 1/1 (v/v), 400 MHz): δ 8.77 (bs, 8H), 8.09 (d, 1H, J = 7.2 Hz), 8.01 (d, 1H, J = 7.2 Hz), 8.84 (d, 1H, J = 7.1 Hz), 7.83 (d, 1H, J = 7.1 Hz), 7.76 (m, 4H), 7.47–7.29 (m, 8H), 7.17–7.11 (m, 2H), 7.04–7.02 (m, 2H), 6.98–6.84 (m, 4H), 6.78 (d, 1H, J = 7.9 Hz), 6.72 (d, 1H, J = 7.7 Hz), 6.49 (d, 1H, J = 8.0 Hz), 6.34 (s, 1H), 6.30 (d, 1H, J = 8.4 Hz), 6.20 (s, 1H), 5.10 (d, 1H, J = 15.4 Hz), 4.21–3.90 (m, 11H), 3.78–3.70 (m, 4H), 3.49–2.92 (m, 20H), 2.83–2.78 (m, 2H), 2.71–2.66 (m, 2H) ppm.

Maldi-TOF MS: (*m*/*z*) 1585.0 $(M)^+$.

Free base twisted meta porphyrin clip (H$_2$5)

A suspension of **11b**, 5,10,15,20-tetrakis(*meso*-*m*-hydroxyphenyl)-porphyrin **13** (1 equiv.), and K$_2$CO$_3$ (50 fold excess) in DMF (concentration of reactants lower than 5×10^{-5} M) was reacted for 16 h under argon atmosphere at 110 °C. After filtration of the salts and evaporation of the solvents the product was purified by column chromatography (3% MeOH in CHCl$_3$ (v/v)) followed by preparative TLC (1/1 toluene/EtOAc (v/v)). The product was dissolved in a minimal amount of CHCl$_3$ and to this solution *n*-hexane was added. A precipitate was formed which was collected by centrifugation and dried under vacuum yielding **H$_2$4** (5–20%) as a purple solid:

^{1}H-NMR (CDCl$_3$, 400 MHz): δ 8.94 (s, 2H), 8.90 (s, 2H), 8.83 (d, 2H, J = 4.8 Hz), 8.80 (d, 2H, J = 4.8 Hz), 8.76 (s, 2H), 8.25 (d, 1H, J = 7.5 Hz), 8.20 (d, 1H, J = 7.5 Hz), 8.05 (s, 1H), 7.96 (d, 1H, J = 7.2 Hz), 7.95 (s, 1H), 7.92 (d, 1H, J = 7.5 Hz), 7.75 (t, 1H, J = 7.9 Hz), 7.72 (t, 1H, J = 7.9 Hz), 7.66 (t, 1H, J = 7.3 Hz), 7.64 (t, 1H, J = 7.8 Hz), 7.40 (s, 1H), 7.37–7.31 (m, 4H) 7.26 (s, 1H), 7.01–6.92 (m, 6H), 6.87–6.82 (m, 3H), 6.63 (d, 1H, J = 7.3 Hz), 6.57 (d, 1H, J = 8.3 Hz), 6.38 (s, 1H), 6.19 (d, 1H, J = 8.4), 6.14 (s, 1H), 5.10 (s, 1H, J = 15.9 Hz), 4.44–4.08 (m, 10H), 3.90–3.60 (m, 14H), 3.55–3.32 (m, 12H), 3.25–3.15 (m, 3H), −2.74 (s, 2H) ppm.

^{13}C-NMR (CDCl$_3$, 75 MHz): δ 156.97, 156.67, 150.20, 147.77, 145.94, 145.63, 143.63, 133.35, 130.91, 130.24, 130.18, 129.62, 128.54, 128.42, 128.11, 128.00, 127.90, 127.80, 127.65, 127.53, 127.41, 127.25, 126.95, 126.31, 126.22, 124.72, 123.00, 122.36, 121.49, 121.26, 119.65, 117.57, 117.01, 115.89, 114.73, 113.32, 84.82, 71.83, 70.76, 70.54, 70.15, 69.53, 69.26, 69.15, 68.92, 68.68, 67.82, 67.72, 67.15, 66.81, 44.98, 44.67, 44.48, 37.18 ppm.

Maldi-TOF MS: (*m*/*z*) 1521.84 $(M)^+$.

Zinc twisted meta porphyrin clip (Zn5)

H$_2$5 and an excess of zinc acetate dihydrate were dissolved in a 1:1 mixture of methanol and dichloromethane. The mixture was stirred at room temperature 5 min. The solvents were evaporated and the salts were removed by chromatography over a plug of silica (eluent 10%

methanol in chloroform (v/v)). After precipitation in hexane, **Zn5** was obtained as a purple solid in a nearly quantitative yield:

^{1}**H NMR** ($CDCl_3/CD_3CN$ 1/1 (v/v), 400 MHz): δ 9.35 (d, 1H, J = 4.6 Hz), 9.16 (d, 1H, J = 4.5 Hz), 9.08 (d, 1H, J = 4.6 Hz), 8.98–8.96 (m, 2H), 8.94 (d, 1H, J = 4.6 Hz), 8.87 (d, 1H, J = 4.5 Hz), 8.70 (d, 1H, J = 4.5 Hz), 8.28 (s, 1H), 8.25 (d, 1H, J = 7.3 Hz), 8.21 (d, 1H, J = 7.3 Hz), 8.16 (s, 1H), 8.01 (s, 1H), 7.83 (d, 1H, J = 7.4 Hz), 7.75–7.65 (m, 4H), 7.42 (d, 1H, J = 8.3 Hz), 7.35 (d, 1H, J = 8.1 Hz), 7.26 (d, 1H, J = 8.4 Hz), 7.13 (d, 1H, J = 8.5 Hz), 6.95 (t, 1H, J = 7.6 Hz), 6.86 (t, 1H, J = 7.4 Hz), 6.69–6.56 (m, 5H), 6.48 (d, 1H, J = 8.2), 6.33 (s, 1H), 6.32 (d, 1H, J = 6.2), 6.19 (d, 1H, J = 7.6 Hz), 6.08 (d, 1H, J = 7.8 Hz), 6.03 (s, 1H), 4.93 (d, 1H, J = 7.2 Hz), 4.63–4.40 (m, 5H), 4.35–4.29 (m, 2H), 4.20–4.25 (m, 2H), 4.08–3.86 (m, 6H), 3.82–3.57 (m, 9H), 3.52–3.40 (m, 3H), 3.31–3.13 (m, 4H), 2.96–2.92 (m, 2H), 2.62–2.53 (m, 4H), 0.99 (d, 1H, J = 14.6), –0.07 (d, 1H, J = 14.7) ppm.

^{13}**C-NMR** ($CDCl_3$, 75 MHz): δ 158.14, 156.83, 156.60, 156.38, 155.82, 154.28, 150.73, 150.12, 149.83, 149.73, 149.58, 149.42, 149.21, 149.02, 148.81, 148.67, 147.84, 144.79, 144.24, 144.10, 141.04, 134.64, 131.97, 131.74, 131.57, 131.16, 130.92, 130.84, 130.59, 130.12, 128.25, 128.06, 127.81, 127.70, 127.55, 127.28, 127.02, 126.79, 126.60, 126.05, 125.78, 125.66, 125.56, 124.96, 124.20, 123.83, 123.28, 121.82, 120.71, 120.51, 119.98, 119.12, 116.95, 115.76, 115.35, 114.77, 112.83, 109.79, 85.68, 81.33, 71.13, 70.68, 69.80, 69.28, 68.94, 68.53, 68.35, 68.27, 68.03, 67.66, 67.06, 65.81, 44.18, 43.77, 42.52, 35.89 ppm.

Maldi-TOF MS: (*m*/*z*) 1585.0 $(M)^+$.

1-Methyl-4-phenyl-pyridinium; hexafluoro phosphate (V3)

4-Phenylpyridine (200 mg, 1.2 mmol) was stirred with an excess of methyl iodide (0.5 mL) in acetonitrile (5 mL) for 48 h. Diethyl ether (5 mL) was added, the resulting precipitate was removed by filtration, washed with diethyl ether, and dried under vacuum. The product was dissolved in a minimal amount of water, and this solution was then added to a saturated aqueous NH_4PF_6 solution to yield, after filtration, washing with water and drying under vacuum, 100 mg (25%) of **V3** as a white solid:

^{1}**H-NMR** ($CDCl_3/CD_3CN$ 1/1 (v/v), 400 MHz): δ 8.61 (d, 2H, J = 6.3 Hz), 8.22 (d, 2H, J = 6.3 Hz), 7.9 (d, 2H, J = 7.3 Hz), 7.67–7.62 (m, 3H), 4.32 (s, 3H) ppm.

^{13}**C-NMR** ($CDCl_3/CD_3CN$ 1/1 (v/v), 75 MHz): δ 155.92, 144.61, 131.94, 129.41, 127.52, 124.47, 116.54, 47.16 ppm.

Determination of association constants:

Solutions of known concentrations of guests were added to concentrations of the selected macrocycle by microsyringe (at 298 K). The spectral changes were recorded by ^{1}H-NMR, UV-Vis or Fluorescence spectroscopes from which the association constant (K_{assoc}) could be determined by non-linear curvefitting using Grafit or Excel according to the formula:

$$\delta_{\mathrm{obs}} = \frac{(\delta_{\mathrm{HG}} - \delta_{\mathrm{H}})}{2 \cdot [\mathrm{H}]_{\mathrm{o}}} \cdot \left([\mathrm{H}]_{\mathrm{o}} + [\mathrm{G}]_{\mathrm{o}} + \frac{1}{K_{\mathrm{assoc}}} - \sqrt{\left([H]_{o} + [G]_{o} + \frac{1}{K_{\mathrm{assoc}}} \right)^{2} - 4 \cdot [\mathrm{H}]_{\mathrm{o}}[\mathrm{G}]_{\mathrm{o}}} \right) + \delta_{\mathrm{H}}$$

where $[\mathrm{H}]_\mathrm{o}$ and $[\mathrm{G}]_\mathrm{o}$ are the known concentrations of receptor and guest, respectively, δ_{obs} is the observed signal (chemical shift of a proton, absorbance at a fixed wavelength, or emission at a fixed wavelength) of the receptor upon addition of guest, δ_H is the signal of the receptor in the absence of guest, and δ_{HG} is the signal of the receptor upon full occupation of the guest (which is obtained by the fit in addition to the value of K_{assoc}).

6. References

1. Changeux, J-P.; Edelstein, S. J. *Science* **2005**, *308*, 1424−1428.
2. Klug, A. *Angew. Chem. Int. Ed.* **1983**, *22*, 585−587.
3. Harman, J. G. *Biochim. Biophys. Acta* **2001**, *1547*, 1−17.
4. Hoffrichter, J.; Sommere, J. H.; Henry, E. R.; Eaton, W. A. *Proc. Natl. Acad. Sci. USA* **1983**, *80*, 2235−2239.
5. Ackers, G. K.; Doyle, M. L.; Myers, D.; Daugherty, M.A. *Science* **1992**, *255*, 5463.
6. Huang, Y.; Doyle, M. L.; Ackers, G. K. *Biophys. J.* **1996**, *71*, 2094−2105.
7. Johnson, M.L. *Methods Enzymol.* **2000**, *323*, 124−155.
8. Williams, D. H.; Stephens, E.; O'Brien, D. P.; Zhou, M. *Angew. Chem. Int. Ed.* **2004**, 43, 6596−6616.
9. Traylor, T. G.; Mitchell, M. J.; Ciconene, J. P.; Nelson, S. *J. Am. Chem. Soc.* **1982**, *104*, 4986−4989.
10. Tabushi, I.; Sasaki, T. *J. Am. Chem. Soc.* **1983**, *105*, 2901−2902.
11. Rebek, J., Jr.; Costello, T.; Marshall, L.; Wattley, R.; Gadwood, R. C.; Onan, K. *J. Am. Chem. Soc.***1985**, *107*, 7481−7487.
12. Ayabe, M.; Ikeda, A.; Kubo, Y.; Takeuchi, M.; Shinkai, S. *Angew. Chem. Int. Ed.* **2002**, *41*, 2790−2792.
13. Takeuchi, M.; Imada, T.; Shinkai, S. *J. Am. Chem. Soc.* **1996**, *118*, 10658−10659.
14. Thordarson, P.; Bijsterveld, E. J. A.; Elemans, J. A. A. W.; Kasak, P.; Nolte, R. J. M.; Rowan. A. E. *J. Am. Chem. Soc.* **2003**, *125*, 1186−1187.
15. Sato, H.; Tashiro, K.; Shinmori, H.; Osuka, A.; Aida, T. *Chem. Commun.* **2005**, 2324−2326.
16. Rebek, J., Jr.; Wattley, R. V. *J. Am. Chem. Soc.* **1980**, *102*, 4853−4854.
17. Sijbesma, R. P.; Nolte, R. J. M. *J. Am. Chem. Soc.* **1991**, *113*, 6695−6696.
18. Kobuke, Y.; Satoh, Y. *J. Am. Chem. Soc.* **1992**, *114*, 789−790.
19. Schneider, H.-J.; Ruf, D. *Angew. Chem. Int. Ed.* **1990**, *29*, 1159−1160.
20. Baldes, R.; Schneider, H.-J. *Angew. Chem. Int. Ed.* **1995**, *34*, 321−323.
21. Thordarson, P.; Coumans, R. G. E.; Elemans, J. A. A. W.; Thomassen, P. J.; Visser, J.; Rowan, A. E.; Nolte, R. J. M. *Angew. Chem. Int. Ed.* **2004**, *43*, 4755−4759.
22. Sato, H.; Tashiro, K.; Shinmori, H.; Osuka, A; Murata, Y.; Komatsu, K.; Aida, T. *J. Am. Chem. Soc.* **2005**, 127, 13086−13087.
23. Heo, J.; Mirkin, C. A. *Angew. Chem. Int. Ed.* **2006**, *45*, 941−944.
24. Darbost, U.; Seneque, O.; Li, Y.; Bertho, G.; Marrot, J.; Rager, M-N.; Reinaud, O.; Jabin, I. *Chem. Eur. J.* **2007**, *13*, 2078−2088.

25. Deng, D.; James, T. D.; Shinkai, S. *J. Am. Chem. Soc.* **1994**, *116*, 4567–4572.
26. Al-Sayah, M. H.; Branda, N. R. *Angew. Chem. Int. Ed.* **2000**, *39*, 945–947.
27. Tobey, S. L.; Anslyn, E. V. *J. Am. Chem. Soc.* **2003**, *125*, 10963–10970.
28. Williams, D. H.; Stephens, E.; O'Brien, D. P.; Zhou, M. *Angew. Chem. Int. Ed.* **2004**, *43*, 6596–6616.
29. Ricard, J.; Cornish-Bowden, A. *Eur. J. Biochem.* **1987**, *166,* 255–272.
30. In which K_X = [RX]/{[R][X]} and K_G=[RG]/{[R][G]}.
31. Conners, K, A.; Binding constants, Wiley: New York, **1987**, 89–93.
32. This value is based on data of titration experiments of reference zinc porphyrins (**Zn6**–**Zn8**) with **A2** and **A3**, which showed that **A2** binds roughly 1.5 times stronger to zinc porphyrins than **A3** in the used solvent mixture.
33. This value is lower than the cooperative effects observed when **A1** and **A2** were used, but the discrepancy of only a factor 2 can be considered to be within experimental error.
34. Ong, W.; Kaifer, A. E. *J. Org. Chem.* **2004**, *69*, 1383–1385.
35. Jeon, Y.-M.; Kim, J.; Whang, D.; Kim, K. *J. Am. Chem. Soc.* **1996**, *118*, 9790–9791.
36. Rebek, J., Jr. *Acc. Chem. Res.* **1984**, *17*, 258–264.
37. Out of curiosity, a UV-Vis titration experiment was performed in which **A2** was titrated into a micromolar mixture of **Zn2** and **V1** (1/1). This titration clearly showed non-isosbestic behavior and the curves could not be fitted with the use of the simple 1:1 binding model, according to theory.
38. Muniappan, S.; Liptsman, S.; Goldberg. I. *Acta Cryst.* **2006**, *C62*, m140–m143.
39. Michaudet, L.; Philippe Richard, P.; Boitrel, B. *Tetrahedron. Lett.* **2000**, *41*, 8289–8292.
40. Most probably there are two binding geometries for **V1** to **Zn5** with similar stabilities: one in which **V1** binds but **Zn5** remains locked and a second in which the geometry is more similar to the complex of **$H_2$5** with **V1**.
41. Hunter, C. A.; Sanders, J. K. M. *J. Am. Chem. Soc.***1990**. *112*, 5525–5534.
42. Elemans, J. A. A. W.; Claase, M. B.; Aarts, P. P. M.; Rowan, A. E.; Schenning, A. P. H. J.; Nolte, R. J. M. *J. Org. Chem.* **1999**, *64*, 7009–7016.

4

Squaring Cooperative Binding Circles. (II) Kinetic aspects

1. Introduction

Cooperative binding effects play an overwhelming role in numerous natural processes. They are utilized to construct the discrete assemblies in nature, but also play crucial roles in information transfer at the cellular level.[1,2] In the previous chapter it was shown that a number of macrocyclic porphyrin receptors show strong positive heterotropic binding effects for bulky axial nitrogen donor ligands and viologen derivatives. The thermodynamic circles for the consecutive binding of the two guests were evaluated thoroughly and it was shown that they all balance beautifully. Moreover, the observed cooperative binding effects were shown to originate from both competitive and enhancing interactions. The competitive interactions obstruct the binding of both types of guests, e.g. due to the binding of solvent molecules or intramolecular coordination within the receptor, and cause that the addition of either of the guests facilitates the binding of the other. The enhancing interactions genuinely strengthen the binding interaction as a result of the interplay between receptor and both guests. It this chapter, the influence of axially coordinating ligands on the kinetics of complex formation between the different receptors and stopper-functionalized viologens is studied. Apart from controlling the kinetics of this so called slippage process by allosteric means, and hence mimicking information transfer observed in natural processes, the main objective is to gain additional approval for the conclusions drawn in Chapter 3. The present study reveals that, apart from the thermodynamic circles, the kinetic circles also balance beautifully, and the results are in full coherence with the conclusions drawn from the thermodynamic study concerning the mechanisms governing the observed cooperative binding effects.

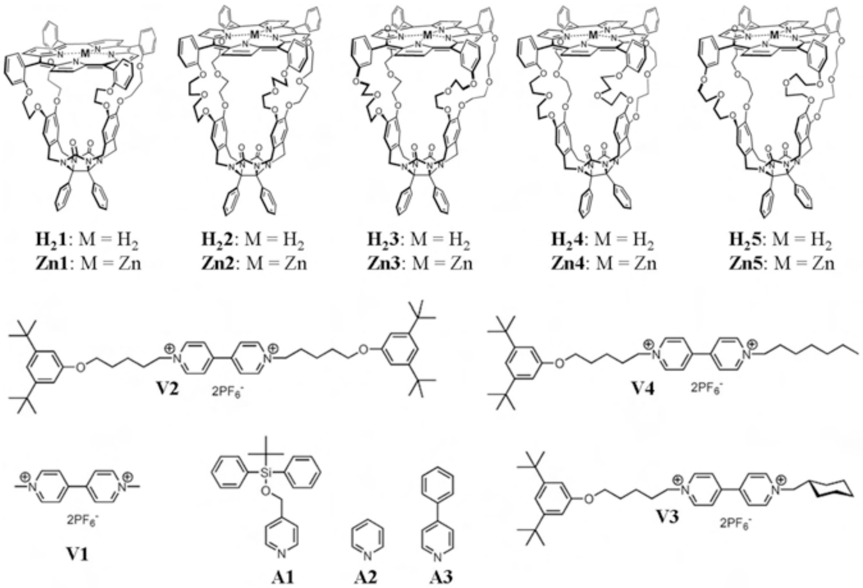

Chart 1. Molecules used in this chapter.

2. Slippage

To be able to accurately measure the kinetics of complex formation between the different receptors and viologen derivatives, it was decided to use the well-reported slippage approach. [3–19] In this approach, complex formation between a macrocyclic receptor and dumbbell-shaped guest molecules is only assessed after surmounting the energy barrier associated with traversing a bulky stopper (Figure 1). The rates of formation of the so called pseudo-rotaxanes[20] (k_{on}) depend strongly upon the size complementarities of macrocycle and stopper. The kinetic stabilities (or the dissociation rates: k_{off}) of the formed pseudo-rotaxane structures depend on both these size complementarities and on the magnitude of the noncovalent binding interactions between macrocycle and guest.

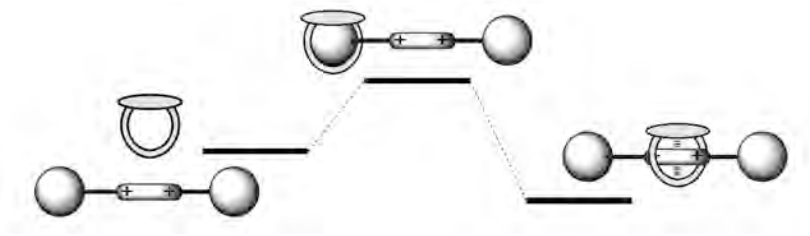

Figure 1. Energy diagram of the slipping of a macrocycle over one of the stoppers of a dumbbell-shaped compound.

Molecular modeling using CPK models revealed that double-blocked viologen **V2**[21] would be an excellent candidate for the slippage studies of the extended macrocycles **2**–**5**, which are just large enough to be able to move over the bulky 3,5-ditert-butylphenyl stoppers. ^{1}H-NMR experiments of mixtures containing **V2** and the different extended receptors (**2**–**5**) in 1/1 $CDCl_3/CH_3CN$ (v/v) indeed revealed complex formation for all the studied combinations. The ^{1}H-NMR spectra of mixtures containing the extended ortho-substituted receptors **2** and **4** revealed a slow evolution of the pseudo-rotaxane species in time (Figure 3). For the extended meta-substituted receptors **3** and **5**, no evolution in time was observed, which indicated that equilibrium was reached within the time-span of the NMR experiment. The fact that both resonances of the free components (**V2** and the receptors) and of the rotaxane complex could be separately observed indicated that the exchange between the free and pseudo-rotaxane species (i.e. the slippage) is slow on the NMR timescale. No pseudo-rotaxane formation was observed between **V2** and **1** because the stoppers of **V2** are too bulky to be traversed by the smaller cavity of **1**.[21] For this reason, viologens **V3** and **V4** (Chart 1) were employed in binding experiments with **1**. These guests have the same bulky moiety as **V2** connected on one side, but contain less bulky substituents connected on the other side that allow the traversing of **1**. Whereas the movement over the cyclohexyl moiety of **V3** involves slippage, and is therefore dominated by the size complementarities and the steric hindrance between stopper and macrocycle, the movement over the *n*-heptyl chain of **V4** involves a threading process,[22] which is governed by the filling of the cavity with the flexible chain and the subsequent movement along this chain. ^{1}H-NMR titrations between **1** and either **V3** and **V4** revealed immediate complex formation.

2.1 Pseudo-rotaxane stabilities and geometries

The ^{1}H-NMR spectra of the formed pseudo-rotaxane complexes contain valuable information about the complexation geometries. As a result of the shielding porphyrin ring current, the central proton resonances of the viologen guests (H^a, H^b, and H^c, see Figure 2 for proton numbering) shifted dramatically upfield in all pseudo-rotaxane complexes (Table 1). The stopper proton resonances (H^d, H^e, and H^f) on the other hand, displayed downfield shifts upon complex formation since they are located in the deshielding zone of the porphyrin ring. The ^{1}H-NMR spectra of the pseudo-rotaxanes of **V2** with **$H_2$2**, **Zn2**, and **$H_2$3**, respectively, appear highly symmetric unlike those of **V2** with receptors **4** and **5**. These observations are evidently the result of the symmetric nature of **2** and **3** compared to the asymmetry of twisted receptors **4** and **5**. Interestingly, only two resonances are observed for all the equivalent viologen protons in the complexes with **4** and **5**. In principle, complexation inside the cavities of the asymmetric receptors should completely break the symmetry of the viologen guests and thus result in a separate resonance for each proton. The absence of this symmetry-breaking therefore indicates that the binding of the viologens inside the cavity is highly dynamic, involving frequent conformational changes within the timescale of the NMR experiment. Also the ^{1}H-NMR spectra of pseudo-rotaxanes of **1** with non-symmetrically substituted viologens **V3** and **V4** display a higher level of symmetry than is expected on the basis of the geometry of the complexes. As will be illustrated later in the text, the aromatic surfaces of

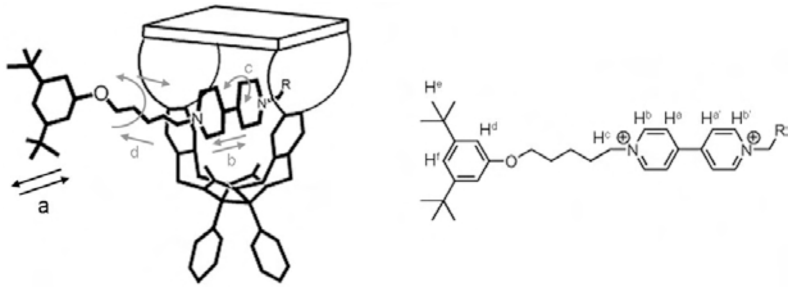

Figure 2. Schematic representation of a pseudo-rotaxane complex between a porphyrin receptor and a viologen guest equipped with stoppers. The grey arrows indicate some of the possible motion pathways of the highly dynamic rotaxane complexes, whereas the black arrows indicate the slippage process.

V3 and **V4** bind parallel to the two cavity sidewalls of receptors **H$_2$1** and **Zn1** (Figure 2). Only one resonance is observed for the individual signals H^a and H$^{a'}$, and for H^b and H$^{b'}$, which is contrary to expectation (based on the formed geometry, a resonance for each bipyridine proton (H^a, H$^{a'}$, H^b and H$^{b'}$) could be expected). Clearly, in these complexes the viologen changes conformation within the receptor multiple times within the NMR timescale. These observations demonstrate the dynamic nature of the pseudo-rotaxane species. Although, on average mainly situated in the thermodynamic minimum corresponding to the optimal binding geometry, the viologen derivatives frequently rotate, shift and move out of the cavity, while remaining on the thread (since dissociation between thread and macrocycle via slippage results in slow exchange on the NMR timescale). The grey arrows in Figure 2 indicate some of the possible motions responsible for the higher level of symmetry observed in the ^{1}H-NMR spectra of these complexes.

Previous studies have revealed two possible main geometries for the binding of viologen derivatives inside the cavities of porphyrin receptors. [23] The viologen either binds with its aromatic surface parallel to the porphyrin plane in a so called face-to-face geometry or it is clamped in between the glycoluril side-walls in an edge-to-face geometry with respect to the porphyrin.[24] The approximate geometries could be determined by monitoring the complexation induced shifts (CIS) of the side-wall proton signals (H^{sw}) and the inner amine proton signals (NH) of the free base derivatives. The face-to-face geometry results in upfield CIS values of the NH proton resonances, whereas the edge-to-face geometry results in upfield CIS values of the side-wall proton resonances. The typical proton resonances (H^{sw}, H^a, H^b, etc; Figure 2) of the non-symmetric complexes were averaged in order to be able to make a good comparison between the different complexes. From the data in Table 1 it becomes clear that the guests in receptors **H$_2$1**, **H$_2$3**, and **H$_2$5** adopt edge-to face geometries. In contrast, the upfield CIS values of the NH proton resonances of **H$_2$2** and **H$_2$4** clearly suggest face-to-face complexation geometries. These geometries are identical to the ones suggested for the complexes between **V1** and the different porphyrin receptors (except for the complex between **2** and **V1**, see Chapters 2 and 3). Apparently,

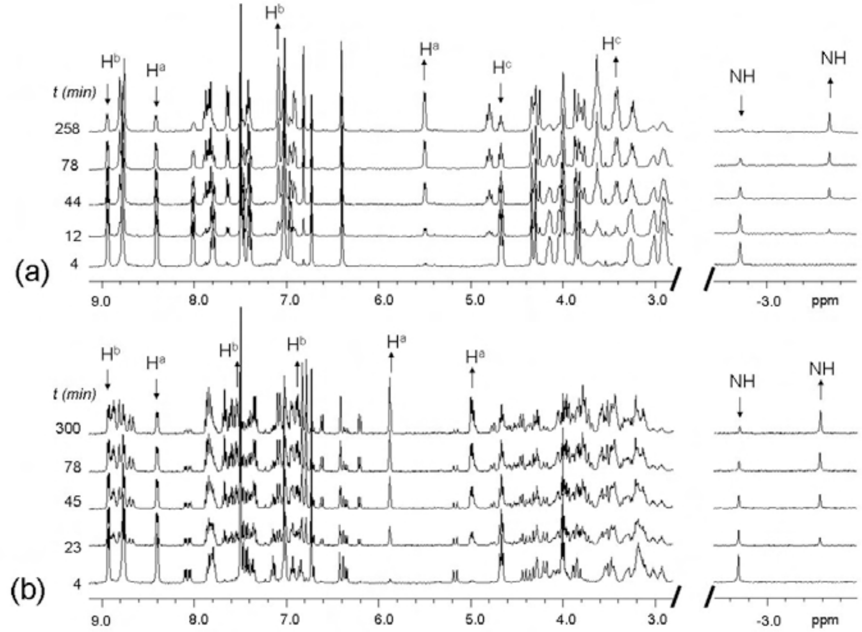

Figure 3. Partial ^{1}H-NMR spectra (400 MHz, 1/1 CDCl$_3$/CD$_3$CN (v/v)) revealing the pseudo-rotaxane formation in time between (**a**) **H$_2$2** and **V2** at 298 K and (**b**) **H$_2$4** and **V2** at 308 K. The arrows indicate a selection of the decreasing signals of the free components and the growing signals of the complex. The signal assignment of H^a, H^b, and H^c is given in Figure 2, and NH is the porphyrin pyrrole NH signal of the receptors. Note the appearance of double viologen signals (H^a and H^b) in (**b**).

the substituents on **V2**, **V3**, and **V4** do not significantly influence the complexation geometries. This also becomes clear from the comparison of the CIS values of a previously synthesized rotaxane of **V2** and **H$_2$1**[25] and the pseudo-rotaxane complexes between **H$_2$1** and **V3**, and **H$_2$1** and **V4**, respectively. Although the rotaxane structure was measured in CDCl$_3$ and the pseudo-rotaxanes in 1:1 CDCl$_3$:CD$_3$CN (v/v), similar CIS values were obtained (Table 1).

The presence of a zinc ion in the porphyrins does not substantially change the geometries of the formed complexes (in line with the complexes of the different receptors with **V1**), since all the proton resonances of the receptors appear at similar positions in the ^{1}H-NMR spectra. The viologen signals, however, consistently appear shifted slightly (0.1–0.2 ppm) upfield in the zinc porphyrin complexes when compared to these signals in the free base porphyrin complexes, which is probably the result of differences in ring current between the free base and zinc porphyrins.

Table 1. Selected calculated CIS values (ppm) of receptor and viologen proton signals upon the formation of pseudo-rotaxane complexes.[a]

Complex	Proton							
	H^{sw}	NH	H^a	H^b	H^c	H^d	H^e	H^f
$H_2$1-V2 [d]	−0.12	−0.03	−3.45	−2.78	−1.35	0.10	0.06	0.04
$H_2$1-V3 [c]	−0.18	−0.05	−4.26	−2.61	−1.11	0.07	0.03	0.02
$H_2$1-V4 [c]	−0.17	−0.06	−4.15	−2.62	−1.06	0.07	0.03	0.02
Zn1-V3 [c]	−0.24	-	−4.41	−2.56	−1.14	0.06	0.02	0.02
Zn1-V4 [c]	−0.24	-	−4.32	−2.60	−1.23	0.06	0.02	0.02
$H_2$2-V2 [c]	0.01	−0.98	−2.91	−1.85	−1.26	0.09	0.06	0.07
Zn2-V2 [c]	0.20	-	−3.02	−1.95	−1.34	0.09	0.07	0.07
$H_2$3-V2 [c]	−0.32	0.16	−3.33	−2.46	−0.72	0.04	0.04	0.04
$H_2$4-V2 [c]	−0.19	−0.89	−2.97	−1.72	−1.27	0.08	0.05	0.06
$H_2$5-V2 [c]	−0.28	0.10	−3.34	−1.54	−1.08	0.03	0.03	0.04

[a] Calculated from ^{1}H-NMR experiments (400 MHz, 298 K). [b] See Figure 2 for proton numbering. [c] In $CDCl_3/CD_3CN$ 1/1 (v/v). [d] In $CDCl_3$.

Similar association constants were obtained for the binding of the stopper-containing viologen derivatives (**V2**, **V3**, and **V4**) as for the binding of **V1** with the different receptors. This is in agreement with the observation that the complexation geometries are not significantly influenced by the substituents on the viologens (See Tables 2 and 3 and Chapter 3). The meta-substituted porphyrin receptors **3** and **5** showed the weakest affinity for the viologen derivatives ($K_{assoc} \approx 10^2–10^3$ M^{-1}) as a result of their wider cavities, that are not able to perfectly accommodate the viologen. The narrower cavities of ortho-substituted porphyrin receptors **1**, **2**, and **4** are better capable of doing so, as is demonstrated by their significantly higher association constants with the viologen derivatives. As observed for the binding of **V1**, the affinity of the receptors for the viologen derivatives increases in the series **4** < **2** < **1**. Although the association constants of the smallest receptor **1** with the different viologen derivatives are roughly of the same order of magnitude, there seems to be a slight increase in association constant upon an increase in size of the viologen substituent. This trend becomes clear when the association constants of **Zn1** with different viologens are compared: (in order of increasing bulkiness) **V1** (8.7×10^5 M^{-1}), N,N'-diethyl viologen (1.2×10^6 M^{-1}), **V4** (5×10^6 M^{-1}) and **V3** (7×10^6 M^{-1}). It is proposed that larger substituents provide some extra stabilizing (van der Waals) interactions that enhance the stability of the complexes.

2.2 Slippage kinetics

The evolution of macrocycle A, guest B and pseudo-rotaxane C in time during the slippage process can be described by equations 1-3.[26] The association constant (K_{assoc}) between macrocycle and guest is described by Equation 4. Equation 1 is the universal formula for any 1:1 binding process and can be employed independently of the relative ratios between the concentration of the macrocycle ($[A]_o$) and the guest ($[B]_o$) or the initial amount of (pseudo-rotaxane) complex present at t = 0 ($[C]_o$). It is therefore not necessary to mix equimolar amounts of macrocycle and guest to calculate accurate rate constants. Equations 1–4 can also be employed to calculate rate constants in deslippage reactions in which $k_{\text{off}} = k_{\text{on}}/K_{\text{assoc}}$.

$$\mathrm{A} + \mathrm{B} \underset{k_{\text{off}}}{\overset{k_{\text{on}}}{\rightleftharpoons}} \mathrm{C}$$

$$[\mathrm{C}] = p\frac{\left(1-\frac{q}{p}\frac{p-[\mathrm{C}]_\mathrm{o}}{q-[\mathrm{C}]_\mathrm{o}}e^{k_{\text{on}}(p-q)t}\right)}{\left(1-\frac{p-[\mathrm{C}]_\mathrm{o}}{q-[\mathrm{C}]_\mathrm{o}}e^{k_{\text{on}}(p-q)t}\right)} \tag{1}$$

$$p = [\mathrm{C}]_{\text{eq}} = \frac{([\mathrm{A}]_\mathrm{o}+[\mathrm{B}]_\mathrm{o}+\frac{1}{K_{\text{assoc}}}) - \sqrt{([\mathrm{A}]_\mathrm{o}+[\mathrm{B}]_\mathrm{o}+\frac{1}{K_{\text{assoc}}})^2 - 4\cdot[\mathrm{A}]_\mathrm{o}\cdot[\mathrm{B}]_\mathrm{o}}}{2} \tag{2}$$

$$q = \frac{[\mathrm{A}]_\mathrm{o}[\mathrm{B}]_\mathrm{o}}{[\mathrm{C}]_{\text{eq}}} \tag{3}$$

$$K_{\text{assoc}} = \frac{[\mathrm{C}]_{\text{eq}}}{\left([\mathrm{A}]_\mathrm{o}-[\mathrm{C}]_{\text{eq}}\right)\cdot\left([B]_\mathrm{o}-[\mathrm{C}]_{\text{eq}}\right)} \tag{4}$$

The rates of pseudo-rotaxane formation between **V2** and receptors **2** or **4** could be calculated from the relative concentrations of the free components and the pseudo-rotaxane complexes in time, which were determined by the integration of the appropriate ^{1}H-NMR signals. Since the kinetics of slippage process was too fast to measure by NMR techniques for all the other combinations of receptors and viologens, experiments were performed at micromolar concentrations in 1/1 (v/v) mixtures of acetonitrile and chloroform and monitored with the help of fluorescence spectroscopy. The viologen-induced quenching of the porphyrin upon complex formation makes this a reliable technique to accurately monitor the kinetics of slippage. Upon the addition of a selected viologen guest to a solution containing receptors **1** or **5**, slow quenching of the porphyrin fluorescence in time was observed from which the rate constants for the slippage could be calculated (for examples see Figures 6 and 13). The slippage of **H$_2$3** over the stoppers of **V2** was too fast to measure even at these low concentrations, since mixing the two components resulted in an immediate drop in fluorescence emission. It was, however, possible to derive a minimum value for the slippage rate of **H$_2$3** and **V2**. The calculated rate constants (k_{on}) and association constants (K_{assoc}), which were simultaneously determined from the slippage experiments, are presented in Tables 2 and 3.

Table 2. Slippage rate constants (k_{on}), association equilibrium constants (K_{assoc}), and activation energy parameters ($\Delta G^{\neq}_{on}$, $\Delta H^{\neq}_{on}$, and $-T\Delta S^{\neq}_{on}$) for the slippage of a variety of porphyrin receptors with **V2** at 25 °C.

Receptor	k_{on} ($M^{-1}s^{-1}$) [c]	K_{assoc} (M^{-1}) [d]	$\Delta G^{\neq}_{on}$ ($kJ\cdot mol^{-1}$) [c]	$\Delta H^{\neq}_{on}$ ($kJ\cdot mol^{-1}$) [c]	$-T\Delta S^{\neq}_{on}$ ($kJ\cdot mol^{-1}$) [c]
$H_2$1 [a]	0	0	-	-	-
$H_2$2 [a]	4.9×10^{-1}	1×10^{5}	75	25	50
$H_2$3 [b]	$>5 \times 10^{2}$	5×10^{2}	<58	-	-
$H_2$4 [a]	3.2×10^{-1}	5×10^{4}	76	21	54
$H_2$5 [b]	1.1×10^{2}	6×10^{2}	62	17	44
Zn1 [a]	0	0	-	-	-
Zn2 [a]	5.5×10^{-2}	1×10^{5}	80	33	47
Zn5 [b]	3.8	1×10^{2}	70	22	48

[a] Determined from ^{1}H-NMR experiments in 1/1 $CDCl_3/CD_3CN$ (v/v) at receptor concentrations of ~10^{-3} M. [b] Determined from fluorescence experiments in 1/1 $CHCl_3/CH_3CN$ (v/v) at receptor concentrations of ~10^{-6} M. [c] Estimated error 15%. [d] Estimated error 40%.

Table 3. Slippage rate constants (k_{on}), association equilibrium constants (K_{assoc}) and activation energy parameters ($\Delta G^{\neq}_{on}$, $\Delta H^{\neq}_{on}$, and $-T\Delta S^{\neq}_{on}$) for the slippage of porphyrin receptors **$H_2$1** and **Zn1** with **V3** and **V4** at 25 °C.[a]

Receptor	Guest	k_{on} ($M^{-1}s^{-1}$) [b]	K_{assoc} (M^{-1}) [d]	$\Delta G^{\neq}_{on}$ ($kJ\cdot mol^{-1}$)	$\Delta H^{\neq}_{on}$ ($kJ\cdot mol^{-1}$) [b]	$-T\Delta S^{\neq}_{on}$ ($kJ\cdot mol^{-1}$) [b]
$H_2$1	**V3**	6.0×10^{5}	1×10^{7}	40	21	19
Zn1	**V3**	7.2×10^{4}	5×10^{6}	45	29	17
$H_2$1	**V4**	1.4×10^{6}	9×10^{6}	38	21	17
Zn1	**V4**	2.0×10^{5}	4×10^{6}	43	[d]	[d]

[a] Determined from fluorescence experiments in 1/1 $CHCl_3/CH_3CN$ (v/v) at receptor concentrations of ~10^{-6} M. [b] Estimated error 15%. [c] Estimated error 40%. [d] Not determined.

The measurements involving the series of extended receptors **$H_2$2**, **$H_2$3**, **$H_2$4**, and **$H_2$5** reveal of a clear trend in the slippage rate over the stoppers of **V2**. In line with the dimensions of the cavities, the rates decrease in the series **$H_2$3** > **$H_2$5** > **$H_2$4** > **$H_2$2**. The smaller the size of the macrocycle, the harder it is to move over the stopper. This is a clear indication that steric hindrance is an important factor in the slippage process. In all cases, the free base receptors slip faster than their zinc analogues, which could be caused by differences in size between free base and zinc porphyrins (and thus by differences in dimensions of the cavities), although it is more likely caused by locking or blocking of the cavity in the case of the zinc-containing receptors, which obstructs the slippage. More detailed investigations concerning the mechanisms follow later in this chapter.

Each of the slippage experiments was monitored at (at least) three different temperatures. The enthalpic ($\Delta H^{\neq}_{on}$) and entropic contributions ($\Delta S^{\neq}_{on}$) to the total free energy of activation ($\Delta G^{\neq}_{on}$) were determined from the straight lines observed in the resulting Eyring Plots. In all cases, slippage is unfavorable both in entropy and in enthalpy (see Tables 2 and 3), which has been frequently observed in literature for related systems.[15,16,27,28] The observation that the activation enthalpy increases with decreasing cavity size in the series of slippage of **V2** with **$H_2$2**, **$H_2$4**, and **$H_2$5** (Table 2) is in good agreement with the idea that steric hindrance is the main rate-determining factor. An absolute comparison for the slippage over the stoppers of the different viologen derivatives is not possible as a result of the different nature of these stoppers. A glance at Tables 2 and 3, however, show a clear trend in entropy of activation. The entropic contribution to the free energy of activation is consistently larger for the extended receptors **2**, **4**, and **5** than for the smaller and more rigid receptor **1** ($\Delta(-T\Delta S^{\neq}_{\mathrm{on}}) \approx 30$ kJ·mol^{-1}), which strongly suggests that the difference in activation entropy is the result of the flexible nature of the extended receptors, which have to fully open their cavities to allow the slippage over the bulky stopper.

3. Squaring kinetic cooperative circles

With the different viologen derivatives in hand, it was decided to study the effects of axially coordinating pyridine ligands on the kinetics and thermodynamics of complex formation by slippage with the zinc porphyrin receptors. Since strong positive cooperative effects were observed for the combined binding of viologen derivatives and pyridine ligands to the different zinc porphyrin receptors (Chapter 3),[29] it was expected that these cooperative effects would also be expressed in the rates of pseudo-rotaxane formation and dissociation in the slippage process. In order to accurately determine all the kinetic cooperative effects, it is of importance to get a good understanding of the experimentally obtained kinetic binding curves of such multicomponent systems. For this reason, the three-component binding models will be first treated theoretically and subsequently illustrated with some experimental examples.

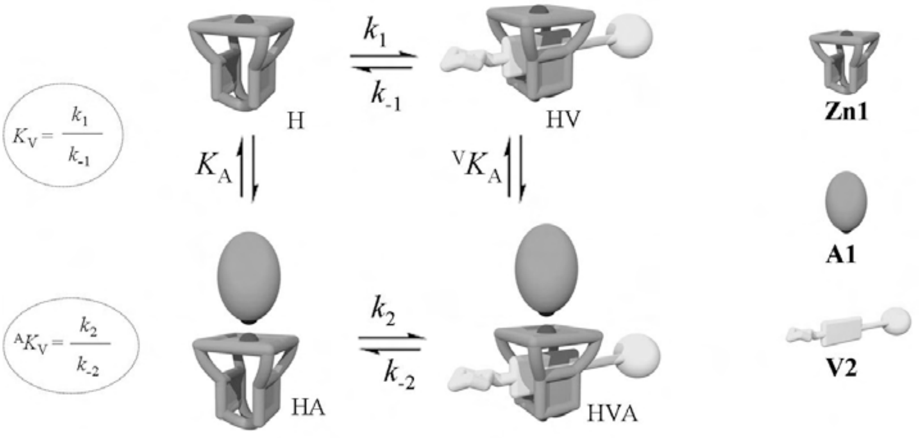

Figure 4. Schematic representation of the combined binding of a bulky pyridine derivative **A1** and a stopper-equipped viologen derivative **V2** to porphyrin receptor **Zn1**.

3.1 Theory

In addition to the thermodynamics involved in multiple component binding schemes, also the kinetic cooperative circles must balance. Under the appropriate conditions, also for these systems the observed experimental kinetic curves can be analyzed with the help of simple 1:1 binding isotherms only. To illustrate this, the three-component binding scheme in Figure 4 is considered. The bulky axial ligand (A) exclusively coordinates to the zinc on the outside of the receptor (H) and is known to cause a strong positive cooperative effect for the binding of viologen derivatives in the cavity (a factor of approximately 65 for **V1**). As a result of the presence of a cyclohexyl "stopper" in **V3**, complex formation with the receptor occurs via a slow slippage process, which allows the determination of the rate constant of complex formation. The cooperative effect of the presence of A on this rate constant can be simply determined by performing a slippage experiment of V and H in the presence of A (Figure 4). The overall binding process then becomes:

$$\mathrm{H + HA + V \rightleftharpoons HV + HVA}$$

with an overall rate equation:

$$v = -\frac{d[\mathrm{V}]}{dt} = -\frac{d([\mathrm{H}]+[\mathrm{HA}])}{dt} = \frac{d([\mathrm{HV}]+[\mathrm{HVA}])}{dt} = k_1[\mathrm{H}][\mathrm{V}] - k_{-1}[\mathrm{HV}] + k_2[\mathrm{HA}][\mathrm{V}] - k_{-2}[\mathrm{HAV}]$$

When the experimental conditions are chosen so that the fractional saturations[30] $y_{\mathrm{H-A}}$ (Eq. 5) and $y_{\mathrm{HV-A}}$ (Eq. 6) remain constant in the course of the kinetic experiment (which can be achieved by adding an excess of A compared to H), the obtained binding curves will display apparent 1:1 binding behavior.

$$y_{\mathrm{H-A}} = \frac{K_{\mathrm{A}} \cdot [\mathrm{A}]}{1 + K_{\mathrm{A}} \cdot [\mathrm{A}]} = \frac{[\mathrm{HA}]}{[\mathrm{H}]+[\mathrm{HA}]} \qquad (5)$$

$$y_{\mathrm{HV-A}} = \frac{{}^{\mathrm{V}}K_{\mathrm{A}} \cdot [\mathrm{A}]}{1 + {}^{\mathrm{V}}K_{\mathrm{A}} \cdot [\mathrm{A}]} = \frac{[\mathrm{HVA}]}{[\mathrm{HV}]+[\mathrm{HVA}]} \qquad (6)$$

This is a result of the unaffected relative ratios [H]/[HA] and [HV]/[HVA] in the course of the kinetic experiment and the overall binding process is given as:

$$\mathrm{H_{tot} + V} \underset{k_{\text{-obs}}}{\overset{k_{\text{obs}}}{\rightleftharpoons}} \mathrm{H_{tot}V}$$

in which $[\mathrm{H_{tot}}] = [\mathrm{H}] + [\mathrm{HA}]$ and $[\mathrm{H_{tot}V}] = [\mathrm{HV}] + [\mathrm{HVA}]$ and the rate equation is consequently:

$$v = -\frac{d[\mathrm{H_{tot}}]}{dt} = \frac{d[\mathrm{H_{tot}V}]}{dt} = k_{\mathrm{obs}}[\mathrm{H_{tot}}][\mathrm{V}] - k_{-\mathrm{obs}}[\mathrm{H_{tot}V}]$$

The kinetic curves of slippage can be simply analyzed with the help of equations 1–4. The observed experimental slippage rates k_{obs} and $k_{-\mathrm{obs}}$ will display apparent values that depend on the concentration of bulky pyridine (A) used in the experiment according to Equations 7 and 8:

$$k_{\mathrm{obs}} = \frac{k_1 + k_2 \cdot K_{\mathrm{A}} \cdot [\mathrm{A}]}{1 + K_{\mathrm{A}} \cdot [\mathrm{A}]} \qquad (7)$$

$$k_{-\mathrm{obs}} = \frac{k_{-1} + k_{-2} \cdot {}^{\mathrm{V}}K_{\mathrm{A}} \cdot [\mathrm{A}]}{1 + {}^{\mathrm{V}}K_{\mathrm{A}} \cdot [\mathrm{A}]} \qquad (8)$$

The apparent association constant (${}^{\mathrm{A}}K_{\mathrm{V}}$-app) is the result of the observed rate constants: ${}^{\mathrm{A}}K_{\mathrm{V}}$-app = $k_{\mathrm{obs}}/k_{-\mathrm{obs}}$. Once again, the cooperative effect for the slippage ($ce_{(+)}$) depends linearly on the fractional saturation of the receptor with the coordinating bulky axial ligand $y_{\mathrm{H-A}}$:

$$k_{\mathrm{obs}} = k_1 \cdot \{1 + y_{\mathrm{H-A}} \cdot (ce_{(+)} - 1)\} \qquad (9)$$

The cooperative effect for the reverse reaction (de-slippage), on the other hand, depends linearly on the fractional saturation of the pseudo-rotaxane with bulky axial ligand $y_{\mathrm{HV-A}}$:

$$k_{-\mathrm{obs}} = k_{-1} \cdot \{1 + y_{\mathrm{HV-A}} \cdot (ce_{(-)} - 1)\} \qquad (10)$$

The kinetic cooperative effects on the overall slippage rate ($ce_{(+)} = k_2 / k_1$) and the de-slippage rate ($ce_{(-)} = k_{-2} / k_{-1}$) add up to give the total observed thermodynamic cooperative effect: $Ce = ce_{(+)} / ce_{(-)}$.
In (other) words, under the appropriate conditions the three-component kinetic binding behavior can be fitted with the help of simple 1:1 binding models. As observed for the thermodynamics, in the kinetics of complex formation and dissociation apparent values for the rate constants will be experimentally obtained that depend linearly upon the fractional saturation with the second guest (ligand) present in solution. The observed thermodynamic cooperative effect (*Ce*) is the quotient of the kinetic cooperative effects of the complexation reaction ($ce_{(+)}$) and the de-complexation reaction ($ce_{(-)}$), respectively, in line with the general relation $K_{\text{assoc}} = k_{\text{on}}/k_{\text{off}}$.

All the above relationships can be observed experimentally, which will be illustrated by experiments in which the cooperative binding circle of the slippage of **Zn1** over the cyclohexane stopper of **V3** in the presence of bulky pyridine **A1** was fully determined. To begin, the association constant of **A1** with the pseudo-rotaxane complex of **Zn1** and **V3** (${}^{V}K_{A}$-app) was determined by a ^{1}H-NMR titration (See Figure 5). An association constant $K_{\text{assoc}} = 8.5 \times 10^{3}$ M^{-1} was obtained, which revealed that also in the pseudo-rotaxane complexes strong positive cooperative binding (*Ce* = 66) is observed with values that are similar to the ones observed for the binding of the same ligand to the complex of **Zn1** with **V1** (*Ce* ≈ 65, Chapter 3). From the ^{1}H-NMR titration it becomes clear that the binding of **A1** does not induce severe conformational changes in the pseudo-rotaxane complex, since all the proton resonances remain at roughly the same positions. Only the resonances of the ortho-phenyl porphyrin protons (top-H), which are positioned on top of the receptor and in the proximity of the coordinating pyridine ligand, are shifted slightly upfield upon coordination of **A1** (Figure 5).

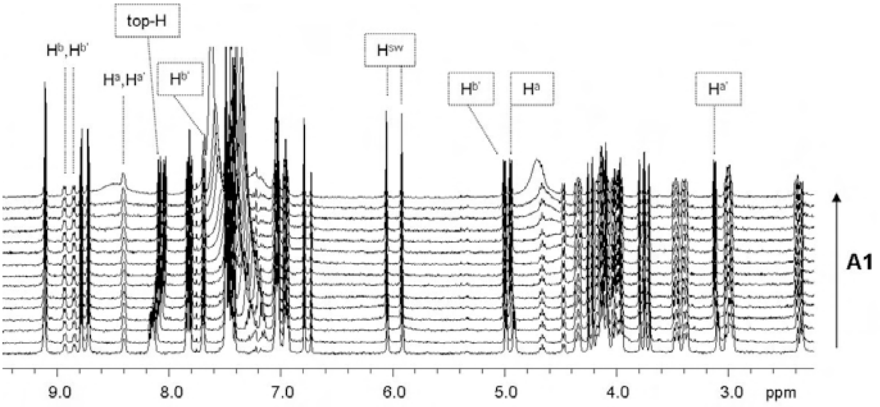

Figure 5. ^{1}H-NMR titration of **A1** to the pseudo-rotaxane complex between **Zn1** and **V3**.

The kinetics and thermodynamics of the slippage process were determined with the help of fluorescence spectroscopy experiments. One equivalent of **V3** was added to solutions containing **Zn1** (in a μM concentration) and various amounts of **A1**. The obtained curves revealed, as expected, a decrease in fluorescence emission in time. All the kinetic curves could be nicely fitted using Equations 1–4, thus confirming the apparent 1:1 binding behavior. Increasing concentrations of **A1** clearly resulted in a stronger binding of **V3** to **Zn1**, as can be observed in Figure 6. The thermodynamic cooperative effect ($Ce = 58$), which was determined indirectly from the calculated apparent association constants, was in accordance with the calculated value from the ^{1}H-NMR titrations ($Ce = 66$). In addition to the association constants, the slippage rate constants (k_{obs}) also increase upon increasing concentrations of **A1**. This is clearly expressed in the steeper initial parts of the binding curves (Figure 6a). The observed increase in rate constants indeed depends linearly on the fractional saturation of the receptor with **A1** coordinating to its outside ($y_{\mathrm{H-A1}}$), as can be seen in Figure 6c. Treating the calculated apparent rate constants k_{obs} with Equation 7 or 9 gave a rate constant: $k_2 = 8.8 \times 10^5\ \mathrm{M^{-1}s^{-1}}$ and a cooperative effect: $ce_{(+)} = 13.8$. The slippage in the presence of **A1** coordinating to the outside of the receptor is therefore almost 14 times faster than the slippage in the absence of this ligand.

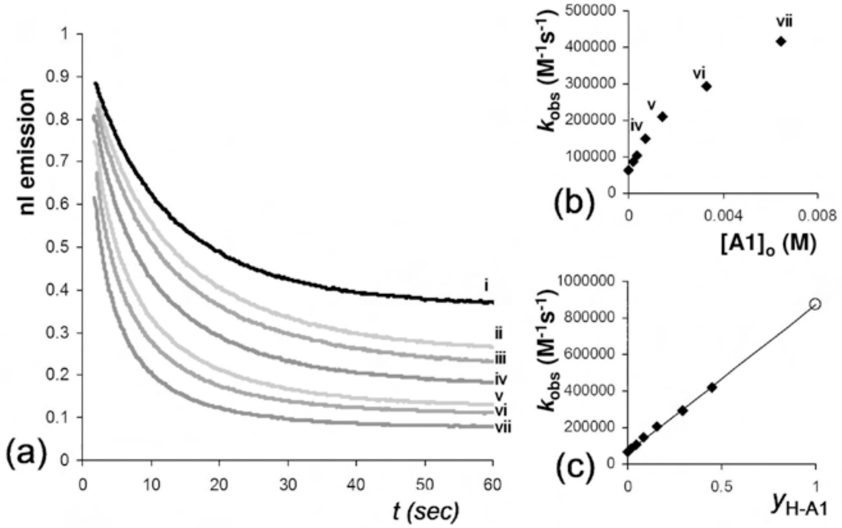

Figure 6. a) Fluorescence emission in time after the addition of 1 equivalent of **V3** to **Zn1** in the presence of (from *i* to *vii*) increasing amounts of **A1**. **b)** Plot of observed slippage rate constants (k_{obs}) against the concentration of **A1**. **c)** Plot of slippage rate constant k_{obs} against the fractional saturation of **Zn1** with **A1** ($y_{\mathrm{H-A1}}$)

Table 4. Slippage rate constants (k_{obs}), association constants (K_{G1}), apparent cooperative effects $ce_{(+)}$ and *Ce*, and the calculated cooperative effects upon full saturation of **Zn1** with **A1** (in bold) for the combined binding of **A1** and **V3** to **Zn1** at 298 K.

		Kinetics		Thermodynamics	
G1	*G2* (conc.)	k_{obs} ($M^{-1}s^{-1}$) [c]	$ce_{(+)}$-app	K_{G1} (M^{-1})	*Ce*-app
A1	No			1.3×10^{2} [a,d]	
A1	**V3** (1.0 mM)			8.5×10^{4} [a,d]	**66**
V3	No	6.4×10^{4}		4.5×10^{6} [b,d]	
V3	**A1** (0.19 mM)	8.6×10^{4}	1.4	1.2×10^{7} [b,d]	2.7
V3	**A1** (0.37 mM)	1.0×10^{5}	1.6	1.6×10^{7} [b,d]	3.6
V3	**A1** (0.74 mM)	1.5×10^{5}	2.3	2.5×10^{7} [b,d]	5.6
V3	**A1** (1.5 mM)	2.2×10^{5}	3.5	4.5×10^{7} [b,d]	10
V3	**A1** (3.3 mM)	2.9×10^{5}	4.6	[e]	
V3	**A1** (6.4 mM)	4.2×10^{5}	6.6	[e]	
V3	**A1** (∞ mM)	**8.8×10^{5}** [f]	**13.8** [f]	**2.6×10^{8}** [d,f]	**58**

[a] From NMR titrations in $CDCl_3/CD_3CN$ 1/1 (v/v). [b] From fluorescence titrations in $CHCl_3/CH_3CN$ 1/1 (v/v) at receptor concentrations of ~10^{-6} M. [c] Estimated error 15%. [d] Estimated error 30%. [e] Association constants too high to determine accurately at the concentrations used. [f] Calculated value at full saturation of **Zn1** with **A1** from the theoretical treatment of the titration series.

The observed cooperative effect on the thermodynamics (*Ce* ≈ 60) is significantly larger than the cooperative effect on the slippage reaction ($ce_{(+)} \approx 14$). These results thus indirectly suggest that the reverse reaction rate (de-slippage, k_{off}) must decrease upon the binding of **A1** to the pseudo-rotaxane complex between **Zn1** and **V3** with a factor of approximately 4.3. To experimentally investigate this decrease, a number of de-slippage experiments were performed. Solutions containing high concentrations (mM) of pseudo-rotaxane complexes between **Zn1** and **V3** were prepared and subsequently rapidly diluted to micromolar concentrations. As a result of this dilution, the equilibrium shifts to a new situation away from the pseudo-rotaxane complex and in the direction of the free components. The resulting increase in fluorescence in time was recorded and the obtained curves were analyzed with the help of Equations 1–4 from which the values k_{-obs} and ${}^{A}K_{V}$-app were calculated. As can be seen in Figure 7a, the de-slippage curves could also be perfectly fitted with the 1:1 binding isotherms. Addition of **A1** results in less 'release' of free components as a result of the increasing stability of the pseudo-rotaxane complex, and is therefore expressed in less fluorescence emission at equilibrium. Also in this series, the calculated thermodynamic cooperative effect (*Ce* = 62) was in line with the ones observed in the other titration series. The de-slippage rates clearly decrease upon increasing concentrations of **A1**, as can be seen from the initial slopes of the curves in Figure 7a. The calculated values of k_{-obs} indeed revealed a linear decrease when plotted against the fractional saturation of pseudorotaxane with **A1** (y_{HV-A1}). The de-slippage rate constant in the presence of **A1** was calculated: $k_{-2} = 3.3 \times 10^{-3}\ s^{-1}$, and revealed a cooperative effect ($ce_{(-)}$) of 0.24. The thermodynamic cooperative effect, determined indirectly from the slippage and de-slippage experiments ($Ce = ce_{(+)}/ce_{(-)}$), was calculated to be *Ce* = 57, which is thus in excellent agreement with the values of 58, 66, and 62 obtained using the other approaches.

These results elegantly show that the cooperative circles balance, also when concerning the kinetics of formation of the three-component binding systems. The highly symmetric observations in the different experimental methods clearly confirm the high accuracy of the data analysis. The individual kinetic and thermodynamic parameters can therefore be determined with excellent precision, which allows the drawing of detailed mechanistic conclusions.

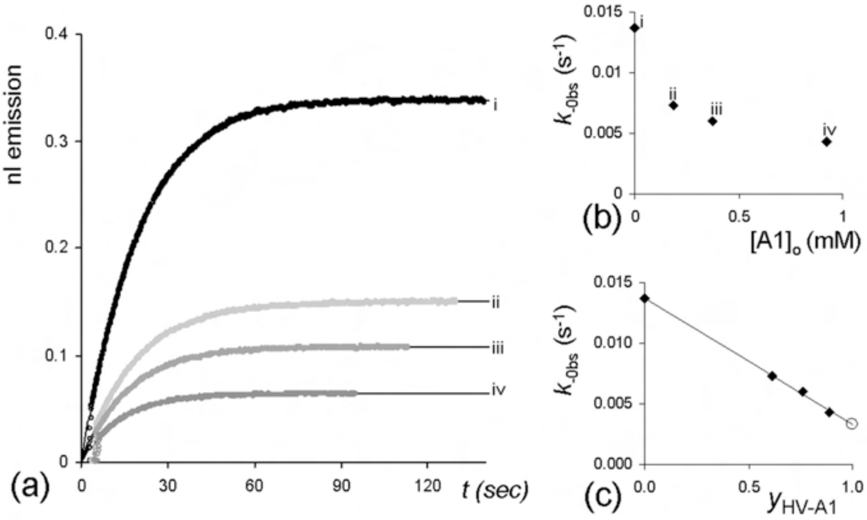

Figure 7. (**a**) Fluorescence emission in time after the dilution of a 1:2 mixture between **Zn1** and **V3** in the presence of (from *i* to *iv*) increasing amounts of **A1**. (**b**) Plot of observed de-slippage rate constants ($k_{-\mathrm{obs}}$) against the concentration of **A1**. (**c**) Plot of slippage rate constants $k_{-\mathrm{obs}}$ against the fractional saturation of the pseudo-rotaxane complex between **Zn1** and **V3** with **A1** ($y_{\mathrm{HV-A1}}$).

Table 5. De-slippage rate constants ($k_{-\mathrm{obs}}$), association constants (K_V-app), and (apparent) cooperative effects ($ce_{(-)}$-app and *Ce*-app) for the combined binding of **A1** and **V3** to **Zn1** at 298 K.[a]

	Kinetics		**Thermodynamics**	
[A1]$_o$ (mM)	$k_{-\mathrm{obs}}$ (s^{-1}) [b]	$ce_{(-)}$-app	K_V-app (M^{-1}) [c]	*Ce*-app
0	1.4×10^{-2}		4.5×10^{6}	
0.19	7.3×10^{-3}	5.3×10^{-1}	1.2×10^{7}	2.7
0.37	6.0×10^{-3}	4.4×10^{-1}	1.8×10^{7}	4.0
0.92	4.3×10^{-3}	3.1×10^{-1}	3.2×10^{7}	7.1
∞	$\mathbf{3.3 \times 10^{-3}}$ [d]	$\mathbf{2.4 \times 10^{-1}}$ [d]	$\mathbf{2.8 \times 10^{8}}$ [d]	**62** [d]

[a] From fluorescence dilution experiments in $CHCl_3/CH_3CN$ 1:1 (v/v) at receptor concentrations of ~10^{-6} M. [b] Estimated error 30%. [c] Estimated error 50%. [d] Calculated value at full saturation of **Zn1** with **A1** from the theoretical treatment of the titration series.

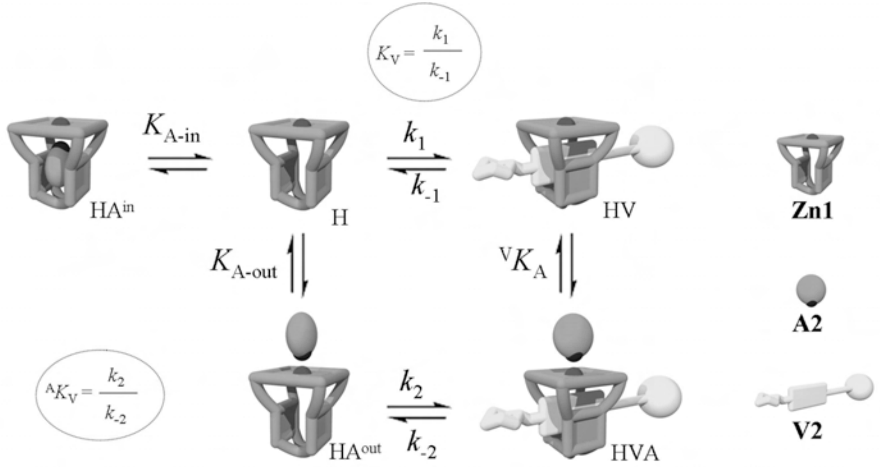

Figure 8. Schematic representation of the combined binding of pyridine (**A2**) and a stopper-equipped viologen derivative **V2** to porphyrin receptor **Zn1**.

3.2 Effects of competition on slippage rate constants

As illustrated in Chapter 3, pyridine (**A2**) coordinates strongly inside the cavity of **Zn1** and inhibits the binding of viologen derivatives. This inhibition should, of course, also fully obstruct the slippage process since the full dimensions of the cavity are needed to allow the passing of the bulky viologen substituents. To illustrate how the apparent rate constants of the slippage process are influenced by molecules that inhibit the cavity, the kinetics and thermodynamics of the cooperative circle for the binding between **Zn1**, **V3**, and **A2** was resolved. In addition, demonstrating the effects of inhibition on kinetic processes should also lead to better insights in the exact mechanism of slippage than the thermodynamic studies only. Figure 9 clearly reveals that, as expected, both the rate constant (k_{obs}) and the association constant ($^{A2}K_{V3}$-app) decrease upon increasing the concentration of **A2**. The values of these constants were calculated with the help of Equation 1–4 and are presented in Table 6. As observed for the binding of **V1** in **Zn1**, the association constant of **V3** ($^{A2}K_{V3}$-app) does not drop to zero upon full saturation of **Zn1** with **A2**, but tends to a value of 2.2 x 10^5 M^{-1}. This decrease of a factor of 21 ($K_{V3}/^{A3}K_{V3}$-app) is in accordance with the decrease of a factor of 29 observed for the binding between **V1** and **Zn1** in the presence of **A2** and is obviously caused by coordination of **A2** to the outside of the receptor. Thus, apart from inhibiting the cavity, **A2** can also cause positive cooperative binding of **V3** on the inside of the cavity (Figure 8). Analogous to the method used in Chapter 3 which is based on the fractional saturation of **Zn1** with **A2**, the cooperative effect could be determined by making use of the assumed magnitude of the association constant of **A2** with the outside of the cavity. The value of $^{A3}K_{V3}$ (Figure 8) was calculated to be 1.9 x 10^8 M^{-1} and thus indirectly suggests a positive cooperative binding effect of Ce = 43 for the combined binding of **V3** and **A2** to **Zn1** (a *Ce*-value of 30 was determined for the combination **V1**, **A2** and **Zn1**). The observation that the rate constant

k_{obs} does not tend to zero but to 6.8 x 10^2 $M^{-1}s^{-1}$ upon full saturation of **Zn1** with **A2** (a decrease of a factor of 93) is in line with the proposed mechanism. Using the same assumptions as were used in case of the fractional saturation of **Zn1** with **A1**, a value of k_2 = 6.0 x 10^5 $M^{-1}s^{-1}$ (Figure 8) was calculated, providing a positive cooperative effect ($ce_{(+)}$ = 9.5) for the slippage of **Zn1** over the cyclohexane substituent of **V3** when **A2** is coordinated to the outside of the cavity. The thermodynamic cooperative effect (*Ce*) is therefore clearly larger than the kinetic cooperative effect for the slippage-on reaction ($ce_{(+)}$) (as observed when using **A1**), which suggests that the rate of the de-slippage reaction of the complex between **Zn1** and **V3** must decrease upon the addition of **A2** to the system, i.e. $ce_{(-)}$ must be smaller than 1.

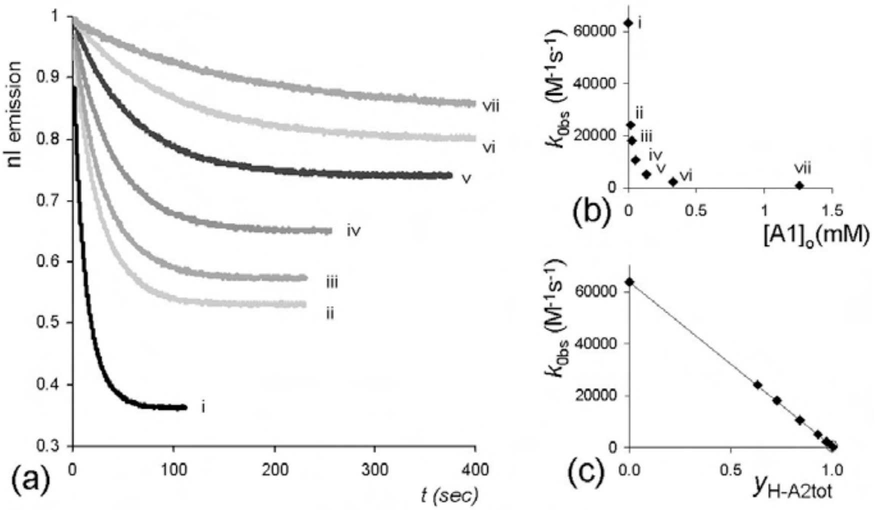

Figure 9. (**a**) Fluorescence emission in time after the addition of one equivalent of **V3** to **Zn1** in the presence of (from *i* to *vii*) increasing amounts of **A2**. (**b**) Plot of observed slippage rate constants k_{obs} against the concentration of **A2**. (**c**) Plot of slippage rate constants k_{obs} against the fractional saturation of **Zn1** with **A2** ($y_{\mathrm{H-A2tot}}$).

Table 6. Slippage rate constants, association constants (K_{G1}) and (apparent) cooperative effects ($ce_{(+)}$-app and Ce-app) for the binding of **A2** and **V3** to **Zn1** at 298 K.

		Kinetics		**Thermodynamics**	
G1	G2 (conc. in M)	k_{obs} ($M^{-1}s^{-1}$)[c]	$ce_{(+)}$-app	K_{G1} (M^{-1})	Ce-app
A2	no			7.5×10^{4} [a,c]	
V3	no	6.4×10^{4}		4.5×10^{6} [b,d]	
V3	**A2** (1.7×10^{-5})	2.4×10^{4}	3.8×10^{-1}	1.8×10^{6} [b,d]	4.0×10^{-1}
V3	**A2** (2.6×10^{-5})	1.8×10^{4}	2.8×10^{-1}	1.4×10^{6} [b,d]	3.1×10^{-1}
V3	**A2** (5.3×10^{-5})	1.1×10^{4}	1.7×10^{-1}	9.0×10^{5} [b,d]	2.0×10^{-1}
V3	**A2** (1.3×10^{-4})	5.0×10^{3}	7.9×10^{-2}	5.3×10^{5} [b,d]	1.2×10^{-1}
V3	**A2** (3.3×10^{-4})	2.5×10^{3}	3.9×10^{-2}	3.5×10^{5} [b,d]	7.8×10^{-2}
V3	**A2** (1.3×10^{-3})	1.1×10^{3}	1.7×10^{-2}	2.5×10^{5} [b,d]	5.4×10^{-2}
V3	**A2** (8.3×10^{-3})	6.8×10^{2}	1.1×10^{-2}	2.2×10^{5} [b,d]	4.9×10^{-2}
V3	**A2** (∞) [e]	$\mathbf{6.8 \times 10^{2}}$ [e]	$\mathbf{1.1 \times 10^{-2}}$ [e]	$\mathbf{2.2 \times 10^{5}}$ [d,e]	4.9×10^{-2}

[a] From UV-Vis titrations in $CHCl_3/CH_3CN$ 1/1 (v/v) at receptor concentrations of ~10^{-6} M. [b] From fluorescence experiments in $CHCl_3/CH_3CN$ 1/1 (v/v). [c] Estimated error 15%. [d] Estimated error 40%. [e] Calculated value at full saturation of **Zn1** with **A1** from the theoretical treatment of the titration series.

To directly measure the magnitude of $ce_{(-)}$, de-slippage experiments were performed in the presence of **A2**. In Figure 10a it can be seen that increases in the concentration of **A2** enhance the kinetic stabilities of the pseudo-rotaxane complexes (thus lower the de-slippage rate constants k_{off} or k_{-obs}), but in the meantime drive the equilibrium situation away from the pseudo-rotaxane species and in the direction of the complex between **A2** and **Zn1** (in which the porphyrin fluorescence emission is not quenched). Apart from being able to calculate the magnitude of k_{-2} (and hence $ce_{(-)}$) from these series of experiments, the value of the association constant of **A2** to the pseudo-rotaxane (${}^{V3}K_{A2}$) could be determined because the observed rate constant k_{-obs} depends linearly on the fractional saturation of the pseudo-rotaxane with **A2** (y_{HV-A2}). A value of 3.2×10^{-3} s^{-1} was found for k_{-2} and a cooperative effect $ce_{(-)} = 0.23$. Curve fitting provided a value of ${}^{V3}K_{A2} = 8.0 \times 10^{3}$ M^{-1} for the binding of **A2** to the outside of the pseudo-rotaxane complex. The values of k_{-2}, $ce_{(-)}$ and ${}^{V3}K_{A2}$ are all very similar to those obtained for the de-slippage reaction in the presence of **A1** ($k_{-2} = 3.3 \times 10^{-3}$ s^{-1}, $ce_{(-)} = 0.24$, ${}^{V3}K_{A2} = 8.5 \times 10^{3}$ M^{-1}), which strongly suggests that both guests play identical roles in the cooperative effects. When coordinated to the inside of the cavity, **A2** totally obstructs the slippage process, but when coordinated to the outside, it induces a similar cooperative effect for the binding of **V3** as **A1** does.

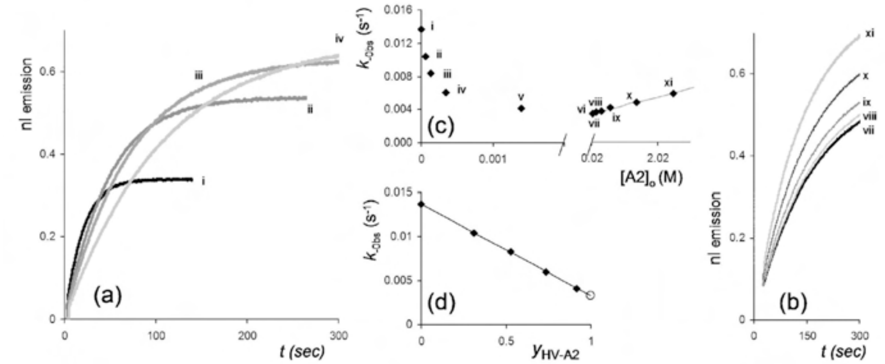

Figure 10. (**a**) Fluorescence emission in time after the dilution of a 1:2 mixture of **Zn1** and **V3** in the presence of (from *i* to *iv*) increasing amounts of **A2**. (**b**) Fluorescence emission in time after the addition of (from *vi* to *xi*) increasing amounts of **A2** to a 1:5 mixture of **Zn1** and **V3**. (**c**) Plot of observed de-slippage rate constants ($k_{-\mathrm{obs}}$) against the concentration of **A2**. (**d**) Plot of slippage rate constants $k_{-\mathrm{obs}}$ against the fractional saturation of the pseudo-rotaxane complex between **Zn1** and **V3** with **A2** ($y_{\mathrm{HV-A2}}$).

Table 7. De-slippage rate constants ($k_{-\mathrm{obs}}$), association constants (K_V-app) and cooperative effects ($ce_{(-)}$-app and Ce-app) for the complexation of **Zn1** with **V3** in the presence of varying amounts of **A2** at 298 K.[a]

	Kinetics		Thermodynamics	
A2 (M)	k_{obs} (s^{-1})	$ce_{(-)}$-app	K_V-app (M^{-1})	Ce-app
0	1.4×10^{-2} [a,c]		4.5×10^{6} [a,d]	
5.6×10^{-5}	1.0×10^{-2} [a,c]	7.6×10^{-1}	1.2×10^{6} [a,d]	2.7×10^{-1}
1.4×10^{-4}	8.4×10^{-3} [a,c]	6.1×10^{-1}	7.5×10^{5} [a,d]	1.7×10^{-1}
3.5×10^{-4}	6.0×10^{-3} [a,c]	4.4×10^{-1}	6.1×10^{5} [a,d]	1.4×10^{-1}
1.4×10^{-3}	4.1×10^{-3} [a,c]	3.0×10^{-1}	3.8×10^{5} [a,d]	8.3×10^{-2}
4.9×10^{-2}	3.1×10^{-3} [a,c]	2.3×10^{-1}	2.6×10^{5} [a,d]	5.7×10^{-2}
1.5×10^{-1}	3.4×10^{-3} [b,c]	2.5×10^{-1}	2.0×10^{5} [b,d]	4.4×10^{-2}
3.0×10^{-1}	3.5×10^{-3} [b,c]	2.6×10^{-1}	8.8×10^{4} [b,d]	2.0×10^{-2}
5.9×10^{-1}	3.8×10^{-3} [b,c]	2.8×10^{-1}	3.9×10^{4} [b,d]	8.6×10^{-3}
1.4	4.5×10^{-3} [b,c]	3.2×10^{-1}	1.2×10^{4} [b,d]	2.6×10^{-3}
2.5	5.5×10^{-3} [b,c]	4.0×10^{-1}	4.0×10^{3} [b,d]	8.9×10^{-4}

[a] From fluorescence dilution experiments in $CHCl_3/CH_3CN$ 1/1 (v/v) at receptor concentrations of ~10^{-6} M. [b] From fluorescence experiments in $CHCl_3/CH_3CN$ 1/1 (v/v). [c] Estimated error 30%. [d] Estimated error 50%.

3.3 Solvent effects

Interestingly, the de-slippage experiments in solutions containing high concentrations of **A2** (> 0.1 M) resulted in deviations from the three-component binding model (Figure 8). Upon increasing concentrations of **A2**, the observed de-slippage rate ($k_{-\mathrm{obs}}$) starts increasing again and the apparent association constant ($^{A2}K_{V3}$) drops even further (Figures 10b and 10c and Table 7). This is most likely the result of significant changes in solvent polarity as a result of the high pyridine concentration. It is known from the literature that changing a solvent system can significantly influence the kinetics of slippage processes.[12,15,16,18,30–32] Considering the high accuracy of the presented studies it is worthwhile to examine and explain these solvent-induced deviations from a mechanistic point of view, which can be achieved with the use of supramolecular host-guest approaches. It is more than likely that the electron-rich pyridines will have a weak affinity for the electron-deficient viologen moieties of the guests. As a result of its high concentration in solution, **A2** will start to compete significantly with the receptor for complex formation with the viologen. As demonstrated above, this will result in a lower apparent association constant of **Zn1** with the viologen derivative, even when only a relatively weak affinity between **A2** and the viologen exists (a matter of fractional saturation). In addition, such interactions will also have effects on the slippage rate constants, since the pyridine might act effectively as a supramolecular blocking group in the de-slippage process. As illustrated above, the pseudo-rotaxane structures are very dynamic and the receptor dissociates off the viologen moiety and onto the side chain numerous times while remaining on the thread and hence in a rotaxane geometry. When the concentration of pyridine in the solution is high, the probability that it binds to the viologen moiety of a rotaxane species in which the receptor is temporarily dissociated from the viologen is significantly increased. This binding blocks the path of the receptor back onto the viologen and thereby increases the probability of de-slippage. This pathway, as presented in Figure 11, will theoretically influence the de-slippage rate constant and the apparent association constant, but not the slippage(-on) rate constant. The slippage-on rate constant, on the other hand, will decrease when pyridines bind to the viologen in the proximity of the stopper (as depicted in Figure 11 as VA'). The observed increase in de-slippage rate and decrease in slippage-on rate depend on the concentration of **A2** and the magnitude of its association constant with the viologen. Although care must be taken, since the model is obviously a simplification of all the possible interactions, it was calculated that an association constant of **A2** to **V1** of only 0.3 M^{-1} would account for the observed experimental increase in de-slippage rate.

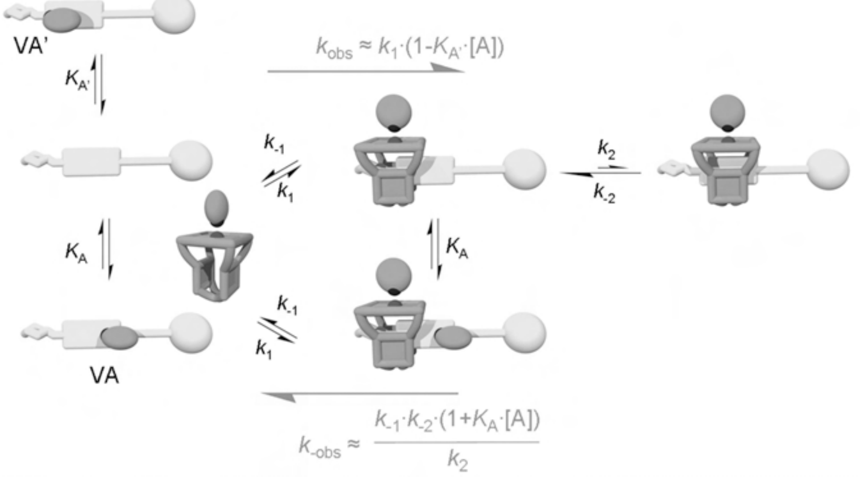

Figure 11. Schematic representation of possible mechanistic pathways that might be responsible for the observed deviations in slippage rate constants at high pyridine concentrations.

The above-mentioned findings shed a light on these kinetic processes in general. Solvent molecules and counter-ions, such as PF_6^- are very likely to play similar roles in the slippage processes and should therefore significantly influence the rates of slippage reactions. In studies that focus on comparing different solvent systems, such supramolecular blocking interactions should, in principle, account for increased de-slippage rates and decreased association constants and slippage-on rate-constants.

4. Comparing kinetic cooperative effects

The results described in the previous section have clearly demonstrated the high accuracy of the experimental analysis of slippage processes involving **Zn1**, viologen guests and pyridine ligands. When the kinetics are concerned, the cooperative circles balance nicely so long as the solvent polarity is not affected by high concentrations of the guests. It is also clear that the observed slippage rate constants have apparent values, and can be strongly influenced by competitive interactions. In the previous chapter it was shown that the positive cooperative effects are a result of both competitive and enhancing interactions (see Figure 14). Removal of the competitive interactions occurring on the inside of the cavity of the receptor by the axial ligand coordinating to the outside should account for an increase in slippage rate of a viologen guest. The enhanced binding strength as a result of the interplay between receptor, guest and ligand, on the other hand, should be expressed in decreased de-slippage rates. In order to evaluate whether such relations could be observed when the kinetic and thermodynamic studies are compared, the effects of coordinating pyridine ligands on the slippage of viologens in different zinc porphyrin receptors (**Zn1**, **Zn2**, and **Zn5**) were investigated.

Analogous to the complexation via slippage of **V3**, the kinetics and thermodynamics of complex formation between **Zn1** and **V4** via threading in the presence of **A1** was monitored with the help of fluorescence spectroscopy. As can be seen in Table 8, the threading rate constant (k_{obs}) and the association constant (K_V-app) of complex formation increase upon increasing concentrations of **A1**.

The slippage of **Zn2** over the stoppers of **V2** in the presence of **A1** and **A3** was monitored with the help of ^{1}H-NMR spectroscopy. **A3** was shown to bind strongly to the inside of the cavity of **Zn2** (Chapter 2) and is therefore inhibiting the binding of **V2**. As a result, the addition of only one equivalent of **A3** to **Zn2** resulted in a clear decrease in slippage rate and apparent association constant for **V2**, as can be seen in Figure 12 and Table 8. The mechanism is analogous to that observed for the slippage of **Zn1** in the presence of **A2**. Addition of an excess of **A1** to **Zn2** caused a clear increase both in slippage rate constant as in association constant for **V2**. The observed rate was 3.8 times higher than in the absence of coordinating pyridines. The association constants (K_V) for **V2** were too high to determine accurately with ^{1}H-NMR at the used experimental concentrations.

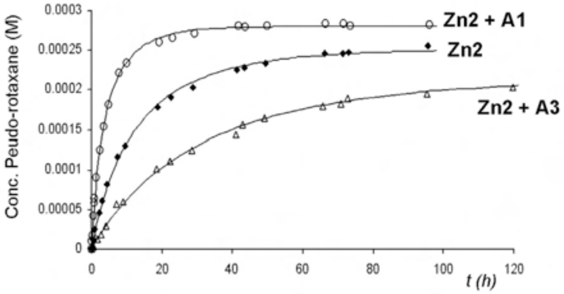

Figure 12. Pseudo-rotaxane formation between **Zn2** (0.3 mM) and **V2** (0.4 mM) and between **Zn2** and **V2** in the presence of **A1** (15 mM) and **A3** (0.3 mM) determined by ^{1}H-NMR spectroscopy at 298 K.

The cooperative effects of the presence of **A1** on the kinetics and thermodynamics of complex formation between **Zn5** and **V2** were determined with the help of fluorescence spectroscopy. As a result of the low association constant between **Zn5** and **V2**, high concentrations of **V2** (400 equivalents) were needed to obtain good quenching curves. Figure 13 clearly reveals the large effect of increasing concentrations of **A1** on both the stability of the pseudo-rotaxane complexes and on the slippage rate. The rate constant (k_{obs}) reveals a linear dependency when plotted against the fractional saturation of **Zn5** with **A1** ($y_{\mathrm{H-A1}}$, $K_{\mathrm{A1}} = 32\ \mathrm{M}^{-1}$). Such a nice linear relation was not observed for the apparent association constant between **Zn5** and **V2**. At higher concentrations of **A1**, small deviations from the straight line can be observed in which lower values for K_{V2}-app are observed than expected. Also in the binding experiments between **A1**, **V1** and **Zn5** such deviations have been observed and the thermodynamic circles did not perfectly balance (Chapter 3). These deviations from the model are most probably the result of the high experimental concentrations of **A1** that start influencing the slippage process, as discussed in the previous section.

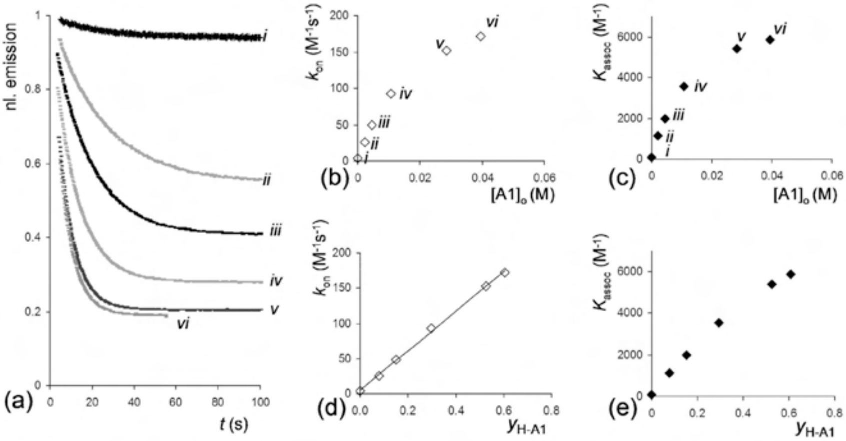

Figure 13. (**a**) Fluorescence emission in time after the addition of 400 equivalents of **V2** to **Zn1** in the presence of (from *i* to *vi*) increasing amounts of **A1** (see Table 8 for values). (**b**) Plot of observed slippage rate constants ($k_{on} = k_{obs}$) against the concentration of **A1**. (**c**) Plot of apparent association constants ($K_{assoc} = K_V$-app) against the concentration of **A1**. (**d**) Plot of slippage rate constants k_{obs} against the fractional saturation of **Zn1** with **A1** (y_{H-A1}). (**e**) Plot of association constants K_V-app against the fractional saturation of **Zn1** with **A1** (y_{H-A1}).

Table 8. Slippage rate constants (k_{obs}), association constants (K_V-app) and (apparent) cooperative effects ($^{A}k_{obs}/k_1$ and $^{A}K_V$-app/K_V) for the complexation of receptors **Zn1**, **Zn2** and **Zn5** with viologens **V2**, **V3** and **V4** in the presence of varying amounts of **A1** or **A3** at 298 K.[a]

Receptor	Viol.	Ligand (conc (mM))	k_{obs} ($M^{-1}s^{-1}$)	$^{A}k_{obs}/k_1$	K_V-app (M^{-1})	$^{A}K_V$-app/K_V
Zn1	**V4**	-	2.0 x 10^{5} [b,c]	-	3.7 x 10^{6} [b,d]	
Zn1	**V4**	**A1** (0.5)	2.5 x 10^{5} [b,c]	1.3	1.1 x 10^{7} [b,d]	3.0
Zn1	**V4**	**A1** (1.2)	3.3 x 10^{5} [b,c]	1.7	2.3 x 10^{7} [b,d]	6.3
Zn1	**V4**	**A1** (4.8)	5.7 x 10^{5} [b,c]	2.8	6.8 x 10^{7} [b,d]	18
Zn2	**V2**	-	5.5 x 10^{-2} [a,c]	-	1 x 10^{5} [a,e]	-
Zn2	**V2**	**A1** (15)	2.0 x 10^{-1} [a,c]	3.6	[f]	[f]
Zn2	**V2**	**A3** (0.3)	1.9 x 10^{-2} [a,c]	0.35	3 x 10^{4} [a,e]	0.33
Zn5	**V2**	**-**	3.8 [b,c]	-	1.0 x 10^{2} [b,d]	-
Zn5	**V2**	**A1** (2.2)	26 [b,c]	6.8	1.1 x 10^{3} [b,d]	11
Zn5	**V2**	**A1** (4.6)	49 [b,c]	13	2.0 x 10^{3} [b,d]	20
Zn5	**V2**	**A1** (11)	92 [b,c]	24	3.6 x 10^{3} [b,d]	36
Zn5	**V2**	**A1** (28)	152 [b,c]	40	5.4 x 10^{3} [b,d]	54
Zn5	**V2**	**A1** (39)	172 [b,c]	46	5.9 x 10^{3} [b,d]	59

[a] Determined from ^{1}H-NMR experiments in 1/1 $CDCl_3/CH_3CN$ (v/v) at receptor concentrations of ~10^{-3} M.[b] Determined from fluorescence experiments in 1/1 $CHCl_3/CH_3CN$ (v/v) at receptor concentrations of ~10^{-6} M.[c] Estimated error 15%.[d] Estimated error 35%.[e] Estimated errors > 50%. [f] Association constant too high to determine at the used experimental concentrations.

Table 9. Calculated cooperative binding effects ($ce_{(+)}$ and Ce) for the combined binding of **A1** and viologen derivatives **V1**, **V2**, **V3**, and **V4** to the different porphyrin receptors, and the difference in affinity of **A1** to the selected porphyrin receptors compared to the reference un-functionalized porphyrins ($K_{\text{ref-A1}}/K_{\text{A1}}$).

Receptor	Guest	$ce_{(+)}$	Ce	$K_{\text{ref-A1}}/K_{\text{A1}}$
Zn1	**V1**	-	65	16
Zn1	**V3**	14	60	
Zn1	**V4**	5.9	47	
Zn2	**V1**	-	15	3.6
Zn2	**V2**	4.0	[a]	
Zn5	**V1**	-	110	63
Zn5	**V2**	75	100	

[a] Association constant was too high to determine accurately at the used mM concentrations

The cooperative effects (both Ce and $ce_{(+)}$) were calculated for each studied system and are listed in Table 9. Independent of employing **V1** or **V2**, **V3** and **V4**, similar thermodynamic cooperative binding effects (Ce) could be observed. The substituents on the viologen therefore do not contribute to the observed cooperative binding, which is in line with the observation that the complexation geometries are not crucially influenced by the substituents. The magnitudes of the cooperative effects on the slippage rate ($ce_{(+)}$) are in all cases lower than those of the thermodynamic cooperative effects (Ce), and consequently the cooperative effects of the de-slippage rates ($ce_{(-)}$) are in all cases lower than 1. As mentioned, guests that inhibit binding, like **A2** and **A3**, cause lower apparent rate constants for the slippage process that depend linearly on the fractional saturation of the receptors with these guests. Consequently, competing interactions like solvent binding inside the cavity and intramolecular locking of the cavity can be expected to also cause lower apparent slippage rate constants that depend on the fractional saturation of the receptor with these competing interactions. The removal of these competitive interactions by the binding of the pyridine ligand to the outside of the receptor can therefore be expected to be expressed in higher slippage rates and thus in positive kinetic cooperative effects for the slippage ($ce_{(+)}$). The presumed magnitudes of the competitive interactions responsible for the observed cooperative binding effects were presented in Chapter 3 ($K_{\text{ref-A1}}/K_{\text{A1}}$, Table 9). The values of $ce_{(+)}$ and $K_{\text{ref-A1}}/K_{\text{A1}}$ (Table 9) have comparable magnitudes in all the cases that involve slippage. These results therefore suggest that exactly the same competing interactions are expressed in the cooperative effect of the slippage rates ($ce_{(+)}$) that cause the lower association constants observed for **A1** with the porphyrin receptors compared to the reference (cavity lacking) porphyrins. The results of the slippage experiments therefore fit nicely into the binding scheme obtained from the series of thermodynamic investigations (Figure 14). Furthermore, it suggests that the presence or absence of a pyridine ligand bound to the outside of the receptor does not significantly influence the geometry of the cavity and, thus, the activation energy of the slippage itself. The observed increase in slippage rate upon the addition of bulky pyridines is rather a result of Michaelis-Menten-like kinetics, in which the pre-equilibrium of undoing the competition effects within the cavity determines the observed slippage rate constants. Unlike the observed rate constant (k_{obs}), the slippage rate constant k_1 (Figure 14) is thus independent of the presence or absence of a pyridine ligand coordinating to the outside of the receptor. Analogously, the enhancing interactions ([4] and [5] in Figure 14, see Chapter 3) which arise as a result of the interplay between viologen, pyridine ligand and porphyrin, are expressed in the cooperative effect of the de-slippage reaction ($ce_{(-)}$), since these interactions genuinely increase the thermodynamic stabilities (and hence the kinetic stabilities) of the pseudo-rotaxane complexes.

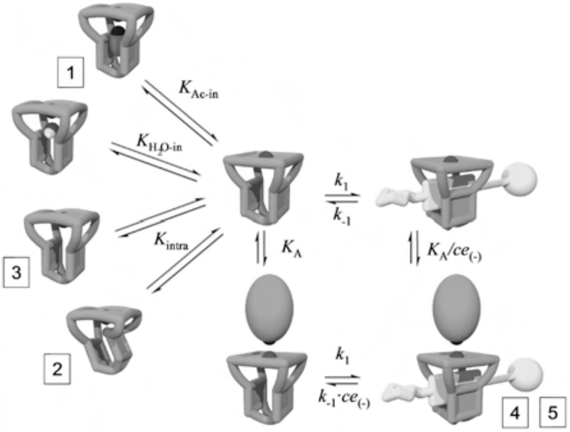

Figure 14. Schematic representation of all the contributions responsible for the observed cooperative effects (both kinetic and thermodynamic) in the combined binding of viologens and pyridine ligands to the porphyrin receptors.

Only the cooperative effect on the threading rate of **Zn1** with **V4** ($ce_{(+)} \approx 6$) is significantly lower than the total of competing interactions proposed to be present in **Zn1** (accounting for a factor of 16). This observation can, in fact, also be rationalized by making use of the proposed model. In Chapter 3 it was shown that apart from inhibition of the cavity of **Zn1** by a coordinated acetonitrile molecule (accounting for a factor of approximately 3.8 or 3.3 $\text{kJ}\cdot\text{mol}^{-1}$), there had to be another competing interaction present (accounting for a factor of roughly 4) that could not be observed with the used methods. It was suggested that this additional competition arose from distant (non-coordinative) electronic interactions between the zinc ion and the cavity, which pin the cavity in a defined conformation which hinders the binding of both coordinating pyridine ligands and viologen guests (conformation [3] in Figure 14). The significant differences in $ce_{(+)}$ between **V3** and **V4** suggest that the threading of the *n*-heptyl chain of **V4** through the cavity of **Zn1** is only obstructed by the acetonitrile coordination, whereas both acetonitrile coordination and pinning of the cavity by electronic interactions are competing with the slippage of the cyclohexyl group of **V3**. Where the full dimensions of the cavity are needed for slippage over the cyclohexyl group of **V3** and the 'electronic pinning' interactions are thus obstructing the slippage, the threading of the flexible *n*-heptyl chain of **V4** is also possible through the pinned conformation of **Zn1**. As a result, the addition of **A1** results in less removal of competing interactions for the threading of **V4** than for the slippage of **V3**, which accounts for the lower value of $ce_{(+)}$ observed for the threading of **V4**.

5. Conclusion

The study presented in this chapter reveals a number of key mechanisms that are responsible for the kinetics of slippage processes of zinc porphyrin-based macrocycles over viologen guests. The use of different macrocycles has shown that the kinetics of slippage is mainly determined by the steric hindrance involved in moving a macrocycle over a bulky side-chain. Larger macrocycles slip faster than smaller macrocycles over identical bulky side-chains. The free energy of activation associated with the slippage is unfavorable in both activation entropy and activation enthalpy. The steric hindrance involved with the slippage process most probably accounts for the extra activation enthalpy, whereas the flexibility of the receptors is expressed in extra activation entropy. The resulting pseudo-rotaxane structures have similar geometries independent of the presence or absence of bulky side-chains on the viologen threads. As a result, similar equilibrium association constants are observed, although increasing viologen-substituent sizes result in a slight increase in the complex stabilities. The presence of bulky side-chains therefore mainly affects the rates of complex formation and dissociation, whereas the thermodynamics remain relatively the same. Very similar positive cooperative thermodynamic data were obtained for the combined binding of coordinating pyridine ligands and bulky side-chain-appended viologen derivatives to the porphyrin receptors in comparison with data obtained with dimethyl viologen as a guest. The addition of bulky pyridine ligands, which coordinate to the outside of the zinc porphyrin receptors, resulted in stronger association equilibrium constants for the viologen guests that are a result of both increasing slippage rates (k_{obs}) and decreasing de-slippage rates ($k_{-\mathrm{obs}}$). In addition to the thermodynamic circles, also the kinetic cooperative circles balance nicely, revealing (according to theory) the general observation K_{assoc}-app = $k_{\mathrm{obs}}/k_{-\mathrm{obs}}$ at any given experimental concentration. As demonstrated for the apparent association constants, the observed rate constants depend linearly on the fractional saturation of the receptors with the other guest present in solution. The experimental observations of cooperative kinetic effects were fully in line with the proposed mechanisms responsible for the observed cooperative thermodynamic effects in Chapter 3. Competing interactions, such as solvent inhibition and intramolecular coordination within the receptor cause lower observed slippage rates. The addition of bulky pyridine ligands removes these competing interactions, resulting in higher observed slippage rates for the viologen guests. The enhancing cooperative interactions are expressed in lower de-slippage rates. The proposed ‘electronic pinning’ of **Zn1** is in competition with the slippage over a bulky cyclohexyl group, whereas it allows the passage of an *n*-heptyl chain involved in a threading process. The presence of high concentrations of pyridines (< 0.1 M) in the solution results in deviations from the perfect apparent binding behavior, which is believed to be mainly the result of direct electronic interactions between the electron-deficient viologen derivatives and the pyridine ligands. The coordinating pyridine ligand acts as a "supramolecular blocking group" that evidently starts influencing the slippage rate constants and association equilibrium constants.

The combined thermodynamic and kinetic investigations on the cooperative binding of viologens and pyridines to the zinc-porphyrin receptors have thus convincingly demonstrated the mechanistic origins of the observed effects. They are the result of a number of causes, which add up to give a total cooperative binding effect. The observed contributions, such as (solvent) inhibition, cavity pinning by electronic interactions, intramolecular coordination within the receptor, and (electronic or steric) interplay between the two guests and the receptor are typically observed in natural systems. These studies therefore demonstrate that the artificial receptors studied in these chapters truly mimic the natural systems with regard to cooperative binding effects.

The used method to determine the cooperative effects can generally be used to square any type of heterotropic cooperative binding circle. It stresses that any rate or association constant is apparent and depends on the fractional saturation of the receptor with either inhibiting or activating ligands. Taking the relatively simple considerations into account should help to clarify the mechanisms involved in the binding of multiple guest molecules to a (natural or artificial) receptor to a crucial extent.

6. Experimental

Materials and methods. Chloroform and acetonitrile used in titration experiments were distilled from $CaCl_2$. All other solvents and chemicals ($CDCl_3$, CD_3CN, **A2**, and **A3**) were commercial materials and used as received. Fluorescence experiments were performed on a Perkin-Elmer LS50B luminescent spectrometer equipped with a thermostatted cuvette holder. UV-Vis spectra were recorded on a Cary 100 Conc (Varian, Middelburg) UV-Vis spectrometer. Maldi-TOF ms was performed on a Bruker Biflex III spectrometer. NMR spectra were taken on a Varian Inova 400 (400 MHz, ^{1}H- and 2D-spectra) or on a Bruker DMX300 (75 MHz, ^{13}C spectra) and calibrated to an internal standard of tetramethylsilane. The synthesis of all porphyrin receptors (**1**, **2**, **3**, **4**, and **5**) is described in Chapters 2 and 3. The syntheses of viologen derivatives **V1** and **V2** and pyridine **A1** is described in Chapter 2. The syntheses of viologen derivatives **V3** and **V4** are presented in Chapters 5 and 6, respectively.

7. Literature

1. Williams, D. H.; Stephens, E.; O'Brien, D. P.; Zhou, M. *Angew. Chem. Int. Ed.* **2004**, 43, 6596−6616.
2. Changeux, J-P.; Edelstein, S. J. *Science* **2005**, *308*, 1424−1428.
3. Harrison, I. T. *J. Chem. Soc., Chem. Commun.* **1972**, 231−232.
4. Harrison, I. T. *J. Chem. Soc., Perkin Trans.1* **1974**, 301−304.
5. Schill, G.; Beckmann, W.; Schweickert, N.; Fritz, H. *Chem. Ber.* **1986**, *119*, 2647−2655.
6. G. Agam, D. Graiver, A. Zilkha, *J. Am. Chem. Soc.* **1976**, *98*, 5206−5216.
7. Ashton, P. R.; Belohradsky, M.; Philp, D.; Stoddart, J. F. *J. Chem. Soc., Chem. Commun.* **1993**, 1269−1274.

8. Ashton, P. R.; Ballardini, R.; Balzani, V.; Belohradsky, M.; Gandolfi, M. T.; Philp, D.; Prodi, L.; Raymo, F. M.; Reddington, M. V.; Spencer, N.; Stoddart, J. F.; Venturi, M.; Williams, D. J. *J. Am. Chem. Soc.* **1996**, *118*, 4931–4951.
9. Macartney, D. H. *J. Chem. Soc., Perkin Trans. 2* **1996**, 2775–2778.
10. Händel, M.; Plevots, M.; Gestermann, S.; Vögtle, F. *Angew. Chem. Int. Ed. Engl.* **1997**, *36,* 1199–1201.
11. Raymo, F. M.; Houk, K. N.; Stoddart, J. F. *J. Am. Chem. Soc.* **1998**, *120*, 9318–9322.
12. Ashton, P. R.; Baxter, I.; Fyfe, M. C. T.; Raymo, F. M.; Spencer, N.; Stoddart, J. F.; White, A. J. P.; Williams, D. J. *J. Am. Chem. Soc.* **1998**, *120*, 2297–2307.
13. Hübner, G. M.; Nachtsheim, G.; Li, Q. Y.; Seel, C.; Vögtle, F. *Angew. Chem. Int. Ed.* **2000***, 39,* 1269–1272.
14. Sohgawa, Y. H.; Fujimori, H.; Shoji, J.; Furusho, Y.; Kihara, N.; Takata, T. *Chem. Lett.* **2001**, *8*, 774–775.
15. Affeld, A.; Hübner, G. M.; Seel, C.; Schalley, C.A. *Eur. J. Org. Chem.* **2001**, 2877–2890.
16. Linnartz, P.; Bitter, S.; Schalley, C. A. *Eur. J. Org. Chem.* **2003**, 4819–4829.
17. Vignon, S.A.; Jarrosson, T.; Iijima, T.; Tseng, H.-R.; Sanders, J. K. M.; Stoddart, J. F. *J. Am. Chem. Soc.* **2004**, *126*, 9884–9885.
18. Murakami, H.; Kawabuchi, A.; Matsumoto, R.; Ido, T.; Nakashima, N. *J. Am. Chem. Soc.* **2005**, *127*, 15891–15899.
19. Tokunaga, Y.; Wakamatsu, N.; Ohbayashi, A.; Akasaka, K.; Saeki, S.; Hisada, K.; Goda, T.; Shimomura, Y. *Tetrahedron Letters* **2006**, *47*, 2679–2682.
20. *Molecular Catenanes, Rotaxanes and Knots,* Sauvage, J.-P.; Dietrich-Buchecker, C. Eds.; Wiley-VCH: Weinheim, Germany, **1999**.
21. Coumans, R. G. E.; Elemans, J. A. A. W.; Nolte, R. J. M.; Rowan, A. E. *Proc. Natl Acad. Sci. USA* **2006**, *103*, 19647–19651.
22. Venturi, M.; Duas, S.; Balzani, V.; Cao, J. G.; Stoddart, J. F, *New J. Chem.* **2004**, *28*, 1032–1037.
23. Elemans, J. A. A. W.; Claase, M. B.; Aarts, P. P. M.; Rowan, A. E.; Schenning, A. P. H. J.; Nolte, R. J. M. *J. Org. Chem.* **1999**, *64*, 7009–7016.
24. Hunter, C. A.; Sanders, J. K. M. *J. Am. Chem. Soc.* **1990***, 112*, 5525–5534.
25. Thesis of R. G. E. Coumans, 2006.
26. Koppelman, S. J.; vanHoeij, M.; Vink, T.; Lankhof, H.; Schiphorst,M. E.; Damas, C.; Vlot, A. J.; Wise, R.; Bouma, B. N.; Sixma, J. J. *Blood* **1996**, *87*, 2292–2300.
27. Asakawa, M.; Ashton, P. R.; Ballardini, R.; Balzani, V.; Belohradsky, M.; Gandolfi, M. T.; Kocian, O.; Prodi, L.; Raymo, F. M.; Stoddart, J. F.; Venturi, M. *J. Am. Chem. Soc.* **1997**, *119,* 302–310.
28. Raymo, F. M.; Stoddart, J. F. *Pure & Appl. Chem.* **1997**, *69*, 1987–1997.
29. Thordarson, P.; Coumans, R. G. E.; Elemans, J. A. A. W.; Thomassen, P. J.; Visser, J.; Rowan, A. E.; Nolte, R. J. M. *Angew. Chem. Int. Ed.* **2004**, *43*, 4755–4759.
30. Ricard, J.; Cornish-Bowden, A. *Eur. J. Biochem.* **1987**, *166,* 255–272.
31. Heim, C.; Affeld, A.; Nieger, M.; Vögtle, F. *Helv. Chim. Acta* **1999**, *82*, 746–759.
32. Elizarov, A. M.; Chang, T.; Chiu, S.-H.; Stoddart, J. F. *Org. Lett.,* **2002**, *4*, 3565–3568.

5

Can a Porphyrin Macrocycle move over a Folded Polymer Chain?

1. Introduction

In our laboratory a method has been developed to study the pseudo-rotaxane formation between a porphyrin macrocycle and viologens after the movement of the macrocycle over polymeric substrates (poly-THF and polybutadiene with lengths up to 55 nanometer).[1,2] Viologens which have a 3,5-ditert-butylphenyl blocking group connected to one side and a polymeric substrate appended to the other side were synthesized. Because the blocking group is too bulky to allow slippage of the porphyrin macrocycle, complex formation between the viologen and the macrocycle can only occur after movement of the macrocycle along the entire polymer chain, thereby providing an elegant method to study the threading process of polymers of different lengths through macrocycles. The observed kinetics of complex formation (threading rate: k_{on}) between the polymeric substrates and the macrocycle is second order and the kinetics of complex dissociation (de-threading rate: k_{off}) is first order. A clear length dependency was observed in which lower (de-)threading rate constants were observed upon an increase in the polymer chain length. One main question regarding the threading process is how the macrocycle threads onto the polymers. It was shown recently in the literature that flexible molecular chains can adopt a back-folded[3,4] (as described by Ko, Kim, Kim & Kim) or a helical[5-10] (by Rebek) geometry when bound to the inside of synthetic cavitands. It has therefore been proposed that it is possible that $\mathbf{H_21}$ threads onto a hairpin-like fold of the polymer and that the movement along the polymer occurs over a double chain (Figure 1b). This mechanism can be expected to be more facile because the macrocycle does not have to find the open end of the polymer chain (as in Figure 1a), but can thread onto the polymer anywhere along its chain. In order to investigate the possibility of this mechanism it was decided to study the kinetics of pseudo-rotaxane formation between the porphyrin macrocycle and viologens after the slippage[11-27] over terminal groups of varying bulkiness. An approach was chosen that is similar to the one used in the studies in which the macrocycle traverses the polymers. Viologen derivatives **V1–V8**, containing the same blocking group on one side and a variety of terminal groups on the other side, among which a cyclododecane moiety and a variety of double-chain appended-alkyl moieties, were synthesized (Chart 1). One of the main advantages in the use of porphyrin macrocycle $\mathbf{H_21}$ in slippage studies is its high affinity for viologen derivatives ($K_{\text{assoc}} \approx 10^5$–$10^7$ M^{-1}). These high association constants, in combination with the UV-Vis and fluorescence spectroscopy properties of the porphyrin, allow the study of complex formation at sub-micromolar concentrations. From these studies rate constants

(k_{on}) with values up to 5 x 10^6 $M^{-1}s^{-1}$ can be accurately derived from simple titration experiments. By studying the kinetic process of complex formation between **$H_2$1** and viologen derivatives **V1–V8**, not only the feasibility of the threading of **$H_2$1** over a folded polymer chain could be determined but, in addition, a clear picture of the effect of terminal group bulkiness in the process of slippage could be provided.

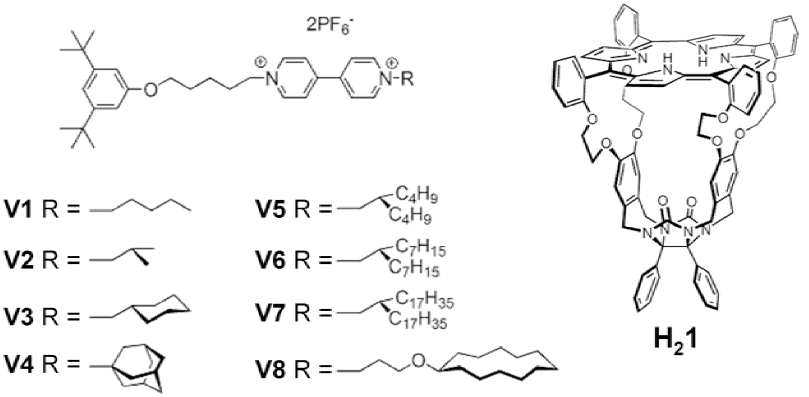

Chart 1. Molecules used in this chapter.

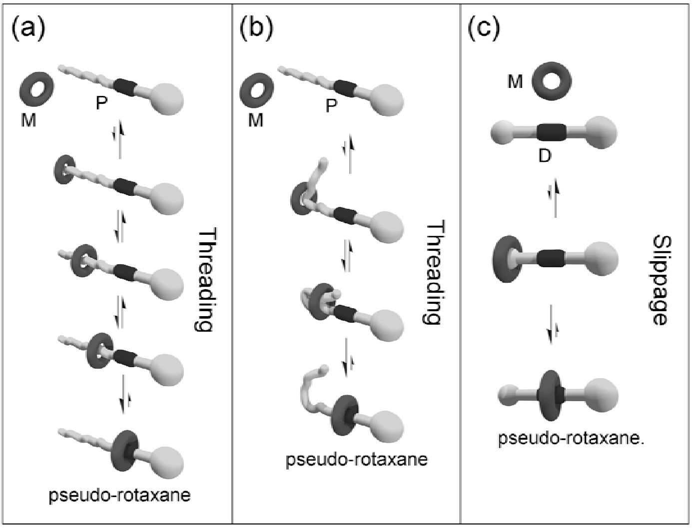

Figure 1. Schematic representation of pseudo-rotaxane formation by threading and slippage processes. (a) Threading mechanism in which the macrocycle threads onto the open end of the polymer and the movement is a random walk along a single chain. (b) Threading mechanism in which the macrocycle binds to and moves over a folded chain. (c) Slippage mechanism in which the rate is determined by the ease of traversing a bulky substituent.

2. Results

2.1 Synthesis of viologen derivatives

Viologen derivatives can be readily synthesized by the substitution reaction of 4,4'-bipyridine (BiPy) with primary halides.[28] Reactions of an excess of BiPy with primary halides can statistically provide monoalkylated bipyridinium compounds. Two main approaches were chosen to synthesize viololgens **V1–V8** (Scheme 1). In the first approach, blocking group-containing monoalkylated bipyridinium **2** was synthesized from BiPy and bromide **1**,[1] after which the terminal groups were appended by a second substitution reaction using primary bromides **3**, **4**, **5**, **6**, **13**, and **14**, to furnish the viologen derivatives **V1–V6** after an ion exchange reaction with NH_4PF_6. In the second approach the terminal group-containing monoalkylated bipyridiniums **16** and **17** were first synthesized, after which the blocking groups were appended by nucleophilic substitution reactions with **1** providing viologen derivatives **V7** and **V8** after an ion exchange reaction with NH_4PF_6. The synthesis of (3-bromo-propoxy)-cyclododecane **6** was achieved by the reaction of 1,3-dibromopropane with cyclododecanol in the presence of NaH.[29] In addition to **6**, the elimination product of **6** was also formed in significant amounts and this product could unfortunately not be separated from **6**. Bromides **13**, **14**, and **15** were synthesized by Wittig reactions[30] of ketones **7**, **8**, and **9** followed by anti-Markovnikov bromination[31] of the resulting alkenes **10**, **11**, and **12**. Monoalkylated bipyridinium **17** was synthesized according to a literature procedure.[32]

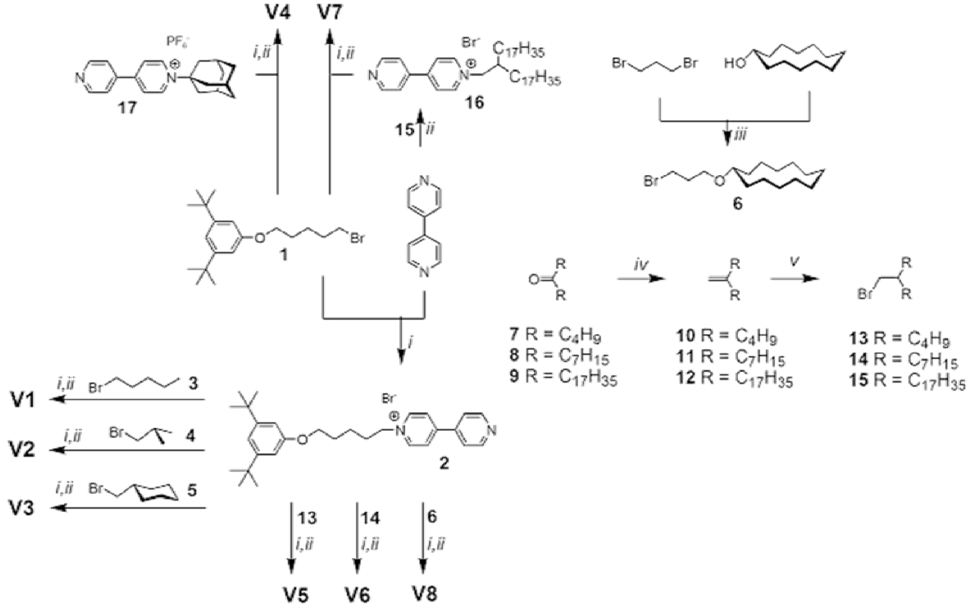

Scheme 1 Synthesis of viologen derivatives **V1**-**V8**. Reagents and conditions: (*i*) DMF, 90 °C, 1–5 d; (*ii*) NH_4PF_6 (aq); (*iii*) NaH, THF; (*iv*) KOtBu, Ph_3PCH_3Br, toluene. (v); 1. $BH_3 \cdot S(CH_3)_2$, NaOH (aq), H_2O_2 (aq), THF; 2. Br_2Ph_3P, pyridine, CH_2Cl_2.

2.2 ^{1}H-NMR investigations

First, pseudo-rotaxane formation of **$H_2$1** with viologens **V1–V8** was investigated with the help of ^{1}H-NMR spectroscopy. Chlorofom/acetonitile solutions (1/1 (v/v)) containing **$H_2$1** (6.8 mM) and a slight excess of the different viologen guests were prepared. Immediate complex formation was observed in the case of viologen derivatives with the least bulky terminal groups **V1**, **V2**, and **V3**. The 400 MHz ^{1}H-NMR spectra revealed only proton resonances of the pseudo-rotaxane complexes between **$H_2$1** and **V1**, **V2**, and **V3**, and resonances of the protons of unbound guests, because the exchange (and hence the slippage) between **$H_2$1** and the different guests (**V1–V3**) is slow on the NMR timescale and no significant coordination between the outside of **$H_2$1** and the viologen derivatives occurs. The ^{1}H-NMR spectra of the solutions containing mixtures of **$H_2$1** and **V4** and **V5**, revealed slow formation of the pseudo-rotaxane complexes (Figure 2). In time, the proton resonances of uncomplexed **$H_2$1** and viologens **V4** and **V5** decreased at the benefit of the proton resonances of the respective pseudo-rotaxane complexes. The slippage over the adamantane group of **V4** is significantly faster than the slippage over the 1-(2-butyl-hexyl) group of **V5**. Whereas full complexation was reached within one hour at room temperature in the slippage experiment with **V4**, for **V5** this was only achieved after three days of standing. The ^{1}H-NMR experiments with **$H_2$1** and **V6–V8** revealed no pseudo-rotaxane formation, even after prolonged standing of the samples at elevated temperatures (50 °C).

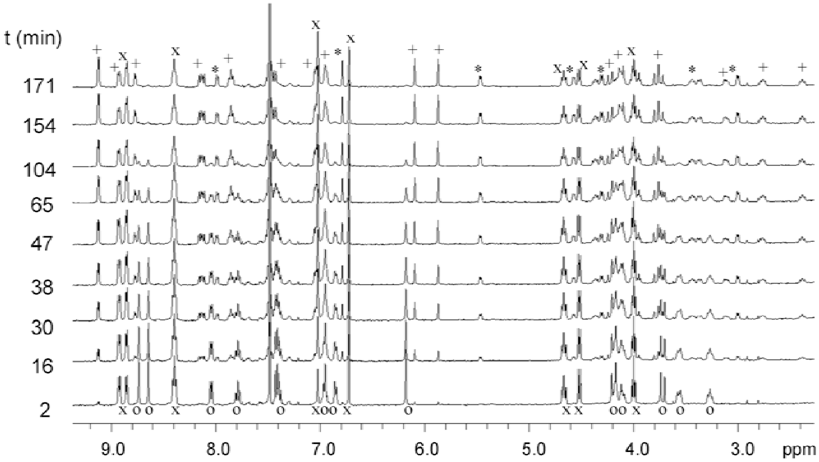

Figure 2 ^{1}H-NMR spectral changes (400 MHz, $CDCl_3/CD_3CN$ 1/1 (v/v)) during the slippage experiment of **$H_2$1** (0.68 mM) and **V5** (1.4 mM, 2 equiv) in time (from bottom to top) at 45 °C, which revealed the total disappearance of the resonances of **$H_2$1** and **V5** on the formation of the non-symmetrical (pseudo-)rotaxane complex. The signals belonging to free **$H_2$1** (^{o}) and free **V5** (^{X}), and to **$H_2$1** ($^+$) and **V5** (*) in the rotaxane self-assembled structure are indicated.

2.3 Thermodynamics and kinetics of pseudo-rotaxane formation

The evolution of macrocycle A, guest B and pseudo-rotaxane C in time in the slippage process can be completely described by Equations 1-3. The association constant (K_{assoc}) between the macrocycle and the guest is described by Equation 4. Equation 1 is the universal formula for the slippage process and can be employed independently of the relative ratios of macrocycle ($[\text{A}]_\text{o}$) and guest ($[\text{B}]_\text{o}$) or the initial amount of pseudo-rotaxane complex present at t = 0 ($[\text{C}]_\text{o}$). It is therefore not necessary to mix equimolar amounts of macrocycle and guest to calculate accurate rate constants. Equations 1–3 can also be employed to calculate rate constants in the deslippage process in which $k_{\text{off}} = k_{\text{on}}/K_{\text{assoc}}$.

$$\text{A} + \text{B} \underset{k_{\text{off}}}{\overset{k_{\text{on}}}{\rightleftharpoons}} \text{C}$$

$$[\text{C}] = p\frac{\left(1-\frac{q}{p}\frac{p-[\text{C}]_\text{o}}{q-[\text{C}]_\text{o}}e^{k_{\text{on}}(p-q)t}\right)}{\left(1-\frac{p-[\text{C}]_\text{o}}{q-[\text{C}]_\text{o}}e^{k_{\text{on}}(p-q)t}\right)} \tag{1}$$

$$p = [\text{C}]_{\text{eq}} = \frac{([\text{A}]_\text{o}+[\text{B}]_\text{o}+\frac{1}{K_{\text{assoc}}}) - \sqrt{([\text{A}]_\text{o}+[\text{B}]_\text{o}+\frac{1}{K_{\text{assoc}}})^2 - 4\cdot[\text{A}]_\text{o}\cdot[\text{B}]_\text{o}}}{2} \tag{2}$$

$$q = \frac{[\text{A}]_\text{o}[\text{B}]_\text{o}}{[\text{C}]_{\text{eq}}} \tag{3}$$

$$K_{\text{assoc}} = \frac{[\text{C}]_{\text{eq}}}{\left([\text{A}]_\text{o}-[\text{C}]_{\text{eq}}\right)\cdot\left([\text{B}]_\text{o}-[\text{C}]_{\text{eq}}\right)} \tag{4}$$

In the ^{1}H-NMR experiments in which the slippage equilibrium is not immediately reached (i.e. in the case of viologen derivatives **V4** and **V5**), the ratios of **$H_2$1**, viologen, and pseudo-rotaxane in time could be easily determined with the relative intensities of the ^{1}H-NMR signals associated with each species. By monitoring the decrease in the relative intensities of **$H_2$1** and viologen the derivatives **V4** and **V5**, with respect to their concomitant appearance in the complexes as a function of time, the rate constants for the slippage processes (k_{on}) could be calculated by using Equations 1–3. At equilibrium, no free **$H_2$1** could be observed at the concentrations used of this receptor and viologen guests **V4** or **V5**, which makes it impossible to derive accurate values for K_{assoc}. Only a lower limit for these association constants could be calculated from the experiments (Table 1).

The process of slippage of **$H_2$1** with **V4** was slightly too fast to calculate accurate rate constants with the help of ^{1}H-NMR techniques (over 50% of pseudo-rotaxane had already been formed after recording the first spectrum). Therefore, it was decided to monitor pseudo-rotaxane formation by UV-Vis spectroscopy at lower concentrations. The addition of **V4** (50 equivalents) to a solution containing **$H_2$1** (1.6 x 10^{-5} M) resulted in spectral changes of the porphyrin Soret band which were monitored. The concentrations of **V4** were chosen such that at equilibrium **$H_2$1** would be nearly completely occupied by **V4**, hence the total change in absorption at any wavelength simply represented the change in the amount of free **$H_2$1** with respect to the pseudo-rotaxane complex between **$H_2$1** and **V4**. The concentration of pseudo-rotaxane in time, $[C]_t$, in the experiment is therefore given by: $[C]_t = [A]_o\{A_t\text{-}A_o\}/\{A_{eq}\text{-}A_o\}$, in which A_o, A_t, and A_{eq} are the absorbance at t = 0, t, and t = ∞, respectively. A small redshift of the porphyrin Soret band and an isosbestic point were observed upon formation of the pseudo-rotaxane complex. The evolution of the absorbances at different wavelengths in time (Figure 3a) could be nicely fitted with the help of Equations 1–3. In fact, such an excess of **V4** was used that the kinetics of the slippage could also be fitted with (pseudo) first order binding isotherms, and the calculated averaged rate constant for the slippage of **$H_2$1** with **V4** (k_{on} = 7.9 $M^{-1}s^{-1}$), was in good agreement with the rate constant determined by ^{1}H-NMR spectroscopy (k_{on} = 8.5 $M^{-1}s^{-1}$).

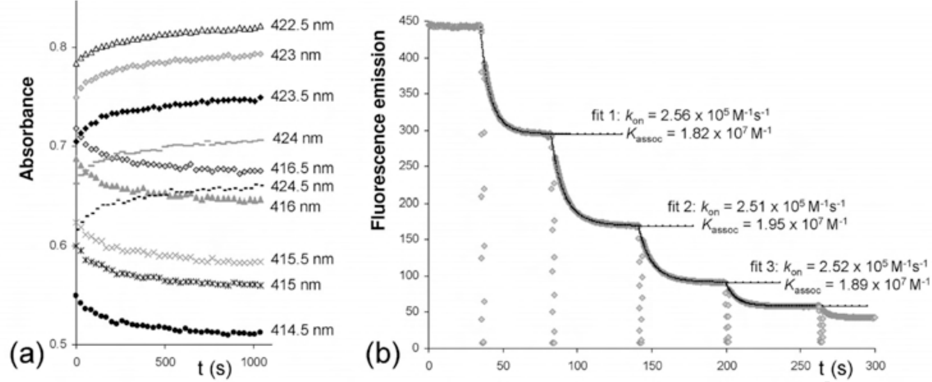

Figure 3. (a) Evolution of the absorbance of the porphyrin Soret band of **$H_2$1** (1.6 x 10^{-5} M) at different wavelengths in time after the addition of 50 equiv of **V4** in $CHCl_3/CH_3CN$ (1/1, v/v) at 25 °C. (b) Fluorescence emission (grey dots) of **$H_2$1** after the addition of increasing amounts of **V3** in time in $CHCl_3/CH_3CN$ (1/1, v/v) at 1 °C. While mixing, the cuvettes were removed from the spectrometer which results in the local drops in fluorescence. The black lines indicate the fits that are obtained from Equations 1–4. The calculated constants of the individual slippage curves are all in the same order of magnitude, which stresses the accuracy of the data analysis.

In order to derive the rate constants for the slippage of **$H_2$1** over the least bulky terminal groups of the viologens, i.e. those of **V1**–**V3**, slippage experiments were performed at low concentrations (10^{-6} M) of **$H_2$1** and these guests in a 1/1 mixture of chloroform and acetonitrile (v/v). Since upon the binding of viologen derivatives the porphyrin fluorescence emission is fully quenched, the kinetics and thermodynamics of complex formation could be easily monitored by recording this fluorescence emission in time. The pseudo-rotaxane concentration [C] is given by $[C]_t = [A]_o\{E_o\text{-}E_t\}/E_o$, in which E_o and E_t are the fluorescence emission at t = 0 and t, respectively. In order to obtain as many data as possible in a short time span, it was decided to perform titration experiments in which low concentrations (2–4 x 10^{-7} M^{-1}) of solutions containing the viologen derivatives were added to a solution containing **$H_2$1**. After each addition, the fluorescence emission slowly reached a new equilibrium position and, at that point, a further solution containing viologen was added (Figure 3b). The fluorescence emission curves in time could be fitted with the use of Equations 1–4, and provided the values of k_{on} and K_{assoc} in plural, thereby significantly minimizing the error in both k_{on} and K_{assoc}.

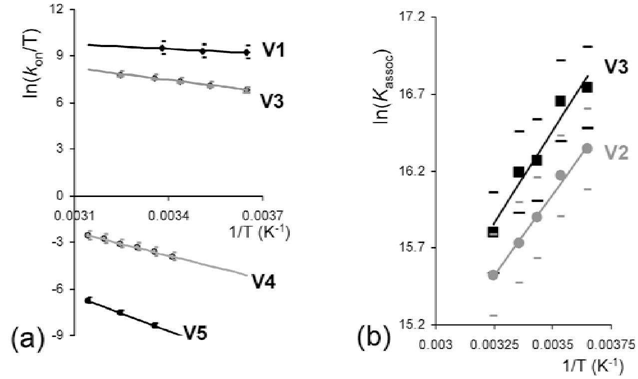

Figure 4. (a) Eyring plots for the slippage of **$H_2$1** over the tails of **V1**, **V3**, **V4**, and **V5**. (b) Van 't Hoff plots for the complexation of **$H_2$1** with **V2** and **V3.**

In order to investigate the effect of the temperature on the kinetics of the process, the slippage of **$H_2$1** over the terminal groups of **V1–V5** was monitored at at least three different temperatures using one of the above-described methods. The enthalpic ($\Delta H^{\neq}_{on}$) and entropic contributions ($\Delta S^{\neq}_{on}$) to the total free energy of activation ($\Delta G^{\neq}_{on}$) were determined from the straight lines of the Eyring Plots (Figure 4a). In addition, the enthalpic (ΔH^{o}) and entropic (ΔS^{o}) contributions to the total free binding energy (ΔG^{o}) of pseudo-rotaxane formation between **$H_2$1** and **V2** or **V3** could be determined with the help of Van 't Hoff plots (Figure 4b). All thermodynamic and kinetic data are listed in Table 1.

Table 1. Rate constants (k_{on}) for the slippage of **$H_2$1** over the tails of **V1**-**V8** and the activation parameters ($\Delta G^{\neq}_{on}$, $\Delta H^{\neq}_{on}$, $\Delta S^{\neq}_{on}$) obtained from the evolution of the kinetic data obtained from Eyring plots, the association constants (K_{assoc}), and the free energies of association (ΔG^{o}) of the formed complexes and the binding parameters (ΔH^{o}, ΔS^{o}) obtained from evolutions of the thermodynamic data using Van 't Hoff plots.

Guest	k_{on} ($M^{-1}s^{-1}$) [g]	$\Delta G^{\neq}_{on}$ (kJ·mol^{-1}) [i]	$\Delta H^{\neq}_{on}$ [j] (kJ·mol^{-1})	$\Delta S^{\neq}_{on}$ [j] (J·mol^{-1}K^{-1})	K_{assoc} (M^{-1}) [h]	ΔG^{o} (kJ·mol^{-1}) [i]	ΔH^{o} (kJ·mol^{-1}) [j]	ΔS^{o} (J·mol^{-1} K^{-1}) [j]
V1[a]	5×10^{6}	35	15	–67	1.0×10^{7}	–40	[e]	[e]
V2[a]	3×10^{6}	36	[d]	[d]	6.8×10^{6}	–39	–18	72
V3[a]	6.0×10^{5}	40	21	–64	1.1×10^{7}	–40	–20	68
V4[b]	7.9	68	42	–87	$> 10^{6}$	[e]	[e]	[e]
V5[c]	7.0×10^{-2}	80	63	–56	$> 10^{6}$	[e]	[e]	[e]
V6-V8	[f]	[f]	[f]	[f]	[f]	[f]	[f]	[f]

[a] Determined by fluorescence titrations in $CHCl_3/CH_3CN$ 1/1 (v/v). [b] Determined by UV-Vis titrations in $CHCl_3/CH_3CN$ 1/1 (v/v). [c] Determined by ^{1}H-NMR experiments in $CDCl_3/CD_3CN$ 1/1 (v/v). [d] Threading rate was too high to accurately measure at the experimental conditions used. [e] Association constant was too high to accurately calculate at the experimental concentrations used. [f] No complex formation was observed. [g] Estimated error < 15%. [h] Estimated error < 35%. [i] Estimated error 1 kJ mol^{-1}. [j] Estimated error 2 kJ·mol^{-1}.

3. Discussion

3.1 Kinetic data

Earlier reports have shown that very subtle changes in terminal groups, such as changing from an ethyl to an isopropyl[33] or from a cyclohexane to a cycloheptane,[20] result in an all-or-nothing effect for the slippage of a macrocycle over these terminal groups. A small increase in terminal group bulkiness can increase the steric hindrance to the level that the barrier for slippage becomes insurmountable. A similar (perhaps even more subtle) all-or-nothing effect was observed in the present study. Whereas a very low value for the rate constant was observed for the slippage of the macrocycle over **V5**, which indicates that **$H_2$1** can only just slip over the 1-(2-butyl-hexyl) group, slippage over the longer substituents of **V6**, **V7**, and over the cyclododecyl moiety of **V8** was impossible. Obviously, the cavity of **$H_2$1** is not large enough to allow slippage over the cyclododecyl terminal group of **V8**. The all-or-nothing effect observed between **V5** and **V6** clearly indicates that very subtle differences in steric bulk govern whether slippage is possible or not. Moreover, it provided a clear hint on the mechanism by which the 1-(2-butyl-hexyl) of **V5** group is traversed. Two plausible mechanisms for this process can be rationalized. A first is one, in which the macrocycle threads onto a single *n*-butyl chain-end of the 1-(2-butyl-hexyl) after which it moves in a second step over both the second chain-end of the 1-(2-butyl-hexyl) and part of the viologen (see Figure 5b), similar to the mechanism reported for the slippage of bis-*p*-phenylene-34-crown-10 over 4-*R*-phenyl-bis(4-*tert*-butyl-phenyl)methane-based stoppers.[19] Assuming this mechanism, the bottleneck of the slippage of **V5** lies in traversing the section where **$H_2$1** needs to simultaneously overcome the steric bulk of the second part of the 1-(2-butyl-hexyl) chain and the viologen. A second possible mechanism is that the two 1-(2-butyl-hexyl) chain ends are ‘tweezed’ in close proximity and the slippage occurs over a double chain, as presented in Figure 5a. The first mechanism can be considered unlikely due to the need for a presumably highly unfavorable back-folding of the alkyl chain onto the viologen moiety, in which case the chain is in close proximity to the repelling positive charge of the viologen (moreover since ^{1}H-NMR spectroscopy and binding studies do not suggest such back-folding). The second mechanism at first sight is also not very likely, since it requires an organization of the highly flexible alkyl chains in a very specifically tweezed geometry, which would, in principle, be entropically highly unfavorable (although the same entropic argument can also be applied to the first mechanism). In order to determine which of the two mechanisms is the most favorable, the circumferences of the van der Waals surfaces of the different transition state conformations (the most bulky part of the terminal groups in their least bulky conformations) were measured with the use of CPK models. Although for **V5** and **V6** the differences in substituent bulkiness were very marginal (within 8%; Figure 5), the transition state conformations of the second mechanism were less ‘bulky’ than those of the first. A measurement of the inner circumference of **$H_2$1** (19.8 Å; Figure 6), moreover, revealed that only the transition state conformation of the 1-(2-butyl-hexyl) group in the second mechanism (Figure 5a, 19.4 Å) is within the dimensions of the cavity. These results strongly suggest that **$H_2$1** slips over the 1-(2-butyl-hexyl) group of **V5** according to the second mechanism, in which the chain ends of the terminal group are tweezed together (Figure 5a). The slightly more bulky terminal group of **V6** just exceeds the dimensions of the cavity and no slippage is observed.

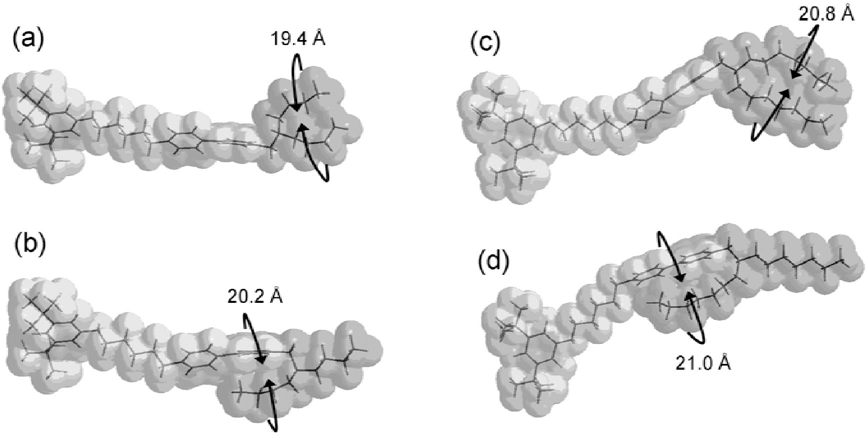

Figure 5. Molecular models of slippage transition state conformations of the terminal groups of **V5** and **V6** for the tweezed double chain mechanism ((a) and (c)) and the back-folding mechanism ((b) and (d)). The maximum circumferences of the van der Waals surfaces in the transition state geometries are indicated to stress that conformation (a) is the least bulky.

The circumferences of the van der Waals surfaces of all the different terminal groups in their transition state geometries were determined and the slippage rate constants were plotted versus these circumferences (Figure 6b). The plot clearly shows that when the circumferences of the terminal groups approach the inner circumference of the macrocycle, the rate constant for the slippage tends towards zero. This is another good indication that the steric hindrance between the terminal group and the macrocycle determines the relative rates and feasibility of the slippage process. The enthalpic contributions to the activation energy ($\Delta H^{\neq}_{\text{on}}$), obtained by evaluation of the slippage at different temperatures, point in the same direction; A clear increase in the enthalpy of activation is observed upon the increase of terminal group bulkiness (Table 1), which is in line with the idea that steric repulsion is enthalpic in origin.

Although in all cases the slippage is entropically unfavorable, no trend could be observed in the entropy of activation ($\Delta S^{\neq}_{\text{on}}$) values. The differences in the obtained activation parameters observed for the slippage over the adamantane group of **V4** and the 1-(2-butyl-hexyl) group of **V5** are intriguing. The rate constant for slippage over the adamantane is more than two orders of magnitude higher than the rate constant for the slippage over the 1-(2-butyl-hexyl) group. Whereas the adamantane has a fixed and nearly spherical geometry and is therefore readily organized for the slippage of **$H_2$1**, the 1-(2-butyl-hexyl) group can be expected to be very flexible and needs to preorganize into its least bulky conformation to allow the slippage of **$H_2$1** to occur. One would therefore, based on these differences in flexibility, expect a more negative value for the entropy of activation ($\Delta S^{\neq}_{\text{on}}$) for the slippage over the 1-(2-butyl-hexyl) terminal group than over the adamantane group. The contrary was, however, derived from the variable temperature experiments and suggests that factors other than the flexibility of the terminal groups, like for instance differences in terminal group solvation, enthalpy-entropy compensation, or the flexibility of the receptor, also play a crucial role in the slippage process. It can also be argued that the 1-(2-butyl-hexyl) group is already preferentially organized in the 'tweezed' conformation in the rather polar solvent mixture. Whatever the exact cause of the experimentally obtained activation parameters, the main difference between the slippage of $\mathbf{H_21}$ over the terminal groups of **V4** and **V5** is reflected in the enthalpy of activation ($\Delta H^{\neq}_{\text{on}}$). This difference is most probably caused by a less favorable fit of the 1-(2-butyl-hexyl) group of **V5** inside the cavity of $\mathbf{H_21}$ compared to the adamantane group of **V4**, which stresses once more that steric hindrance is the main rate determining factor in the slippage.

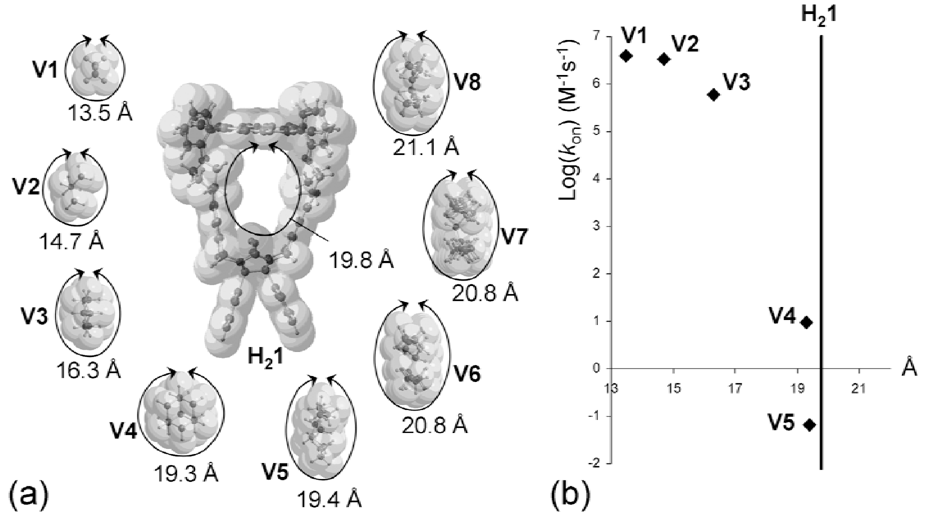

Figure 6. (a) Circumferences of the terminal groups of **V1**–**V8** that $\mathbf{H_21}$ has to surmount before complex formation can occur and the inner circumference of the cavity of $\mathbf{H_21}$, based on van der Waals surfaces. (b) Rate constants for the slippage of $\mathbf{H_21}$ over the different terminal groups plotted against the circumference of these groups and the inner circumference of the cavity of $\mathbf{H_21}$.

3.2 Thermodynamic data

The free binding energy of the pseudo-rotaxane complexes of $\mathbf{H_21}$ with **V2** and **V3** are a result of both favorable enthalpic (ΔH^{o}) and entropic contributions (ΔS^{o}), as can be concluded from the data given in Table 1. In addition to stabilizing non-covalent binding interactions (such as π-π interactions, van der Waals interactions, and dipole-dipole interactions) between $\mathbf{H_21}$ and the viologen derivatives, which are most likely enthalpic in origin, there is also a strong entropic driving force for complex formation. This is most probably the result of desolvation of the viologen moieties upon formation of the pseudo-rotaxane complex. The association constant of $\mathbf{H_21}$ with **V3** is significantly larger than that of $\mathbf{H_21}$ with **V2** (Table 1). This observation is in line with our previous findings that an increase in the size of the viologen substituents results in stronger complex formation with **$H_2$1** (and other porphyrin macrocycles).[1,34] Although the electronic properties of viologen derivatives with different substituents are expected to be slightly different (hence also the viologen-macrocycle interactions), this effect is proposed to be mainly the result of extra stabilizing (van der Waals) interactions of the substituents in the formed receptor-guest complex. For this reason, the cyclohexyl group of **V3** can provide more of these stabilizing interactions in the complex with **$H_2$1** than the isopropyl group of **V2**. The validity of this hypothesis is emphasized by the different enthalpic contributions (ΔH^o) to the binding free energy (ΔG^o), which reveal a more favorable enthalpy of binding in the complex between **$H_2$1** and **V3** than in the complex between **$H_2$1** and **V2**. The results also show that it is entropically more favorable to form the complex between **$H_2$1** and **V2** than the complex between **$H_2$1** and **V3**. This could be the result of a relatively better solvation of **V3** compared to **V2** in the solvent system used (because of the larger nonpolar cyclohexyl substituents compared to the isopropyl substituents), which reduces the relative 'need' for **V3** to form a complex with **$H_2$1** compared to **V2**. It is also possible that the extra stabilization of the complex between **$H_2$1** and **V3** by the cyclohexyl group is entropically demanding.

4. Conclusion

The present study indicates that the rate of the slippage of the porphyrin macrocycle **$H_2$1** over a variety of terminal groups depends strongly on the size complementarities and subsequent steric hindrance between the van der Waals surfaces of the macrocycle and the terminal group. The rate constants decrease upon increasing bulkiness and when the dimensions of the van der Waals surface of the terminal group exceeds that of the inner van der Waals surface of the macrocycle, the barrier for the slippage becomes insurmountable, which results in an all-or-nothing effect. The presented results strongly suggest that movement of **$H_2$1** over a looped polymeric chain is highly unfavorable (if not impossible). The experiments revealed no slippage over the terminal groups of **V6**, **V7**, and **V8** and a very low rate constant for the slippage over the terminal group of **V5**. The observed rate constant for the slippage over the 1-(2-butyl-hexyl) terminal group is more than five orders of magnitude lower than that for the movement of **$H_2$1** over a poly-THF terminal group of 54 nm. From these results it can therefore be concluded that in threading polymeric substrates, **$H_2$1** first binds onto the open end of the polymer after which it has to traverse the complete polymer chain before it reaches the viologen binding site.

5. Experimental section

Materials and methods. Chloroform and acetonitrile used in titration experiments were distilled from $CaCl_2$. All other solvents and chemicals were commercial materials and used as received. Fluorescence experiments were performed on a Perkin-Elmer LS50B luminescence spectrometer equipped with a thermostatted cuvette holder. UV-Vis spectra were recorded on a Cary 100 Conc (Varian, Middelburg) UV-Vis spectrometer. Maldi-TOF ms was performed on a Bruker Biflex III spectrometer. NMR spectra were taken on a Varian Inova 400 (400 MHz, ^{1}H and 2D spectra) or on a

Bruker DMX300 (75 MHz, ^{13}C spectra) and calibrated to an internal standard of tetramethylsilane. Porphyrin macrocycle $\mathbf{H_21}$ was synthesized according to a literature procedure.[35,36]

(3-Bromo-propoxy)-cyclododecane (6)

To a suspension of NaH (0.11 g of 60% NaH in mineral oil, 2.8 mmol) in dry THF (3 mL) at 0 °C was added a solution of cyclododecanol (0.26 g, 1.1 mmol) in dry THF (4 mL) dropwise over a period of 10 min under an argon atmosphere. The reaction mixture was warmed to room temperature, stirred for 1 hour and cooled to 0 °C before 1,3-dibromopropane (2.2 mL, 24 mmol) was slowly added. The reaction mixture was warmed to room temperature again, stirred for 1 h, cooled to 0 °C, mixed with diethyl ether (14 mL), neutralized with 1.0 M HCl (14 mL) and then stirred for 1 h at room temperature. The ether layer was washed with aqueous 1.0 M HCl (1x), brine (2x) and dried over $MgSO_4$. The drying agent was removed by filtration, the solvents evaporated, and the remaining 1,3-dibromopropane distilled off to obtain 70 mg of a mixture of **6** and its alkene derivative as a white solid in an approximate 1:2 ratio, respectively.

^{1}H-NMR (400 MHz, $CDCl_3$) Alkene characteristics: δ 5.92 (m, 1H, $H_2C{=}CH$), 5.27 (m, 1H, $CH_2CH{=}CH_{trans}$), 5.15 (m, 1H, $CH_2CH{=}CH_{cis}$), 3.98 (dt, 2H, $C{=}CHCH_2$, J = 5.6 Hz, J = 1.2 Hz), 3.47 (m, 1H, cyclododecaneC*H*), 1.28−1.36 (m, 22H, cyclododecane$(CH_2)_{11}$). Bromide characteristics: δ 3.55 (t, 2H, OCH_2, J = 6 Hz), 3.53 (t, 2H, $BrCH_2$, J = 6.8 Hz), 2.07 (q, 2H, $BrCH_2CH_2$, J = 5.2 Hz), 3.42 (m, 1H, cyclododecaneC*H*), 1.28−1.36 (m, 22H, cyclododecane$(CH_2)_{11}$) ppm.

General synthesis of the methylene compounds 10, 11, and 12[30]

At room temperature, KOtBu (1.2 g, 11 mmol) was added in four portions to a solution of methyltriphenylphosphonium bromide (3.3 g, 9.3 mmol) in dry toluene (70 mL). The mixture was refluxed for 1 h under an argon atmosphere and then cooled to room temperature. A mixture of the corresponding ketone in dry toluene was added dropwise and then stirred for 30 min. A saturated aqueous NH_4Cl solution (30 mL) was added to the reaction mixture, which was then extracted with diethyl ether (3x). The combined organic phases were washed with brine (2x) and then dried over $MgSO_4$. The drying agent was filtered off and the filtrate was evaporated in the presence of an excess of silica to avoid clogging of the column by the remaining organic salts. The silica mixture was put on a flash silica column and the product eluted to obtain the corresponding methylene product.

5-Methylene-nonane (10)

Ketone mixture: **7** (1.0 g, 7.0 mmol) in toluene (5 mL). Eluent: *n*-pentane. Yield = 0.63 g as a colorless liquid (4.5 mmol, 64%):

^{1}H-NMR (400 MHz, $CDCl_3$): δ 4.69 (q, 2H, $C{=}CH_2$, J = 0.8 Hz), 2.00 (t, 4H,$CH_2{=}CCH_2$, J = 8.0 Hz), 1.40 (m, 8H, $CH_2{=}CCH_2CH_2CH_2$), 0.91 (t, 6H, CH_3, J = 7.2 Hz) ppm.

8-Methylene-pentadecane (11)

Ketone mixture: **8** (2.1 g, 9.2 mmol) in 5 mL of toluene. Eluent: *n*-heptane. Yield = 1.5 g as a white solid (6.7 mmol, 72%):

^{1}H-NMR (400 MHz, $CDCl_3$): δ 4.68 (q, 2H, $C{=}CH_2$, J = 1.2 Hz), 1.99 (t, 4H,$CH_2{=}CCH_2$, J = 8.0 Hz), 1.41 (q, 4H, $CH_2{=}CCH_2CH_2$, J = 6.8 Hz), 1.28 (m, 16H, $CH_2{=}CCH_2CH_2CH_2CH_2CH_2CH_2$), 0.88 (t, 6H, CH_3, J = 7.2 Hz) ppm.

18-Methylene-pentatriacontane (12)

Ketone mixture: **9** (4.6 g, 9.2 mmol) in 10 mL of toluene. Eluent: *n*-heptane. Yield = 1.34 g as a white solid (2.66 mmol, 30%):

^{1}H-NMR (400 MHz, $CDCl_3$): δ 4.68 (m, 2H, $C{=}CH_2$), 1.99 (t, 4H,$CH_2{=}CCH_2$, J = 7.2 Hz), 1.40 (dd, 4H, $CH_2{=}CCH_2CH_2$, J = 6.8 Hz), 1.26 (m, 56H, $CH_2{=}CCH_2CH_2\,(CH_2)_{14}$), 0.88 (t, 6H, CH_3, J = 7.2 Hz) ppm.

Synthesis of the primary bromides 13, 14, and 15:[31]

(**Alcohol synthesis**): A solution of the corresponding methylene (**10**, **11**, or **12**) in dry THF was treated dropwise with a 2.0 M solution of borane dimethyl sulfide in toluene at 0 °C. After 2 hours of stirring at 0 °C, the reaction mixture was warmed to room temperature, stirred for an additional 2.5 h, cooled to 0 °C, and neutralized with ethanol, 3.0 M NaOH (aq), and 35 % H_2O_2 (aq). After 30 min of stirring, the reaction mixture was warmed to room temperature and stirred overnight. The basic mixture was treated with 1 M HCl (aq), the organic layer was separated, and the aqueous layer was extracted with diethyl ether (3x). The combined organic phases were washed with brine (2x) and then dried over $MgSO_4$. The drying agent was filtered off and the filtrate was evaporated. The crude mixture was subjected to a flash silica column to obtain the corresponding methanol product.

5-Methanol-nonane

Methylene solution: **10** (0.40 g, 2.9 mmol) in THF (30 mL). Borane solution: 0.90 mL, 1.8 mmol. Neutralization solutions: ethanol (6 mL), aqueous 3.0 M NaOH (35 mL) and aqueous 35% H_2O_2 (35 mL). Eluent: *n*-pentane/diethyl ether, 9/1 (v/v). Yield = 0.32 g as a colourless liquid (2.0 mmol, 69%):

^{1}H-NMR (400 MHz, $CDCl_3$): δ 3.54 (t, 2H, $HOCH_2$, J = 5.6 Hz), 1.45 (m, 1H, $HOCH_2CH$), 1.38-1.22 (m, 12H, $HOCH_2\text{-}CHCH_2CH_2CH_2$), 1.18 (t, 1H, OH, J = 5.6 Hz), 0.90 (t, 6H, CH_3, J = 7.2 Hz) ppm.

^{13}C-NMR (75 MHz, $CDCl_3$) δ = 65.14, 40.00, 30.14, 28.62, 22.61, 13.57 ppm.

8-Methanol-pentadecane

Methylene solution: **11** (1.5 g, 6.7 mmol) in THF (50 mL). Borane solution: 2.3 mL, 4.6 mmol. Neutralization solutions: ethanol (12 mL), aqueous 3.0 M NaOH (75 mL) and aqueous 35% H_2O_2 (75 mL). Eluent: *n*-heptane/diethyl ether, 1/1 (v/v). Yield = 1.5 g as a white solid (6.2 mmol, 93%):

^{1}H-NMR (400 MHz, $CDCl_3$): δ 3.54 (m, 2H, $HOCH_2$), 1.45 (m, 1H, $HOCH_2CH$), 1.36–1.20 (m, 24H, $HOCH_2\text{-}CH(CH_2)_6$), 1.20 (s, 1H, OH), 0.88 (t, 6H, CH_3, J = 7.2 Hz) ppm.

18-Methanol-pentatriacontane

Methylene solution: **12** (1.3 g, 2.7 mmol) in THF (30 mL). Borane solution: 0.9 mL, 1.8 mmol). Neutralization solutions: ethanol (5 mL), aqueous 3.0 M NaOH (30 mL) and aqueous 35% H_2O_2 (30 mL). Eluent: *n*-heptane/diethyl ether, 1/1 (v/v). Yield = 1.0 g as a white solid (1.9 mmol, 72%):

^{1}H-NMR (400 MHz, $CD_3CN/CDCl_3$, 1/1 (v/v)): δ 3.43 (t, 2H, HOC*H₂*, J = 5.6 Hz), 2.18 (m, 1H, $HOCH_2$C*H*), 2.13-2.04 (m, $HOCH_2$-CHC*H₂*chain), 1.35−1.10 (m, CH_3C*H₂*chain), 1.25 (t, under methylC*H₂*chain, 1H, O*H*), 0.88 (t, 6H, C*H₃*, J = 7.2 Hz) ppm.

(**Bromination reaction**): To a suspension of triphenylphosphine dibromide in dry CH_2Cl_2 at 0 °C was added a solution of the corresponding methanol-alkane and pyridine in dry CH_2Cl_2. The reaction mixture was stirred at 0 °C for 15 min before being stirred for 1 hour at room temperature, and neutralized with 10% sodium bisulfite (aq). The organic layer was separated and the aqueous layer extracted with CH_2Cl_2 (2x) and diethyl ether (1x). The combined organic phases were dried over $MgSO_4$, filtered and then evaporated in the presence of an excess of silica to avoid the clogging of the column by the remaining organic salts. The product was purified on a flash silica column and the eluent was evaporated to obtain the corresponding primary bromide.

5-(Bromomethyl)-nonane (13)

The triphenylphosphine dibromide suspension was prepared from triphenylphosphine (0.55 g, 2.1 mmol) and bromine (0.11 mL, 2.1 mmol) in CH_2Cl_2 (9 mL). Methanol-alkane solution: 5-methanol-nonane (0.25 g, 1.6 mmol) and pyridine (0.40 mL, 5.0 mmol) in CH_2Cl_2 (2 mL). Eluent: *n*-pentane. Yield = 0.22 g as a colorless liquid (0.99 mmol, 62%):

^{1}H-NMR (400 MHz, $CDCl_3$): δ 3.45 (d, 2H, BrC*H₂*, J = 4.8 Hz), 1.60 (m, 1H, $BrCH_2$C*H*), 1.44−1.17 (m, 12H, C*H₂*), 0.91 (t, 6H, C*H₃*, J = 7.2 Hz) ppm.

8-(Bromomethyl)-pentadecane (14)

The triphenylphosphine dibromide suspension was prepared from triphenylphosphine (1.4 g, 5.4 mmol) and bromine (0.28 mL, 5.5 mmol) in CH_2Cl_2 (20 mL). Methanol-alkane solution: 8-methanol-pentadecane (1.0 g, 4.1 mmol) and pyridine (0.90 mL, 11 mmol) in CH_2Cl_2 (4 mL). Eluent: *n*-heptane. Yield = 1.0 g as a white solid (3.3 mmol, 80%):

^{1}H-NMR (400 MHz, $CDCl_3$): δ 3.45 (d, 2H, BrC*H₂*, J = 4.8 Hz), 1.59 (m, 1H, $BrCH_2$C*H*), 1.43−1.19 (m, 24H, C*H₂*), 0.89 (t, 6H, C*H₃*, J = 7.2 Hz) ppm.

18-(Bromomethyl)-pentatriacontane (15)

The triphenylphosphine dibromide suspension was prepared from triphenylphosphine (0.66 g, 2.5 mmol) and bromine (0.13 mL, 2.5 mmol) in CH_2Cl_2 (10 mL). Methanol-alkane solution: 18-methanol-pentatriacontane (1.0 g, 1.9 mmol) and pyridine (0.40 mL, 5.0 mmol) in CH_2Cl_2 (2 mL). Eluent: *n*-heptane. Yield = 0.90 g as a white solid (1.5 mmol, 79%):

^{1}H-NMR (400 MHz, $CDCl_3$) δ = 3.45 (d, 2H, BrC*H₂*, J = 4.8 Hz), 1.58 (m, 1H, $BrCH_2$C*H*), 1.43−1.19 (m, 24H, C*H₂*), 0.88 (t, 6H, C*H₃*, J = 7.2 Hz) ppm.

N-Adamantane-[4,4']-bipyridin-1-ium hexafluorophosphate (17)

This compound was synthesized according to a literature procedure:[32]

^{1}H-NMR (400 MHz, $CD_3CN/CDCl_3$, 1/1 (v/v)): δ 9.04 (d, 2H, Bipy*H*, J = 6.8 Hz), 8.85 (d, 2H, Bipy*H*, J = 6.4 Hz), 8.33 (d, 2H, Bipy*H*, J = 6.4 Hz), 7.82 (d, 2H, Bipy*H*, J = 6.4 Hz), 2.39 (m, 3H, adamantaneC*H*), 2.32 (m, 6H, amantaneC*H₂*), 1.84 (m, 6H, adamantaneC*H₂*) ppm.

Half viologen 16

Bromide **15** (450 mg, 0.77 mmol) and 4,4'-bipyridine (1.4 g, 9.4 mmol) were dissolved in dry MeCN (20 mL) and the mixture was gently refluxed for 7 d under an argon atmosphere. After cooling to room temperature, the mixture was precipitated from diethyl ether (2x), toluene (2x) and then dried in vacuo to obtain **16** as a white solid in a yield of 300 mg (0.41 mmol, 53%). In addition to **16**, also $C_{34}H_{69}$ and $C_{32}H_{65}$ alkyl substitution products, which must be the result of impurities in the commercially available ketone, were found to be present in the product:

^{1}H-NMR (400 MHz, $CDCl_3$): δ 9.39 (d, 2H, Bipy*H*, J = 6.8 Hz), 8.88 (d, 2H, Bipy*H*, J = 6.0 Hz), 8.36 (d, 2H, Bipy*H*, J = 7.2 Hz), 7.71 (d, 2H, Bipy*H*, J = 6.0 Hz), 4.87 (d, 2H, NCH_2, J = 7.6 Hz), 2.06 (m, 1H, C*H*), 1.44-1.16 (m, 64H, CH_2), 0.88 (t, 6H, CH_3, J = 6.8 Hz) ppm.

^{13}C-NMR (75 MHz, $CDCl_3$): δ 153.24, 151.02, 145.47, 140.27, 125.08, 120.95, 65.23, 40.01, 31.44, 29.97, 29.22, 25.58, 22.20, 13.63 ppm.

Maldi-TOF MS (*m/z*): 661.50 (M), 633.46 (M R-$C_{34}H_{69}$), 605.43 (M R- $C_{32}H_{65}$).

General synthesis of viologen derivatives V1, V2, V3, V5, and V6:

In a 25 mL flask equipped with a septum, a solution of **2** and primary bromide (**3**, **4**, **5**, **6**, **13**, or **14**) in DMF was stirred for 3 d at 95 °C. After cooling, diethyl ether was added and the precipitate was removed by filtration and washed with diethyl ether (20 mL). The resulting solid was dissolved in acetone (2 mL) followed by the addition of an excess of NH_4PF_6 (s) before the resulting product was precipitated by the addition of water (10 mL). The precipitate was filtered off, washed with water (40 mL) followed by diethyl ether (10 mL), and then dried to obtain the corresponding viologen.

V1

Bromide solution: **3** (182 mg, 0.36 mmol) and **2** (540 mg, 3.6 mmol) in DMF (2 mL). Yield = 1.9 g as a white solid (2.4 mmol, 67%):

^{1}H-NMR (400 MHz, $CD_3CN/CDCl_3$, 1/1 (v:v)): δ 8.93 (d, 2H, Bipy*H*, J = 6.8 Hz), 8.91 (d, 2H, Bipy*H*, J = 6.8 Hz), 8.40 (m, 4H, Bipy*H*), 7.02 (s, 1H, Ar*H*), 6.73 (d, 2H, ortho-Ar*H*, J = 0.8 Hz), 4.67 (t, 2H, NCH_2, J = 7.6 Hz), 4.62 (t, 2H, NCH_2, J = 7.2 Hz), 4.00 (t, 2H, OCH_2, J = 6.4 Hz), 2.14 (dd, 2H, CH_2, J = 8 Hz), 2.04 (dd, 2H, CH_2, J = 7 Hz), 1.86 (dd, 2H, Ar-OCH_2-CH_2, J = 7.6 Hz), 1.61 (dd, 2H, CH_2, J = 7.2 Hz), 1.40 (m, 4H, CH_2) 1.30 (s, 18H, CH_3), 0.93 (t, 3H, CH_3, J = 6.8 Hz) ppm.

^{13}C-NMR (75 MHz, $CD_3CN/CDCl_3$, 1:1 (v:v)): δ 158.17, 151.71, 149.44, 149.38, 145.10, 126.82, 114.34, 108.35, 66.60, 61.84, 61.73, 34.33, 30.62, 30.43, 30.34, 28.11, 27.29, 22.10, 21.38, 12.94 ppm.

Maldi-TOF MS (*m/z*): 502.43 (M−2PF_6).

V2

Bromide solution: **2** (91 mg, 0.18 mmol) and **4** (26 mg, 0.19 mmol) in DMF (1 mL). Yield = 20 mg as a white solid (0.026 mmol, 14%):

^{1}H-NMR (400 MHz, $CD_3CN/CDCl_3$, 1/1 (v/v)): δ 8.93 (d, 2H, Bipy*H*, J = 6.4 Hz), 8.87 (d, 2H, Bipy*H*, J = 6.4 Hz), 8.40 (m, 4H, Bipy*H*), 7.02 (s, 1H, para-Ar*H*), 6.73 (d, 2H, ortho-Ar*H*, J = 1.2 Hz), 4.67 (t, 2H, NCH_2, J = 7.2 Hz), 4.47 (d, 2H, NCH_2, J = 7.2 Hz), 4.00 (t, 2H, OCH_2, J = 6.4 Hz), 2.32 (m, 1H, C*H*), 2.15 (m, under water peak, 2H, C*H*$_2$), 1.86 (dd, 2H, C*H*$_2$, J = 7.6 Hz), 1.61 (dd, 2H, C*H*$_2$, J = 7.2 Hz), 1.30 (s, 18H, C*H*$_3$), 1.02 (d, 6H, C*H*$_3$, J = 6.4 Hz) ppm.

^{13}C-NMR (75 MHz, CD$_3$CN/CDCl$_3$, 1/1 (v/v)): δ 158.18, 151.74, 145.19, 145.13, 126.82, 126.79, 114.37, 108.32, 67.94, 66.59, 61.68, 34.29, 30.51, 28.08, 22.09, 18.04 ppm.

Maldi-TOF MS (*m/z*): 488.18 (M−2PF$_6$).

V3

Bromide solution: **2** (91 mg, 0.18 mmol) and **5** (33 mg, 0.19 mmol) in DMF (1 mL). Yield = 50 mg as a white solid (0.061 mmol, 34%):

^{1}H-NMR (400 MHz, CD$_3$CN/CDCl$_3$, 1/1 (v:v)): δ 8.94 (d, 2H, Bipy*H*, J = 7.2 Hz), 8.85 (d, 2H, Bipy*H*, J = 7.2 Hz), 8.42 (d, 2H, Bipy*H*, J = 3.6 Hz), 8.41 (d, 2H, Bipy*H*, J = 3.2 Hz), 7.02 (t, 1H, para-Ar*H*, J = 1.6 Hz), 6.73 (d, 2H, ortho-Ar*H*, J = 1.6 Hz), 4.67 (t, 2H, NC*H*$_2$, J = 7.6 Hz), 4.48 (d, 2H, NC*H*$_2$, J = 7.6 Hz), 4.00 (t, 2H, OC*H*$_2$, J = 6.4 Hz), 2.12 (dd, 2H, C*H*$_2$, J = 7.6 Hz), 2.00 (m, 1H, C*H*), 1.86 (dd, 2H, C*H*$_2$, J = 7.6 Hz), 1.78 (m, 2H), 1.71 (m, 1H), 1.64 (m, 2H), 1.61 (m, 2H, C*H*$_2$), 1.30 (s, 18H, C*H*$_3$), 1.26 (m, 3H), 1.13 (m, 2H) ppm.

^{13}C-NMR (75 MHz, CD$_3$CN/CDCl$_3$, 1/1 (v/v)): δ 158.15, 151.72, 149.42, 145.13, 126.83, 126.72, 114.35, 108.32, 67.11, 66.57, 61.72, 39.04, 34.33, 30.61, 30.45, 28.94, 28.11, 25.19, 24.72, 22.12 ppm.

Maldi-TOF MS (*m/z*): 528.21 (M−2PF$_6$).

V5

Bromide solution: **2** (91 mg, 0.18 mmol) and **13** (220 mg, 1.0 mmol) in DMF (1 mL). Yield = 17 mg as a white solid (0.020 mmol, 11%):

^{1}H-NMR (400 MHz, CD$_3$CN/CDCl$_3$, 1/1 (v/v)): δ 8.95 (d, 2H, Bipy*H*, J = 6 Hz), 8.88 (d, 2H, Bipy*H*, J = 6.4 Hz), 8.45 (m, 4H, Bipy*H*), 7.01 (s, 1H, para-Ar*H*), 6.73 (d, 2H, ortho-Ar*H*, J = 1.2 Hz), 4.68 (t, 2H, NC*H*$_2$, J = 7.6 Hz), 4.53 (d, 2H, NC*H*$_2$, J = 7.2 Hz), 4.00 (t, 2H, OC*H*$_2$, J = 6.4 Hz), 2.15 (m, under water peak, 2H, C*H*$_2$), 2.08 (m, 1H, C*H*), 1.86 (dd, 2H, C*H*$_2$, J = 7.6 Hz), 1.62 (dd, 2H, C*H*$_2$, J = 7.2 Hz), 1.40-1.20 (m, 12H, C*H*$_2$), 1.30 (s, 18H, C*H*$_3$), 0.90 (t, 6H, C*H*$_3$, J = 6.8 Hz) ppm.

^{13}C-NMR (75 MHz, CD$_3$CN/CDCl$_3$, 1/1 (v/v)): δ 158.15, 151.70, 149.51, 149.35, 145.33, 145.11, 126.86, 126.76, 114.34, 108.34, 66.59, 65.45, 61.77, 39.51, 34.35, 30.67, 30.45, 29.33, 28.13, 27.38, 22.16, 13.18 ppm.

Maldi-TOF MS (*m/z*): 572.10 (M−2PF$_6$).

V6

Bromide solution: **2** (91 mg, 0.18 mmol) and **14** (520 mg, 1.7 mmol) in DMF (1 mL). Yield = 33 mg as a white solid (0.035 mmol, 19%):

^{1}H-NMR (400 MHz, CD$_3$CN/CDCl$_3$, 1/1 (v/v)): δ 8.95 (d, 2H, Bipy*H*, J = 5.6 Hz), 8.86 (d, 2H, Bipy*H*, J = 6 Hz), 8.45 (bs, 4H, Bipy*H*), 7.02 (s, 1H, para-Ar*H*), 6.73 (s, 2H, ortho-Ar*H*), 4.68 (t, 2H, NC*H*$_2$, J = 7.6 Hz), 4.51 (d, 2H, NC*H*$_2$, J = 7.6 Hz), 4.00 (t, 2H, OC*H*$_2$, J = 6 Hz), 2.14 (m, 2H, C*H*$_2$), 2.08 (m, under water peak, 1H, C*H*), 1.86 (dd, 2H, C*H*$_2$, J = 6.8 Hz), 1.63 (dd, 2H, C*H*$_2$, J = 7.2 Hz), 1.45-1.15 (m, 24H, C*H*$_2$), 1.30 (s, 18H, C*H*$_3$), 0.88 (t, 6H, C*H*$_3$, J = 6.8 Hz) ppm.

^{13}C-NMR (75 MHz, $CD_3CN/CDCl_3$, 1/1 (v/v)): δ 151.73, 145.33, 145.12, 126.89, 126.77, 114.39, 108.29, 66.53, 65.54, 61.90, 61.82, 39.64, 34.37, 31.19, 30.72, 30.50, 29.66, 29.07, 28.56, 28.14, 25.28, 22.04, 13.40 ppm.
Maldi-TOF MS (*m/z*): 656.18 ($M-2PF_6$).

Viologen derivative V4.
In a 25 mL flask equipped with a septum, a solution of **1** (53 mg, 0.15 mmol) and **17** (50 mg, 0.11 mmol) in DMF (1 mL) was stirred for 4 d at 90 °C. After cooling, diethyl ether was added and the precipitate was filtered off and washed with diethyl ether (20 mL). The resulting solid was mixed with acetone (2 mL) followed by the addition of an excess of NH_4PF_6 (s). The product was precipitated by the addition of water (10 mL). The precipitate was filtered off, washed with 40 mL of water followed by diethyl ether (10 mL) and then dried to obtain **V4** in a yield of 11 mg as a white solid (0.013 mmol, 12%):
^{1}H-NMR (400 MHz, $CD_3CN/CDCl_3$, 1:1 (v:v)): δ 9.18 (d, 2H, Bipy*H*, J = 6.8 Hz), 8.93 (d, 2H, Bipy*H*, J = 6.4 Hz), 8.43 (m, 4H, Bipy*H*), 7.02 (s, 1H, para-Ar*H*), 6.73 (s, 2H, ortho-Ar*H*), 4.67 (t, 2H, NCH_2, J = 7.6 Hz), 4.00 (t, 2H, OCH_2, J = 6.4 Hz), 2.43 (m, 3H, C*H*), 2.34 (m, 6H, CH_2), 2.15 (m, under water peak, 2H, CH_2), 1.86 (m, under adamantane proton peaks, 2H, CH_2), 1.85 (m, 6H, CH_2), 1.61 (dd, 2H, CH_2, J = 7.2 Hz), 1.30 (s, 18H, CH_3) ppm.
^{13}C-NMR (75 MHz, $CD_3CN/CDCl_3$, 1/1 (v/v)): δ 151.73, 148.90, 145.09, 142.07, 126.85, 126.48, 114.39, 108.30, 66.58, 61.72, 41.51, 34.21, 30.60, 29.68, 28.11, 22.15 ppm.
Maldi-TOF MS (*m/z*): 566.30 ($M-2PF_6$).

Viologen derivative V7
In a 25 mL flask equipped with a septum, a solution containing **1** (1.4 g, 4.0 mmol) and **16** (250 mg, 0.34 mmol) in DMF (4 mL) was stirred for 6 d at 90 °C. After cooling, diethyl ether was added and the precipitate was removed by filtration and washed with diethyl ether (20 mL) and toluene (20 mL). The resulting solid was mixed with 2 mL of acetone followed by the addition of an excess of NH_4PF_6 (s) after which the product was precipitated by the addition water (10 mL). The precipitate was filtered, washed with water (40 mL) followed by diethyl ether (10 mL) and then dried to obtain 306 mg of **V7** as a white solid (0.25 mmol, 73%):
^{1}H-NMR (400 MHz, $CD_3CN/CDCl_3$, 1/1 (v/v)): δ 8.95 (d, 2H, Bipy*H*, J = 6.8 Hz), 8.86 (d, 2H, Bipy*H*, J = 6.8 Hz), 8.42 (t, 4H, Bipy*H*, J = 6.4 Hz), 7.02 (t, 1H, para-Ar*H*, J = 1.6 Hz), 6.73 (d, 2H, ortho-Ar*H*, J = 1.6 Hz), 4.68 (t, 2H, NCH_2, J = 7.6 Hz), 4.51 (d, 2H, NCH_2, J = 7.6 Hz), 4.00 (t, 2H, OCH_2, J = 6 Hz), 2.11 (m, under water peak, 2H, CH_2), 2.04 (m, under water peak, 1H, C*H*), 1.86 (dd, 2H, CH_2, J = 7.2 Hz), 1.62 (dd, 2H, CH_2, J = 7.2 Hz), 1.45-1.15 (m, 64H, CH_2), 1.30 (s, 18H, CH_3), 0.88 (t, 6H, CH_3, J = 6.8 Hz) ppm.
^{13}C-NMR (75 MHz, $CD_3CN/CDCl_3$, 1/1 (v/v)): δ 158.14, 151.73, 149.44, 149.29, 145.34, 145.13, 126.84, 126.74, 114.37, 108.31, 66.57, 65.45, 61.74, 39.54, 34.33, 31.31, 30.61, 29.54, 29.07, 28.11, 25.19, 22.08, 13.34 ppm.
Maldi-TOF MS (*m/z*): 936.65 ($M-2PF_6$), R-$C_{34}H_{69}$: 908.60 ($M-2PF_6$), R-$C_{32}H_{65}$: 880.54 ($M-2PF_6$)

Viologen derivative V8.

In a 25 mL flask equipped with a septum, a solution of **2** (44 mg, 0.087 mmol) and ~62 mg of **6** (0.092 mmol) in DMF (1 mL) (108 mg of the mixture containing **6** and the elimination product of **6**) was stirred for 3 d at 95 ^{o}C. After cooling, diethyl ether was added and a gel was formed; the gel was sonicated and the solvents were evaporated. The crude product was dissolved in MeCN, precipitated with diethyl ether, the precipitate was filtered off and then washed with diethyl ether (20 mL). The resulting solid was suspended with acetone (2 mL) followed by the addition of an excess of NH_4PF_6 (s). The product was precipitated by the addition of water (10 mL). The white precipitate was filtered, washed with water (40 mL) followed by diethyl ether (10 mL) and then dried to obtain **V8** in a yield of 8 mg (0.0085 mmol, 9.8%):

^{1}H-NMR (400 MHz, $CD_3CN/CDCl_3$, 1/1 (v/v)): δ 8.94 (bd, 4H, Bipy*H*), 8.40 (bd, 4H, Bipy*H*), 7.02 (s, 1H, para-Ar*H*), 6.73 (d, 2H, ortho-Ar*H*, J = 1.6 Hz), 4.75 (t, 2H, NCH_2, J = 6.8 Hz), 4.68 (t, 2H, NCH_2, J = 7.2 Hz), 4.00 (t, 2H, OCH_2, J = 5.6 Hz), 3.53 (t, 2H, cyclododecaneOCH_2, J = 5.6 Hz), 3.37 (m, 1H, C*H*), 2.27 (dd, 2H, CH_2, J = 5.6 Hz), 2.12 (m, under water peak, 2H, CH_2), 1.87 (dd, 2H, CH_2, J = 7.6 Hz), 1.63 (m, 2H, CH_2), 1.30 (s, 18H, CH_3), 1.28-1.36 (m, 22H, cyclododecane$(CH_2)_{11}$) ppm.

6. Literature

1. Coumans, R. G. E.; Elemans, J. A. A. W.; Nolte, R. J. E.; Rowan, A. E. *Proc. Natl Acad. Sci. USA* **2006**, *103*, 19647–19651.
2. Hidalgo Ramos, P. ; Coumans, R. G. E.; Deutman, A. B. C.; Smits, Jan. M. M.; de Gelder, R.; Elemans, J. A. A. W.; Nolte, R. J. M.; Rowan, A. E. *J. Am. Chem. Soc.* **2007**, *129*, 5699–5702.
3. Turro, N. J.; Okubo, T.; Chung, C.-J. *J. Am. Chem. Soc.* **1982**, *104*, 1789–1794.
4. Ko, Y. H.; Kim, H.; Kim, Y.; Kim, K. *Angew. Chem. Int. Ed.* **2008**, *47*, 4106–4109.
5. Trembleau, L.; Rebek Jr., J. *Science* **2003**, *301*, 1219–1220.
6. Scarso, A.; Trembleau, L.; Rebek Jr., J. *Angew. Chem. Int. Ed.* **2003**, *42*, 5499–5502.
7. Scarso, A.; Trembleau, L.; Rebek Jr., J. *J. Am. Chem. Soc.* **2004**, *126*, 13512–13518.
8. Scramm, M. P.; Rebek Jr., J. *Chem. Eur. J.* **2006**, *12*, 5924–5933.
9. Purse, B. W.; Rebek Jr., J. *Proc. Natl. Acad. Sci. USA* **2006**, 103, 2530–2534.
10. Rebek Jr., J. *Chem. Commun.* **2007**, 2777–2789.
11. Harrison, I. T. *J. Chem. Soc., Chem. Commun.* **1972**, 231–232.
12. Harrison, I. T. *J. Chem. Soc., Perkin Trans.1* **1974**, 301–302.
13. Schill, G.; Beckmann, W.; Schweickert, N.; Fritz, H. *Chem. Ber.* **1986**, *119*, 2647–2655.
14. G. Agam, D. Graiver, A. Zilkha, *J. Am. Chem. Soc.* **1976**, *98*, 5206–5216.
15. Ashton, P. R.; Belohradsky, M.; Philp, D.; Stoddart, J. F. *J. Chem. Soc., Chem. Commun.* **1993**, 1269–1274.
16. Ashton, P. R.; Ballardini, R.; Balzani, V.; Belohradsky, M.; Gandolfi, M. T.; Philp, D.; Prodi, L.; Raymo, F. M.; Reddington, M. V.; Spencer, N.; Stoddart, J. F.; Venturi, M.; Williams, D. J. *J. Am. Chem. Soc.* **1996**, *118*, 4931–4951.
17. Macartney, D. H. *J. Chem. Soc., Perkin Trans. 2* **1996**, 2775–2778.

18. Händel, M.; Plevots, M.; Gestermann, S.; Vögtle, F. *Angew. Chem.* **1997***, 109*, 1248, *Angew. Chem. Int. Ed. Engl.* **1997**, *36,* 1199–1201.
19. Raymo, F. M.; Houk, K. N.; Stoddart, J. F. *J. Am. Chem. Soc.* **1998**, *120*, 9318–9322.
20. Ashton, P. R.; Baxter, I.; Fyfe, M. C. T.; Raymo, F. M.; Spencer, N.; Stoddart, J. F.; White, A. J. P.; Williams, D. J. *J. Am. Chem. Soc.* **1998**, *120*, 2297–2307.
21. Hübner, G. M.; Nachtsheim, G.; Li, Q. Y.; Seel, C.; Vögtle, F. *Angew. Chem. Int. Ed.* **2000***, 39,* 1269–1272.
22. Sohgawa, Y. H.; Fujimori, H.; Shoji, J.; Furusho, Y.; Kihara, N.; Takata, T. *Chem. Lett.* **2001**, *8*, 774–775.
23. Affeld, A.; Hübner, G. M.; Seel, C.; Schalley, C.A. *Eur. J. Org. Chem.* **2001**, 2877–2890.
24. Linnartz, P.; Bitter, S.; Schalley, C. A. *Eur. J. Org. Chem.* **2003**, 4819–4829.
25. Vignon, S.A.; Jarrosson, T.; Iijima, T.; Tseng, H.-R.; Sanders, J. K. M.; Stoddart, J. F. *J. Am. Chem. Soc.* **2004**, *126*, 9884–9885.
26. Murakami, H.; Kawabuchi, A.; Matsumoto, R.; Ido, T.; Nakashima, N. *J. Am. Chem. Soc.* **2005**, *127*, 15891–15899.
27. Tokunaga, Y.; Wakamatsu, N.; Ohbayashi, A.; Akasaka, K.; Saeki, S.; Hisada, K.; Goda, T.; Shimomura, Y. *Tetrahedron Lett.* **2006**, *47*, 2679–2682.
28. Monk, P. M. S, The Viologens: Physicochemical properties, Synthesis and applications of the salts of 4,4'-bipyridine. *John Wiley & Sons Ltd* **1999**. ISBN 0470866411 (0-470-86641-1).
29. Del Pozo, C.; I. Keller, A.; Nagashima, T.; P. Curran, D. *Org. Lett.* **2007**, *9*, 4167–4170.
30. Courillon, C.; Marie, J-C.; Malacria, M. *Tetrahedron* **2003**, *59*, 9759–9766.
31. L. Ornstein, P.; K. Augenstein, N.; Brian Arnold, M. *J. Org. Chem* **1994**, *59*, 7862–7869.
32. Woon Park, J.; Eun Song, H.; Yeon Lee, S. *J. Phys. Chem. B* **2002**, *106*, 7186–7192.
33. Asakawa, M.; Ashton, P. R.; Ballardini, R.; Balzani, V.; Belohradsky, M.; Gandolfi, M. T.; Kocian, O.; Prodi, L.; Raymo, F. M.; Stoddart, J. F.; Venturi, M. *J. Am. Chem. Soc.* **1997**, *119*, 302–310.
34. Chapters 4 and 8 in this thesis.
35. Elemans, J. A. A. W.; Claase, M. B.; Aarts, P. P. M.; Rowan, A. E.; Schenning, A. P. H. J.; Nolte, R. J. M. *J. Org. Chem.* **1999**, *64*, 7009–7016.
36. Elemans, J. A. A. W.; Bijsterveld, E. J. A.; Rowan, A. E.; Nolte, R. J. M. *Eur. J. Org. Chem.* **2007**, 751–757.

6

The Threading Model

1. Introduction

In previous papers[1,2] a method has been described for studying the process of threading polymers through macrocyclic porphyrin receptors. Polymers that are blocked on one side with a di-*tert*-butylphenyl group and have, in close proximity to this blocking group, a trap for the porphyrin, viz. a viologen moiety, which has a high affinity for the receptor were synthesized (Chart 1). The porphyrin receptor can only reach the viologen trap by binding to the open end of the polymer and subsequently fully traversing the chain (Figure 1). The threading process can be followed by recording the fluorescence emission spectra of the porphyrin, which is quenched when it has reached the viologen trap. From the first studies,[1] in which the porphyrin receptor **$H_2$1** and polymers of different lengths (**P3**, **P5**, and **P7**; Chart 1) were used, three conclusions were drawn: (i) threading is a length-dependent process; it takes more time to traverse longer polymers; (ii) the kinetics of the threading-on and threading-off processes are second and first order, respectively, and the relationship $K_{\text{assoc}} = k_{\text{on}}/k_{\text{off}}$ is obeyed. The polymeric chain can thus be seen as one single energy barrier that has to be crossed and this barrier becomes higher with increasing polymer

Chart 1

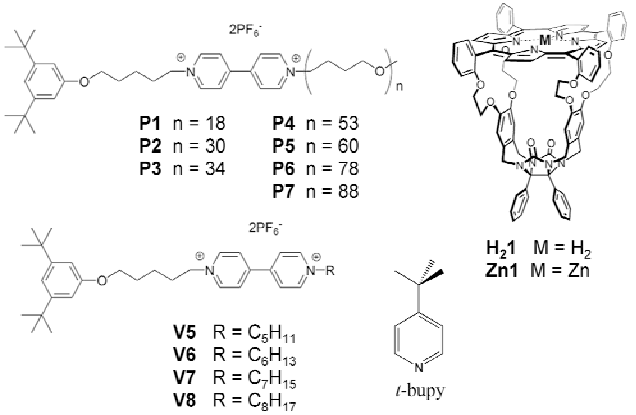

P1 n = 18
P2 n = 30
P3 n = 34
P4 n = 53
P5 n = 60
P6 n = 78
P7 n = 88

V5 R = C_5H_{11}
V6 R = C_6H_{13}
V7 R = C_7H_{15}
V8 R = C_8H_{17}

t-bupy

$H_2$1 M = H_2
Zn1 M = Zn

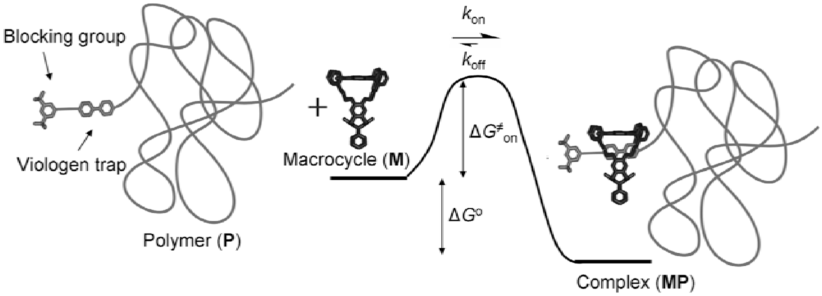

Figure 1. Energy diagram of the overall threading and de-threading process.

length (Figures 1 and 3b); (iii) the length dependency of the threading process is entropic of origin, i.e. the Eyring plots of the different polymers clearly show that the value of $\Delta S^{\neq}_{on}$ becomes more negative upon increasing polymer length, whereas the value of $\Delta H^{\neq}_{on}$ remains constant (Table 1). A second study[2] showed that the presence of a zinc ion in the porphyrin (**Zn1)** has significant effects on the observed threading rates. These rates were lower than those observed for free base derivative **H$_2$1** and could either be increased by the addition of bulky pyridines, which coordinate to the outside of **Zn1**, or decreased by the addition of pyridine, which blocks the cavity (analogous to the mechanisms described in Chapters 3 and 4). The movement along the polymer chain, however, appeared to be unaffected by the insertion of a zinc ion in the porphyrin receptor or the addition of axial ligands, since the decrease in rate constant versus polymer length showed parallel evolutions in all cases (Figure 3). This strongly suggests that the observed differences in rate constants are the result of differences in the initial process of binding **H$_2$1** and **Zn1** to the polymer, whereas the movement along the polymer is apparently unaffected. In order to gain a better understanding of the experimental observations, a simple model has been developed that describes the threading process as a consecutive hopping process. Although it is most probably an oversimplification of the situation, it will be shown that this model actually describes the experimental observations with high accuracy.

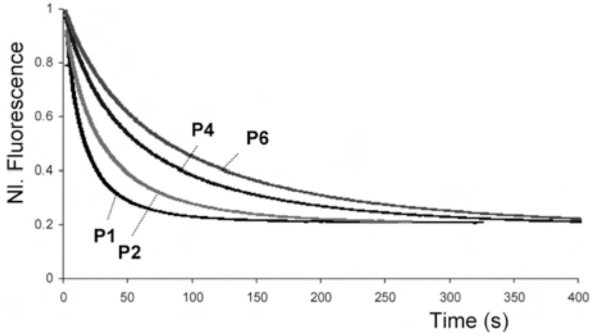

Figure 2. Fluorescence threading curves of a selection of polymers, which clearly reveal the length dependency of the process.

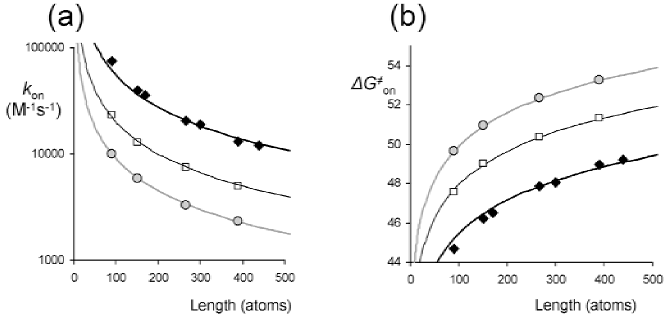

Figure 3. (a) Rate constants (k_{on}) and (b) free energies of activation ($\Delta G^{\neq}_{on}$) for the threading of **$H_2$1**(◆), **Zn1**(●), and **Zn1** in the presence of ***t*-bupy** (□) plotted versus polymer chain length and the fits with Equation 1.

2. Results and Discussion

2.1 A consecutive hopping model

If we have a detailed look at the threading process, it is surprising that the overall threading-on of the macrocycle onto the polymer is a second order process because once the macrocycle has found the open end of the polymer, the rest of the threading process should involve a sequence of first order events. It is not clear what the exact contributions to the threading process of finding the open end of the polymer chain and movement along the polymer are as the quenching of the porphyrin fluorescence emission occurs only after these consecutive events. One can envisage that many possible mechanisms are involved in the observed length dependency of the threading process, including polymer solvation, chain entanglements, end-group availability, or effects of stretching of the open chain ends. The simplest way of describing the threading process is by envisaging a so called 'consecutive hopping model' (Figure 4).[3] After finding the open end of the polymer (P), upon which the macrocycle (M) has to overcome an initial barrier ($\Delta G^{\neq}_{\text{initial}}$), it finds a first local energy minimum on the chain (C_1) with a corresponding binding free energy ($\Delta G^{o}_{\text{polymer}}$). After this initial binding event, the macrocycle can move further along the polymer. This process of movement is proposed to be a consecutive hopping process in which the macrocycle hops randomly from one local energy minimum to the other (C_2, C_3…C_n) and thereby surmounts small energy barriers. The hopping over each of these barriers is a first order process with a rate constant k_{hop} and an energy barrier $\Delta G^{\neq}_{\text{hop}}$. The number of local energy minima on the polymer chain (n) depends linearly on its length. If it is assumed that the motion of the macrocycle along the chain is independent of its position on the chain, and that (consequently) all the energy states of the local energy minima ($\Delta G^{o}_{\text{polymer}}$) are equal, the energy diagram becomes as simple as presented in Figure 4. After traversing the polymer (P_1–P_n), the macrocycle finally reaches the energy sink when it forms a complex with the viologen (V) with a binding free energy $\Delta G^{o}_{\text{viologen}}$.

The macrocycle can of course dissociate back, off the viologen and onto the chain again with a rate constant $k_{\text{V-off}}$.

Table 1. Rate constants (k_{on}) for the threading of **$H_2$1**, **Zn1**, and **Zn1** in the presence of ***t*-bupy** over the chains of the different viologen derivatives and the enthalpic and entropic contributions to the activation energy for the threading of **$H_2$1** over a selection of the chains.[a]

		k_{on}[b] ($M^{-1}s^{-1}$)			$\Delta H^{\neq}_{\text{on}}$[c] ($kJ \cdot mol^{-1}$)	$\Delta S^{\neq}_{\text{on}}$[d] ($J \cdot mol^{-1}K^{-1}$)
Guest	Length (atoms)	**$H_2$1**	**Zn1**	**Zn1+*t*-bupy**	**$H_2$1**	
V5	5	5.0×10^6	8.1×10^5	3.8×10^6	15	–67
V6	6	2.4×10^6	3.2×10^5	1.6×10^6	22	–50
V7	7	1.5×10^6	1.7×10^5	1.1×10^6	21	–56
V8	8	1.3×10^6	1.4×10^5	8.9×10^5	19	–65
P1	90	7.5×10^4	1.0×10^4	2.3×10^4	[e]	[e]
P2	150	4.0×10^4	5.9×10^3	1.3×10^4	[e]	[e]
P3	170	3.6×10^4	[e]	[e]	20	–88
P4	266	2.1×10^4	3.3×10^3	7.4×10^3	[e]	[e]
P5	300	1.9×10^4	[e]	[e]	20	–94
P6	390	1.3×10^4	2.3×10^3	5.0×10^3	[e]	[e]
P7	440	1.2×10^4	[e]	[e]	21	–97

[a] Determined by fluorescence spectroscopy in a 1/1 (v/v) mixture of acetonitrile and chloroform at 295 K. [b] Estimated error 25%. [c] Estimated error 4 $kJ \cdot mol^{-1}$. [d] Estimated error 8 $J \cdot mol^{-1}K^{-1}$. [e] Not determined.

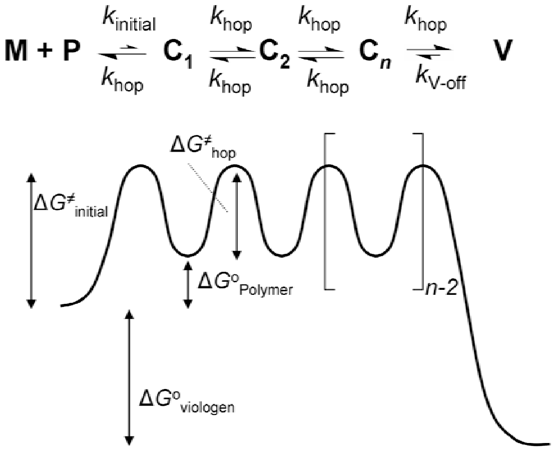

Figure 4. Energy diagram of the threading model with the rate constants and energy levels of all the individual processes.

One of the important experimental observations was the absence of complex formation between unfunctionalized polybutadienes or polytetrahydrofuranes and macrocycles of type **1**. This indicates that the macrocycles have very little affinity for the polymer chain itself. As a result, the value $\Delta G^{o}_{\text{polymer}}$ can be supposed to be positive (unfavorable) and therefore $k_{\text{initial}} < k_{\text{hop}}$. The concentration of macrocycle present on the chain will therefore be at all times very low and consequently also the variation of this concentration in the threading process will be very low. These are exactly the requirements to treat the presented model with the Bodenstein steady state approximation.[4] As a consequence, the observed overall threading rates $k_{\text{on-overall}}$ and $k_{\text{off-overall}}$ will be second and first order, respectively (as experimentally observed). Moreover, it can be derived that these rates evolve as a function of chain length (n) according to Equations 1 and 2.

$$k_{\text{on-overall}} = \frac{k_{\text{initial}}}{n+1} \tag{1}$$

$$k_{\text{off-overall}} = \frac{k_{\text{V-off}}}{n+1} \tag{2}$$

The overall rate constants depend solely on the rate of initial binding to the polymer chain (k_{initial} and $k_{\text{V-off}}$) and on the number of local energy minima on the chain (n), not on the magnitude of k_{hop}. This implies that the speed of movement along the chain (which is directly related to k_{hop}) is not expressed in the overall threading rates and therefore, that the complicated dynamics involved with translocation of polymers through the macrocycle[5-13] can be ignored. The factor $1/(n+1)$ simply describes the probability of reaching the other end of the chain after the initial binding event. It highlights that, in order to arrive at the viologen trap, the macrocycle statistically needs to bind twice as often to the open end of the chain upon each doubling in the length of the polymer.

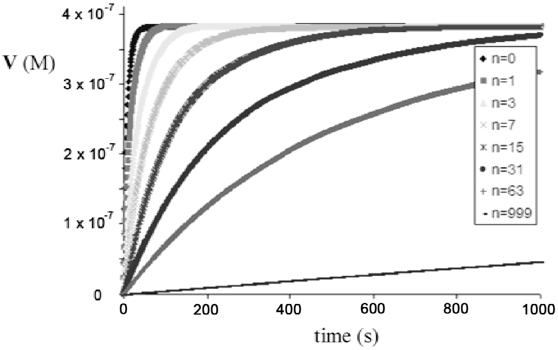

Figure 5. A selection of simulated threading curves in which complex formation between the macrocycle and a binding site after the traversing of *n* local energy minima. These clearly display the length dependency of the process.

In order to verify the above derivations, the presented model was programmed in Mathematica® and threading simulations were performed in which the concentrations of macrocycle (H) and polymer (P) and the values of k_{initial}, k_{hop}, $k_{\text{V-off}}$, and n were varied (the concentrations of H and P were kept below 2 µm, in line with the actual threading experiments). The simulated threading curves (some are presented in Figure 5) indeed revealed the predicted second order threading-on and first order threading-off kinetics that evolved with n according to Equations 1 and 2. As long as $\Delta G^{o}_{\text{polymer}}$ was kept positive ($k_{\text{initial}}/k_{\text{hop}} = K_{\text{polymer}} < 1$) and the difference between $\Delta G^{o}_{\text{polymer}}$ and $\Delta G^{o}_{\text{viologen}}$ was considerable (> 25 kJ·mol^{-1}), these relations were obeyed, up to values of $n \approx 1000$. Only by increasing the affinity for the polymer, the simulated threading curves could be seen to deviate from perfect second order-on and first order-off behavior and consequently could no longer be fitted according to 1:1 binding kinetics (the precise conditions will be discussed in more detail in Section 2.4).

As can be seen in Figure 3, the consecutive hopping model describes the experimentally obtained data with high accuracy. The experimentally observed threading rates as a function of chain length evolve nicely in accordance with Equation 1, independent of the presence of a zinc ion in the porphyrin macrocycle or the subsequent addition of coordinating pyridine axial ligands. These observations allow the drawing of a number of important conclusions concerning the threading process:
(i) The observed different threading rates for macrocycles **H$_2$1** and **Zn1** (in the presence or absence of coordinating pyridine ligands) are solely a result of differences in the initial binding event, not a result of differences in speed of motion along the chain.
(ii) The speeds of motion along the chain (polymer translocation) are presumably different for each individual macrocycle. The experimentally obtained curves, however, do not contain any information about this speed since the overall rates are independent of the magnitude of the hopping steps k_{hop}. The events on the chain are, for all the macrocycles, simply a lot faster than the initial binding event and the observed overall threading rates are therefore dominated by the initial binding event and the chance that such an initial binding also results in the complete traversing of the chain.
(iii) The fact that the length dependency evolves according to Equation 1 reveals that the magnitude of k_{initial} is independent of polymer length. Typical polymer behavior, like entanglements, solvation, and end-group availability, therefore does not contribute to the observed rates or has equal contributions for all polymers.

2.2 Implications of the consecutive hopping model for the Eyring plot analysis

Clearly, the experimentally observed length dependency of the threading rates is a result of an initial binding event (k_{initial}) and the chance that this initial binding event leads to the complete traversing of the chain ($1/(n+1)$). This has important consequences for the values of the activation entropy ($\Delta S^{\neq}_{\text{on}}$) and activation enthalpy ($\Delta H^{\neq}_{\text{on}}$), which are obtained by performing Eyring plots of the threading rates at different temperatures. The initial binding event (k_{initial}) has, of course, its inherent activation entropy ($\Delta S^{\neq}_{\text{initial}}$) and activation enthalpy ($\Delta H^{\neq}_{\text{initial}}$). The statistical factor $1/(n+1)$, on the other hand, is independent of temperature and will therefore only regard the activation entropy $\Delta S^{\neq}$. This can be demonstrated analytically by substituting Equation 1 into the Eyring equation (eq. 3).

$$\ln\frac{k_{\text{on-overall}}}{T}=\frac{-\Delta H^{\neq}}{R}\cdot\frac{1}{T}+\ln\frac{k_B}{h}+\frac{\Delta S^{\neq}}{R}\tag{3}$$

$$\ln\frac{\left(\dfrac{k_{\text{initial}}}{n+1}\right)}{T}=\frac{-\Delta H^{\neq}}{R}\cdot\frac{1}{T}+\ln\frac{k_B}{h}+\frac{\Delta S^{\neq}}{R}\tag{4}$$

Since:

$$\ln\left(\frac{k_{\text{initial}}}{n+1}\right)=\ln(k_{\text{initial}})-\ln(n+1):$$

$$\ln\frac{k_{\text{on-overall}}}{T}=\ln\frac{k_{\text{initial}}}{T}-\ln(n+1)\tag{5}$$

and hence:

$$\ln\frac{k_{\text{on-overall}}}{T}=\frac{-\Delta H^{\neq}_{\text{initial}}}{R}\cdot\frac{1}{T}+\ln\frac{k_B}{h}+\frac{\Delta S^{\neq}_{\text{initial}}}{R}-\ln(n+1)\tag{6}$$

An Eyring plot ($\ln\frac{k_{\text{on-overall}}}{T}$ *vs*. 1/*T*) will therefore have a slope of $\frac{-\Delta H^{\neq}_{\text{initial}}}{R}$ and an intercept of $\ln\frac{k_B}{h}+\frac{\Delta S^{\neq}_{\text{initial}}}{R}-\ln(n+1)$. As a result, the calculated activation enthalpy $\Delta H^{\neq}_{\text{overall}}$ is equal to the activation enthalpy of the initial binding event and remains unaffected upon the changing of the chain length. The calculated activation entropy $\Delta S^{\neq}_{\text{overall}}$ decreases (becomes more negative) upon increasing the chain length and evolves according to Equation 7.

$$\Delta S^{\neq}_{\text{overall}}=\Delta S^{\neq}_{\text{initial}}-R\ln(n+1)\tag{7}$$

The experimentally calculated values $\Delta S^{\neq}_{\text{on}}$ and $\Delta H^{\neq}_{\text{on}}$ for the threading of **H₂1** indeed revealed that $\Delta H^{\neq}_{\text{on}}$ remains constant, whereas $\Delta S^{\neq}_{\text{on}}$ becomes more negative (by a value of approximately –*R*ln(*n*+1), independent of the chosen magnitude of *n* upon lengthening the chain; Table 1 entries **P3**, **P5**, and **P7**). This observation therefore further supports the consecutive hopping model and all the subsequently drawn conclusions. The decrease in $\Delta S^{\neq}_{\text{on}}$ upon the lengthening of the chain is thus a result of the statistical factor 1/(*n*+1), which is independent of the temperature. This is in contrast to the earlier drawn conclusion that the observed decrease in activation entropy was presumably a penalty associated with length dependent differences in the stretching of the open end of the polymer chain.[1]

2.3 The entron effect

The model presented in the previous sections provides an excellent explanation for the experimentally observed length dependency for the threading of the macrocycles over the polymer chains (**P1–P7**). Although it is clear that the overall threading rate drops by a factor of two upon each doubling of the polymer chain length (since 1/(*n*+1) ≈ 1/*n* as *n* becomes considerably large), it does not contain any information about the number of local energy minima (steady state intermediates) n or about the actual magnitude of the initial binding rate k_{initial} because any differently chosen magnitude of n (for instance: atom, picometer, or monomer length) will also provide a different value for k_{initial}. To get insight into the actual magnitudes of these values it was decided to study the threading of the macrocycles onto viologens equipped with short alkyl chains (**V5**–**V8** Chart 1).

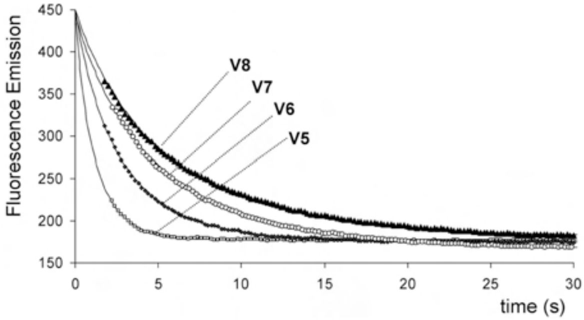

Figure 6. Fluorescence emission in time upon the addition of one equivalent of viologen derivatives **V5**–**V8** to **Zn1** (1 μM) in a 1/1 (v/v) mixture of chloroform and acetonitrile.

Fluorescence binding studies of **H$_2$1**, **Zn1**, and **Zn1** in the presence of a large excess of *t*-bupy with viologen derivatives **V5**–**V8** were performed (Figure 6) and the obtained curves were analyzed. The rate constants are presented in Table 1. All association constants were similar to those obtained in earlier studies (Chapter 4). The threading over the shorter chains is, as expected, significantly faster than the threading over the polymer chains. As observed for the polymers, the obtained rate constants in the series **V5**–**V8** decrease upon increasing the chain length. The length dependency of the threading rates over the short chains, however, is clearly different from that observed for the polymer chains. Instead of a length dependency according to Equation 1 (with slope of −1 in the log-log plot; Figure 7), the relative decrease in rate constant upon each additional atom in the chain is significantly higher (slope < −1). The observed rate constants for the threading over a chain of six atoms is consistently more than a factor 2 lower than for the threading over a chain of five atoms (Table 1 entries **V5**, **V6**). Independent of the chosen magnitude of n, Equation 1 can therefore never describe the observed length dependency. We propose that this deviation of the model is a result of a so called 'entron effect'. Both experimental[14] and theoretical[15] studies revealed that the filling of pores or channels with the initial part of polymer chains is relatively fast (kinetically easy) compared to the subsequent movement of the polymer through the channel. In the present system, the filling of the cavity of the macrocycle with the initial atoms of the polymer chain should therefore also be kinetically easier than its subsequent translocation through the cavity. It is impossible to predict the precise thermodynamic energy path of the filling of the cavity with the first few atoms. In the process of filling the cavity, however, it will always be kinetically easier to thread the chain out of the cavity than to further fill the cavity (Figure 8). The filling of the cavity will therefore always be a

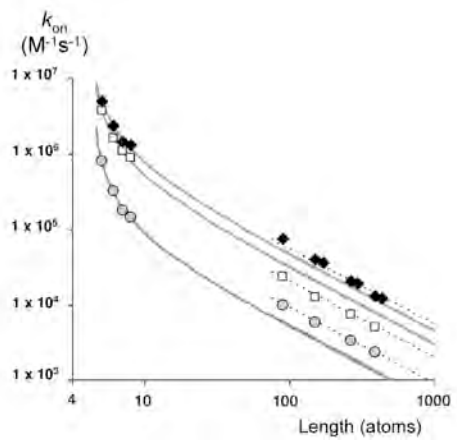

Figure 7. Log-log plot of threading rate constant k_{on} versus oliogomer and polymer chain length for **H₂1** (◆), **Zn1** (○), and **Zn1** in the presence of ***t*-bupy** (□).

kinetically uphill process, independent of the thermodynamic profile (compare Figures 8a and 8b). The highest free-hopping activation energy is therefore only reached at the moment that the cavity is fully filled with the chain. Molecular modeling revealed that approximately five main chain atoms are required to fill the dimensions of the cavities of **H₂1** and **Zn1**. This results in an entron effect, in which the filling of the cavity with these first five atoms should have an overall kinetic barrier that is roughly as large as the barrier associated with the movement over the sixth atom. The effect can be simply introduced into the consecutive hopping model by adding one overall energy minimum that describes the binding to the entron (Figure 8). The number of chain atoms involved in the entron is x and the threading onto the entron has a second order rate constant k_{entron}, whereas the threading off the entron has a first order rate constant $k_{\text{entron-off}}$. All the other hopping steps that describe the subsequent movement along the chain have a rate constant k_{hop}. The overall threading rate using this model was determined with the help of the steady state approximation and is given by Equation 8.

$$k_{\text{on-overall}} = \frac{k_{\text{entron}}}{\frac{k_{\text{entron-off}}}{k_{\text{hop}}}(n-x)+1} \qquad (8)$$

The length dependencies of the short chain viologens (**V5–V8**) can indeed be perfectly fitted with Equation 8 (see Figure 7). Either by fixing $k_{\text{entron-off}}/k_{\text{hop}}$ at 1 (and so defining the approximate length of the entron x) or by fixing x at 5 (hence determining the relative rate of traversing the sixth atom compared to the first five atoms) very good fits are obtained. The data in Table 2 clearly reveal that in all the studied macrocycles the length of the entron is approximately five atoms, which is fully in line with the dimensions of the cavity. Moreover, in the case of **H₂1**, the fit nearly describes the threading over the polymer derivatives that contain oxygen atoms (Figure 7), which indicates that the initial binding to the entron has similar rates for both the alkyl- and the poly-THF chains. For **Zn1** and **Zn1** in the presence of *t*-bupy, the fit clearly deviates from the polymer threading rates, which is most likely a result of significant interactions between the zinc ion and the oxygen atoms in the polymer chains.

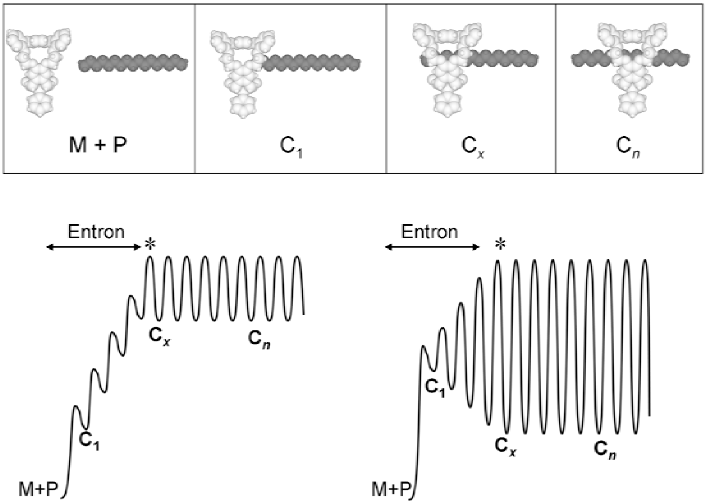

Figure 8. Energy diagrams of the threading of a macrocycle onto the initial atoms of a chain revealing the entron effect. M+P: chain and macrocycle free in solution. C_1: The first chain atom threads the cavity. C_x: The entire cavity is filled with chain atoms. C_n: The macrocycle has threaded further along the chain. Left diagram; the filling of the chain inside the cavity is thermodynamically unfavorable. Right diagram: After the binding of the first atom, the rest of the filling of the cavity is thermodynamically favorable. Independent of the exact energy profile, these two diagrams will result in equal overall threading rate constants when concerning the studied system. In both diagrams, the first overall-rate determining intermediate is only reached when the cavity is fully filled with the chain.

Table 2. Calculated values for x, $k_{\text{entron-off}}/k_{\text{hop}}$, and k_{entron} as obtained by curve fitting with Equation 8 and the reduced Chi-squared values to illustrate that equal fits are obtained independent of varying x or $k_{\text{entron-off}}/k_{\text{hop}}$.

Macrocycle	*no.* atoms (x)	$k_{\text{entron-off}}/k_{\text{hop}}$	k_{entron} ($M^{-1}s^{-1}$)	red Chi squared
H$_2$1	5 [a]	1.1	5.0×10^6	1.2×10^{10}
	5.1	1 [a]	4.5×10^6	1.2×10^{10}
Zn1	5 [a]	1.6	8.1×10^5	2.3×10^8
	5.4	1 [a]	5.0×10^5	2.3×10^8
Zn1 + **t-bupy**	5 [a]	1.2	3.8×10^6	5.7×10^9
	5.2	1 [a]	3.0×10^6	5.7×10^9

[a] Values were fixed in the calculations.

2.4 Theoretical investigations about the speed of translocation

The discussion in the previous section suggests that the observed chain length dependency of threading totally originates from the rate of initial binding of the entron and the chance that this binding event also results in the complete movement along the polymer chain. Although the relative rates can be calculated, the absolute magnitudes of k_{hop} and $k_{\text{entron-off}}$ are unknown and it is therefore impossible to derive any quantitative values for the speed of motion along the chain. In order to get a feeling for the speed of movement along the chain, in relation to the relative magnitudes of k_{hop} and the number of steady state intermediates n, it was decided to further evaluate the consecutive hopping model. The two important events in the threading process − the initial binding to the open end of the chain and the movement along the chain − will be treated separately and expressed in terms of half-life times ($t_{1/2}$) to better appreciate the relative magnitudes of these processes.

The initial binding of the macrocycle to the open end of the chain is, of course, a second order process. Consequently, the observed rates depend upon the concentrations of the macrocycle and the polymer present in solution. The time it takes for half of the concentration of macrocycles to bind to the open end of the polymer chain ($t_{1/2\text{-entron}}$) is given by Equation 9.

$$t_{1/2\text{-entron}} \approx 1/(k_{\text{entron}}\cdot[\text{P}]_{\text{o}}) \qquad (9)$$

It is clear that at higher concentrations of polymer (or macrocycle), the half-life $t_{1/2\text{-entron}}$ decreases. The chance that the initial binding event results in the complete movement along the chain (chance of arrival: *ca*) depends on the number of steady state intermediates n (Equation 10).

$$ca = 1/(n+1) \qquad (10)$$

The movement along the chain in the presented model is described as a series of consecutive hopping steps. In principle, this movement resembles a simple one-dimensional random walk, which is, of course, an oversimplification of the actual translocation process. Many theoretical studies have been undertaken on the translocation of polymers through pores,[5–13] most of them involving complicated Monte Carlo computer simulations that focus on aspects of polymer dynamics and interactions within the pores, but also external stimuli. Although in combination these studies are far from conclusive, they revealed that the mean translocation time t is a function of polymer length N ($t \propto N^{\alpha}$, with α ranging from 2 to 2.6). To determine to what extent the presented consecutive hopping model deviates from the far more sophisticated Monte Carlo computer simulations in terms of translocation times, some computer simulations regarding the consecutive hopping process were performed using the computer program Mathematica®. A consecutive hopping model according to the energy profile in Figure 9a was programmed that allows a concentration of macrocycle (M) to arrive in an infinitely deep well (W) after a number (n) of consecutive hopping steps. Translocation simulations were performed in which the hopping rate constant (k_{hop}) and the chain length (n) were varied (since it is a sequence of first-order steps the chosen concentration M has no effect on the obtained half-lives). Some of the threading simulations are presented in Figure 9b, and these show that the arrival time decreases as the length of the chain increases. The obtained sigmoid curves could not be fitted with the help of any simplified overall rate equation. The arrival time of half the concentration of macrocycle in the well ($t_{1/2\text{-translocation}}$) was plotted against chain length, from which an overall formula that closely describes this arrival time was empirically derived (Equation 11).

$$t_{1/2-\text{translocation}} = \frac{\ln(2)}{k_{\text{hop}}} n^{\alpha} \text{ in which } \alpha = 1.6755 + 0.0383\cdot\ln(n) \qquad (11)$$

Assuming values of n up to 1000, α only varies from 1.68 to 1.71 and the general relationship $t_{1/2\text{-translocation}} \propto n^{1.7}$ is therefore obtained from the consecutive hopping model. The evolution of arrival time against chain length is thus similar to the Monte Carlo simulation studies (with $t \propto N^{\alpha}$), but the factor α is significantly smaller. As a result, the arrival time, as obtained by the consecutive hopping model will start to deviate from the more reliable Monte Carlo studies significantly with increasing values of n. This could be expressed in $t_{1/2\text{-translocation}}$ values that are almost two orders of magnitude lower than the mean arrival time values predicted by the Monte Carlo simulation studies. In fact, according to the consecutive hopping model, the movement of a polymer through the pore is faster than that of a free polymer, which has an (experimentally derived)[16,17] relaxation time of $\sim t \propto N^{2.18}$. The fact that translocating polymer chains (without external stimuli) can simply not move faster than the free polymers strongly suggests that the consecutive hopping model fails to accurately describe the translocation process.

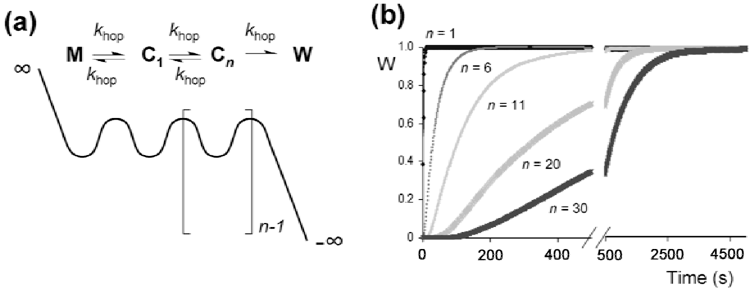

Figure 9. (a) Energy diagram in which a macrocycle (M) falls into an infinitely deep well (W) after randomly traversing a number (n) of local energy minima. (b) Simulated translocation curves of a macrocycle threading over a chain according to the energy diagram in Figure 9a in which the hopping steps all have magnitude $k_{\text{hop}} = 0.5\ \text{s}^{-1}$, W represents the normalized concentration of macrocycle that reaches the well.

The consecutive hopping model can however be utilized to gain a more general insight into what types of threading curves can be expected in future studies. These studies can be focused, for instance, on the threading over significantly longer polymers or on macrocycles that have a higher affinity for the polymer chain.

First the evolution of half-lives $t_{1/2\text{-translocation}}$ with changing values of n and k_{hop} will be studied. The values will then be compared with the half-lifes $t_{1/2\text{-entron}}$ that can be calculated from the k_{entron} values and the known experimental polymer concentration $[\mathbf{P}]_o$ following Equations 9 and 11. As long as $k_{\text{entron}} < k_{\text{hop}}$, the macrocycle has an association constant for a local energy minimum on the polymer (K_{Polymer}) which is smaller than 1 M^{-1} and the binding to the polymer chain is therefore unfavorable. For values of n up to 1000 the data in Table 3 show that $t_{1/2\text{-entron}}$ is significantly larger than $t_{1/2\text{-translocation}}$ when $K_{\text{Polymer}} < 1\ \text{M}^{-1}$. The translocation is therefore significantly faster than the initial binding event. As a result, the overall threading curves will depend solely on the (overall-rate determining) rate of initial binding and the chance that this initial binding results in the full traversing of the chain (*ca*), according to Equations 1 or 8. The situation becomes more interesting when the macrocycle has an actual affinity for the polymer chain ($K_{\text{Polymer}} = k_{\text{hop}}/k_{\text{entron}} > 1$). Depending on the values of k_{hop} and n, $t_{1/2\text{-translocation}}$ is now of the same order of magnitude as, or even higher than $t_{1/2\text{-entron}}$. In this case, the translocation process can also be expected to play a significant role in the observed overall threading curves. A number of threading simulations were performed to investigate how the overall threading curves evolve when the affinity of the macrocycle for the polymer chain increases (Figure 10).

Table 3. Calculated half-lives for the initial binding event ($t_{1/2\text{-entron}}$) and the translocation process ($t_{1/2\text{-translocation}}$) as a function of the number of local energy minima (n) and the rate constant of the hopping steps (k_{hop}).

	k_{entron} ($\text{M}^{-1}\text{s}^{-1}$)	k_{hop} (s^{-1})					
	5×10^{6}	1×10^{7}	1×10^{6}	1×10^{5}	1×10^{4}	1×10^{3}	1×10^{2}
N	$t_{1/2\text{-entron}}$ (s)	$t_{1/2\text{-translocation}}$ (s)					
67	0.2	9×10^{-5}	9×10^{-4}	9×10^{-3}	9×10^{-2}	**0.9**	**8.5**
125	0.2	2×10^{-4}	2×10^{-3}	2×10^{-2}	**0.2**	**2.5**	**25**
250	0.2	8×10^{-4}	8×10^{-3}	8×10^{-2}	**0.8**	**8.1**	**81**
500	0.2	3×10^{-3}	3×10^{-2}	**0.3**	**2.7**	**27**	**267**
1000	0.2	9×10^{-3}	8×10^{-2}	**0.9**	**8.8**	**88**	**884**

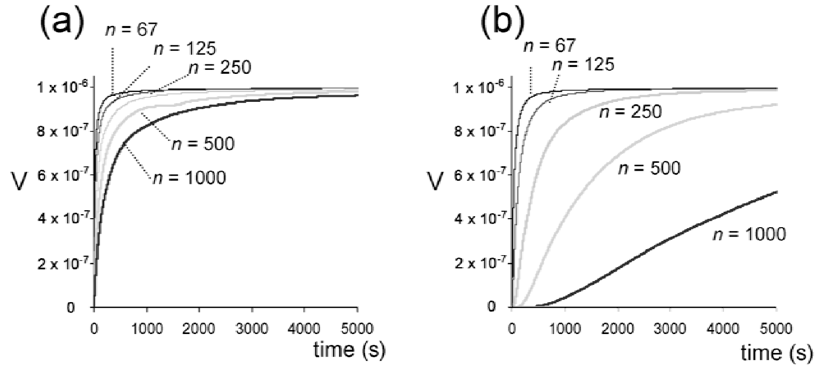

Figure 10. Simulated threading curves revealing the evolution of the macrocycle on the viologen binding trap (V) in time after traversing a chain containing n local energy minima. (a) Situation in which there is little affinity of the macrocycle for the chain ($k_{\text{entron}} = 5 \times 10^{6}\ \text{M}^{-1}\text{s}^{-1}$, $k_{\text{hop}} = 1 \times 10^{7}\ \text{s}^{-1}$). b) Situation in which the macrocycle has strong affinity for the chain ($k_{\text{entron}} = 5 \times 10^{6}\ \text{M}^{-1}\text{s}^{-1}$, $k_{\text{hop}} = 1 \times 10^{2}\ \text{s}^{-1}$).

The simulations show that when the affinity for the polymer chain increases (lower k_{hop}), upon an increase in n, the curves start to slowly deviate from the curves in which there is low affinity for the polymer chain. The translocation becomes slowly apparent in the overall threading curves, which is expressed in slower evolution of the complex formation, but also in the appearance of sigmoid curve shapes. By comparing the simulated curves and the values of $t_{1/2\text{-entron}}$ and $t_{1/2\text{-translocation}}$ (Table 3), it can be seen that the deviations start to become apparent once both half-lives are of the same order of magnitude. They are expressed to larger extents when $t_{1/2\text{-translocation}}$ becomes larger than $t_{1/2\text{-entron}}$, which is a logical consequence of the fact that the slowest process is rate determining. When the half-lives have equal magnitudes, both will contribute to the observed overall threading curve. There are a number of important conclusions that can be drawn with regards to the experimentally obtained threading curves when the translocation process becomes apparent in the overall threading process:

(i) The threading curves slowly become sigmoidal and show an initial delay before fluorescence quenching is observed. As a result, the overall threading curves can no longer be fitted to 1:1 binding kinetics and the threading-on is no longer purely second order; neither is the de-threading first order. Given that the initial delay lies within the initial part of the curves, which is in most cases during the experimental mixing time, these deviations from perfect 1:1 binding kinetics might not be directly apparent experimentally. The fact that a single threading experiment does not concern one chain of discrete length but a distribution of chains with many different lengths might also hide the appearance of the sigmoidal shapes. Thus, the experimenter may well mistake such a sigmoidal threading-on isotherm for a second order isotherm and hence obtain an incorrect value for the overall rate constant.

(ii) At different experimental concentrations, different threading rate constants will be calculated. At increasing polymer concentrations, the half-life time $t_{1/2\text{-entron}}$ will decrease, whereas $t_{1/2\text{-translocation}}$ remains constant because it is overall first-order and therefore concentration independent. As a result, the deviations from the 1:1 binding kinetics will be expressed more at higher polymer concentration.

(iii) An increasing affinity of the macrocycle for the chain will also start to influence the observed association equilibrium constant for the viologen moiety. The binding to the chain competes with the binding to the viologen and it can therefore be expected that an increase in chain length would result in less binding to the latter (hence less fluorescence quenching and lower apparent association equilibrium constants). Another important consequence is that this will also result in the formation of polyrotaxane species in which several macrocycles are threaded onto a single chain,[18–22] which would dramatically complicate the consecutive hopping model.

(iv) The calculated length dependency (whether or not analyzed with the right kinetic isotherms) will start deviating from Equations 1 or 8 (Figure 11). The experimental rates will become lower as a function of n. A general equation for the observed length dependency is therefore as given in Equation 12, in which f is an additional factor larger than 1 that depends on n and the affinity of the macrocycle for the polymer.

$$k_{\text{on-overall}} \approx \frac{k_{\text{initial}}}{(n+1)*f} \tag{12}$$

In other words, the experimental length dependency should at least reveal a halving in the observed rate constant upon the doubling of polymer chain length, but upon increasing polymer affinity and/or increasing chain length this value experiences more than a halving upon each doubling in length.

(v) When the translocation process starts to significantly influence the overall threading process, this will have dramatic consequences for the calculated parameters of activation entropy and enthalpy in the Eyring plot analyses. As mentioned, when the overall threading curve is solely determined by the initial binding event and the factor 1/(n+1) (which is temperature independent), the increase in the activation energy of threading upon lengthening the chain will involve only a change in activation entropy. When the translocation process starts playing a role, this will no longer be the case since it will definitely be temperature dependent. How the different parameters will be expressed in the overall activation enthalpy and entropy is unclear and will depend on the mechanisms of polymer translocation.

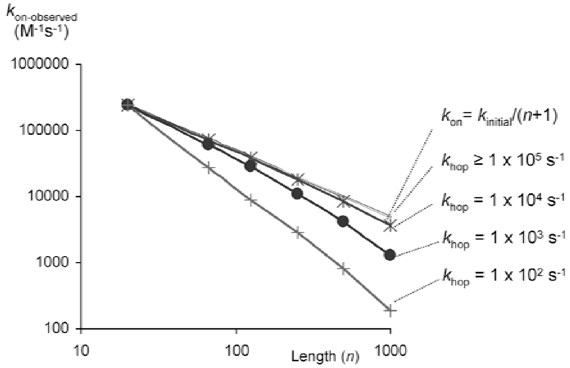

Figure 11. Log-log plot of rate constant *vs*. chain length (n), revealing that as the affinity for the chain increases (and hence the rate constant k_{hop} decreases) the observed length dependency starts to deviate significantly from the length dependency according to Equation 1.

3. Conclusion

The consecutive hopping model provides a very satisfying description for the experimental threading process, which is purely the result of the little affinity of the macrocycles for the polymer chains. The experimentally obtained rates depend solely on the initial binding event and the chain length dependent chance of the falling off of the macrocycle at the other end of the chain. In order to traverse a longer chain, there are simply more initial binding events needed. Such events can be nicely described with the help of a kinetically favorable entron effect involving the filling of the cavity with the initial atoms of the chain. The observation that the initial binding event is independent on the length of the polymer strongly suggests that polymer entanglements play no significant role in the studied system. Quite cynically, the experiments concerning the threading over the polymer chains have therefore only provided quantitative information about the initial binding event and not about the translocation process. The translocation speed of the chains through the cavity therefore remains unsolved. The only grounded statement that can be made is that, independent of the polymer length, the translocation process is faster than the initial binding event. Based on theoretical investigations, however, a minimal mean translocation speed (MTS) can be carefully estimated. For this it is necessary to make two consecutive assumptions: the first is that the macrocycle has little affinity for the chain and that k_{hop} is therefore as large as, or larger than k_{entron}. The second is that each local energy barrier involves the traversing of a single carbon-carbon or a carbon-oxygen bond in the chain. In that case the value n simply becomes the number of chain-atoms N. The mean translocation time $t_{1/2\text{-translocation}}$ can now be calculated with the use of Equation 11 in which α is estimated to be 2.3 (a rough estimation based on the literature values). The mean translocation times and the subsequently calculated values of the mean translocation speeds (MTS) are given in Table 4.

Table 4. Calculated translocation half-lives ($t_{1/2\text{-translocation}}$) and mean translocation speeds (MTS) for the traversing of the chain by the macrocycle.

N	length (nm)	$t_{1/2\text{-translocation}}$ (s)	MTS (nm/s)
62.5	8	9.4×10^{-3}	8.3×10^{2}
125	16	4.6×10^{-2}	3.4×10^{2}
250	31	2.3×10^{-1}	1.4×10^{2}
500	62	1.2	5.5×10^{1}

The calculated mean translocation speeds are in the order of tens to hundreds of nm per second. The values decrease upon the lengthening the chain, which is of course not the result of slower translocation speeds, but of the random walk of the macrocycle along the chain. The calculated values are the minimum ones and it is likely that the actual speed is even orders of magnitude higher. An increase in k_{hop} with a factor will result in an increase in MTS with the same factor. Considering that the value of k_{hop} might have values of up to 1×10^{8} s^{-1} (two orders of magnitude higher than assumed in the calculations), the MTS values might also be two orders of magnitude higher (up to tens of micrometers per second). By comparing these values with the estimated translocation speeds of previous reports[1,23] of 1 $pm \cdot s^{-1}$ and 750 $pm \cdot s^{-1}$, it is clear that those studies have severely underestimated the speed of the translocation process. The question whether the catalytic process of oxidizing the double bonds of a polybutadiene by the manganese variant of **$H_2$1** is sequentially processive or randomly processive (i.e., does the catalyst convert every double bond it encounters, or does it, every now and then, perform a catalytic action while moving along the polymer chain) is therefore presumably answered in favor of the latter (although a real comparison between this system and the catalytically manganese-receptor/polybutadiene system can of course not be made). Considering that the catalytic process displays turnover numbers of the order of only 300 per hour (1.4×10^{-3} s^{-1}), one might even ask whether the catalytic process is even processive (does the catalyst perform multiple catalytic actions while remaining bound to the polymer substrate). In order to obtain a synthetic catalyst that is capable of performing catalysis in a sequentially processive fashion, the rate of motion of the catalyst and the catalytic rate have to balance. This requires the slowing down of the translocation process and/or the acceleration of the catalytic reaction. To slow down the speed of motion, the catalyst should have a high affinity for the chain.

In that case, the rate of dissociation from one polymer fragment onto the next fragment of the chain, which is determined by the interactions between the catalyst and the chain, will determine the translocation speed. The catalytic activity of manganese porphyrins is nowhere near the activities observed in processive enzymatic systems such as the replisome (1000 nucleotide insertions per second). Improving the catalytic rates of the synthetic catalysts to the extent that they are able to keep up with the speeds of brownian motion-induced translocation would require years of extensive research.

4. Experimental Section

Materials and methods. All syntheses were carried out under an inert nitrogen or argon atmosphere. Chloroform and acetonitrile used in titration experiments were distilled from $CaCl_2$. All other solvents and chemicals were commercial materials and used as received. Merck silica gel (60H) was used for column chromatography and Merck silica gel F254 plates were used for thin layer chromatography (TLC) and preparative TLC. Molecular modeling calculations were performed with the use of Spartan. Fluorescence experiments were performed on a Perkin-Elmer LS50B luminescent spectrometer equipped with a thermostatted cuvette holder. Maldi-TOF MS was performed on a Bruker Biflex III spectrometer. NMR spectra were taken on a Varian Inova 400 (400 MHz, ^{1}H and 2D spectra) or on a Bruker DMX300 (75 MHz, ^{13}C spectra) and calibrated to an internal standard of tetramethylsilane. Abbreviations used are s, singlet; d, doublet; t, triplet; dd, double doublet; m, multiplet. Macrocycles **$H_2$1** and **Zn1** were synthesized according to literature procedures.

Synthesis of Alkyl substituted viologens (V5, V6, V7, and V8)

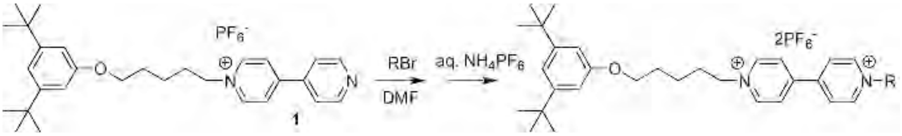

A solution of mono-alkylated hexafluorophosphate bipyridinium salt **1**[1] (250 mg, 0.43 mmole) and an excess of the selected 1-bromo-alkane (>10 equiv.) in DMF (5 mL) was stirred at 100°C for 10–80 h. After cooling, diethyl ether was added and the precipitate was filtered off and dissolved in a mixture of water and a minimal amount of acetone. After the addition of an aqueous saturated NH_4PF_6 solution the product precipitated as a white solid, which was filtered off and dried.

V5 (65 mg, 19%)

^{1}H-NMR (400 MHz, $CDCl_3/CD_3CN$ 1/1 (v/v)): δ 8.93 (dd, 4H, J = 7.4), 8.40 (bs, 4H), 7.03 (s, 1H), 6.73 (s, 2H), 4.67 (t, 2H, J = 7.7 Hz), 4.62 (t, 2H, J = 7.6 Hz), 4.00 (t, 2H, J = 6.1 Hz),

2.15−2.10 (m, 2H), 2.10−2.00 (m, 2H), 1.90−1.82 (m, 2H), 1.65−1.59 (m, 2H), 1.43−1.37 (m, 4H), 1.30 (s, 18H), 0.94 (t, 3H, J = 6.6 Hz) ppm.
^{13}C-NMR (75 MHz, $CDCl_3/CD_3CN$ 1/1 (v/v)): δ 157.80, 151.34, 149.07, 149.01, 144.72, 126.44, 113.97, 107.98, 66.22, 61.47, 61.36, 33.96, 30.25, 30.06, 29.97, 27.74, 26.92, 21.73, 21.01, 12.57 ppm.
MALDI-TOF: *m/z*: 502.64 $(M-2PF_6)^+$.

V6 (130 mg, 37%)
^{1}H-NMR (400 MHz, $CDCl_3/CD_3CN$ 1/1 (v/v)): δ 8.93 (d, 2H, J = 6.8 Hz), 8.91 (d, 2H, J = 6.9 Hz), 8.40 (t, 4H, J = 5.4 Hz), 7.03 (s, 1H), 6.73 (s, 2H), 4.65 (t, 2H, J = 7.6 Hz), 4.62 (t, 2H, J = 7.6 Hz), 4.00 (t, 2H, J = 6.2 Hz), 2.15−2.10 (m, 2H), 2.10−2.00 (m, 2H), 1.89−1.82 (m, 2H), 1.65−1.57 (m, 2H), 1.42−1.33 (m, 4H), 1.30 (s, 20H), 0.91 (t, 3H, J = 6.7 Hz) ppm.
^{13}C-NMR (75 MHz, $CDCl_3/CD_3CN$ 1/1 (v/v)): δ 157.79, 151.33, 149.05, 148.99, 144.72, 126.43, 113.96, 107.96, 66.21, 61.47, 61.34, 33.94, 30.23, 30.05, 30.00, 27.73, 24.53, 21.72, 21.32, 12.71 ppm.
MALDI-TOF: *m/z*: 516.45 $(M-2PF_6)^+$.

V7 (76 mg, 21%)
^{1}H-NMR (400 MHz, $CDCl_3/CD_3CN$ 1/1 (v/v)): δ 8.94 (d, 2H, J = 6.7 Hz), 8.91 (d, 2H, J = 7.0 Hz), 8.41 (bs, 4H), 7.02 (s, 1H), 6.73 (s, 2H), 4.67 (t, 2H, J = 7.6 Hz), 4.62 (t, 2H, J = 7.6 Hz), 4.00 (t, 2H, J = 6.2 Hz), 2.15−2.11 (m, 2H), 2.06−2.00 (m, 2H), 1.89−1.82 (m, 2H), 1.66−1.57 (m, 2H), 1.43−1.34 (m, 4H), 1.30 (bs, 22H), 0.90 (t, 3H, J = 6.3 Hz) ppm.
^{13}C-NMR (75 MHz, $CDCl_3/CD_3CN$ 1/1 (v/v)): δ 157.78, 151.35, 149.01, 144.72, 126.42, 113.98, 107.94, 66.20, 61.46, 61.33, 33.93, 30.46, 30.29, 30.20, 30.07, 27.72, 27.54, 24.82, 21.73, 21.48, 12.82 ppm.
MALDI-TOF: *m/z*: 530.50 $(M-2PF_6)^+$.

V8 (45 mg, 12%)
^{1}H-NMR (400 MHz, $CDCl_3/CD_3CN$ 1/1 (v/v)): δ 8.94 (d, 2H, J = 6.5 Hz), 8.91 (d, 2H, J = 6.6 Hz), 8.41 (bs, 4H), 7.02 (s, 1H), 6.73 (s, 2H), 4.67 (t, 2H, J = 7.6 Hz), 4.62 (t, 2H, J = 7.5 Hz), 4.00 (t, 2H, J = 6.0 Hz), 2.15−2.10 (m, 2H), 2.06−2.00 (m, 2H), 1.89−1.84 (m, 2H), 1.65−1.59 (m, 2H), 1.42−1.37 (m, 4H), 1.30 (bs, 24H), 0.89 (t, 3H, J = 5.9 Hz) ppm.
^{13}C-NMR (75 MHz, $CDCl_3/CD_3CN$ 1:1 (v/v)): δ 157.79, 151.34, 149.02, 144.72, 126.42, 113.96, 107.95, 66.21, 61.47, 61.33, 33.94, 30.67, 30.22, 30.06, 27.96, 27.84, 27.73, 24.88, 21.73, 21.59, 12.88 ppm.
MALDI-TOF: *m/z*: 544.52 $(M-2PF_6)^+$.

Synthesis of polymer-appended viologens P1, P2, P4 and P6.
The polymers were synthesized according to a literature procedure:[1] to a flame-dried Schlenk vessel under an argon atmosphere, freshly distilled THF (20 mL) was added at room temperature.

To initiate the polymerization, MeOTf (28 µL, 0.25 mmol) was added by syringe and the mixture was stirred for *x* minutes, after which **1** (150 mg, 0.26 mmol) was added. The resulting solution was then stirred overnight. The solvent was evaporated and the residue was dissolved in $CHCl_3/CH_3CN$ (7/1, v/v). This solution was washed with an aqueous saturated NH_4PF_6 solution. The organic layer was separated and dried with Na_2SO_4, filtered, and the solvent was removed by rotary evaporation. The resulting crude product was subjected to size exclusion column chromatography. The desired fraction was evaporated to dryness and the resulting solid was sonicated several times in n-hexane and dried in vacuo. This procedure was applied to compounds **P1**, **P2**, **P4**, and **P6** and was only varied in the polymerization time *x*. Some data are given below.

P1

Polymerization time *x* = 3. Yield 35 mg (10%).
^{1}H-NMR (400 MHz, $CDCl_3/CD_3CN$ 1/1 (v/v)): δ 8.94 (d, 4H, J = 6.9 Hz), 8.42 (d, 4H, J = 6.8 Hz), 7.02 (t, 1H, J = 1.6 Hz), 6.73 (d, 2H, J = 1.6 Hz), 4.68 (d, 4H, J = 7.8 Hz), 4.00 (t, 2H, J = 6.2), 3.52–3.33 (m, 72H), 3.29 (s, 3H), 2.17–2.11 (m, 4H), 1.89–1.82 (m, 2H), 1.67–1.52 (m, 74H), 1.30 (s, 18H) ppm. Mn = 2034 g·mol^{-1} (^{1}H-NMR), Mn = 1789 g·mol^{-1} (MALDI-TOF), PDI = 1.04 (MALDI-TOF). Length of chain: ~90 atoms.

P2

Polymerization time *x* = 10. Yield 100 mg (15%).
^{1}H-NMR (400 MHz, $CDCl_3/CD_3CN$ 1/1 (v/v)): δ 8.94 (d, 4H, J = 6.7 Hz), 8.42 (d, 4H, J = 6.6 Hz), 7.02 (t, 1H, J = 1.5 Hz), 6.73 (d, 2H, J = 1.6 Hz), 4.68 (d, 4H, J = 7.7 Hz), 4.00 (t, 2H, J = 6.1), 3.44–3.33 (m, 122H), 3.29 (s, 3H), 2.19–2.11 (m, 4H), 1.90–1.82 (m, 2H), 1.66–1.53 (m, 126H), 1.30 (s, 18H) ppm; Mn = 2900 g·mol^{-1} (^{1}H-NMR), Mn = 2560 g·mol^{-1} (MALDI-TOF), PDI = 1.04 (MALDI-TOF). Length of chain: ~150 atoms.

P4

Polymerization time *x* = 30. Yield 150 mg (15%).
^{1}H-NMR (400 MHz, $CDCl_3/CD_3CN$ 1/1 (v/v)): δ 8.94 (d, 4H, J = 4.4), 8.42 (bs, 4H), 7.02 (s, 1H), 6.73 (s, 2H), 4.69 (d, 4H, J = 7.6), 4.00 (t, 2H, J = 5.9), 3.55–3.25 (m, 213H), 3.29 (s, 3H), 2.18–2.07 (m, 4H), 1.90–1.84 (m, 2H), 1.71–1.45 (m, 216H), 1.30 (s, 18H) ppm; Mn = 4558 g·mol^{-1} (^{1}H-NMR), Mn = 4782 g·mol^{-1} (MALDI-TOF), PDI = 1.07 (MALDI-TOF). Length of chain: ~266 atoms.

P6

Polymerization time *x* = 50. Yield 150 mg (12%).
^{1}H-NMR (400 MHz, $CDCl_3/CD_3CN$ 1/1 (v/v)): δ 8.95 (d, 4H, J = 6.4 Hz), 8.43 (d, 4H, J = 5.1 Hz), 7.02 (s, 1H), 6.73 (s, 2H), 4.69 (d, 4H, J = 7.7), 4.00 (t, 2H, J = 6.1), 3.49–3.32 (m, 312H), 3.29 (s, 3H), 2.18–2.09 (m, 4H), 1.90–1.81 (m, 2H), 1.67–1.53 (m, 316H), 1.30 (s, 18H) ppm; Mn

= 6360 g·mol^{-1} (^{1}H-NMR), Mn = 6115 g·mol^{-1} (MALDI-TOF), PDI = 1.10 (MALDI-TOF). Length of chain: ~390 atoms.

Threading rate constants. Prior to performing the experiments, the porphyrin macrocycles **$H_2$1** and **Zn1** were purified by preparative TLC followed by a short column and precipitation with pentane. The threading kinetics were measured by using the time drive application of the spectrometer software. The sample was excited at the wavelength corresponding to the maximum absorbance of the porphyrin Soret band and the emission at the wavelength corresponding to the maximum emission was recorded in time. Typically, to a weighed solution containing 0.8 μM of **Zn1**, a known amount of viologen derivative was added and the solution mixed. After the mixing time (1.5 s) the measurement was started. The data were analyzed according to standard 1:1 kinetic isotherms that describe the kinetics involved in complex formation between A and B, forming C (Equations 13−15).[24] From the fit, both the rate constant k_{on} and equilibrium association constant K_{assoc} were obtained. All the experiments were performed in plural and at different concentrations of the viologen derivative to decrease the experimental error.

$$\mathrm{A} + \mathrm{B} \underset{k_{\text{off}}}{\overset{k_{\text{on}}}{\rightleftharpoons}} \mathrm{C}$$

$$[\mathrm{C}] = p\frac{\left(1 - \dfrac{q}{p}\dfrac{p-[\mathrm{C}]_{\mathrm{o}}}{q-[\mathrm{C}]_{\mathrm{o}}}e^{k_{\text{on}}(p-q)t}\right)}{\left(1 - \dfrac{p-[\mathrm{C}]_{\mathrm{o}}}{q-[\mathrm{C}]_{\mathrm{o}}}e^{k_{\text{on}}(p-q)t}\right)} \tag{13}$$

$$p = [\mathrm{C}]_{\mathrm{eq}} = \frac{([\mathrm{A}]_{\mathrm{o}} + [\mathrm{B}]_{\mathrm{o}} + \dfrac{1}{K_{\text{Assoc}}}) - \sqrt{([\mathrm{A}]_{\mathrm{o}} + [\mathrm{B}]_{\mathrm{o}} + \dfrac{1}{K_{\text{Assoc}}})^2 - 4\cdot[\mathrm{A}]_{\mathrm{o}}\cdot[\mathrm{B}]_{\mathrm{o}}}}{2} \tag{14}$$

$$q = \frac{[\mathrm{A}]_{\mathrm{o}}[\mathrm{B}]_{\mathrm{o}}}{[\mathrm{C}]_{\mathrm{eq}}} \tag{15}$$

$$K_{\text{assoc}} = \frac{[\mathrm{C}]_{\mathrm{eq}}}{\left([\mathrm{A}]_{\mathrm{o}} - [\mathrm{C}]_{\mathrm{eq}}\right)\cdot\left([\mathrm{B}]_{\mathrm{o}} - [\mathrm{C}]_{\mathrm{eq}}\right)} = \frac{k_{\text{on}}}{k_{\text{off}}} \tag{16}$$

Simulation experiments using Mathematica. The presented models and their rate constants were programmed in Mathematica® as presented in two examples below and threading simulations were performed in which the concentrations of macrocycle (H) and polymer (P) and the values of k_{initial}, k_{hop}, $k_{\text{V-off}}$, and n were varied. When possible (i.e. when displaying apparent second and first order kinetics for the on and the off process, respectively) the obtained threading simulations were analyzed with the help of Equations 13-16.

Example of computer language programmed in Mathematica representing the consecutive hoping model according to Figure 4 in which *n* = 4.

```
ClearAll["Global`*"]
kthr=3*^3;
kini=3*^4;
Kp = 1000;(*associatieconstante polymeer*)
Ka = 1*^5;(*associatieconstante viologeen*)
kon= kini*Kp;
koff=(kthr*Kp)/Ka;

A = 1*^-6; (*concentratie host*)
B = 1*^-6; (*concentratie pol*)
U = 0;
Z= 0;
solution = NDSolve[{
        CA'[t]==kini*CU1[t] - kon*CA[t]*CB[t],
        CB'[t]==kini*CU1[t] - kon*CA[t]*CB[t],
        CU1'[t]== kon*CA[t]*CB[t]-kthr*CU1[t]+kthr*CU2[t]-kini*CU1[t],
        CU2'[t]== kthr*CU1[t]-2*kthr*CU2[t]+kthr*CU3[t],
        CU3'[t]== kthr*CU2[t]-2*kthr*CU3[t]+kthr*CU4[t],
        CU4'[t]== kthr*CU3[t]-2*kthr*CU4[t]+koff*CZ[t],
        CZ'[t]==  kthr*CU4[t]- koff*CZ[t],
        CA[0]==A,
        CB[0]==B,
        CU1[0]==U,
        CU2[0]==U,
        CU3[0]==U,
        CU4[0]==U,
        CZ[0]== Z},{CA, CB, CU1, CU2,CU3,CU4, CZ}, {t, 0,  50.}];
Resultaat=Table[CZ[t]/.solution,{t,0,50,1/100}]
NumberForm[Resultaat,NumberFormat□(#1"E"#3&)];
SetDirectory["C:\Documents and Settings\Alexander\Desktop"];                    (*hier wordt alles
neergezet*)
filename="alex_test5.csv";                                                  (*maak file met Mijn
Computer en dan hier naam invullen*)
Export[filename,Resultaat];
```

Example of computer language programmed in Mathematica representing the consecutive hoping model according to Figure 9a in which *n* = 4.

```
ClearAll["Global`*"]

k=0.05;

U = 1*^-6; (*concentration macrocycle*)

Z= 0;
solution = NDSolve[{

        CU1'[t]==k*CU2[t]-k*CU1[t],
        CU2'[t]==k*CU1[t]- k*CU2[t]+k*CU3[t]-k*CU2[t],
```

```
    CU3'[t]==k*CU2[t]- k*CU3[t]+k*CU4[t]-k*CU3[t],
    CU4'[t]==k*CU3[t]- k*CU4[t]+k*CU5[t]-k*CU4[t],
    CU5'[t]==k*CU4[t]- k*CU5[t]-k*CU5[t],
    CU6'[t]==k*CU5[t],
    CU1[0]==U,
    CU2[0]==Z,CU3[0]==Z,CU4[0]==Z,CU5[0]==Z,CU6[0]==Z},{ CU1, CU2, CU3,CU4,CU5,CU6}, {t, 0,
5000.}];
Resultaat=Table[CU6[t]/.solution,{t,0,5000,1}]
NumberForm[Resultaat,NumberFormat□(#1"E"#3&)];
SetDirectory["C:\Documents and Settings\Alexander\Desktop"];                    (*hier wordt alles
neergezet*)
filename="alex_U6.csv";                                                 (*maak file met Mijn
Computer en dan hier naam invullen*)
Export[filename,Resultaat];
```

5. Literature

1. Coumans, R. G. E.; Elemans, J. A. A. W.; Nolte, R. J. M.; Rowan, A. E. *Proc. Natl Acad. Sci. USA* **2006**, *103*, 19647−19651.
2. Hidalgo Ramos, P.; Coumans, R. G. E.; Deutman, A. B. C.; Smits, J. M. M.; de Gelder, R.; Elemans, J. A. A. W.; Nolte, R. J. M.; Rowan, A. E. *J. Am. Chem. Soc.* **2007**, *129*, 5699−5702.
3. Herrmann, W.; Keller, B.; Wenz, G. *Macromolecules* **1997**, *30*, 4966−4972.
4. Hammett, L. P. *Physical Organic Chemistry*, 2nd ed., McGraw-Hill, New York, **1970**, p. 112.
5. Sung, W.; Park, P. J. *Phys. Rev. Lett.* **1996**, *77*, 783−786.
6. Muthukumar, M. *J. Chem. Phys.* **1999**, 111, 10371.
7. Storm, A. J.; Storm, C.; Chen, J.; Zandbergen, H.; Joany, J.-F.; Dekker C. *Nano Lett.* **2005**, *5*, 1193−1197.
8. Kasioanowicz, J. J.; Brandin, E.; Branton, D.; Deamer, D. W. *Proc. Natl Acad. Sci. U.S.A.* **1996**, *93*, 13770−13773.
9. Kantor, Y.; Kardar, M. *Phys. Rev. E.* **2004**, *69*, 021806.
10. A. B. Kolomeisky, *Biophysical Journal* **2008**, *94*, 1547−1548.
11. Muthukumar, M. *Annu. Rev. Biophys. Biomol. Struct.* **2007**, *36*, 435−450.
12. Gauthier, M. G.; Slater, G. W.; *J. Chem. Phys.* **2008**, *128*, 205103.
13. Gauthier, M. G.; Slater, G. W.; *J. Chem. Phys.* **2008**, *128*, 175103.
14. Meller, A.; Nivon, L.; Branton, D. *Phys. Rev. Lett.* **2001**, *86*, 3435−3438.
15. Slonkina, E.; Kolomeisky, A. B. *J. Chem. Phys.* **2003**, *118*, 7772−7778.
16. Chuang, J.; Kantor, Y.; Kardar, M. *Phys. Rev. E. Stat. Nonlin. Soft Matter Phys.* **2001**, *65*, 011802.
17. Milchev, A.; Binder, K.; Bhattacharya, A. *J. Chem. Phys.* **2004**, *121*, 6042−6051.
18. Zhang, W.; Dichtel, W. R.; Stieg, A. Z.; Benitez, D.; Gimzewski, J. K.; Heath, J. R.; Stoddart, J. F. *Proc. Natl Acad. Sci. U.S.A.* **2008**, *105*, 6514−6519.
19. Wu, J.; Leung, K. C.-F.; Stoddart, J. F. *Proc. Natl Acad. Sci. U.S.A.* **2007**, *104*, 17266−17271.
20. Osaki, M.; Takashima, Y.; Yamaguchi, H.; Harada, A. *J. Am. Chem. Soc.* **2007**, *129*, 14452−14457.

21. Wenz, G.; Han, B. H.; Müller, A. *Chem. Rev.* **2006**, *106*, 782−817.
22. Daniell, H. W.; Klotz, E. J. F.; Odell, B.; Claridge, T. D. W.; Anderson, H. L. *Angew. Chem. Int. Ed.* **2007**, 46, 6845−6848.
23. Thordarson, P.; Bijsterveld, E. J. A.; Rowan, A. E.; Nolte, R. J. M. *Nature* **2003**, *424*, 915−918.
24. Koppelman, S. J.; vanHoeij, M.; Vink, T.; Lankhof, H.; Schiphorst, M. E.; Damas, C.; Vlot, A. J.; Wise, R.; Bouma, B. N.; Sixma, J. J. *Blood* **1996**, *87*, 2292−2300.

7

Threading of Flexible Porphyrin Macrocycles

1. Introduction

In our laboratory, a method has been developed to study the threading of polymers through macrocyclic porphyrin receptors. It is based on the formation of strong macrocycle-viologen pseudo-rotaxane complexes which are only formed once the macrocycle has threaded on and completely traversed a polymer chain. In previous work,[1,2] the threading of **H$_2$1** and **Zn1** (Chart 1) on chains varying in length from 1 to 55 nm was studied (Chapters 5 and 6). The observed length dependencies of the threading process could be perfectly explained by using a consecutive hopping model[3] in which the observed overall threading-on rate is determined by the initial binding event (involving an entron effect) and the chance of arriving at the other end of the chain.[4] In this chapter, the threading of the larger and more flexible macrocycles **H$_2$2** and **Zn2** is studied and compared to the threading of **H$_2$1** and **Zn1**.

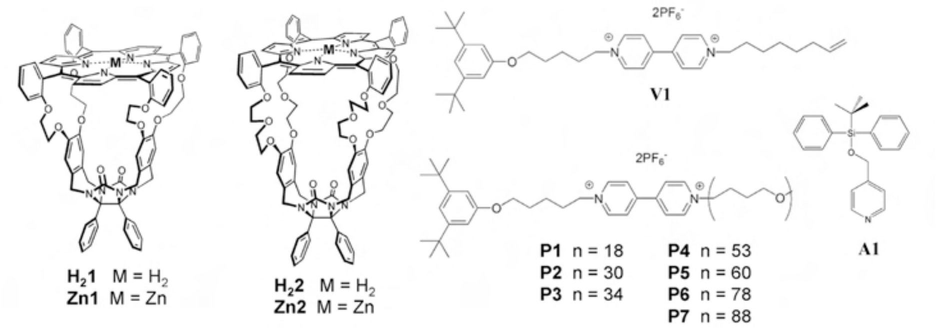

Chart 1. Molecules used in this chapter.

2. Results and discussion

Extended macrocycles **H$_2$2** and **Zn2** were shown to be excellent receptors for a variety of viologen- and pyridine-based guest molecules (Chapter 2). In contrast to the smaller and more rigid macrocycles **H$_2$1** and **Zn1**, binding of these guests occurred by an induced-fit mechanism. In order to gain further information about the effects of cavity size and flexibility on the threading process, threading experiments were performed using **H$_2$2** and **Zn2** with the polymer derivatives **P1**–**P7** (Chart 1). Although these extended macrocycles were observed to be capable of traversing the blocking groups of the viologen derivatives via slippage (Chapter 4), the slippage process is orders of magnitudes slower than the threading process of the polymer chains and therefore has a negligible effect on the observed threading curves (slippage rate constants: 0.05–0.5 M^{-1}s^{-1}, threading rate constants: 10^{3}–10^{5} M^{-1}s^{-1}).

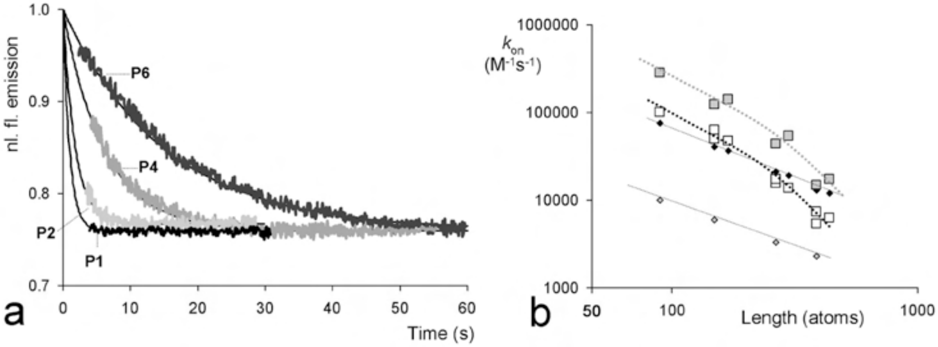

Figure 1. (a) Fluorescence emission in time after the addition of 2.5 equivalents of polymers **P1**, **P2**, **P4** and **P6** to **H$_2$2** (1.0 μM) in a 1/1 (v/v) mixture of chloroform and acetonitrile. The black lines drawn through the curves are fits according to 1:1 kinetic binding models. (b) Threading rate constants (k_{on}) at 296 K for **H$_2$1** (◆), **Zn1**(◇), **H$_2$2** (□), and **Zn2** (▣) plotted versus polymer chain length.

2.1 Threading of H$_2$2

The threading of **H$_2$2** over the different polymer derivatives (**P1**–**P7**, Chart 1) was studied with the help of fluorescence spectroscopy in 1/1 (v/v) mixtures of acetonitrile and chloroform, analogous to the previous threading studies involving **H$_2$1** and **Zn1**. As was observed for **H$_2$1** and **Zn1**, binding of viologen derivatives onto **H$_2$2** resulted in the complete quenching of the porphyrin fluorescence emission. The concentrations of free macrocycle and pseudo-rotaxane complex in time during the threading experiments could therefore be easily determined with fluorescence spectroscopy. Unfortunately, the fluorescence binding curves were qualitatively inferior to the ones obtained in the threading experiments with **H$_2$1** and **Zn1** (Figure 1a), which is due to the significantly lower association constant of **H$_2$2** ($K_a \approx 1 \times 10^5$ M^{-1}) with the viologen derivatives compared to the association constants with **H$_2$1** and **Zn1** ($K_a \approx 1 \times 10^7$ M^{-1}). At the experimental concentrations (~μM), the addition of 2.5 equivalents of any of the polymers to **H$_2$2** results in a less than 25% decrease of the fluorescence emission, whereas the addition of only 1 equivalent to **H$_2$1** results in an 80% decrease at equilibrium. The obtained binding curves clearly revealed a polymer length dependency for the threading process. In Figure 1a it can be seen that it takes longer to reach equilibrium upon an increase in polymer length. Independent of polymer length, a similar degree of fluorescence quenching is observed at equilibrium, which indicates that **H$_2$2** binds to all the polymers with similar association constants. The data were analyzed with second order 1:1 kinetic binding isotherms, from which the threading-on rate constants k_{on} and the equilibrium association constants K_{a} were calculated (Table 1). As can be seen from the fits in Figure 1a, the 1:1 kinetic binding isotherms nicely describe the experimental curves indicating apparent second order kinetics for the threading-on and first order kinetics for the threading-off processes as was observed earlier for **Zn1** and **H$_2$1**. The length dependency observed for the threading of **H$_2$2** was strikingly different compared to that observed for **H$_2$1** and **Zn1** (Figure 1b). The larger and more flexible receptor **H$_2$2** threads by a factor 1.5 faster over the shortest polymer **P1** than **H$_2$1**, whereas the rate of threading over the longest polymer **P7** is almost a factor of 2 lower than for **H$_2$1**. Instead of a halving in rate constant upon each doubling of chain length according to Equation 1 (that is, a straight line in the log-log plot with a slope of −1, as was observed for **Zn1** and **H$_2$1** in Figure 1b; Chapter 6), the rate constant of **H$_2$2** decreases significantly by more than a factor of 2 upon each doubling in chain length. The energy barrier associated with traversing the polymer chains upon increasing polymer lengths therefore increases more for **H$_2$2** than for **H$_2$1** (Figure 2a).

$$k_{\mathrm{on-overall}} = \frac{k_{\mathrm{initial}}}{n+1} \qquad (1)$$

Table 1. Threading rate constants (k_{on}, $M^{-1}s^{-1}$), association equilibrium constants (K_{a}, M^{-1}), and the activation parameters ($\Delta G^{\neq}_{\mathrm{on}}$, $\Delta H^{\neq}_{\mathrm{on}}$, $-T\Delta S^{\neq}_{\mathrm{on}}$, in kJ·mol^{-1}), and binding parameters (ΔG^{o}, ΔH^{o}, $-T\Delta S^{\mathrm{o}}$, in kJ·mol^{-1}) for the complex formation between **H$_2$2** and viologen derivatives **P1**–**P7**.[a]

Guest	Length (atoms)	**Kinetics**				**Thermodynamics**			
		k_{on} [b,c]	$\Delta G^{\neq}_{\mathrm{on}}$	$\Delta H^{\neq}_{\mathrm{on}}$ [d]	$-T\Delta S^{\neq}_{\mathrm{on}}$ [d,f]	K_{a} [b,d]	ΔG^{o}	ΔH^{o} [e]	$-T\Delta S^{\mathrm{o}}$ [e,f]
P1	90	1.0×10^{5}	45	−19 [f]	64 [f]	1.4×10^{5}	−29	−23	−6
P2	150	5.6×10^{4}	46	−6 [f]	52 [f]	1.2×10^{5}	−29	−23	−6
P3	170	4.7×10^{4}	47	−27 [g]	74 [g]	1.3×10^{5}	−29	−30	0
P4	266	1.6×10^{4}	49	−3 [f]	52 [f]	1.4×10^{5}	−29	−23	−7
P5	300	1.4×10^{4}	49	−17 [g]	67 [g]	1.4×10^{5}	−29	−28	−1
P6	390	6.4×10^{3}	51	8 [f]	43 [f]	1.4×10^{5}	−29	−26	−3
P7	440	6.3×10^{3}	51	−14 [g]	65 [g]	1.5×10^{5}	−29	−31	1

[a] Determined by fluorescence spectroscopy in 1:1 (v/v) mixtures of chloroform and acetonitrile. [b] rate constant at T = 296 K. [c] Estimated error: 30%. [d] Estimated error ± 15 kJ/Mole. [e] T = 298 K, estimated error ± 3 kJ·mol^{-1}. [f] Concentration **H$_2$2**: 1.5 μM. [g] Concentration **H$_2$2**: 0.6 μM.

As explained in the previous chapter, the observed threading rates for rigid macrocycles **H$_2$1** and **Zn1** depend solely on the (chain length-independent) initial binding event and on the (chain length-dependent) chance of falling off at the other end of the chain (Equation 1). The translocation process is, for both of those macrocycles, too fast to be expressed in the overall threading curves, which results in the observed parallel length dependencies for the threading process. The fact that the threading of **H$_2$2** deviates from this length dependency suggests that the translocation process is significantly slower and has a rate determining influence on the overall threading process. The observed threading rate of **H$_2$2** depends thus on (i) the initial binding event (with rate constant k_{entron}); (ii) the statistical chance of falling-off at the other end of the chain ($\propto$

$1/N$, in which $N \propto$ polymer length); and (iii) the chain length dependent translocation process ($\propto N^{\alpha}$, with α ranging from 2 to 2.6)[5–13]. The traversing of the shortest polymers is faster for **$H_2$2** than for **$H_2$1**, which indicates that the rate of initial binding to the open end of the chain is higher for **$H_2$2** than for **$H_2$1**. This is in line with expectation, since the cavity of **$H_2$2** is larger than that of **$H_2$1**. The slower translocation of **$H_2$2** compared to **$H_2$1** must be the result of relatively favorable interactions between **$H_2$2** and the polymer chain, which slow down the motion along the chain, i.e., decreases the hopping rates. As was discussed in Chapter 2, **$H_2$2** is a potent receptor for a variety of substrates, mainly due to the flexible spacers that are capable of accommodating guest molecules in ideal binding geometries. Such induced-fit binding interactions with the polymer chain might also be responsible for the slower translocation of **$H_2$2** compared to the rigid macrocycles **$H_2$1** and **Zn1**, which cannot accommodate the chain in an ideal geometry inside the compact electron-rich cavity.

Deriving quantitative values for the individual rates of the initial binding process and the translocation process is not possible. In the previous chapter it was shown that the threading-on process starts deviating from perfect second order behavior when, in addition to the initial binding event, the translocation process starts to become rate determining. The rates of the two consecutive events, initial binding and translocation, will both be expressed in the measured overall rate constant. The calculated threading rate constant obtained by curve-fitting is thus an apparent one and is not strictly second order (as assumed in the fitting procedure). It will, therefore, most probably deviate upon changing the experimental concentrations. This could be an explanation for the apparently large experimental error observed for the threading of **$H_2$2** compared to the nearly perfect evolution of the length dependencies observed for **$H_2$1** and **Zn1** (Figure 1b). In order to obtain a measure for the observed effects without having to solve or even fully understand the exact consecutive hopping mechanism of **$H_2$2** and all the rate constants therein, the experimentally observed free energy of activation ($\Delta G^{\neq}_{\text{overall}}$) can be divided into three parts (Equation 2).

$$\Delta G^{\neq}_{\text{overall}} = \Delta G^{\neq}_{\text{initial}} + \Delta G^{\neq}_{\text{ca}} + \Delta G^{\neq}_{\text{translocation}} \qquad (2)$$

Equation 2 simply discriminates the deviations from the length dependency according to Equation 1; $\Delta G^{\neq}_{\text{initial}}$ is the free energy of activation associated with the initial binding process, $\Delta G^{\neq}_{\text{ca}}$ is the additional free energy of activation corresponding to the length dependent <u>c</u>hance of <u>a</u>rrival (ca), and $\Delta G^{\neq}_{\text{translocation}}$ is the observed extra free energy of activation as a result of the translocation process. The individual activation energies are given by Equations 3–5.

$$\Delta G^{\neq}_{\text{initial}} = -RT \ln\left(\frac{k_{\text{initial}} \cdot h}{kT}\right) \qquad (3)$$

$$\Delta G^{\neq}_{\text{ca}} = RT \ln(n+1) \qquad (4)$$

$$\Delta G^{\neq}_{\text{translocation}} = n \cdot \Delta G^{\neq}_{\text{atom}} \qquad (5)$$

Equations 3 and 4 follow directly from the consecutive hopping model (Chapter 6). Equation 5 provides the (apparent) free energy of activation of traversing a single atom ($\Delta G^{\neq}_{\text{atom}}$) in which n is the number of atoms in the chain. The experimentally observed activation energies of the threading process could be described with the help of Equation 2, as can be seen in Figure 2a. The calculated values for k_{initial} and $\Delta G^{\neq}_{\text{atom}}$ are presented in Table 2. The values for $\Delta G^{\neq}_{\text{atom}}$ should not be mistaken for the free energy of activation of moving over a single atom in the polymer chain ($\Delta G^{\neq}_{\text{hop}}$). It is solely a factor to describe the experimentally obtained deviations from the threading length-dependency as observed for **H$_2$1** and **Zn1**. For **H$_2$2** the total free energy of activation is simply the free energy of activation according to the consecutive hopping model with an additional 9.5 J·mol^{-1} per chain atom. Later in this chapter the variations in $\Delta G^{\neq}_{\text{atom}}$ upon changes in the experimental conditions will help in providing important conclusions about the translocation processes.

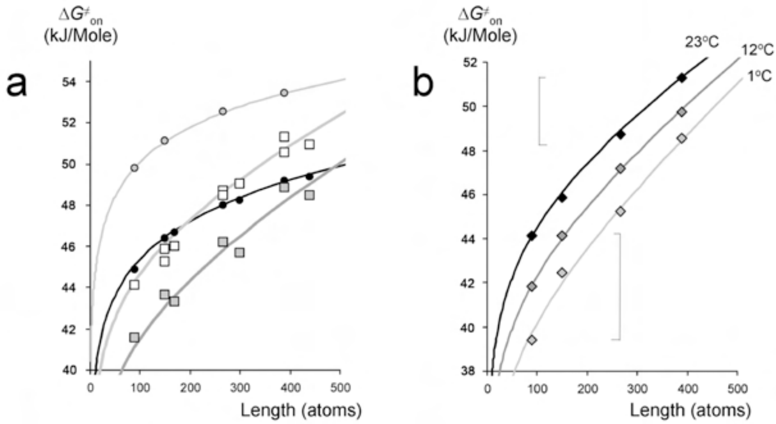

Figure 2. (a) Free energies of activation ($\Delta G^{\neq}_{\text{on}}$ at T = 296 K) for the threading-on process versus chain length for **H$_2$1** (●), **Zn1** (○), **H$_2$2** (□), and **Zn2** (▨) with curve fits according to Equation 2. (b) Free energies of activation ($\Delta G^{\neq}_{\text{on}}$) for the threading of **H$_2$2** at different temperatures with curve fits according to Equation 2. For short chain lengths, the difference in $\Delta G^{\neq}_{\text{on}}$ at different temperatures is larger than for longer chain lengths, which indicates that the deviations from the behavior according to Equation 1 become larger upon the lowering of the temperature.

Table 2. Rate constants calculated with the help of Equation 2 for the initial binding event (k_{initial}) and apparent extra activation energy $\Delta G^{\neq}_{\text{atom}}$ values for the threading over the polymer chains for **H$_2$1**, **Zn1**, **H$_2$2**, and **Zn2**.[a]

Macrocyle	k_{initial} (M^{-1}s^{-1}) [b]	$\Delta G^{\neq}_{\text{atom}}$ (J·mol^{-1}) [c]
H$_2$1	6.5 x 10^{6}	1.5
Zn1	9.0 x 10^{5}	0
H$_2$2	1.2 x 10^{7}	9.5
Zn2	4.7 x 10^{7}	12.5

[a] T = 296 K. [b] Estimated error 50% [c] Estimated error 30%

2.2 Variable temperature analysis of the threading process.

Threading experiments with **H$_2$2** were performed at various temperatures in order to derive the entropic ($\Delta S^{\neq}_{\text{on}}$) and enthalpic ($\Delta H^{\neq}_{\text{on}}$) contributions to the free energy of activation ($\Delta G^{\neq}_{\text{on}}$). In addition to the threading-on rate constants (k_{on}), the association constants (K_{a}) at different temperatures were also calculated from the fits. The entropic (ΔS^{o}) and enthalpic (ΔH^{o}) contributions to the free binding energy (ΔG^{o}) could be calculated with the help of van 't Hoff plots[14] (Table 1).

Thermodynamic data. The calculated values for the thermodynamic parameters (ΔH^{o} and ΔS^{o}) of flexible macrocycle **$H_2$2** will be compared to those of the rigid cavity **$H_2$1** that were obtained in Chapter 5. As can be seen in Table 1, the binding enthalpy (ΔH^{o}) for the complex formation between **$H_2$2** and the viologen derivatives has values of, on average -26 kJ·mol^{-1}, whereas the entropic contribution $-T\Delta S^{\mathrm{o}}$ is approximately -3 kJ·mol^{-1} at 298 K. The total binding free energy (ΔG^{o}) of -29 kJ·mol^{-1} is therefore mainly the result of favorable binding enthalpy. These parameters deviate significantly from the ones calculated for the complex formation between rigid **$H_2$1** and viologen derivatives involved in pseudo-rotaxane formation via slippage as described in Chapters 4 and 5. Typical values of $\Delta H^{\mathrm{o}} \approx -19$ kJ·mol^{-1} and $-T\Delta S^{\mathrm{o}} \approx -21$ kJ·mol^{-1} were calculated, and these contributed to a total binding free energy of -40 kJ·mol^{-1}. Complex formation with viologens is thus entropically more favorable for **$H_2$1** than for **$H_2$2**, whereas in terms of enthalpy the opposite is the case. This suggests that the larger flexible cavity of **$H_2$2** accommodates the viologen derivatives better than the smaller and rigid cavity of **$H_2$1** (hence the higher value of $-\Delta H^{\mathrm{o}}$), which is, however, not expressed in a higher association constant and $-\Delta G^{\mathrm{o}}$ value due to the entropic penalty associated with the ordering of the flexible chains in the ideal complexation geometry. The favorable binding entropy involved with desolvation of the viologen, as observed for **$H_2$1**, is therefore canceled in the case of **$H_2$2**. Similar conclusions regarding the flexibility of **$H_2$2** (and other macrocycles with extended cavities) were drawn in Chapter 4, in which comparable entropic differences were observed in the $\Delta S^{\neq}_{\mathrm{on}}$ values for the slippage of **$H_2$1** and **$H_2$2** over bulky stoppers

Kinetic data. The entropic ($\Delta S^{\neq}_{\mathrm{on}}$) and enthalpic ($\Delta H^{\neq}_{\mathrm{on}}$) contributions to the total free energy of activation ($\Delta G^{\neq}_{\mathrm{on}}$) for the threading of **$H_2$2** were calculated with the help of Eyring plots (Table 1).[15] Although slight changes in the experimental concentrations resulted in significant deviations in the activation parameters (Figure 3b), some clear trends could be observed. The activation enthalpy ($\Delta H^{\neq}_{\mathrm{on}}$) for the overall threading process is negative and increases (become less negative) upon an increase in chain length. The values for $-T\Delta S^{\neq}_{\mathrm{on}}$ are positive and reveal a general decrease upon the lengthening of the polymer chain. These data are completely different to those observed for the threading of **$H_2$1** over the same polymers, which revealed no changes in the *positive* value of $\Delta H^{\neq}_{\mathrm{on}}$ (≈ 20 kJ·mol^{-1}) and an *increase* in $-T\Delta S^{\neq}_{\mathrm{on}}$ in the measured series from 15 kJ·mol^{-1} to 29 kJ·mol^{-1} upon an increase in the chain length, in accordance with the consecutive hopping model. For **$H_2$1** an increase in the chain length is therefore only expressed in extra activation entropy, whereas for **$H_2$2** it leads to both a decrease in activation entropy and an increase in activation enthalpy. Assuming that the experimental differences in polymer length dependency are caused by the translocation process, which is only expressed in the threading curves of **$H_2$2** and not in the curves of $\mathbf{H_2 1}$, it can be tentatively concluded from the parameters obtained for $\mathbf{H_2 2}$ that this process is entropically favorable and enthalpically unfavorable.

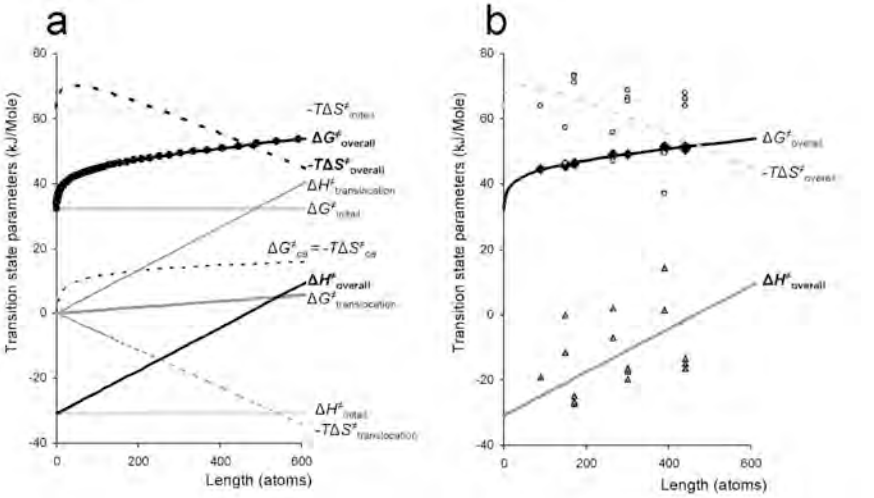

Figure 3. (a) Evolution of the individual activation parameters responsible for the observed length dependency versus chain length according to data analysis with Equation 2. (b) Experimentally obtained activation parameters $\Delta G^{\neq}_{\text{overall}}$ (◆), $\Delta H^{\neq}_{\text{overall}}$ (▲), and $-T\Delta S^{\neq}_{\text{overall}}$ (●) versus chain length with the fits according to the model described by Equation 2.

In order to better comprehend the activation parameters obtained for the threading of $\mathbf{H_2 2}$, the dependency of the threading on polymer chain length at different temperatures and different concentrations was analyzed using Equation 2. The fits obtained by using this method gave the values of k_{initial} and $\Delta G^{\neq}_{\text{atom}}$ at all the conditions used (Figure 2b). From these values, the activation parameters $\Delta H^{\neq}_{\text{initial}}$, $\Delta S^{\neq}_{\text{initial}}$, $\Delta H^{\neq}_{\text{atom}}$, and $\Delta S^{\neq}_{\text{atom}}$ could subsequently be calculated. The value derived for k_{initial} increased upon lowering the experimental temperature (25 ^{o}C: $k_{\text{initial}} \approx 1.4 \times 10^{7}$ $M^{-1}s^{-1}$, 3 ^{o}C: $k_{\text{initial}} \approx 3.5 \times 10^{7}$ $M^{-1}s^{-1}$), hence the initial binding of $\mathbf{H_2 2}$ to the open end of the polymer is faster at lower temperatures. This consequently results in a calculated negative value for the activation enthalpy ($\Delta H^{\neq}_{\text{initial}} = -31 \pm 10$ kJ·mol^{-1}). The calculated value for the activation entropy revealed that the initial binding is entropically highly unfavorable ($-T\Delta S^{\neq}_{\text{initial}} = 63 \pm 10$ kJ·mol^{-1}). The values derived for $\Delta G^{\neq}_{\text{atom}}$ increased upon lowering the temperature (25 ^{o}C: $\Delta G^{\neq}_{\text{atom}} \approx 9.4$ J·mol^{-1}, 3 ^{o}C: $\Delta G^{\neq}_{\text{atom}} \approx 13.6$ J·mol^{-1}). This indicates that the deviations from the behavior according to Equation 1 are larger at lower temperatures (as can be seen in Figure 2b). It can therefore be concluded that the translocation process is slower at lower temperatures.[16] From the values of $\Delta G^{\neq}_{\text{atom}}$ at different temperatures, the values of $\Delta H^{\neq}_{\text{atom}}$ (66 $\pm$ 20 J·mol^{-1}) and $-T\Delta S^{\neq}_{\text{atom}}$ (-57 ± 20 J·mol^{-1} (T = 298 K)) were calculated. Apparently, the translocation process is entropically favorable, and enthalpically unfavorable. This last conclusion is in line with the tentative conclusion that was drawn from the series of activation parameters for the overall threading process of $\mathbf{H_22}$. To give an idea of how the observed activation parameters evolve as a function of chain length according to the presumed model, all the calculated values of the individual parameters ($\Delta G^{\neq}_{\text{initial}}$, $\Delta H^{\neq}_{\text{initial}}$, $\Delta S^{\neq}_{\text{initial}}$, $\Delta G^{\neq}_{ca} = \Delta S^{\neq}_{ca}$, $\Delta G^{\neq}_{\text{translocation}}$, $\Delta H^{\neq}_{\text{translocation}}$, $\Delta S^{\neq}_{\text{translocation}}$, $\Delta G^{\neq}_{\text{overall}}$, $\Delta H^{\neq}_{\text{overall}}$, and $\Delta S^{\neq}_{\text{overall}}$) are presented in Figure 3a. Figure 3b presents the experimentally derived activation parameters and a fit of the calculated overall parameters ($\Delta G^{\neq}_{\text{overall}}$, $\Delta H^{\neq}_{\text{overall}}$, and $\Delta S^{\neq}_{\text{overall}}$) versus chain length. The theory describes the experimentally observed trends with good accuracy, and provides a guide for the drawing of conclusions concerning the mechanisms of initial binding and polymer translocation processes.

2.3 Mechanism of threading of $\mathbf{H_22}$

The mechanism proposed for the overall threading process of $\mathbf{H_22}$ is presented in Figure 4. The initial binding of the macrocycle to the open end of the polymer chain is entropically highly unfavorable ($-T\Delta S^{\neq}_{\text{initial}}$ = 63 kJ·mol^{-1}), which can be ascribed to the loss of conformational freedom of both the flexible cavity and the open end of the polymer chain upon binding. The negative value for the activation enthalpy of the initial binding event (and the overall threading) is highly uncommon. In all comparable supramolecular binding processes described in the literature[17-20] and in this thesis, the rates of complexation decrease upon the lowering of the temperature and these processes have positive activation enthalpies. In some enzyme systems, however, negative activation enthalpies for binding processes have been reported[21,22] and these are mainly associated with protein folding. For the threading process of $\mathbf{H_22}$, the observed negative activation enthalpy can be explained by its specific conformational behavior. In Chapter 2 it was described that $\mathbf{H_22}$ adopts a geometry in which the crown ether spacers fill the space in between the glycoluril moiety and the porphyrin. Variable temperature ^{1}H-NMR spectroscopic experiments revealed that, upon lowering the temperature, the cavity becomes slightly more opened (this was concluded from the strong downfield shifting of the spacer proton signals, which indicated that they move out of the proximity of the porphyrin ring). It can therefore be expected that the cavity is more available for the binding of the open end of the polymer chain at lower temperatures. This opening of the cavity would provide an explanation for the observed increase in initial threading rate at lower temperatures and thus for the negative value for the activation enthalpy. In other words, you can state that the closed conformation of the cavity is enthalpically unfavorable and entropically driven. The binding of the open chain end inside the cavity therefore has an entropic penalty, but is favorable in enthalpy. Such an effect is not observed for the slippage of $\mathbf{H_22}$ over a bulky blocking group because, in that case, it requires the full opening of the dimensions of the cavity, a process that costs a lot of energy and involved positive activation enthalpies.

Once $\mathbf{H_22}$ has threaded onto the open end of the polymer chain and filled the dimensions of its cavity it starts moving randomly along the polymer chain. The chance of reaching the viologen, which is located on the other end of the polymer, is proportional to the chain length. For $\mathbf{H_21}$ and **Zn1**, where the translocation process is too fast to be expressed in the overall threading curves, this statistical chance fully determines the observed length dependency and is expressed as extra activation entropy upon increasing chain lengths. This entropic effect, however, is not observed for **$H_2$2** because it is compensated by the entropically favorable translocation process.

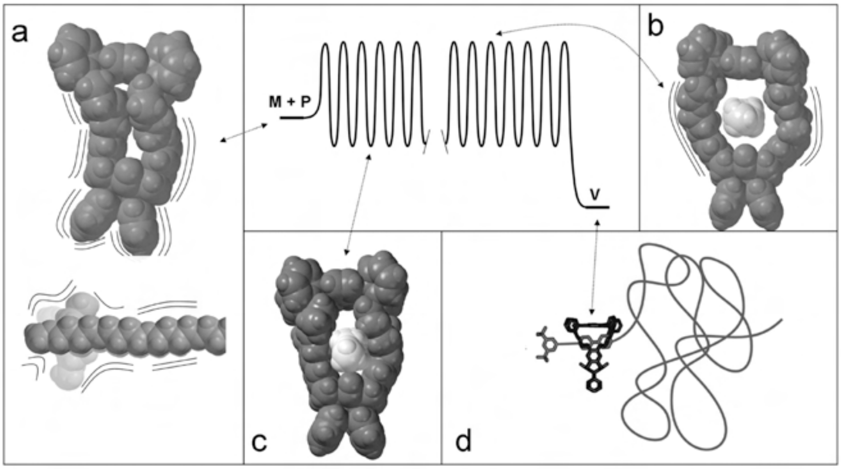

Figure 4. Schematic representation of the threading process of **$H_2$2** onto the polymer derivatives with a consecutive hopping energy landscape as a guide. (a) Molecular models of the very flexible macrocycle and open end of the polymer when they are free in solution. The initial binding between the two is entropically highly unfavorable as a result in the loss of conformational freedom of both macrocycle and open chain end. (b) In order to 'hop' along the chain, the macrocycle needs to release the tight binding from the chain, which is enthalpically demanding, but entropically favorable since both the macrocycle and the chain gain more conformational freedom in such a relaxed conformation. (c) Molecular model after the threading of the macrocycle onto the chain. The macrocycle finds local energy minima in which it binds with an induced-fit mechanism onto the chain. This binding is enthalpically favorable as a result of favorable van der Waals interactions between the chain and the cavity, but it is also accompanied by the loss of conformational freedom of the macrocycle and hence entropically unfavorable. (d) The macrocycle reaches the viologen moiety, which quenches the fluorescence emission.

The derived values for $\Delta H^{\neq}_{\text{atom}}$ and $\Delta S^{\neq}_{\text{atom}}$ suggest that the translocation process is entropically favorable and enthalpically unfavorable. This is rather surprising because one would a priori expect that the movement along the polymer chain requires the stretching and ordering of the polymer chain, which should be entropically unfavorable. The experimental observations, on the other hand, strongly suggest that **$H_2$2** has a relatively strong affinity for the chain, which might be more of a rate-determining factor for the translocation than the stretching of the polymer chain. In a sense, it can be expected that the activation parameters observed for the initial binding event will be counterbalanced by activation parameters with opposite signs in the translocation process. Upon initial binding, **$H_2$2** adopts an ideal binding geometry on the chain, which is enthalpically favorable as a result in the loss of the enthalpically unfavorable closed form of **$H_2$2** in addition to stabilising van der Waals interactions between the chain and the cavity. This initial binding is entropically unfavorable as a result in the loss of conformational freedom of the cavity and the chain. In order to move along the chain, **$H_2$2** first has to adopt a more relaxed conformation in which it releases the tight binding geometry with the chain. This release, and hence the movement along the chain, will therefore be enthalpically unfavorable but entropically favorable. This results in the observed general increase in overall activation enthalpy and the decrease in overall activation entropy upon increasing polymer lengths because the translocation process becomes significantly more apparent in the experimental threading curves upon increasing chain length.

2.4 Threading of Zn2

The threading of **Zn2** over polymers **P1–P7** was also investigated. Some of the experimental fluorescence threading curves are presented in Figures 5a and b. Data analysis surprisingly revealed that the threading of **Zn2** is considerably faster than the threading of **$H_2$2**; the calculated threading rates of **Zn2** are on average a factor 2.9 higher than those of **$H_2$2**. This threading behavior is in contrast to that observed for **$H_2$1** and **Zn1** (of which the latter threads considerably slower), but also in contrast to the slippage over bulky stoppers of **$H_2$2** and **Zn2** (of which the latter slips a factor of 8.9 slower). The length dependency for the threading process, however, was similar to that observed for **$H_2$2** (Figures 1b and 2a) and also the calculated activation parameters revealed similar values and length dependencies, i.e., upon an increase in chain length a negative and increasing value was obtained for $\Delta H^{\neq}_{\mathrm{on}}$ and positive and decreasing value observed for $-T\Delta S^{\neq}_{\mathrm{on}}$ (Table 3). For this reason, it was assumed that also in the threading of **Zn2**, the translocation process plays an overall rate determining role.

Table 3. Threading rate constants (k_{on}, $\mathrm{M^{-1}s^{-1}}$), association equilibrium constants (K_{a}, $\mathrm{M^{-1}}$), activation parameters ($\Delta G^{\neq}_{\mathrm{on}}$, $\Delta H^{\neq}_{\mathrm{on}}$, $-T\Delta S^{\neq}_{\mathrm{on}}$; kJ·mol^{-1}), and binding free energy (ΔG^{o}, kJ·mol^{-1}) for complex formation between **Zn2** and viologen derivatives **P1_P7**.[a]

		Kinetics				Thermodynamics	
Guest	Length (atoms)	k_{on} [b,c]	$\Delta G^{\neq}_{\mathrm{on}}$	$\Delta H^{\neq}_{\mathrm{on}}$ [d]	$-T\Delta S^{\neq}_{\mathrm{on}}$ [d,e]	K_{a} [c]	ΔG^{o} [e]
P1	90	2.9×10^5	42	–8	50	3.0×10^5	–31
P2	150	1.2×10^5	44	–3	47	3.1×10^5	–31
P3	170	1.4×10^5	43	[f]	[f]	3.2×10^5	–31
P4	266	4.3×10^4	46	2	44	3.5×10^5	–31
P5	300	5.4×10^4	46	[f]	[f]	3.6×10^5	–31
P6	390	1.5×10^4	49	3	46	3.6×10^5	–31
P7	440	1.7×10^4	49	[f]	[f]	3.3×10^5	–31

[a] Determined by fluorescence spectroscopy in 1:1 (v/v) chloroform/acetonitrile. [b] T = 296 K. [c] Estimated error: 20%. [d] Estimated error ± 15 kJ·mol^{-1}. [e] T = 298 K, estimated error ± 3 kJ·mol^{-1}. [f] Not determined.

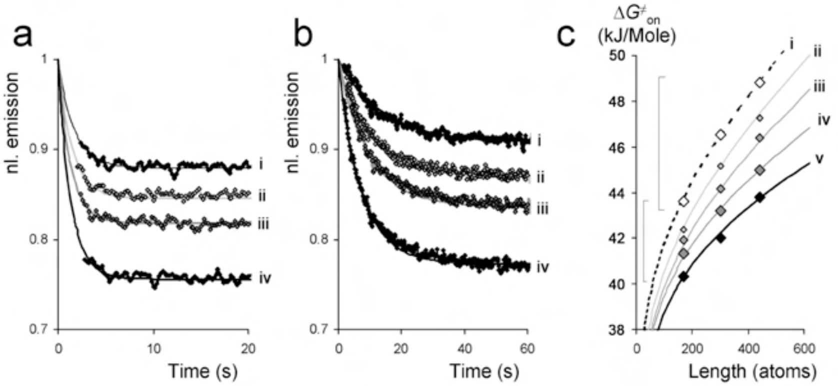

Figure 5. (a) Fluorescence emission in time after the addition of 1 equiv. of **P3** to **Zn2** (~1 μM) in the presence of increasing concentrations of **A1**. (b) Fluorescence emission in time after the addition of 1 equiv. of **P7** to **Zn2** in the presence of increasing concentrations of **A1**. (c) Free energy of activation ($\Delta G^{\neq}_{on}$) for the threading of **Zn2** versus chain length, with fits according to Equation 2, clearly which reveal that at increasing concentrations of **A1** the deviations from the length dependency according to Equation 1 become smaller as illustrated by the fact that the difference in $\Delta G^{\neq}_{on}$ becomes larger upon increasing chain lengths. Conditions: i: [**A1**]$_o$ = 0, ii: [**A1**]$_o$ = 0.32 mM, iii: [**A1**]$_o$ = 0.76 mM, iv: [**A1**]$_o$ = 2.76 mM, v: calculated values for a situation in which **Zn2** is fully saturated with **A1**. All the experiments were performed at 298 K in 1/1 (v/v) chloroform/acetonitrile.

2.5 Threading of Zn2 in the presence of bulky coordinating ligands

To get more insight into the role of the zinc centre on the threading behavior, it was decided to perform threading experiments of **Zn2** in the presence of bulky pyridine **A1**. In Chapter 2 it was shown that **A1** binds exclusively to the zinc ion on the outside of the cavity of **Zn2** with an association constant $K_a = 550\ \mathrm{M}^{-1}$ in 1:1 (v/v) mixtures of acetonitrile and chloroform at 298 K. It was also shown in Chapters 3 and 4 that **A1** causes large positive thermodynamic and kinetic heterotropic cooperative binding effects for the complexation of viologen derivatives inside the cavity of **Zn2** (cooperative effect on the association equilibrium constant: *Ce* = 10, cooperative effect on slippage rate constants: $ce_{(+)}$ = 4). The kinetic binding effects were shown to originate from the fact that the bulky pyridine ligand induces the removal of solvent molecules that are coordinated to the zinc ion and of intramolecular zinc-oxygen interactions inside the cavity of **Zn2**. The complexation of **A1** can therefore activate the cavity of **Zn2** for the binding of viologen (and other) derivatives. Similar positive cooperative binding effects were therefore expected to be observed for the threading of **Zn2** in the presence of **A1**, but more importantly, when the binding of **A1** to **Zn2** on the outside of the cavity also has an effect on the translocation process, it might have an additional effect on the overall threading length dependencies.

Threading experiments were performed between **Zn2** and polymers **P3**, **P5**, and **P7**, respectively, in solutions containing **A1** at three different concentrations. In addition, titrations of **V1** to **Zn2** were performed on solutions containing **A1** at different concentrations as a reference. The threading studies revealed that both the binding constants and the threading rate constants increase upon an increase in the concentrations of **A1**, as can be seen in Figures 5a and 5b and Table 4. From the obtained data, the cooperative kinetic and thermodynamic effects ($ce_{(+)}$ and Ce, respectively) could be calculated using the methods based on the fractional saturation of **Zn2** with **A1** as presented in Chapters 3 and 4.

Positive cooperative thermodynamic binding effects (Ce) ranging from 5.8 to 7.1 were observed for the combined binding of the polymers and **A1** to **Zn1** (K_a). These values deviated slightly from the value of Ce = 12.4 obtained for the combined binding of **V1** and **A1** to **Zn1**. This suggests that **A1** enhances the binding of polymer-appended viologen derivatives (**P3**, **P5**, and **P7**) to **Zn2** to a lesser extent than the binding of **V1**. It should be noted that the values for the association constants (K_a) of the polymers were derived from the equilibrium situations of only three threading experiments at different polymer concentrations (hence a fit through only three data points). These values are therefore considerably less accurate than the values obtained for the binding of **V1** to **Zn2**, which were obtained by performing full titrations consisting of at least 15 additions of **V1**. It was therefore decided to determine the cooperative effect of the combined binding of **A1** and **P3** to **Zn2** by ^{1}H-NMR titration experiments. To this end, **A1** was titrated to a mixture containing **P3** and **Zn2** in a 1/1 (v/v) mixture of $CDCl_3$ and CD_3CN. The titration revealed an association constant ($^{P3}K_{A1}$) of 5.8 x 10^4 M^{-1} and hence (since K_{A1} = 550 M^{-1}) a cooperative effect of a factor 10.5 ($\Delta\Delta G^o = -5.8$ $kJ{\cdot}mol^{-1}$). This more accurate value for the cooperative effect is in better agreement with the one of 12.4 obtained for the combination of **V1** and **A1** and with the values obtained in Chapter 3. The thermodynamic data obtained from the fluorescence threading experiments are therefore presumably not very accurate, although the observed deviations might also be due to considerable interactions of **Zn2** with the polymer chains.

Table 4. Threading rate constants (k_{on}) and association equilibrium constants (K_a) for complex formation between **Zn1** and viologen derivatives **V1**, **P3**, **P5**, and **P7** in the presence of various concentrations of **A1**, and the magnitudes of the kinetic ($ce_{(+)}$) and thermodynamic (Ce) cooperative binding effects.[a]

	k_{on} ($M^{-1}s^{-1}$) [b]				K_a (M^{-1}) [c]			
[A1]$_o$ (mM)	**P3**	**P5**	**P7**		**V1**	**P3**	**P5**	**P7**
0	1.4 x 10^5	4.3 x 10^4	1.7 x 10^4		1.3 x 10^5	3.2 x 10^5	3.0 x 10^5	3.3 x 10^5
0.32	2.3 x 10^5	7.5 x 10^4	3.2 x 10^4		3.5 x 10^5	4.9 x 10^5	5.4 x 10^5	6.2 x 10^5
0.76	2.8 x 10^5	1.1 x 10^5	4.6 x 10^4		5.8 x 10^5	7.0 x 10^5	7.6 x 10^5	8.1 x 10^5
2.32	3.5 x 10^5	1.7 x 10^5	8.2 x 10^4		9.4 x 10^5	1.2 x 10^6	1.3 x 10^6	1.4 x 10^6
$y_{\text{Zn2-A1}}$=1 [d]	*5.5 x 10^5*	*2.6 x 10^5*	*1.3 x 10^5*		*1.6 x 10^5*	*1.8 x 10^6*	*2.1 x 10^6*	*2.3 x 10^6*
$ce_{(+)}$	3.9	6.2	7.4	Ce	12.4	5.8	7.0	7.1
$\Delta\Delta G^{\neq}_{on}$	–3.4	–4.5	–4.9	$\Delta\Delta G^o$	–6.2	–4.3	–4.8	–4.9

[a] Determined by fluorescence spectroscopy at T = 298 K in 1/1 acetonitrile/chloroform (v/v). [b] Estimated error 25%. [c] Estimated error 40%. [d] Calculated values for k_{on} and K_a suggesting **Zn2** is fully occupied with **A1** and hence the fractional saturation of **Zn2** with **A1** equals 1.

Increased threading rates (k_{on}) were observed on an increase in concentration of **A1** and the calculated kinetic cooperative effects ($ce_{(+)}$) revealed higher values upon an increase in chain length (Table 4). Since for each of the polymers the initial binding event is equal independent of chain length, this strongly suggests that the binding of **A1** also has an effect on the translocation process. In addition to the accelerated rates as a result of the activation of the cavity (expressed in higher values of k_{initial}), the translocation process is apparently accelerated, which leads to higher values of $ce_{(+)}$ upon increasing chain lengths. This effect could be demonstrated by analyzing the length dependencies at different concentrations of **A1** with the use of Equation 2 (Figure 5c). The calculated values of $\Delta G^{\neq}_{\mathrm{atom}}$ decreased upon an increasing concentration of **A1** ($\Delta G^{\neq}_{\mathrm{atom}} \approx 10$ J·mol^{-1} for $[\mathbf{A1}]_o = 0$; $\Delta G^{\neq}_{\mathrm{atom}} \approx 5$ J·mol^{-1} for $[\mathbf{A1}]_o = 2.3$ mM). In the presence of increasing amounts of **A1**, the deviations from the length dependency according to Equation 1 become smaller, which suggests that the translocation is accelerated.

Although the experimental errors are large and the absolute effects are relatively small, these observations can be ascribed to interactions between the zinc ion and the polymer oxygen atoms. Porphyrin zinc centers are known to be capable of coordinating to ether oxygen atoms with low association constants (typically between 1 and 50 M^{-1}; Chapter 2). Nevertheless, when the oxygen atoms are located in the proximity of the zinc, and consequently the effective molarities are high, these interactions become significant. This was demonstrated by the intramolecular zinc-oxygen coordination observed in the flexible porphyrin macrocycles in Chapter 3. Likewise, when **Zn2** is threaded onto the polymer chain, the polymer oxygen atoms are likely to coordinate to the zinc centre. The local energy minima on the chain will therefore be substantially lower in energy, which results in slower translocation of the chain through the macrocycle (Figure 6). The binding of **A1** to the outside of **Zn2** competes for the fifth coordination place on the zinc ion with the polymer oxygen atoms and therefore accelerates the translocation process, which results in the observed trend. In the smaller and rigid **Zn1**, these interactions are also likely to play a role in the translocation process, but this is not expressed in the overall threading curves since, for this receptor, the translocation process is still considerably faster than the initial binding event.

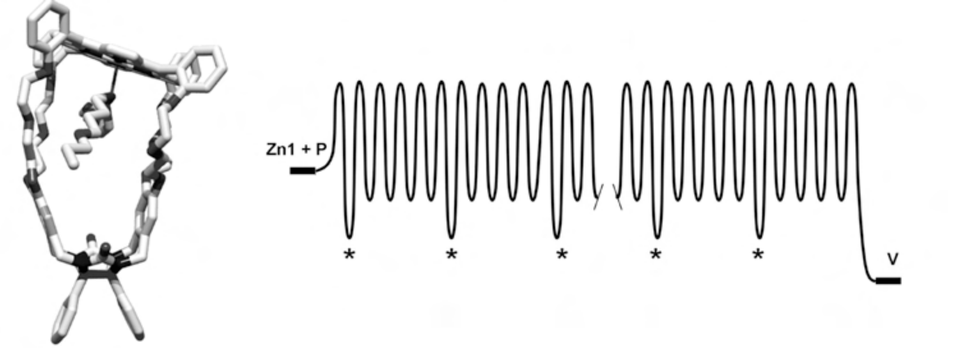

Figure 6. Molecular model of **Zn2** and part of a poly-THF chain (left) in which a polymer oxygen atom is coordinated to the porphyrin zinc centre inside the cavity. This interaction is believed to provide extra stabilization of the local energy minima on the chain, as can be seen in the consecutive hopping energy landscape on the right, and hence leads to slower translocation speeds. Bulky pyridine ligands coordinate to the zinc ion on the outside of **Zn2** and compete with the coordination of the polymer, resulting in accelerated translocation along the chain.

4. Conclusion

The threading of the larger and more flexible porphyrin macrocycle **$H_2$2** over polymer chains was found to be completely different than the threading of the smaller and more rigid macrocycle **1**. The difference was expressed in the polymer chain length dependencies, but also in the obtained activation parameters from the Eyring plots. An important finding was that **$H_2$2** exhibits considerably slower translocation speeds when compared to **1**. Receptor **1** has little affinity for the chain, which results in a fast translocation process that is not expressed in the overall threading curves. In contrast, the flexible macrocycle **$H_2$2** has a considerable affinity for the chain, presumably as a result of induced-fit binding effects, leading to a slower translocation process, which is expressed in the overall threading curves. This results in deviations of the calculated rate constants and to extreme deviations in the calculated activation parameters upon slight changes in the experimental concentrations. The initial binding of **$H_2$2** to the polymer chain has a (highly uncommon) negative activation enthalpy, which can be ascribed to the opening of the cavity at lower temperatures. The translocation process on the other hand is enthalpically favorable and entropically demanding and can be ascribed to the release of the tight binding of the macrocycle to the chain upon translocation.

The zinc derivative **Zn2** was found to thread faster than **$H_2$2**. This is surprising because in all preceding studies the kinetics of pseudo-rotaxane complex formation for zinc-porphyrin macrocycles has been shown to be slower compared to their free-base derivatives. Although, the exact causes of this observation remain to be uncovered, it emphasizes that the initial threading process has a very different mechanism than for instance slippage processes and that the rate of initial complex formation between chain and flexible cavity is determined by very subtle differences in the properties of the cavity.

Upon binding of the bulky pyridine **A1** to the outside of **Zn2**, the threading process was accelerated as a result of an activation of the cavity by the removal of obstructing interactions inside the cavity. In addition, the observed length dependencies changed, which suggests that **A1** also accelerates the translocation process by inhibiting the coordination site on the zinc ion and thereby obstructs the coordinative interactions that decelerate the translocation speed.

The presented study clearly reveals that the threading process is highly dependent on the nature of the macrocycle. It would be interesting to study the threading of the flexible cavities of **$H_2$2** and **Zn2** further and unravel the threading process even more. Threading over shorter chains should provide more details about the initial binding mechanism, whereas the threading over longer polymers will reveal information about the translocation process. It would be desirable to have a binding site connected to the chains that has higher affinity for the cavity of **$H_2$2** than a viologen. This would lead to better binding curves and hence reduced experimental errors.

4. Experimental Section

Materials and methods. Chloroform and acetonitrile used in titration experiments were distilled from $CaCl_2$. K_2CO_3 was dried in an oven (150 °C). All other solvents and chemicals were commercial materials and used as received. Merck silica gel (60H) was used for column chromatography and Merck silica gel F254 plates were used for thin layer chromatography (TLC) and preparative TLC. Molecular modeling calculations were performed with the use of Spartan. Fluorescence experiments were performed on a Perkin-Elmer LS50B luminescent spectrometer equipped with a thermostatted cuvette holder. UV-Vis spectra were recorded on a Cary 100 Conc (Varian, Middelburg) UV-Vis spectrometer. Maldi-TOF MS was performed on a Bruker Biflex III spectrometer. NMR spectra were taken on a Varian Inova 400 (400 MHz, ^{1}H and 2D spectra) and calibrated to an internal standard of tetramethylsilane. The syntheses of **$H_2$1**,$^{\text{Chapter 3}}$ **Zn1**, $^{\text{Chapter 3}}$ **$H_2$2**, $^{\text{Chapter 2}}$ **Zn2**, $^{\text{Chapter 2}}$ **P1–P7**, $^{\text{Chapter 6}}$ and **A1** $^{\text{Chapter 2}}$ have been described elsewhere in this thesis. **V1** was synthesized according to a literature procedure.[1]

Determination of threading rate constants. Prior to performing the experiments, the porphyrin macrocycles **$H_2$2** and **Zn2** were purified by preparative TLC, followed by a short silica column and precipitation in pentane. The threading kinetics were measured by using the time drive application of the fluorescence spectrometer software. The sample was excited at the wavelength corresponding to the maximum absorbance of the porphyrin Soret band and the emission at the wavelength corresponding to the maximum emission was recorded in time. Typically, to a weighed solution of 1 μM of porphyrin macrocycle, a known amount of viologen derivative was added and the solution mixed. After the mixing time (1.5 s) the measurement was started. The data were analysed according to standard 1:1 kinetic isotherms that describe the kinetics involved in complex formation between A and B, to form C (Equations 6–9).[23] From the fit, both the rate constant k_{on} and equilibrium association constant K_{assoc} were obtained. All the experiments were performed in plural and at different concentrations of polymer and porphyrin macrocycle to decrease the experimental error.

$$\mathrm{A} + \mathrm{B} \underset{k_{\text{off}}}{\overset{k_{\text{on}}}{\rightleftharpoons}} \mathrm{C}$$

$$[\mathrm{C}] = p\frac{\left(1-\frac{q}{p}\frac{p-[\mathrm{C}]_\mathrm{o}}{q-[\mathrm{C}]_\mathrm{o}}e^{k_{\text{on}}(p-q)t}\right)}{\left(1-\frac{p-[\mathrm{C}]_\mathrm{o}}{q-[\mathrm{C}]_\mathrm{o}}e^{k_{\text{on}}(p-q)t}\right)} \tag{6}$$

$$p = [\mathrm{C}]_{\text{eq}} = \frac{([\mathrm{A}]_\mathrm{o}+[\mathrm{B}]_\mathrm{o}+\frac{1}{K_{\text{assoc}}})-\sqrt{([\mathrm{A}]_\mathrm{o}+[\mathrm{B}]_\mathrm{o}+\frac{1}{K_{\text{assoc}}})^2-4\cdot[\mathrm{A}]_\mathrm{o}\cdot[\mathrm{B}]_\mathrm{o}}}{2} \tag{7}$$

$$q = \frac{[\mathrm{A}]_\mathrm{o}[\mathrm{B}]_\mathrm{o}}{[\mathrm{C}]_{\text{eq}}} \tag{8}$$

$$K_{\mathrm{assoc}} = \frac{[\mathrm{C}]_{\mathrm{eq}}}{\left([\mathrm{A}]_{\mathrm{o}} - [\mathrm{C}]_{\mathrm{eq}}\right)\cdot\left([\mathrm{B}]_{\mathrm{o}} - [\mathrm{C}]_{\mathrm{eq}}\right)} = \frac{k_{\mathrm{on}}}{k_{\mathrm{off}}} \qquad (9)$$

5. References

1. Coumans, R. G. E.; Elemans, J. A. A. W.; Nolte, R. J. E.; Rowan, A. E. *Proc. Nat. Acad. Sci. USA* **2006**, *103*, 19647–19651.
2. Hidalgo Ramos, P.; Coumans, R. G. E.; Deutman, A. B. C.; Smits, J. M. M.; de Gelder, R.; Elemans, J. A. A. W.; Nolte, R. J. M.; Rowan, A. E. *J. Am. Chem. Soc.* **2007**, *129*, 5699–5702.
3. Herrmann, W.; Keller, B.; Wenz, G. *Macromolecules* **1997**, *30*, 4966–4972.
4. For a detailed description, see Chapter 6 of this thesis.
5. Sung, W.; Park, P. J. *Phys. Rev. Lett.* **1996**, *77*, 783–786.
6. Muthukumar, M. *J. Chem. Phys.* **1999**, 111, 10371–10374.
7. Storm, A. J.; Storm, C.; Chen, J.; Zandbergen, H.; Joany, J.-F.; Dekker C. *Nano Lett.* **2005**, *5*, 1193–1197.
8. Kasioanowicz, J. J.; Brandin, E.; Branton, D.; Deamer, D. W. *Proc. Nat. Acad. Sci. U.S.A.* **1996**, *93*, 13770–13773.
9. Kantor, Y.; Kardar, M. *Phys. Rev. E.* **2004**, *69*, 021806.
10. Kolomeisky, A. B. *Biophysical Journal* **2008**, *94*, 1547–1548.
11. Muthukumar, M. *Annu. Rev. Biophys. Biomol. Struct.* **2007**, *36*, 435–450.
12. Gauthier, M. G.; Slater, G. W. *J. Chem. Phys.* **2008**, *128*, 205103.
13. Gauthier, M. G.; Slater, G. W. *J. Chem. Phys.* **2008**, *128*, 175103.
14. van't Hoff, J. H. *Etudes de Dynamique Chimique,* **1884**, F. Muller, Amsterdam.
15. Eyring, H. *Chem. Rev.* **1935**, *17*, 65–77.
16. Although care must be taken: since the initial binding event is faster at lower temperatures, $t_{1/2\text{-initial}}$ is also larger, which could, in principle, cause the translocation process, without actually being slower, to be expressed to a larger extent in the measured length dependency (hence an increase in calculated value of $\Delta G^{\neq}{}_{\mathrm{atom}}$).
17. Affeld, A.; Hübner, G. M.; Seel, C.; Schalley, C. A. *Eur. J. Org. Chem.* **2001**, 2877–2890.
18. Linnartz, P.; Bitter, S.; Schalley, C. A. *Eur. J. Org. Chem.* **2003**, 4819–4829.
19. Asakawa, M.; Ashton, P. R.; Ballardini, R.; Balzani, V.; Belohradsky, M.; Gandolfi, M. T.; Kocian, O.; Prodi, L.; Raymo, F. M.; Stoddart, J. F.; Venturi, M. *J. Am. Chem. Soc.* **1997,** *119,* 302–310.
20. Raymo, F. M.; Stoddart, J. F. *Pure & Appl. Chem.* **1997**, *69*, 1987–1997.
21. Oliveberg, M.; Tan, Y.-J.; Fersht, A. R. *Proc. Nat. Acad. Sci. USA* **1995**, *92*, 8926–8929.
22. Schneider, W. *Proc. Nat. Acad. Sci. USA* **1979**, *76*, 2283–2287.
23. Koppelman, S. J.; van Hoeij, M.; Vink, T.; Lankhof, H.; Schiphorst, M. E.; Damas, C.; Vlot, A. J.; Wise, R.; Bouma, B. N.; Sixma, J. J. *Blood* **1996**, *87*, 2292–2300.

8

Threading by an Intramolecular Looping Mechanism

1. Introduction

The translocation of biopolymers through pores and channels plays a critical role in numerous biological processes, such as DNA replication,[1–3] protein transport through membranes,[4–6] and infection of cells by viruses.[7,8] In the replication process circular clamp proteins are critical components of the DNA replication machinery.[9] They encircle the DNA and keep the polymerases bound to their template to ensure that the replication proceeds with high fidelity. The Nolte group has previously reported a synthetic analogue of such naturally occurring catalytic rotaxane systems. [10] In contrast to the clamps in nature, which can load onto the DNA at specific positions along the chain, the synthetic analogue had to find the open end of the polymer chain in order to thread on. The intriguing question is how this initial event actually occurs, since it also plays a critical role in the first step of biopolymer translocation. In post-translational protein translocation across membranes in eukaryotes, the biopolymer contains a signal sequence, which is selectively recognized by a binding site on/or in the vicinity of the channel after which the protein is actively translocated through the channel into the next cellular compartment (Figure 1).[11] This initial binding event accounts for the selectivity and the efficiency of many natural polymer translocation systems. The Nolte group has developed synthetic analogues of such polymer translocation systems that allow the determination of threading rates of polymers through synthetic macrocycles with unequalled accuracy.[12,13] It makes use of the host-guest binding properties between macrocyclic porphyrin receptors and viologen derivatives, which are substituted with oligomer or polymer derivatives on one side and a bulky blocking group on the other. Pseudo-rotaxane[14–16] complex formation can only be assessed after the complete movement of the polymer along the chain. The length dependencies of traversing molecular chains can be rationalized with the help of a consecutive hopping model[17] that involves an entron effect. In this chapter, the threading of macrocycles over middle ranged chain lengths (8 to 22 atoms) and the threading onto polymers of newly synthesized macrocycles with an affinity for the viologen moiety on the outside of the cavity will be discussed.

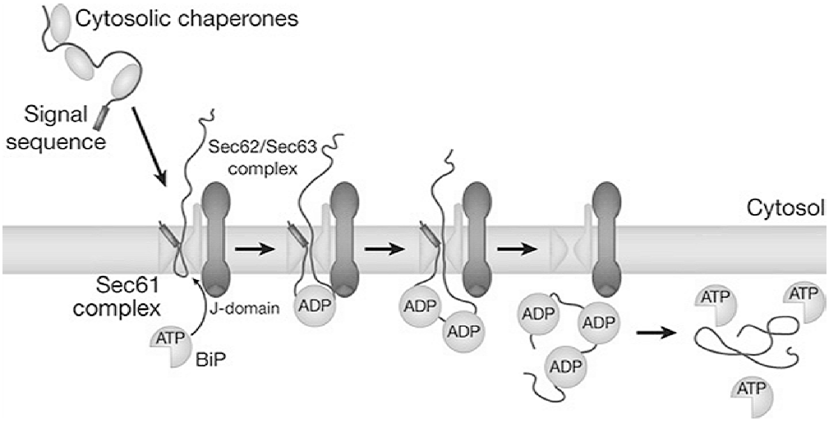

Figure 1. Proposed model of post-translational translocation of proteins in eukaryotes. After the protein synthesis by the ribosome, chaperones assist in keeping the signal sequence-containing protein in its unfolded state. Translocation begins with the binding of a translocation substrate to the channel. During this step, all cytosolic chaperones are released from the substrate. Once the polypeptide is inserted into the channel, its translocation occurs by a ratcheting mechanism. The polypeptide chain in the channel can slide in either direction by means of brownian motion, but its binding to BiP (an endoplasmic reticulum chaperone) inside the lumen of the endoplasmic reticulum prevents movement back into the cytosol, which results in a net forward translocation. ATP-bound BiP with an open peptide-binding pocket interacts with the J-domain of Sec63, which causes rapid ATP hydrolysis and closure of the peptide-binding pocket around the translocation substrate. J-domain-activated BiP has a low binding specificity that allows it to interact with essentially any polypeptide segment that emerges from the channel into the lumen of the endoplasmic reticulum. When the polypeptide has moved sufficiently in the forward direction, the next BiP molecule can bind. This process is repeated until the polypeptide chain has completely traversed the channel. Finally, exchange of ADP for ATP opens the peptide binding pocket and releases BiP.[5]

2. Results and discussion

2.1 Kinetics and thermodynamics of pseudo-rotaxane formation

The series of viologen derivatives containing chains varying in length between 5−8 carbon atoms (**V5**−**V8**; Chart 1 and Chapter 6) was initially extended with decyl- and octadecyl-substituted **V10** and **V18** (Chart 1). Preliminary fluorescence threading experiments with **$H_2$1** and **Zn1** and these newly synthesized viologen derivatives revealed, surprisingly, that instead of the expected decrease in threading rate (k_{on}) upon the lengthening of the chains, the rates showed a slight increase as can be seen in Figure 2. Both **$H_2$1** and **Zn1** traverse a chain of 18 atoms faster than a chain of eight atoms, which is completely counterintuitive. To further evaluate this intriguing effect, the other viologen derivatives shown in Chart 1 (**V9**, **V12**, **V13**, **V20**, and **V22**) were also synthesized.

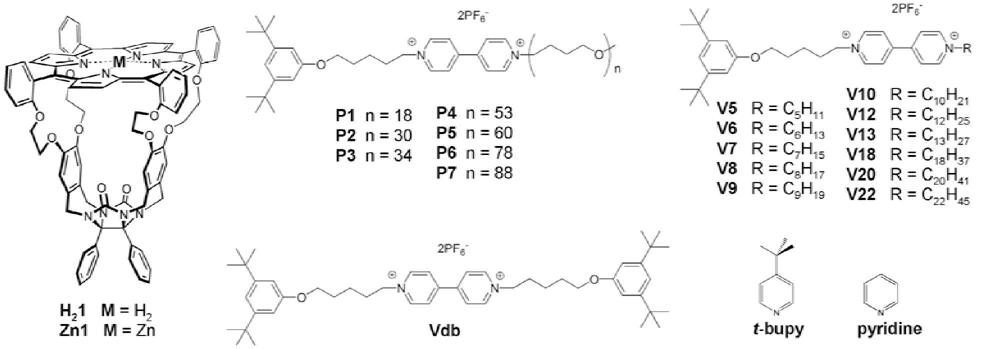

Chart 1. Molecules used in this chapter.

It was decided to fully investigate the kinetic and thermodynamic evolution of complex formation versus chain length. The threading rate constants (k_{on}) were determined for **$H_2$1**, **Zn1**, and **Zn1** in the presence of *t*-bupy (84 mM) with the help of fluorescence spectroscopy at sub-micromolar concentrations. The de-threading rates (k_{off}) of **Zn1** were measured by recording the increase of the porphyrin fluorescence in time after an approximate thousand-fold dilution of the pseudo-rotaxane complexes (see Chapter 4 for the method). In addition, the dissociation rates of the pseudo-rotaxane complexes between **Zn1** and the viologen derivatives as a result of competitive inhibition of the cavity of **Zn1** by pyridine (Chart 1) were measured at three different concentrations of pyridine (0.15 M, 0.30 M, and 1.4 M). The individual experiments provided both the rate constants (k_{on}, $^{\text{t-bupy}}k_{on}$, k_{off}, and $^{\text{pyridine}}k_{off}$) and the equilibrium association constants (K_V, $^{t\text{-bupy}}K_V$-app, and $^{\text{pyridine}}K_V$-app) for the binding of **Zn1** and **$H_2$1**, respectively, with the series of viologen derivatives and in the presence of coordinating pyridines. Some of the experimental curves are presented in Figures 2 and 3, and the extrapolated data are presented in Figure 4 and Tables 1 and 2.

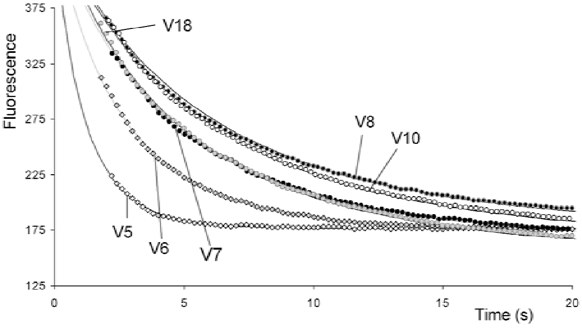

Figure 2. Fluorescence emission curves of threading processes between **Zn1** and **V5**, **V6**, **V7**, **V8**, **V10**, and **V18**, respectively, which reveal the decrease in threading rate in the series **V5**–**V8** after which the rates increase when the chain becomes longer than eight atoms (**V10** and **V18**).

Complex formation of H_21 and Zn1. A nice evolution was observed in the experimentally observed threading-on rates (k_{on}) of **H_21** and **Zn1** when plotted versus chain length of the viologen derivatives (Figure 4a), which suggests little experimental error in the individually obtained rate constants. When the chain becomes longer than circa eight atoms, the threading rate of both **H_21** and **Zn1** increases to the extent that a chain of 22 atoms is traversed faster than a chain of eight atoms. The calculated values for the association constants were not as accurate as the values for the rate constants, as can be seen from the plots of evolution of K_{assoc} versus chain length (Figure 4c). This is due to the fact that it is not possible to derive association constants higher than ~ 8×10^6 M^{-1} very accurately at the used experimental concentrations.[18] Although the values remain in the same order of magnitude for each receptor, independent of chain length, a slight increase in association constant upon an increase in substituent size could be observed. This is a phenomenon that has been described before in the literature[12] and in this thesis[19] and can be attributed to small additional interactions between the substituents and the macrocycle in the pseudo-rotaxane complexes. Also in the de-threading rate constants (k_{off}) of **Zn1**, a relative increase could be observed for chains longer than eight atoms (Figure 4b). The measured de-threading rate constants were in excellent agreement (with errors less than a factor of 2) with the values of k_{off} that were calculated indirectly by using the relationship $K_{assoc} = k_{on}/k_{off}$. This further indicates that the threading is in accordance with the assumed kinetic and thermodynamic 1:1 binding model.

Table 1. Threading/de-threading rate constants (k_{on} and k_{off}) and the association equilibrium constants (K_V) for the complex formation of **H_21** and **Zn1** with the series of viologen derivatives and polymers.[a]

	H_21		**Zn1**		
	k_{on} ($M^{-1}s^{-1}$)	K_v [d] (M^{-1})	k_{on} [c] ($M^{-1}s^{-1}$)	k_{off} [d] (s^{-1})	K_v [d] (M^{-1})
V5	5.0×10^6 [d]	1.0×10^7	8.1×10^5	1.7×10^{-1}	3.9×10^6
V6	2.4×10^6 [c]	1.2×10^7	3.2×10^5	6.5×10^{-2}	4.8×10^6
V7	1.5×10^6 [c]	2.2×10^7	1.7×10^5	3.8×10^{-2}	4.4×10^6
V8	1.3×10^6 [c]	2.4×10^7	1.4×10^5	3.1×10^{-2}	4.8×10^6
V9	[e]	[e]	1.4×10^5	2.9×10^{-2}	5.0×10^6
V10	1.5×10^6 [c]	1.6×10^7	1.4×10^5	3.1×10^{-2}	4.7×10^6
V12	[e]	[e]	1.5×10^5	3.0×10^{-2}	5.2×10^6
V13	[e]	[e]	1.6×10^5	3.2×10^{-2}	5.1×10^6
V18	1.7×10^6 [c]	1.8×10^7	1.7×10^5	3.1×10^{-2}	5.5×10^6
V20	1.6×10^6 [c]	2.5×10^7	1.6×10^5	3.3×10^{-2}	5.2×10^6
V22	[e]	[e]	1.6×10^5	[e]	6.7×10^6
P1	7.5×10^4 [b]	2.6×10^7	1.0×10^4	[e]	8.5×10^6
P2	4.0×10^4 [b]	2.8×10^7	5.9×10^3	[e]	1.2×10^7
P3	3.6×10^4 [b]	2.8×10^7	[e]	[e]	[e]
P4	2.1×10^4 [b]	2.7×10^7	3.3×10^3	[e]	1.3×10^7
P5	1.9×10^4 [b]	2.9×10^7	[e]	[e]	[e]
P6	1.3×10^4 [b]	3.0×10^7	2.3×10^3	[e]	1.3×10^7
P7	1.2×10^4 [b]	3.0×10^7	[e]	[e]	[e]

[a] In 1/1 acetonitrile/chloroform (v/v) at 295 K. [b] Estimated error 15%. [c] Estimated error 25%. [d] Estimated error 35%. [e] Not determined.

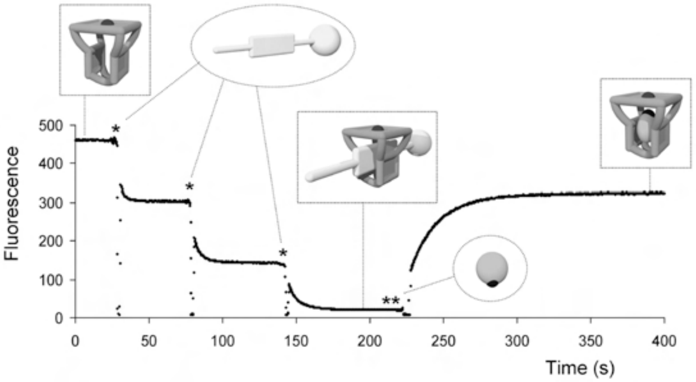

Figure 3. An example of a fluorescence titration experiment involving three additions of **V5** (*) to **Zn1**, that results in three binding isotherms from which the threading rate constant k_{on} and the association equilibrium constant K_{V} for the pseudo-rotaxane formation can be accurately determined. Finally, an excess (0.5 mL) of pyridine was added (**), which clearly provokes the equilibrium to shift away from the pseudo-rotaxane complex and in the direction of a complex in which pyridine is bound inside the cavity of **Zn1** (which displays fluorescence emission). This final isotherm provides both the dissociation (de-threading) rate constant ($^{\text{Py}}k_{\text{off}}$) in the presence of pyridine and an apparent association constant ($^{\text{Py}}K_{\text{V}}$-app), from which, on the basis of the known association constant between **Zn1** and pyridine (K_{Py}), the association constant between **Zn1** and **V5** with pyridine coodinating to the outside of the cavity $^{\text{Py}}K_{\text{V}}$ can be derived.

Table 2. Threading/de-threading rate constants ($^{t\text{-bupy}}k_{\text{on}}$ and $^{\text{Py}}k_{\text{off}}$) and apparent association equilibrium constants ($^{t\text{-bupy}}K_{\text{V}}$ and $^{\text{Py}}K_{\text{V}}$) for the complex formation between **Zn1** and the different viologen derivatives in the presence of coordinating axial ligands *t*-bupy and pyridine.[a]

	t-bupy		Pyridine					
	[*t*-bupy]$_{\text{o}}$ = 0.084 M		[pyridine]$_{\text{o}}$ = 0.15 M		[pyridine]$_{\text{o}}$ = 0.30 M		[pyridine]$_{\text{o}}$ =1.4 M	
	$^{t\text{-bupy}}k_{\text{on}}$ ($\text{M}^{-1}\text{s}^{-1}$)	$^{t\text{-bupy}}K_{\text{V}}$ (M^{-1})	$^{\text{Py}}k_{\text{off}}$ [d] (s^{-1})	$^{\text{Py}}K_{\text{V}}$ [d] (M^{-1})	$^{\text{Py}}k_{\text{off}}$ [d] (s^{-1})	$^{\text{Py}}K_{\text{V}}$ [d] (M^{-1})	$^{\text{Py}}k_{\text{off}}$ [d] (s^{-1})	$^{\text{Py}}K_{\text{V}}$ [d] (M^{-1})
V5	$3.8 \text{ x } 10^{6}$ [d]	$>1 \text{ x } 10^{8}$	$2.5 \text{ x } 10^{-2}$	$1.6 \text{ x } 10^{8}$	$3.6 \text{ x } 10^{-2}$	$1.0 \text{ x } 10^{8}$	$4.2 \text{ x } 10^{-2}$	$3.4 \text{ x } 10^{7}$
V6	$1.6 \text{ x } 10^{6}$ [c]	$>1 \text{ x } 10^{8}$	$9.5 \text{ x } 10^{-3}$	$1.9 \text{ x } 10^{8}$	$1.3 \text{ x } 10^{-2}$	$1.3 \text{ x } 10^{8}$	$1.8 \text{ x } 10^{-2}$	$3.6 \text{ x } 10^{7}$
V7	$1.1 \text{ x } 10^{6}$ [c]	$>1 \text{ x } 10^{8}$	$5.2 \text{ x } 10^{-3}$	$1.9 \text{ x } 10^{8}$	$7.2 \text{ x } 10^{-3}$	$1.3 \text{ x } 10^{8}$	$9.0 \text{ x } 10^{-3}$	$3.4 \text{ x } 10^{7}$
V8	$8.9 \text{ x } 10^{5}$ [c]	$>1 \text{ x } 10^{8}$	$4.3 \text{ x } 10^{-3}$	$2.0 \text{ x } 10^{8}$	$5.4 \text{ x } 10^{-3}$	$1.3 \text{ x } 10^{8}$	$6.7 \text{ x } 10^{-3}$	$3.7 \text{ x } 10^{7}$
V9	$7.5 \text{ x } 10^{5}$ [c]	$>1 \text{ x } 10^{8}$	$3.8 \text{ x } 10^{-3}$	$2.0 \text{ x } 10^{8}$	$4.9 \text{ x } 10^{-3}$	$1.4 \text{ x } 10^{8}$	$6.2 \text{ x } 10^{-3}$	$3.7 \text{ x } 10^{7}$
V10	$8.3 \text{ x } 10^{5}$ [c]	$>1 \text{ x } 10^{8}$	$3.9 \text{ x } 10^{-3}$	$2.1 \text{ x } 10^{8}$	$4.8 \text{ x } 10^{-3}$	$1.4 \text{ x } 10^{8}$	$6.2 \text{ x } 10^{-3}$	$3.4 \text{ x } 10^{7}$
V12	$8.3 \text{ x } 10^{5}$ [c]	$>1 \text{ x } 10^{8}$	$3.7 \text{ x } 10^{-3}$	$2.1 \text{ x } 10^{8}$	$4.7 \text{ x } 10^{-3}$	$1.5 \text{ x } 10^{8}$	$5.7 \text{ x } 10^{-3}$	$4.7 \text{ x } 10^{7}$
V13	$7.7 \text{ x } 10^{5}$ [b]	$>1 \text{ x } 10^{8}$	$3.6 \text{ x } 10^{-3}$	$2.2 \text{ x } 10^{8}$	$4.4 \text{ x } 10^{-3}$	$1.5 \text{ x } 10^{8}$	[e]	[e]
V18	$7.3 \text{ x } 10^{5}$ [b]	$>1 \text{ x } 10^{8}$	$3.0 \text{ x } 10^{-3}$	$2.3 \text{ x } 10^{8}$	$3.6 \text{ x } 10^{-3}$	$1.7 \text{ x } 10^{8}$	$4.2 \text{ x } 10^{-3}$	$5.2 \text{ x } 10^{7}$
V20	$6.6 \text{ x } 10^{5}$ [b]	$>1 \text{ x } 10^{8}$	$2.8 \text{ x } 10^{-3}$	$2.1 \text{ x } 10^{8}$	$3.4 \text{ x } 10^{-3}$	$1.6 \text{ x } 10^{8}$	[e]	[e]
V22	$5.5 \text{ x } 10^{5}$ [b]	$>1 \text{ x } 10^{8}$	[e]	[e]	[e]	[e]	[e]	[e]
P1	$2.3 \text{ x } 10^{4}$ [b]	$>1 \text{ x } 10^{8}$	[e]	[e]	[e]	[e]	[e]	[e]
P2	$1.3 \text{ x } 10^{4}$ [b]	$>1 \text{ x } 10^{8}$	[e]	[e]	[e]	[e]	[e]	[e]
P4	$7.5 \text{ x } 10^{3}$ [b]	$>1 \text{ x } 10^{8}$	[e]	[e]	[e]	[e]	[e]	[e]
P6	$5.0 \text{ x } 10^{3}$ [b]	$>1 \text{ x } 10^{8}$	[e]	[e]	[e]	[e]	[e]	[e]

---

[a] In 1/1 acetonitrile/chloroform (v/v) at 295 K. [b] Estimated error 15%. [c] Estimated error 25%. [d] Estimated error 35%. [e] Not determined.

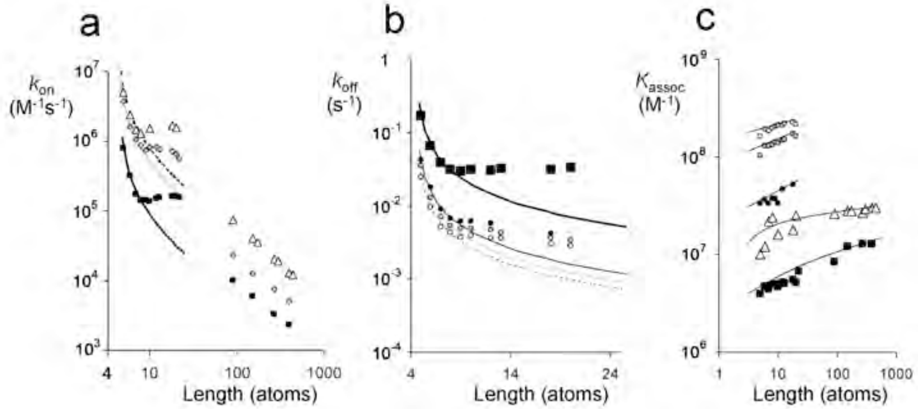

Figure 4. Rate constants for the threading (k_{on}; (a)) and de-threading (k_{off}; (b)) processes and the association equilibrium constants K_{assoc} (c) for the threading of viologens with various chain lengths by **$H_2$1** (△), **Zn1** (■), **Zn1** in the presence of *t*-bupy (◇), and **Zn1** in the presence of increasing concentrations of pyridine: 0.15 M (○), 0.30 M (◎), and 1.4 M (●).

Threading of Zn1 in the presence of coordinating pyridine ligands. As expected the threading rates of **Zn1** in the presence of *t*-bupy ($^{t\text{-bupy}}k_{on}$) were higher than in its absence as a result of the activation of the cavity by coordination of the ligand to its outside (Chapter 4). Also in the presence of *t*-bupy, a change in trend was observed for chains longer than eight atoms. The increase in threading rate was, however, less pronounced compared to the threading through **$H_2$1** and **Zn1** (Figure 4a), which indicates that *t*-bupy somehow has a 'smoothing effect' on the observed change in trend. The presence of pyridine on the de-threading of **Zn1** revealed a similar effect on the rate constants $^{Py}k_{off}$ as the presence of *t*-bupy on $^{t\text{-bupy}}k_{on}$. Although the length dependency clearly deviates from the expected length dependency according to the consecutive hopping model, the changes are less pronounced than those observed in the absence of pyridine (Figure 4b). Higer concentrations of pyridine (up to 1.4 M) also start to significantly influence the calculated experimental rate and association constants: upon increasing concentrations of pyridine, the rate constants $^{Py}k_{off}$ increase and the association constants $^{Py}K_V$ decrease (see Table 2 and Figures 4b and 4c). Theoretically, these values should be identical at the used pyridine concentrations since, in all cases, the pseudo-rotaxane complexes are fully (>99.9%) saturated with pyridine bound to the outside of the cavity of **Zn1**.[20] The deviations in the k_{off} values are most likely caused by changes of the solvent polarity as a result of the high pyridine concentration, as discussed in Chapter 4. The deviations in $^{Py}K_V$ are possibly a combination of these changes in polarity and non-coordinative binding of pyridine inside the cavity. In addition, a close look at Figure 4b reveals that the change in trend after a chain length of 8 atoms slowly becomes less pronounced upon increasing concentrations of pyridine. This indicates that it can not solely be the binding of pyridine to the outside of the cavity of **Zn1** that causes the smoothing effect on the change in trend.

^{1}H-NMR spectroscopic experiments. In order to verify that the experimental observations are not an artefact, for instance, caused by a binding stoichiometry between macrocycle and guest other than 1:1, ^{1}H-NMR experiments were performed. Titrations of **H$_2$1** with **V5** and **V20** in 1/1 $CDCl_3/CD_3CN$ (v/v) revealed the formation of 1:1 complexes (Figure 5). Although the signals of the pseudo-rotaxane complexes slightly shift and broaden when small amounts of the viologen derivatives were added to the 1:1 complexes, which could be the result of the formation of very small amounts of 2:1 macrocycle/viologen complexes, the main complexation geometry is that of the 1:1 complex independent of the concentration of viologen. Considering that the fluorescence binding experiments are performed at a thousand-fold lower concentration than the ^{1}H-NMR experiments, it can be safely concluded that at those concentrations only 1:1 complexes will be formed.[21] These observations are therefore fully in line with the reversible 1:1 binding processes derived from the fluorescence binding isotherms. The increase in the association constant value upon an increase in chain length, as observed in the fluorescence titration experiments, was moreover confirmed by competition ^{1}H-NMR experiments between **V5** and **V20** for the cavity of **H$_2$1**, which revealed that **V20** binds approximately a factor 1.3 stronger to **H$_2$1** than **V5**.

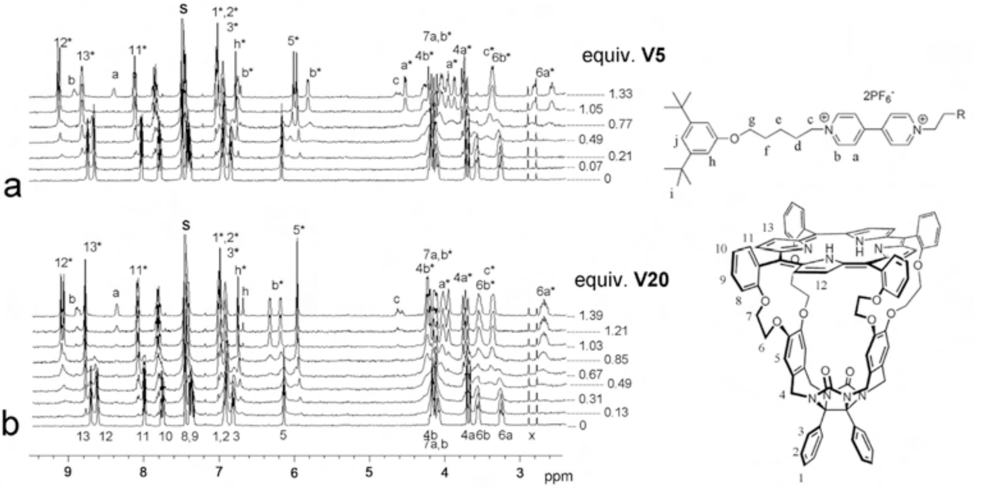

Figure 5. ^{1}H-NMR spectra of titrations of (from bottom to top) increasing amounts of (a) **V5** and (b) **V20** added to **H$_2$1**.

2.2 The intramolecular looping mechanism

The above measurements have clearly demonstrated that (at least at the used experimental concentrations, <μM), the threading rates increase for viologens with chain lengths in the range of 8−22 atoms, which significantly deviates from the expected length dependency according to the consecutive hopping model. The polymer chains, on the other hand, are traversed significantly slower and the length dependency can be described with the use of the consecutive hopping model

(Chapter 6). Apparently, for chains with lengths varying from eight to 22 atoms, a different threading pathway must be operative. Initially, a model was envisaged in which the macrocycle threads on by a loop in the polymer chain (Figure 8c). This model was however discarded on the basis of slippage studies, which revealed that the cavity of **H$_2$1** is too narrow to accommodate a folded chain (see Chapter 5). A second mechanism was therefore considered in which the threading is initiated and guided by interactions between the chain and the outside of the macrocycle, which leads to accelerated rates by means of transition state stabilization.[22]

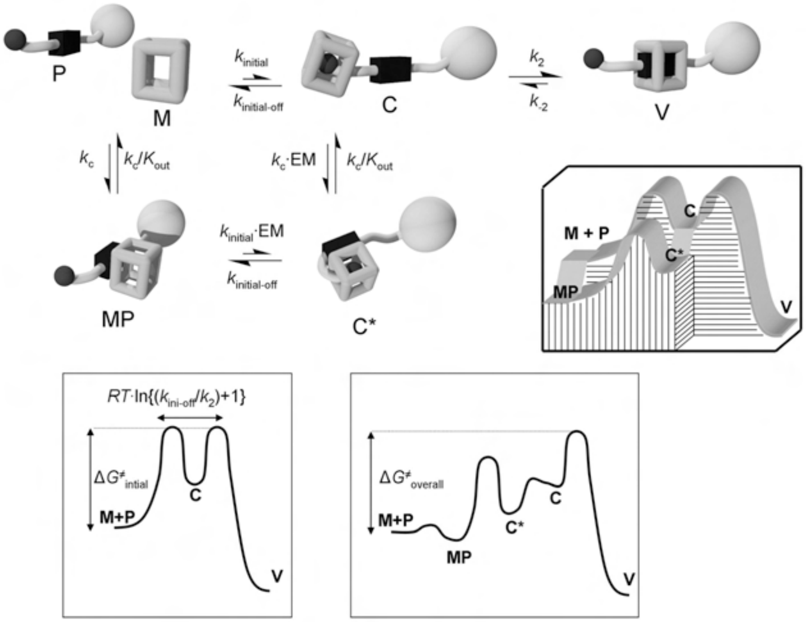

Figure 6. Simple two-step threading mechanism revealing how interactions between the binding site and the outside of the receptor can lead to transition state stabilization and enhanced overall threading rates. The bottom left energy profile represents the energy diagram of the intermolecular threading process and the bottom right energy profile the intramolecular looping pathway.

In order to show, using a simple example how this ‘intramolecular looping’ mechanism can cause accelerated threading rates, the binding scheme in Figure 6 was considered. The box represents the macrocycle (M) and the chain on the viologen derivative (P) contains one specific local energy minimum (represented by the sphere on the chain). The normal ‘intermolecular’ threading process would occur by first finding the local energy minimum on the chain (C), followed by the movement over the chain and the subsequent binding to the recognition site (V). In the alternative pathway, the macrocycle binds first to the recognition site (MP) with an association constant K_{out}, after which the initial binding of the open end of the chain inside the cavity (C*) has become an intramolecular process, very similar to a ring closure reaction. For this reason, the effective molarities (EM) of the two reactive components, i.e., the open end of the chain and the cavity, have to be taken into account. The effective molarity is a parameter that describes the relative ease of ring-closure reactions compared to intermolecular reactions under otherwise identical conditions.[23] Some literature values[24] of effective molarities of chains composed of skeletal single bonds are presented in Table 3. These experimentally obtained values, which were derived from a large number of different studies, represent the intramolecular reactivity that is corrected for the inherent reactivity of the end groups and therefore contain all the intrinsic parameters of the chains upon ring-closure, such as ring strain[25] and torsional entropy.[26] These data can therefore be used straightforward in our presented model. The initial binding of the chain inside the cavity by intramolecular 'ring-closure' (MP→C*) has a rate constant of magnitude $k_{\text{initial}}\cdot\text{EM}$. After having arrived on the chain (C*), the macrocycle can move further along this chain in the direction of the binding site (V). This can, however, only be achieved by first releasing the recognition site from the outside of the macrocycle (forming C), after which the last part of the chain can be traversed. When the experimental concentrations of MP (and consequently C and C*) are low compared to the free components M and P, which is the case for values lower than 5 x 10^4 M^{-1} for K_{out} at the experimental (~μM) concentrations, the expected overall rates can be derived with the use of the steady state approximation.[27] The intermolecular route will have an overall rate constant for the threading-on reaction according to Equation 1, whereas, when the intramolecular process is also allowed, the overall rate constant will evolve according to Equation 2 as a function of K_{out} and EM (these relations were confirmed by computer simulations using the program mathematica®).[28]

$$k_{\text{on-overall}} \approx \frac{k_{\text{initial}} \cdot k_2}{k_{\text{initial-off}} + k_2} \tag{1}$$

$$k_{\text{on-overall}} \approx \frac{k_{\text{initial}} \cdot k_2 \cdot (1 + K_{\text{out}} \cdot \text{EM})}{k_{\text{initial-off}} \cdot (1 + K_{\text{out}} \cdot \text{EM}) + k_2} \tag{2}$$

Therefore, even at low values (of ~ 1 or higher) of $K_{\text{out}}\cdot\text{EM}$, the overall threading can be considerably accelerated as a result of the intramolecular process. This is best illustrated with the energy profiles of the intermolecular and the intramolecular process as presented in Figure 6 (bottom). The overall activation energy of the intermolecular process depends on both the activation energy of the initial binding event ($\Delta G^{\neq}_{\text{initial}}$) and on the statistical chance of falling off the chain and onto the recognition site, which is determined by the relative magnitudes of $k_{\text{initial-off}}$ and k_2 (which adds another $RT\cdot\ln\{(k_{\text{initial-off}}/k_2)+1\}$ $\text{kJ}\cdot\text{mol}^{-1}$ to the overall activation energy). The activation energy of the initial binding event in the intramolecular process will be stabilized (with a magnitude of $-RT\cdot\ln(K_{\text{out}}\cdot\text{EM})$) and this barrier can therefore reduce in energy compared to the barrier associated with the traversing of the rest of the chain (C→V). As a result of this stabilization, the relative height (compared to the starting situation (M+P)) of this last barrier can become fully rate determining (Figure 6b), and the initial binding event is no longer expressed in the overall rate.

From the data in Table 3 it becomes clear that only small association constants (K_{out}) are required to obey the relation $K_{\text{out}}\cdot\text{EM}>1$ and hence to observe accelerated threading at the experimental concentrations. Even with a low association constant K_{out} of only 15 M^{-1} such a phenomenon of increased threading rates can already be expected for chains with lengths up to 20 atoms. In order to determine whether viologen derivatives indeed coordinate weakly to the outside of the cavities of **$H_2$1** and **Zn1** and therefore cause the observed phenomenon, a ^{1}H-NMR titration of **Zn1** with **Vdb** (a molecule that can not enter the cavity because of its blocking groups; Chart 1) was performed. The titration indeed revealed the formation of a complex in which the viologen binds to the outside of the receptor molecule. Figure 7 shows a selection of the shifting proton resonances upon the addition of **Vdb**. It can be clearly seen that the resonances of the β-pyrollic protons of **Zn1** that are located above the side walls (H-13; see Figure 7 for proton numbering scheme) shift downfield due to the deshielding effects of the viologen rings, whereas the resonances of the other β-pyrollic protons (H-12) remain in the same positions. The resonances of the side-wall protons (H-5) reveal an upfield shift upon the addition of **Vdb** as a result of shielding by the viologen ring-currents. The guest's proton resonances VH-a and VH-b show a clear downfield shift upon increasing concentrations of **Vdb**, which indicates that they are being shielded in the complex as a result of the side-wall and porphyrin ring-currents. These complexation-induced shifts therefore suggest that the viologen binds flat against one of the benzene side-walls of the cavity, as depicted in Figure 7. The titration curves could be nicely fitted to give an association constant (K_{out}) of 40 M^{-1}, a value that is theoretically large enough to result in accelerated threading rates for viologen derivatives with side-chain lengths of up to 40 atoms (Table 3). This is in agreement with the observation that the polymer chains (with lengths from 90–450 atoms) apparently do not benefit from this 'intramolecular looping' mechanism. Molecular modeling, moreover, revealed that only viologen derivatives containing chains longer than circa eight atoms can form a viologen complex on the outside of the receptor while simultaneously looping the open end of their chain inside the cavity. The intramolecular route can therefore only concern chains longer than eight atoms, which is in excellent agreement with the experimental observation that the change in trend of the accelerated threading rates occurs when the side-chains are longer than eight atoms (Figure 4).

Table 3. Literature[24] values of the EM's of molecular chains and the calculated values of K_{out} where $K_{out} \cdot EM = 1$, in which *n* is the number of skeletal single bonds.

n	EM (M)	K_{out} (M^{-1})
1	4.8 x 10^{5}	
2	6.4 x 10^{4}	
3	8.6 x 10^{3}	
4	1.1 x 10^{3}	
5	1.5 x 10^{2}	0.01
6	2.0 x 10	0.05
7	2.7	0.4
8	1.0	1.0
9	6.7 x 10^{-1}	1.5
10	4.7 x 10^{-1}	2.1
12	2.6 x 10^{-1}	3.9
14	1.6 x 10^{-1}	6.3
16	1.1 x 10^{-1}	9.1
20	6.9 x 10^{-2}	15
25	4.9 x 10^{-2}	20
30	3.8 x 10^{-2}	26
40	2.5 x 10^{-2}	40
50	1.8 x 10^{-2}	56

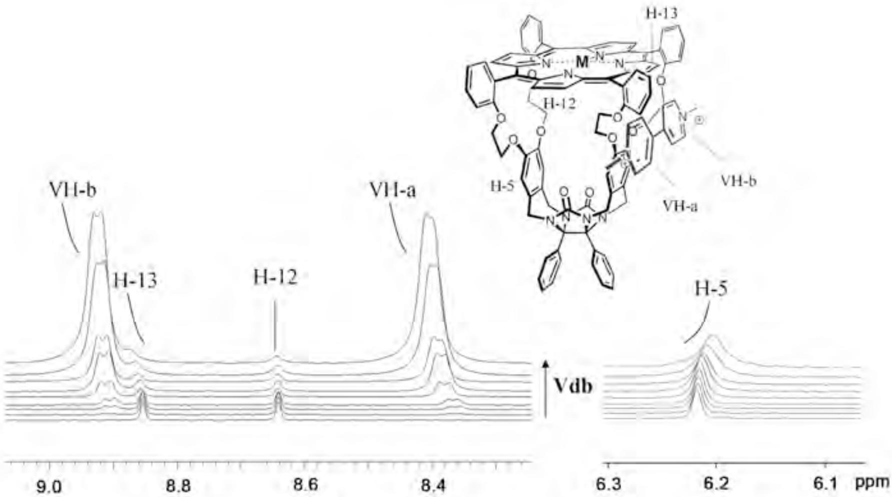

Figure 7. ^{1}H-NMR spectra of the titration of **Zn1** with (from bottom to top) increasing amounts of added **Vdb** and the proposed complexation geometry.

The overall model is, of course, slightly more complicated than that presented in Figure 6 since the threading is involved in a consecutive hopping model more analogous to that shown in Figure 8. So long as $K_{\mathrm{out}} \cdot \mathrm{EM} > 1$, the initial binding step (represented as k_{entron} in Figure 8) is more favorable when it can occur by the intramolecular route. Once bound to the chain, however, the macrocycle starts moving randomly along the chain. Each step that the macrocycle moves further in the direction of the viologen moiety results in an increase in effective molarity of the interacting components, i.e., the viologen moiety and the outside of the cavity. The movement in the direction of the binding site will therefore be both thermodynamically and kinetically downhill (directional). The resulting directional movement continues until the ring is fully closed and all but the last eight chain atoms are threaded inside or through the cavity (C_{c*} in Figure 8b). In order to move over these last eight chain atoms, the macrocycle has to release the viologen from the outside after which the last eight atoms can be traversed in a non-stabilized fashion. The threading over all the (n−8) chain atoms can, in principle, be accelerated to the extent that the traversing of the last eight chain atoms becomes fully rate limiting, which is in good agreement with the observation that the experimentally observed threading rates never become significantly higher than the rate observed for the traversing of eight chain atoms. It should be noted that one of the implications of the model is that when the ring is fully closed (C_{c*} in Figure 8b and in the energy diagram), the rate of threading off the chain (and reaching the starting situation M+P) is larger than the rate of dissociation from the outside of the cavity and subsequent movement along the final atoms of the chain to reach the viologen moiety (V).

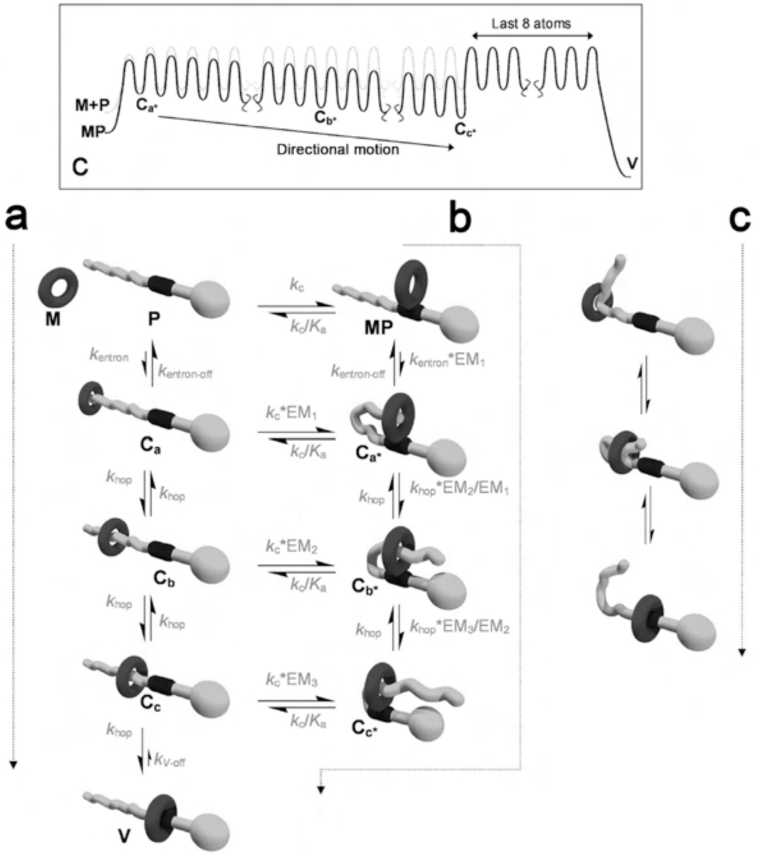

Figure 8. Binding scheme and energy diagram of the threading process represented as consecutive hopping steps. (a) Intermolecular process of threading. (b) Threading by intramolecular looping. (c) Threading over a folded chain. The energy diagram (top) represents the profile of the intramolecular path b. The energy profile of the intermolecular path a is shown in light grey to illustrate that the hopping over the initial chain atoms is lower in energy (faster) for the intramolecular process than for the intermolecular process.

The above described mechanism provides an excellent explanation for the observed relative increase in threading rates in the region between eight and 22 atoms. The intramolecular process can be expected to have a significant influence on the overall rates in the region of viologen chains where $K_{out}\cdot EM \geq 1$. This condition is not met for the polymer derivatives, of which the major part of the chains is traversed by the non-stabilized intermolecular pathway. The fact that the relative increase in rates is less pronounced in the presence of high concentrations of coordinating pyridine ligands suggests that the value K_{out} is lower under these conditions. This is most likely the result of a solvent effect, i.e., interactions between the pyridines and the viologen derivatives that compete with the outside complexation with the macrocycles (which also cause the observed lower association constants for the inside of the cavity at increasing concentrations of pyridine ligand). Another explanation could be that, in addition to the complexation geometry of **Vdb** with **Zn1** proposed in Figure 7, the viologen derivatives also bind weakly to the porphyrin roof of the macrocycle, a binding site that is obviously obstructed by the coordinating pyridine ligands.

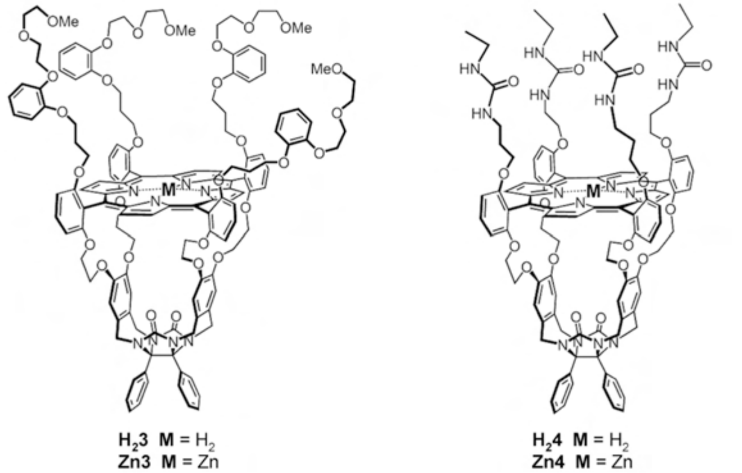

Chart 2. Porphyrin macrocycles **$H_2$3**, **Zn3**, **$H_2$4**, and **Zn4** bearing substituents on their roofs that could display affinity for the viologen moieties and thereby facilitate transition state stabilization during the threading process.

2.3 Synthesis of new macrocycles

In order to further confirm the proposed mechanism, it was decided to synthesize some new porphyrin macrocycles bearing the same cavity as **$H_2$1** and **Zn1**, but with additional functionalities for the binding of viologen derivatives located on the roof of the porphyrin. Higher binding constants of viologen derivatives to the outside of the macrocycle should, in principle, also result in accelerated threading over the appended polymer chains by the intramolecular looping mechanism. **$H_2$3** and **Zn3** (Chart 2) were chosen as good candidates since they contain crown ether functionalities which should, in principle, be capable of embracing the positive charges of the viologen moieties. Also **$H_2$4**, which was previously synthesised in the groups of Nolte and Rowan,[29] might also have an affinity to bind viologens to the outside of the cavity as a result of interactions between the guests and the urea-containing tails.

The synthesis of **$H_2$3** and **Zn3** is presented in Scheme 1. Tosylate **5**[30] was reacted with catechol (**6**) in the presence of K_2CO_3 to form compound **7** in a moderate yield. Alcohol **7** was then reacted with 1,3-dibromopropane in the presence of base to yield, after purification, bromide **8**. The bromide was reacted with the tetrahydroxy porphyrin macrocycle **$H_2$2** in the presence of K_2CO_3 to give **$H_2$3** in a yield of 43% after purification by column chromatography, preparative TLC, and precipitation. **$H_2$3** could be quantitatively converted into its zinc derivative (**Zn3**) by the reaction with excess zinc acetate dihydrate in a 1/1 (v/v) mixture of chloroform and methanol.

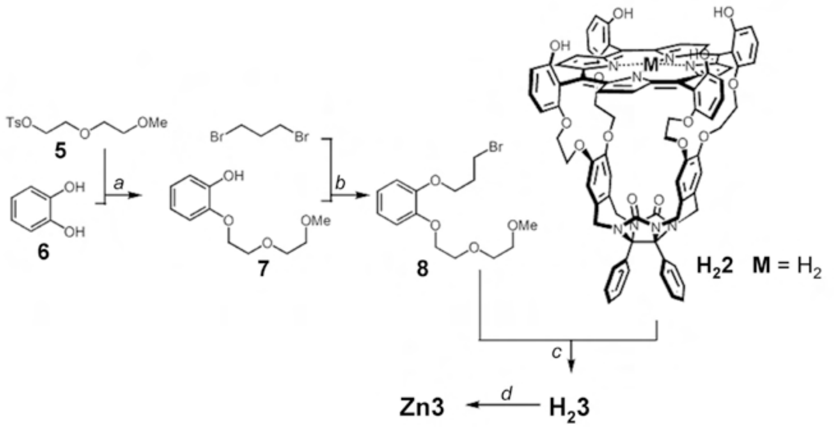

Scheme 1. Synthesis of porphyrin macrocycles **$H_2$3** and **Zn3**. Reagents and conditions: *a*) K_2CO_3, DMF, 100 °C, 58%; *b*) K_2CO_3, DMF, 50 °C, 12h, 53%; *c*) K_2CO_3, DMF, 50 °C, 48h, 43%; d) $Zn(OAc)_2 \cdot 2H_2O$, $CHCl_3$/MeOH 1/1 (v/v).

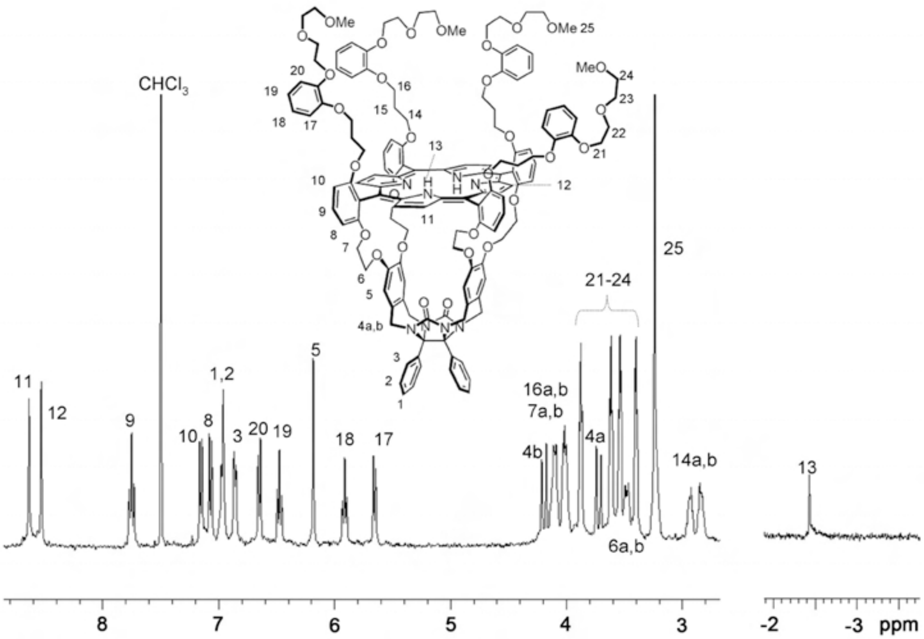

Figure 9. Partial 400 MHz ^{1}H-NMR spectrum of **$H_2$3** in 1/1 (v/v) $CDCl_3/CD_3CN$ with proton assignments.

The ^{1}H-NMR spectrum of $\mathbf{H_23}$, in which all the relevant resonances can be seen, is shown in Figure 9. The upfield shifts of the spacer *o*-dialkoxyphenyl proton resonances (17, 18, 19, and 20) compared to those values of **8** (on average $\Delta\delta = -0.58$ ppm) indicate that the 'binding clamps' are located nicely on top of the roof of the macrocycle. The cavity resonances are located at similar positions as those of $\mathbf{H_21}$, which suggests that the cavity is not occupied by the spacers (either intramolecularly or intermolecularly).

2.4 Threading of $\mathbf{H_23}$, Zn3, and $\mathbf{H_24}$

^{1}H-NMR titration experiments of $\mathbf{H_23}$ and $\mathbf{H_24}$ with **Vdb** revealed that, contrary to expectation, the substituents on top of the macrocycles were not capable of binding the viologen moiety of the guest. The addition of large quantities of **Vdb** did not lead to significant shifts of the proton resonances belonging to these substituents, and the binding constants K_{out} were of the same order of magnitude ($<< 100$ M^{-1}) as those observed for the binding of **Vdb** to **Zn1**. As a result, no enhanced threading over the polymer chains as a result of the intramolecular pathway was expected. Fluorescence threading experiments with $\mathbf{H_23}$, **Zn3,** and $\mathbf{H_24}$ confirmed this hypothesis. The threading rate constants plotted versus chain length for $\mathbf{H_23}$, **Zn3**, and $\mathbf{H_24}$ are presented in Figures 11a-c; the rates of reference receptors (either $\mathbf{H_21}$ or **Zn1**) and the expected evolution, based on the threading over the shortest chains according to the consecutive hopping model, are added as a guide. Both $\mathbf{H_23}$ and $\mathbf{H_24}$ traverse each of the individual chains slower than $\mathbf{H_21}$, and no relative increase in threading rates were observed in the polymer region. For both receptors the relative increase in the region between eight and 22 chain atoms is less pronounced than for $\mathbf{H_21}$, which suggests that the value of K_{out} is even lower for $\mathbf{H_23}$ and $\mathbf{H_24}$ than for $\mathbf{H_21}$. The rates of traversing the shortest chains are faster for **Zn3** than for **Zn1**, which is presumably the result of activation of the cavity of **Zn3** by interactions between the zinc ion and the oxygen atoms of the substituents on the roof of the macrocycle. This was confirmed by the observation that the proton resonances of these substituents appeared slightly broadened in the ^{1}H-NMR spectrum of **Zn3**, which is indicative of intramolecular zinc-oxygen coordination. This 'outside' coordination is expected to compete with possible obstructing elements inside the cavity, such as solvent molecules, and it thereby activates the cavity for the threading process. The rates of traversing the polymer chains are comparable for **Zn3** and **Zn1**, which indicates that the relative difference in rate between traversing the short and the long chains is larger for **Zn3** than for **Zn1**. The combined data therefore suggest that instead of an anticipated increase in threading rates over the polymer chains as a result of the intramolecular pathway, this pathway is less favorable for macrocycles $\mathbf{H_23}$, **Zn3** and $\mathbf{H_24}$ when compared with $\mathbf{H_21}$ and **Zn1**.

2.5 Threading of $\mathbf{H_22}$ and Zn2

Surprisingly, ^{1}H-NMR and UV-Vis titration experiments revealed that $\mathbf{H_22}$ (the precursor of $\mathbf{H_23}$ and $\mathbf{H_24}$) and **Zn2** have a substantial affinity for **Vdb** (Figure 10). Association constants of $K_{\text{out}} = 2 \times 10^4$ M^{-1} and $K_{\text{out}} = 5 \times 10^4$ M^{-1} were calculated for the binding of **Vdb** with **Zn2** and $\mathbf{H_22}$, respectively, and these high values are plausibly the result of stabilizing interactions between the

OH-functionalities of the receptors and the viologen moiety of the guest. In contrast to all the other macrocycles studied in the previous section, **H$_2$2** and **Zn2** revealed accelerated threading over the polymer chains of **P1**, **P2**, **P4**, and **P6** (Figures 11d and 11e). **H$_2$2** traverses the viologens that are appended with short chains at lower rates than **H$_2$1**, but the polymer-appended viologens are traversed significantly faster than **H$_2$1**(on average by a factor of 2.2). The observed trend is even more obvious when **Zn2** is used as the receptor (Figure 11e). The traversing of chains varying in length from five to 22 atoms is slightly faster for **Zn1** than for **Zn2**. The threading over the shorter polymer chains, however, is significantly faster for **Zn2** than for **Zn1**. **Zn2** threads a polymer chain of 90 atoms more than four times faster than **Zn1** and the difference between traversing a chain of eight atoms and a chain of 90 atoms is only a factor three in rate constant for **Zn2**, whereas it is a factor 14 for **Zn1**. The higher association constant between the outside of the cavity and the viologen binding site clearly results in enhanced threading over the polymer chains, in full agreement with the proposed mechanism.

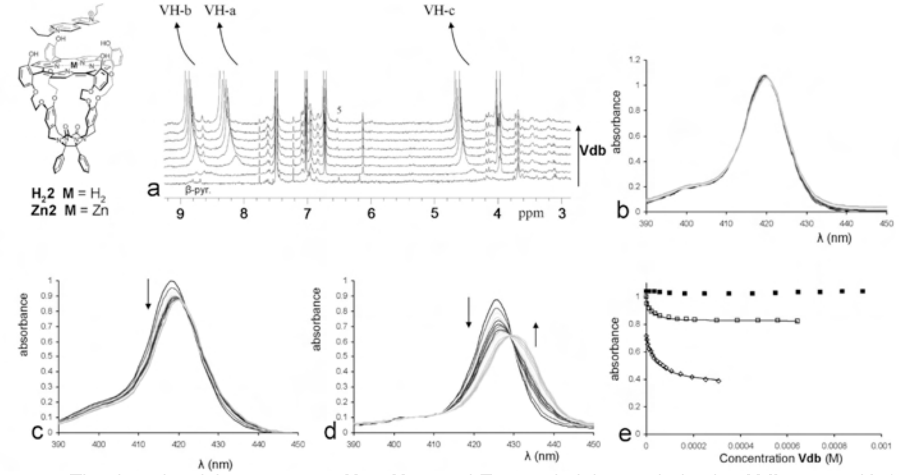

Figure 10. Titrations involving receptors **H$_2$1**, **H$_2$2**, and **Zn2** and viologen derivative **Vdb** at 298 K. (a) 400 MHz ^{1}H-NMR spectra of **H$_2$1** with (from bottom to top) increasing amounts of added **Vdb** in 1/1 (v/v) $CDCl_3/CD_3CN$. (b) UV-Vis titration of **H$_2$1** with **Vdb** in 1/1 (v/v) $CHCl_3/CH_3CN$. (c) UV-Vis titration of **H$_2$2** with **Vdb** in 1/1 (v/v) $CHCl_3/CH_3CN$. (d) UV-Vis titration of **Zn2** with **Vdb** 1/1 (v/v) $CHCl_3/CH_3CN$. (e) Plot of the maximum absorbance of **H$_2$1** (■), **H$_2$2** (□) and **Zn2** (◇) respectively versus the concentration of **Vdb**, and the curve fits assuming 1:1 complex stoichiometry.

The presence of the zinc ion in the porphyrin surface of **Zn2**, moreover, allowed for the inhibition of the viologen binding site on the roof of the macrocycle by coordinating a bulky pyridine ligand. *t*-Bupy coordinated with an association constant of 1200 M^{-1} to the zinc ion on the outside of **Zn2**. Threading experiments of **Zn2** in the presence of a large excess of *t*-bupy (84 mM) revealed that the relative increase in traversing the polymer chains, as was observed for **Zn2**, completely disappeared (Figure 11f) and the observed length dependency became similar to that of **Zn1** in the presence of the same concentration of *t*-bupy.

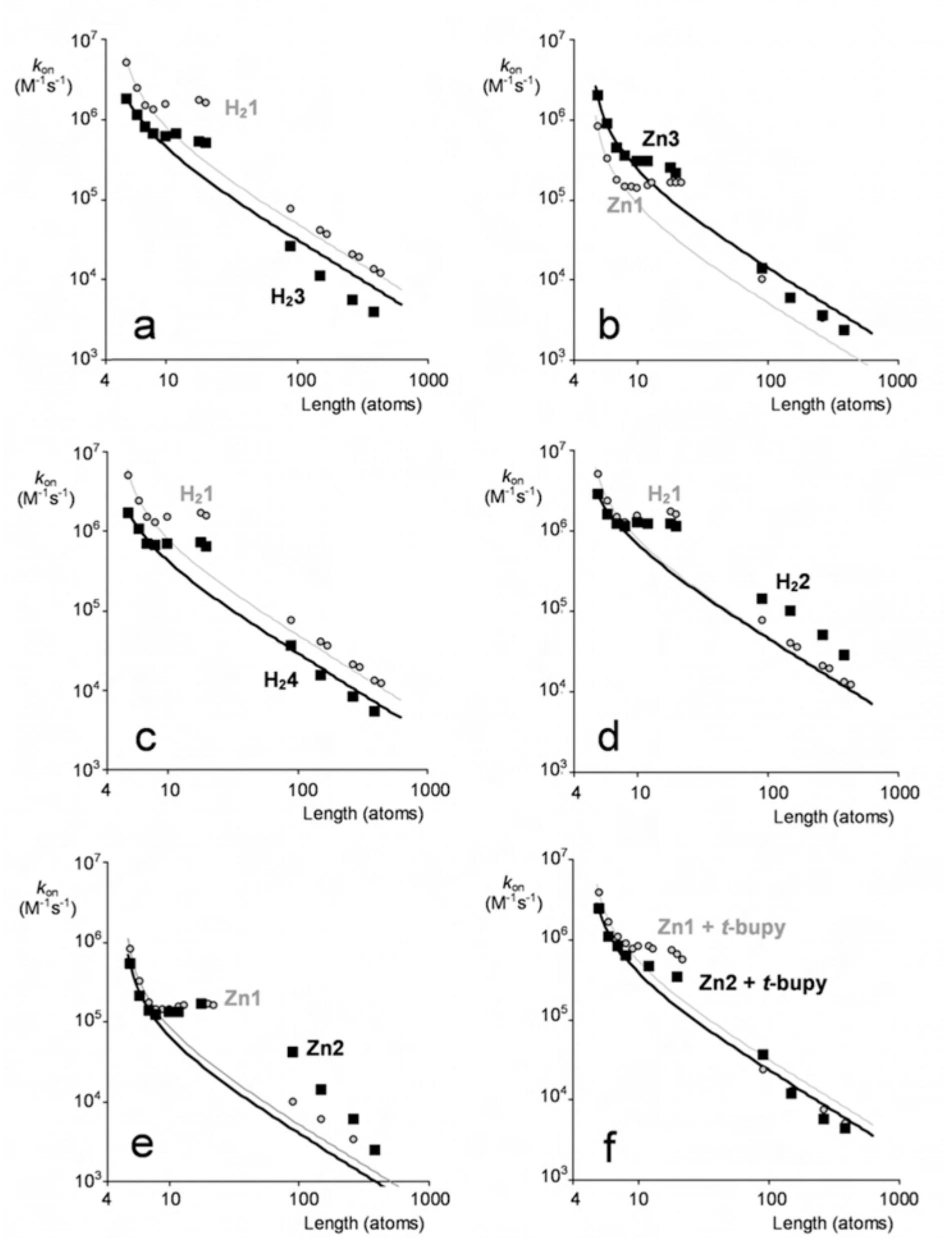

Figure 11. Threading-on rate constants (k_{on}) versus chain length of the appended viologen guests used for the study of the macrocycles at 295 K in 1/1 (v/v) acetonitrile/chloroform.

These results clearly demonstrate that the increase in threading over the polymer chains of the viologens, as observed for **$H_2$2** and **Zn2**, is the result of threading by the intramolecular pathway. On the obstruction of the binding site of **Zn2** by the coordination of a bulky axial ligand, this intramolecular pathway was no longer possible and the threading occurs by the normal intermolecular route.

3. Conclusion

The results described in this chapter have manifested another intriguing aspect of the mechanisms that govern the translocation of polymer chains through pores. Interactions between the outside of the hosting macrocycle and the viologen guest initiate and favorably guide the threading of the viologen side-chain through the cavity. Considering the known values of effective molarities, only very low association constants between the chains and the binding sites in the vicinity of the pores are required to dramatically accelerate the threading process. It is therefore very likely that similar interactions guide the threading process of the catalytic manganese-containing derivatives of the macrocycles over the polybutadiene substrate. The observed mechanism is, in fact, very similar to the mechanisms observed for protein transport through membranes in nature. In these processes, the translocation is initiated and guided by interactions between a signal sequence on the biopolymer and a binding site in the vicinity of the pore, which results in a high efficiency and selectivity of the process.[4–6,11] The results presented in this chapter reveal that the occurrence of binding events prior to the actual (threading) reaction is not only something that can be observed in natural systems, but can be an intrinsic property of reacting molecules in general. According to the presented theory and in the case of the specific model system used, the translocation process should locally be directional as a result of the stepwise increase in the effective molarity of the chain. Future molecular machines[31–39] could, in principle, also be driven by changes in the effective molarities of molecular chains.

4. Experimental Section

Materials and methods. All syntheses were carried out under an inert nitrogen or argon atmosphere. Chloroform and acetonitrile used in titration experiments were distilled from $CaCl_2$. All other solvents and chemicals were commercial materials and used as received. Merck silica gel (60H) was used for column chromatography and Merck silica gel F254 plates were used for thin layer chromatography (TLC) and preparative TLC. Molecular modeling calculations were performed with the use of Spartan. Fluorescence experiments were performed on a Perkin-Elmer LS50B luminescence spectrometer equipped with a thermostatted cuvette holder. Maldi-TOF MS was performed on a Bruker Biflex III spectrometer. NMR spectra were taken on a Varian Inova 400 (400 MHz, ^{1}H and 2D spectra) or on a Bruker DMX300 (75 MHz, ^{13}C spectra) and calibrated to an internal standard of tetramethylsilane. Abbreviations used are s, singlet; d, doublet; t, triplet; dd, double doublet; m, multiplet. Macrocycles **$H_2$1**,[40] **Zn1**,[40] **$H_2$2**,[41] **Zn2**,[41] and **$H_2$4**[42] as well as **Vdb**[12] and tosylate **5**[30] were synthesized according to literature procedures. The syntheses of viologen derivatives **V5–V8** and the polymer derivatives **P1–P8** are presented in Chapter 6 of this thesis.

Alkyl-substituted viologens (V9- V22)

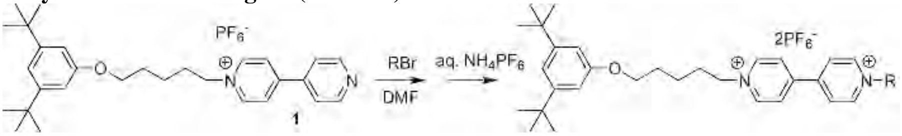

A solution of mono-alkylated hexafluorophosphate bipyridinium salt **1**[12] (250 mg, 0.43 mmol) and an excess of the selected 1-bromo-alkane (>10 equiv.) in DMF (5 mL) was stirred at 100 °C for 10-80 h. After cooling, diethyl ether was added and the precipitate was filtered off and dissolved in a mixture of water and a minimal amount of acetone. After the addition of aqueous NH_4PF_6 the product precipitated as a white solid, which was filtered off and dried.

V9 (125 mg, 34%):

^{1}H-NMR (400 MHz, $CDCl_3/CD_3CN$ 1/1 (v/v)): 8.92 (bt, 4H, J = 7.6 Hz), 8.41 (bs, 4H), 7.02 (s, 1H), 6.73 (s, 2H), 4.65 (t, 2H, J = 7.2), 4.62 (t, 2H, J = 6.7 Hz), 4.00 (t, 2H, J = 6.0), 2.14–2.10 (m, 2H), 2.06–2.00 (m, 2H), 1.90–1.82 (m, 2H), 1.65–1.58 (m, 2H), 1.43–1.36 (m, 4H), 1.30 (bs, 26H), 0.89 (t, 3H, J = 6.6 Hz) ppm.

^{13}C-NMR (75 MHz, $CDCl_3/CD_3CN$ 1/1 (v/v)): δ 157.80, 151.34, 149.04, 149.00, 144.73, 126.44, 113.97, 107.97, 66.22, 61.49, 61.35, 33.96, 30.82, 30.25, 30.07, 28.27, 28.16, 27.91, 27.74, 24.90, 21.74, 21.66, 12.94 ppm.

MALDI-TOF: *m/z* 558.68 $(M{-}2PF_6)^+$.

V10 (110 mg, 29%):

^{1}H-NMR (400 MHz, $CDCl_3/CD_3CN$ 1/1 (v/v)): δ 8.94 (d, 2H, J = 6.4 Hz), 8.91 (d, 2H, J = 6.5 Hz), 8.41 (bs, 4H), 7.02 (s, 1H), 6.73 (s, 2H), 4.67 (t, 2H, J = 7.5 Hz), 4.62 (t, 2H, J = 7.5 Hz), 4.00 (t, 2H, J = 5.9 Hz), 2.2–2.11 (m, 2H), 2.08–2.00 (m, 2H), 1.90–1.83 (m, 2H), 1.65–1.59 (m, 2H), 1.43–1.35 (m, 4H), 1.30 (bs, 28H), 0.89 (t, 3H, J = 5.8 Hz) ppm.

^{13}C-NMR (75 MHz, $CDCl_3/CD_3CN$ 1/1 (v/v)): δ 157.79, 151.36, 149.03, 148.99, 144.73, 126.45, 113.99, 107.96, 66.21, 61.50, 61.36, 33.97, 30.89, 30.33, 30.25, 30.09, 28.47, 28.33, 28.29, 27.92, 27.75, 24.93, 21.76, 21.69, 12.96 ppm.

MALDI-TOF: *m/z* 572.65 $(M{-}2PF_6)^+$.

V12 (55 mg, 14%):

^{1}H-NMR (400 MHz, $CDCl_3/CD_3CN$ 1/1 (v/v)): δ 8.93 (d, 2H, J = 6.5 Hz), 8.91 (d, 2H, J = 6.5 Hz), 8.40 (bs, 4H), 7.03 (s, 1H), 6.73 (s, 2H), 4.67 (t, 2H, J = 7.6 Hz), 4.61 (t, 2H, J = 7.5 Hz), 4.00 (t, 2H, J = 6.1 Hz), 2.14–2.09 (m, 2H), 2.06–1.99 (m, 2H), 1.89–1.83 (m, 2H), 1.65–1.57 (m, 2H), 1.42–1.35 (m, 4H), 1.30 (s, 18H), 1.28 (bs, 12H) 0.88 (t, 3H, J = 6.6 Hz) ppm.

^{13}C-NMR (75 MHz, $CDCl_3/CD_3CN$ 1/1 (v/v)): δ 157.81, 151.37, 149.06, 144.75, 126.48, 114.00, 107.98, 66.23, 61.54, 61.40, 33.99, 30.96, 30.30, 30.11, 28.66, 28.56, 28.39, 27.97, 27.78, 24.97, 21.78, 21.73, 13.01 ppm.
MALDI-TOF: *m/z* 600.53 $(M-2PF_6)^+$.

V13 (120 mg, 31%):
^{1}H-NMR (400 MHz, $CDCl_3/CD_3CN$ 1/1 (v/v)): δ 8.94 (d, 2H, J = 6.7 Hz), 8.91 (d, 2H, J = 6.7 Hz), 8.41 (t, 4H, J = 4.6 Hz), 7.03 (s, 1H), 6.73 (d, 2H, J = 1.3 Hz), 4.67 (t, 2H, J = 7.6 Hz), 4.62 (t, 2H, J = 7.6 Hz), 4.00 (t, 2H, J = 6.1 Hz), 2.16−2.11 (m, 2H), 2.07−2.00 (m, 2H), 1.89−1.83 (m, 2H), 1.65−1.58 (m, 2H), 1.43−1.35 (m, 4H), 1.30 (s, 18H), 1.27 (bs, 14H) 0.88 (t, 3H, J = 6.7 Hz) ppm.
^{13}C-NMR (75 MHz, $CDCl_3/CD_3CN$ 1/1 (v/v)): δ 157.80, 151.35, 149.03, 144.73, 126.44, 113.98, 107.96, 66.22, 61.50, 61.36, 33.96, 30.94, 30.25, 30.08, 28.67, 28.54, 28.36, 27.95, 27.75, 24.94, 21.75, 21.71, 12.97 ppm.
MALDI-TOF: *m/z* 614.59 $(M-2PF_6)^+$.

V16 (140 mg, 34%):
^{1}H-NMR (400 MHz, $CDCl_3/CD_3CN$ 1/1 (v/v)): δ 8.94 (d, 2H, J = 6.3 Hz), 8.91 (d, 2H, J = 6.4 Hz), 8.41 (bs, 4H), 7.02 (s, 1H), 6.73 (d, 2H, J = 1.3 Hz), 4.67 (t, 2H, J = 7.5 Hz), 4.61 (t, 2H, J = 7.6 Hz), 4.00 (t, 2H, J = 6.0 Hz), 2.17−2.11 (m, 2H), 2.06−2.00 (m, 2H), 1.90−1.83 (m, 2H), 1.65−1.59 (m, 2H), 1.44−1.35 (m, 4H), 1.30 (s, 18H), 1.27 (bs, 22H) 0.88 (t, 3H, J = 6.4 Hz) ppm.
^{13}C-NMR (75 MHz, $CDCl_3/CD_3CN$ 1/1 (v/v)): δ 157.79, 151.32, 149.02, 148.97, 144.70, 126.41, 113.94, 107.95, 66.21, 61.46, 61.33, 33.93, 30.92, 30.30, 30.21, 30.04, 28.68, 28.53, 28.35, 27.93, 27.72, 24.92, 21.69, 12.94 ppm.
MALDI-TOF: *m/z* 656.59 $(M-2PF_6)^+$.

V18 (95 mg, 22%):
^{1}H-NMR (400 MHz, $CDCl_3/CD_3CN$ 1/1 (v/v)): δ 8.94 (d, 2H, J = 6.2 Hz), 8.91 (d, 2H, J = 6.3 Hz), 8.41 (bs, 4H), 7.02 (s, 1H), 6.73 (s, 2H), 4.67 (t, 2H, J = 7.4 Hz), 4.61 (t, 2H, J = 7.4 Hz), 4.00 (t, 2H, J = 6.9 Hz), 2.14−2.09 (m, 2H), 2.07−1.99 (m, 2H), 1.90−1.82 (m, 2H), 1.66−1.58 (m, 2H), 1.42−1.35 (m, 4H), 1.30 (s, 18H), 1.26 (bs, 26H), 0.88 (t, 3H, J = 6.2 Hz) ppm.
^{13}C-NMR (75 MHz, $CDCl_3/CD_3CN$ 1/1 (v/v)): δ 157.79, 151.33, 149.01, 148.98, 144.71, 126.40, 113.95, 107.95, 66.20, 61.46, 61.32, 33.93, 30.91, 30.30, 30.20, 30.05, 28.68, 28.54, 28.35, 27.93, 27.72, 24.92, 21.70, 12.93 ppm.
MALDI-TOF: *m/z* 684.67 $(M-2PF_6)^+$.

V20 (110 mg, 25%):
^{1}H-NMR (400 MHz, $CDCl_3/CD_3CN$ 1/1 (v/v)): δ 8.94 (d, 2H, J = 6.3 Hz), 8.91 (d, 2H, J = 6.4 Hz), 8.41 (bs, 4H), 7.03 (s, 1H), 6.73 (s, 2H), 4.67 (t, 2H, J = 7.5 Hz), 4.62 (t, 2H, J = 7.5 Hz), 4.00

(t, 2H, J = 6.0 Hz), 2.18–2.10 (m, 2H), 2.06–1.99 (m, 2H), 1.89–1.82 (m, 2H), 1.65–1.59 (m, 2H), 1.43–1.35 (m, 4H), 1.30 (s, 18H), 1.26 (bs, 30H), 0.88 (t, 3H, J = 6.4 Hz) ppm.
^{13}C-NMR (75 MHz, $CDCl_3/CD_3CN$ 1/1 (v/v)): δ 157.79, 151.32, 149.02, 148.96, 144.72, 126.41, 126.38, 113.94, 107.94, 66.20, 61.45, 61.32, 33.92, 30.91, 30.30, 30.19, 30.04, 28.67, 28.63, 28.53, 28.34, 27.93, 27.71, 24.91, 21.70, 21.67, 12.92 ppm.
MALDI-TOF: *m/z* 712.53 $(M-2PF_6)^+$.

V22 (135 mg, 30%):
^{1}H-NMR (400 MHz, $CDCl_3/CD_3CN$ 1/1 (v/v)): δ 8.94 (d, 2H, J = 6.2 Hz), 8.91 (d, 2H, J = 6.3 Hz), 8.41 (bs, 4H), 7.02 (s, 1H), 6.73 (s, 2H), 4.67 (t, 2H, J = 7.5 Hz), 4.61 (t, 2H, J = 7.5 Hz), 4.00 (t, 2H, J = 5.9 Hz), 2.16–2.08 (m, 2H), 2.06–2.00 (m, 2H), 1.89–1.83 (m, 2H), 1.66–1.58 (m, 2H), 1.43–1.33 (m, 4H), 1.30 (s, 18H), 1.26 (bs, 32H), 0.88 (t, 3H, J = 6.4 Hz) ppm.
^{13}C-NMR (75 MHz, $CDCl_3/CD_3CN$ 1/1 (v/v)): δ 157.79, 151.29, 149.00, 148.94, 144.65, 126.37, 126.34, 113.89, 107.93, 66.18, 61.39, 61.26, 33.88, 30.88, 30.24, 30.12, 29.98, 28.63, 28.51, 28.31, 27.90, 27.67, 24.87, 21.64, 12.86 ppm.
MALDI-TOF: *m/z* 740.66 $(M-2PF_6)^+$.

2-[2-(2-Methoxy-ethoxy)-ethoxy]-phenol (7)
A suspension of catechol (**6**, 2.0 g, 18 mmol), tosylate **5**[30] (1.0 g, 3.6 mmol) and K_2CO_3 (1 g, 7.2 mmol) in DMF (50 mL) was stirred for 12 h under an argon atmosphere at 100°C. After cooling and evaporation of the solvent, the product was purified by column chromatography (eluent: 3/1 (v/v) chloroform/ethyl acetate) to yield **7** (0.45 g, 48%) as a colorless oil.
^{1}H-NMR (400 MHz, $CDCl_3$) δ = 6.92 (m, 3H), 6.80 (m, 1H), 6.58 (s, 1H), 4.18 (m, 2H), 3.82 (m, 2H), 3.72 (m, 2H), 3.60 (m, 2H), 3.41 (s, 3H) ppm.

1-(3-Bromo-propoxy)-2-[2-(2-methoxy-ethoxy)-ethoxy]-benzene (8)
A suspension of **7** (300 mg, 1.4 mmol), dibromopropane (2.0 mL, 5 mmol) and K_2CO_3 (1 g, 7.2 mmol) in DMF (250 mL) was stirred for 16 h under an argon atmosphere at 60°C. After cooling, filtration of the salts and evaporation of the solvent the product was purified by column chromatography (eluent: 5/1 (v/v) toluene/ethyl acetate) to yield **8** (248 mg, 53%) as a colorless oil.
^{1}H-NMR (400 MHz, $CDCl_3$) δ = 6.92 (s, 4H), 4.17 (m, 2H), 4.14 (t, 2H, J = 5.8 Hz), 3.88 (t, 2H, J = 5.0 Hz), 3.75 (m, 2H), 3.65 (t, 2H, J = 6.5 Hz), 3.57 (m, 2H), 3.39 (s, 3H), 2.32 (m, 2H) ppm.

Free base porphyrin clip ($H_2$3)
A suspension of **8** (100 mg, 0.30 mmol), tetra-hydroxy-porphyrin clip **$H_2$2** (15 mg, 11 μmol) and K_2CO_3 (100 mg, 0.72 mmol) in DMF (250 mL) was stirred for 48 h under an argon atmosphere at 50 °C. After cooling, filtration of the salts, and evaporation of the solvent, the product was purified by column chromatography (eluent: 3% methanol in $CHCl_3$ (v/v)) followed by preparative TLC (eluent: 7/7/1 toluene/ethylacetate/acetonitrile (v/v/v)). The product was dissolved in a minimal

amount of $CHCl_3$ and to this solution *n*-hexane was added. A precipitate was formed, which was collected by centrifugation and dried under vacuum yielding 11 mg (43%) of **$H_2$3** as a purple solid:
^{1}H-NMR (400 MHz, $CDCl_3$) δ = 8.67 (s, 4H), 8.56 (s, 4H), 7.69 (t, 4H, J = 8.3 Hz), 7.09 (d, 4H, J = 8.5 Hz), 6.99 (d, 4H, J = 8.3 Hz), 6.94 (m, 6H), 6.81 (m, 4H), 6.70 (d, 4H, J = 7.8 Hz), 6.58 (t, 4H, J = 7.6 Hz), 6.20 (m, 8H), 5.89 (d, 4H, J = 7.9 Hz), 4.23 (d, 4H, J = 15.9 Hz), 4.17 (m, 4H), 4.09 (m, 4H), 3.98 (m, 16H), 3.74 (d, 4H, J = 9.2 Hz), 3.72 (m, 8H), 3.63 (m, 8H), 3.47 (m, 8H), 3.41 (m, 4H), 3.32 (m, 12H), 3.01 (m, 4H), 2.91 (m, 4H), 1.31 (m, 8H), −2.49 (s, 2H) ppm.
MALDI-TOF: *m/z* 2481.0 $(M)^+$.

Zinc porphyrin clip (Zn3).
$H_2$3 (5 mg, 2.1 μmol) and zinc acetate dihydrate (10 mg 0.05 mmol), were dissolved in a 1:1 mixture of methanol and dichloromethane (10 mL). The mixture was stirred at room temperature for one hour. The solvents were evaporated and the salts were removed by chromatography over a plug of silica (eluent: methanol/chloroform 1:10 (v/v)). After precipitation in n-hexane 5 mg (97%) of **Zn3** was obtained as a purple solid:
^{1}H-NMR (400 MHz, $CDCl_3$): δ 8.75 (s, 4H), 8.67 (s, 4H), 7.69 (t, 4H, J = 8.3 Hz), 7.09 (d, 4H, J = 8.5 Hz), 7.00 (d, 4H, J = 8.3 Hz), 6.94 (m, 6H), 6.80 (m, 4H), 6.63 (d, 4H, J = 7.8 Hz), 6.57 (t, 4H, J = 7.6 Hz), 6.33 (t, 4H, J = 7.5), 6.18 (s, 4H), 6.09 (d, 4H, J = 7.8), 4.25–4.07 (m, 16H), 4.01–3.97 (m, 4H), 3.94–3.81 (m, 16H), 3.76–3.69 (m, 8H), 3.59–3.54 (m, 12H), 3.38 (bs, 8H), 3.33, 3.29 (m, 8H), 3.27–3.22 (m, 4H), 3.19–3.12 (m, 4H), 3.07–2.94 (m, 12H), 2.85 (bs, 12H), 1.31 (m, 8H) ppm.
MALDI-TOF: *m/z* 2419.2 $(M)^+$.

Determination of threading rate constants and association constants. Prior to performing the experiments, the porphyrin macrocycles were purified by preparative TLC, a short column and precipitation. The threading kinetics were measured by using the time drive application of the spectrometer software. The sample was excited at the wavelength corresponding to the maximum absorbance of the porphyrin Soret band and the emission at the wavelength corresponding to the maximum emission was recorded in time. Typically, to a weighed solution of 1 μM of porphyrin macrocycle, a known amount of viologen derivative was added and mixed. After the mixing time (1.5 s) the measurement was started. The data were analyzed according to standard 1:1 kinetic isotherms that describe the kinetics involved in complex formation between A and B, ti form C (Equations 3-6).[43] From the fit, both the rate constant k_{on} and equilibrium association constant K_{assoc} were obtained. All the experiments were performed in plural and at different concentrations of polymer and porphyrin macrocycle to decrease the experimental error.

$$A + B \underset{k_{\mathrm{off}}}{\overset{k_{\mathrm{on}}}{\rightleftharpoons}} C$$

$$[\mathrm{C}] = p\frac{\left(1-\dfrac{q}{p}\dfrac{p-[\mathrm{C}]_\mathrm{o}}{q-[\mathrm{C}]_\mathrm{o}}e^{k_\mathrm{on}(p-q)t}\right)}{\left(1-\dfrac{p-[\mathrm{C}]_\mathrm{o}}{q-[\mathrm{C}]_\mathrm{o}}e^{k_\mathrm{on}(p-q)t}\right)} \tag{3}$$

$$p = [\mathrm{C}]_\mathrm{eq} = \frac{([\mathrm{A}]_\mathrm{o}+[\mathrm{B}]_\mathrm{o}+\dfrac{1}{K_\mathrm{assoc}}) - \sqrt{([\mathrm{A}]_\mathrm{o}+[\mathrm{B}]_\mathrm{o}+\dfrac{1}{K_\mathrm{assoc}})^2 - 4\cdot[\mathrm{A}]_\mathrm{o}\cdot[\mathrm{B}]_\mathrm{o}}}{2} \tag{4}$$

$$q = \frac{[\mathrm{A}]_\mathrm{o}[\mathrm{B}]_\mathrm{o}}{[\mathrm{C}]_\mathrm{eq}} \tag{5}$$

$$K_\mathrm{assoc} = \frac{[\mathrm{C}]_\mathrm{eq}}{\left([\mathrm{A}]_\mathrm{o}-[\mathrm{C}]_\mathrm{eq}\right)\cdot\left([\mathrm{B}]_\mathrm{o}-[\mathrm{C}]_\mathrm{eq}\right)} = \frac{k_\mathrm{on}}{k_\mathrm{off}} \tag{6}$$

De-threading kinetics. Solutions of **Zn1** and a slight excess of a selected viologen derivative (~mM) in 1/1 (v/v) mixtures of $CDCl_3$ and CD_3CN were prepared and a ^{1}H-NMR spectrum was recorded to confirm the exact stoichiometries. These solutions were added to a 1/1 (v/v) mixture of chloroform and acetonitrile thereby diluting the pseudo-rotaxane concentration (~µM). The sample was excited at 426 nm and the emission at 607 nm was recorded in time using the time drive application of the spectrometer software. After the experiment, a UV-Vis spectrum was recorded to confirm the exact experimental concentration. The obtained de-threading curves could be analyzed with the use of Equations 3–6 assuming the relationship $K_\mathrm{assoc}=k_\mathrm{on}/k_\mathrm{off}$. The fits provided both the values of k_off and K_assoc. All the experiments were performed in plural to decrease the experimental error.

5. Notes and references

1. Johnson, A.; O'Donnell, M. *Annu. Rev. Biochem.* **2005**, *74*, 283–315.
2. Indiani, C.; O'Donnell, M. *Nat. Rev. Mol. Cell Biol.* **2006**, *7*, 751–761.
3. Ellison, V.; Stillman, B. *Cell* **2001**, *106*, 655–660.
4. Wickner, W.; Schekman, R. *Science* **2005**, *310*, 1452–1456.
5. Rapoport, T. A. *Nature* **2007**, *450*, 663–669.
6. Beckmann, R.; Bubeck, D.; Grassucci, R.; Penczek, P.; Blobel, G.; Frank, J. *Science* **1997**, *278*, 2123–2126.
7. Mancini, E.J.; Kainov, D.E.; Grimes, J.M.; Tuma, R.; Bamford, D.H.; Stuart, D.I. *Cell* **2004**, *118*, 743–755.
8. Song, L. Z.; Hobaugh, M. R.; Shustak, C.; Cheley, S.; Bayley, H.; Gouaux, J. E.; *Science* **1996**, *274*, 1859–1866.
9. Greorgescu, R. E.; Kim, S. S.; Yurieva, O.; Kuriyan, J.; Kong, X. P.; O'Donnell, M. *Cell* **2008**, *132*, 43–54.

10. Thordarson, P.; Bijsterveld, E. J. A.; Rowan, A. E.; Nolte, R. J. M. *Nature* **2003**, *424*, 915–918.
11. Moore, M. S.; Blobel, G. *Nature* **1993**, *365*, 661–663.
12. Coumans, R. G. E.; Elemans, J. A. A. W.; Nolte, R. J. E.; Rowan, A. E. *Proc. Nat. Acad. Sci.* **2006**, *103*, 19647–19651.
13. Hidalgo Ramos, P.; Coumans, R. G. E.; Deutman, A. B. C.; Smits, J. M. M.; de Gelder, R.; Elemans, J. A. A. W.; Nolte, R. J. M.; Rowan, A. E. *J. Am. Chem. Soc.* **2007**, *129*, 5699–5702.
14. Ashton, P. R.; Ballardini, R.; Balzani, V.; Belohradsky, M.; Gandolfi, M. T.; Philp, D.; Prodi, L.; Raymo, F. M.; Reddington, M. V.; Spencer, N.; Stoddart, J. F.; Venturi, M.; Williams, D. J. *J. Am. Chem. Soc.* **1996**, *118*, 4931–4951.
15. Affeld, A.; Hübner, G. M.; Seel, C.; Schalley, C.A. *Eur. J. Org. Chem.* **2001**, 2877–2890.
16. *Molecular Catenanes, Rotaxanes and Knots,* Sauvage, J.-P.; Dietrich-Buchecker, C. Eds.; Wiley-VCH: Weinheim, Germany, **1999**.
17. Herrmann, W.; Keller, B.; Wenz, G. *Macromolecules* **1997**, *30*, 4966–4972.
18. Conners, K, A. *Binding constants*, Wiley: New York, **1987**.
19. Chapters 4, 5, and 6 of this thesis.
20. Considering the known association constant of pyridine to the outside of pseudo-rotaxane complexes between **Zn1** and viologen derivatives of $^{V}K_{Py} \approx 8 \times 10^3$ M^{-1} (Chapter 4), it can easily be calculated that the fractional saturation of pseudo-rotaxane complex with pyridine has values higher that 0.999 at concentrations of [pyridine]$_o$ = 0.15 M^{-1} ($y_{Zn1V\text{-}Py}$ = $[Py]\cdot K_{Py}/(1+[Py]\cdot K_{Py})$).
21. The feasibility of 2:1 (receptor/guest) complex formation depends to a great extent on the receptor concentration. A thousand-fold decrease in receptor concentration leads to an approximate million-fold decrease in the equilibrium situation of the 2:1 complex. Considering that only very small amounts of 2:1 complex possibly form at millimolar concentrations of receptor, it can be safely assumed that virtually no 2:1 complex will form at micromolar concentrations.
22. Warshel, A.; Sharma, P. K.; Kato, M.; Xiang, Y.; Liu, H.; Olsson, M. H. M. *Chem. Rev*, **2006**, *106*, 3210–3235.
23. Mandolini, L. *Adv. Phys. Org. Chem.* **1986**, *22*, 1–111.
24. Galli, C.; Mandolini, L. *Eur. J. Org. Chem.* **2000**, 3117–3125.
25. Brown, H. C.; Fletcher, R. S.; Johannesen, R. B. *J. Am. Chem. Soc.* **1951**, *73*, 212–221.
26. Laatikainen, R.; Tuppurainen, K. *Tetrahedron Lett.* **1988**, *29*, 5021–5024.
27. Hammett, L. P. *Physical Organic Chemistry*, 2nd ed., McGraw-Hill, New York, **1970**, p. 112.
28. When the initial fraction of MP becomes higher (MP/{MP+M}>0.05), the obtained threading curve will no longer evolve according to a 1:1 kinetic binding isotherm because the molar fraction MP/{M+MP} will start changing in the course of the experiment (provided that P is not present in excess). The computer simulations using mathematica® moreover revealed that under these conditions the overall evolutions of pseudo-rotaxane formation became slower again.
29. See the thesis of Pilar Hidalgo Ramos, and forthcoming publications.
30. Naemura, K.; Fukunaga. R.; Komatsu, M.; Yamanaka, M.; Chikamatsu, H. *Bull. Chem. Soc. Jpn.* **1989**, *62*, 83–88.
31. Browne, W. R.; Feringa, B. L. *Nat. Nanotech.* **2006**, *1*, 25–35.

32. Schliwa, M. (ed.) *Molecular Motors* (Wiley-VCH, Weinheim, Germany **2003**).
33. Davis, A. P. *Nature* **1999**, *401*, 120–121.
34. Hawthorne, M. F.; Zink, J. I.; Skelton, J. M.; Bayer, M. J.; Liu, C.; Livshits, E.; Baer, R.; Neuhauser, D. *Science* **2004**, *303*, 1849–1851.
35. Kelly, T. R.; De Silva, H.; Silva, R. A. *Nature* **1999**, *401*, 150–152.
36. Leigh, D. A.; Wong, J. K. Y.; Dehez, F.; Zerbetto, F. *Nature* **2003**, *424*, 174–179.
37. Hernandez, J. V.; Kay, E. R.; Leigh, D. A. *Science* **2004**, *306*, 1532–1537.
38. Koumura, N.; Zijlstra, R. W. J.; van Delden R. A.; Harada, N.; Feringa, B. L. *Nature* **1999**, *401*, 152–155.
39. Bissell, R. A., Cordova, E., Kaifer, A. E.; Stoddart, J. F. *Nature* **1994**, *369*, 133–137.
40. Elemans, J. A. A. W.; Claase, M. B.; Aarts, P. P. M.; Rowan, A. E.; Schenning, A. P. H. J.; Nolte, R. J. M. *J. Org. Chem.* **1999**, *64*, 7009–7016.
41. Thordarson, P.; Coumans, R. G. E.; Elemans, J. A. A. W.; Thomassen, P. J.; Visser, J.; Rowan, A. E.; Nolte, R. J. M. *Angew. Chem. Int. Ed.* **2004**, *43*, 4755–4759.
42. Thesis of P. Hidalgo Ramos. In preparation.
43. Koppelman, S. J.; van Hoeij, M.; Vink, T.; Lankhof, H.; Schiphorst, M. E.; Damas, C.; Vlot, A. J.; Wise, R.; Bouma, B. N.; Sixma, J. J. *Blood* **1996**, *87*, 2292–2300.

9

Thermodynamics and Kinetics of Guest-Induced Switching between 'Basket Handle' Porphyrin Isomers

1. Introduction

Host-guest chemistry provides a valuable platform for studying binding processes observed in Nature with the help of relatively simple mimics. Many artificial receptors have been designed and synthesized, which display typical binding features observed in natural systems, viz. induced-fit binding,[1-3] lock and key mechanisms,[4] and cooperative or allosteric binding effects.[5-10] The majority of these studies is focused on the thermodynamic aspects of these binding processes. In a recent review,[11] Houk et al. showed convincingly that the origins of binding affinities between receptors (ranging from small synthetic cavitands to large proteins) and guests are now well-understood, and that enzymes do not show any outstanding binding properties for their substrates when compared to artificial receptors. This conclusion is a powerful reminder that the ability of enzymes to catalyze reactions arises from specific transition state binding interactions, and not necessarily from (strong) substrate binding interactions. Understanding the combination of chemical effects responsible for the catalytic proficiencies of enzymatic systems remains a significant challenge. By studying the kinetics (transition states) of relatively simple artificial receptor-guest interactions, in addition to thermodynamics (equilibrium situations), better insights into how chemical interactions affect transition states and reaction rates should be obtained.

For many artificial receptor-guest systems, the kinetics of guest-induced processes (e.g. conformational selection[12–16] and cooperative binding interactions) are simply too fast to study accurately with the use of general methods such as NMR and UV-Vis spectroscopy. To circumvent this time-resolution problem, a newly developed receptor that can interconvert between two isomers by atropisomerisation, at an extremely slow rate, will be described in this chapter. As a result, not only the guest-induced kinetics of interconversion between these two isomers could be studied accurately but, in addition, the binding properties of each of the two separate isomers with different guests could be determined with good precision. A complete kinetic and thermodynamic picture of the guest-induced 'switching' was obtained, which revealed that the binding of guests not only influences the thermodynamic outcome of the switching process as expected on the basis of the obtained individual equilibrium association constants but, in addition, results in accelerated switching as a result of transition state-stabilizing interactions in the switching process.

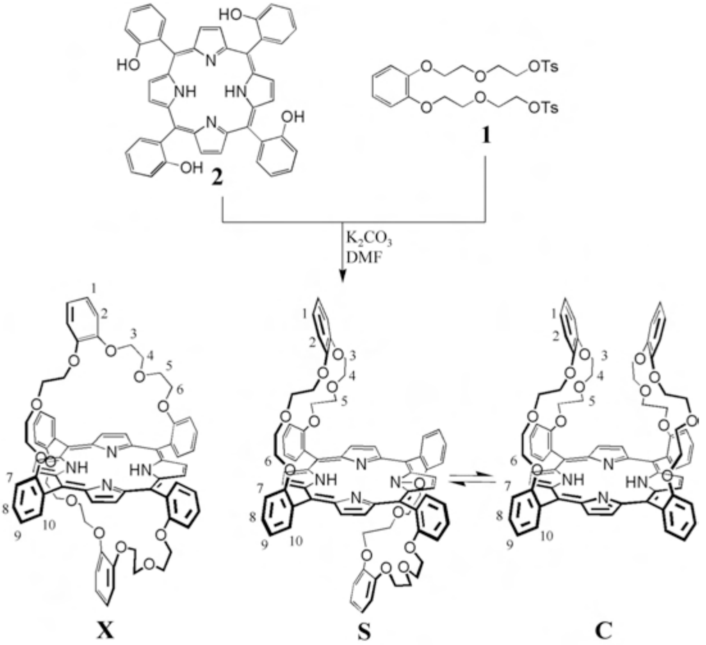

Scheme 1. Synthesis of basket handle isomers **X**, **S**, and **C**.

2. Results and discussion

2.1 Design

It was decided to make use of the atropisomerisation[17–30] properties of phenyl-substituted porphyrins in the design of the receptor. It is known that the restricted rotation of the aryl rings in many ortho-phenyl-substituted porphyrins can be extremely slow[31–31] (rates between 10^{-4} s^{-1} and 10^{-9} s^{-1} depending on the substitution pattern and metal ion present in the porphyrin), which often allows the isolation of the individual atropisomers. By appending two adjacent-linked binding pockets (‘handles’) to the porphyrin ortho-phenyl positions, two ‘basket handle’ porphyrin isomers[33–36] (trans-linked **S** and cis-linked **C**; Scheme 1) are obtained that can interconvert slowly via atropisomerisation, requiring the rotation around two aryl rings. By appending crown ether handles that are specifically designed for the complexation of viologen derivatives, the adjacent-linked ‘basket handle’ porphyrins are expected to become excellent receptor molecules for these guests. The cis-linked isomer **C** was expected to have higher affinity for the viologen derivatives than trans-linked isomer **S** as a result of the interplay of two crown ether handles on the same side of the porphyrin plane in the former isomer. The addition of viologen derivatives should therefore result in the slow switching of the equilibrium in the direction of isomer **C**; a process that allows the accurate determination of both the thermodynamics and the kinetics involved.

2.2. Synthesis

A mixture of 'basket handle' porphyrin isomers **X**, **C** and **S** (Scheme 1) was prepared in an overall yield of 52% by the reaction of ditosylate **1**[37] with 5,10,15,20-tetrakis(*meso-o*-hydroxyphenyl)porphyrin **2** under basic conditions in DMF at 110 °C. The three different isomers could be separated by preparative TLC and were obtained in a ratio of **X**:**S**:**C** = 4:8:1.

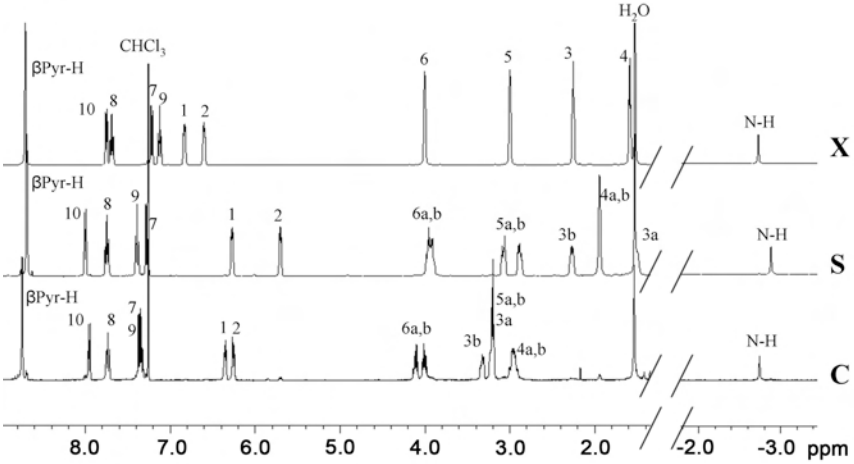

Figure 1. 400 MHz ^{1}H-NMR spectra of basket handle porphyrin isomers **X**, **S**, and **C** in $CDCl_3$ with proton numbering as derived from 2D COSY and ROESY ^{1}H-NMR experiments. See Scheme 1 for proton numbering.

The individual isomers could be identified with the help of ^{1}H-NMR spectroscopy (Figure 1) and an X-Ray crystal structure was determined of the adjacent-trans-linked isomer **S** (Figure 2). The cross-trans-linked isomer **X** has S_2 symmetry and consequently the ^{1}H-NMR spectrum revealed only four resonances for all the 32 crown ether protons H-3, H-4, H-5, and H-6 and one single resonance for the *β*-pyrrolic porphyrin protons. The adjacent-trans linked isomer **S** and adjacent-cis-linked isomer **C** have C_{2h} and C_{2v} symmetry, respectively. As a result, the crown ether proton resonances show a/b patterns in the ^{1}H-NMR spectra and two distinct resonances were observed for the *β*-pyrrolic protons in a 1/1 (v/v) mixture of $CDCl_3$ and CD_3CN. The handle proton resonances of **S** are shifted upfield significantly compared to those of **C** (Figure 1), which indicates that they experience more shielding from the porphyrin ring-current. In **S** there is space to position both handles in the proximity of the porphyrin, whereas in **C** this is sterically impossible. The inner amine proton resonances of **S**

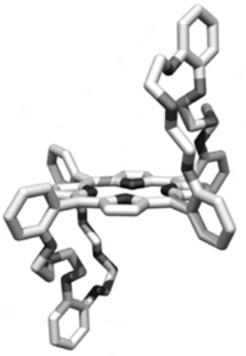

Figure 2. Crystal structure of adjacent-trans-linked isomer S.

are also shifted upfield compared with those of **C**, which suggests that the two handle phenyl ring-currents shield the centre of the porphyrin more in **S** than in **C**. These observations indicate that, unlike in the crystal structure of **S**, in which the handles bend away from the porphyrin plane (Figure 2), in solution ($CDCl_3$, and also $CDCl_3/CD_3CN$ 1/1 (v/v)) the handles are on average folded over the porphyrin plane. This was also confirmed by a 2D-ROESY NMR measurement that showed NOE contacts between the resonances of handle phenyl protons (H-1 and H-2) and the β-pyrrole protons and H-10, respectively.

2.3 Isomerisation

As observed in other adjacent-linked 'basket handle' porphyrins[35] the adjacent-cis-linked isomer and the adjacent-trans-linked isomer slowly interconvert in time. Figure 3 reveals that upon standing, the resonances of **S** in the ^{1}H-NMR spectra increase in intensity at the expense of those of **C**. Isomer **S** is significantly more thermodynamically stable than isomer **C**, since equilibrium is reached at a ratio of **S**/**C** = 7.6. This observation is in contrast with results in a previous report, in which the switching of a hexyl-bridged basket-handle porphyrin resulted in equimolar amounts of the adjacent-cis-linked and adjacent-trans-linked isomers at equilibrium,[38] as would statistically be expected. The rate constants for the isomerisation process ($k_{C\rightarrow S}$) could be simply determined by first order analysis of the decrease in the relative intensities[39] of the resonances of **C** in time.

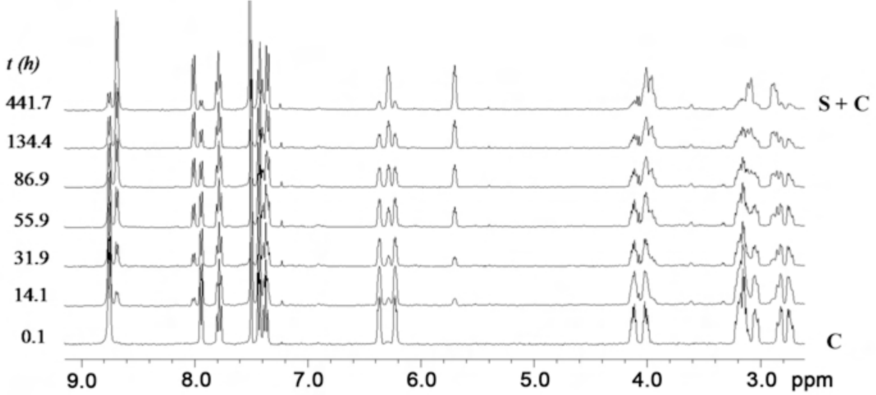

Figure 3. Partial 400 MHz ^{1}H-NMR spectra in time revealing the decrease in abundance of cis-linked isomer **C** in favor of the thermodynamically more stable trans-linked isomer **S** at 25 °C in $CDCl_3/CD_3CN$ 1/1 (v/v).

The equilibrium constants ($K_{S/C} = [S]_{eq}/[C]_{eq}$) were obtained at different temperatures from the ratio between **S** and **C** at equilibrium, after which the rate constant $k_{S\rightarrow C}$ could be calculated indirectly from $K_{S/C} = k_{C\rightarrow S}/k_{S\rightarrow C}$. Isomerisation experiments in which the switching from **S** to **C** was monitored provided identical values for $k_{S\rightarrow C}$ as were obtained by the indirect method via $K_{S/C}$ and $k_{C\rightarrow S}$. The calculated constants are presented in Table 1.

Table 1. Calculated rate constants for the switching of **C** to **S** ($k_{C\rightarrow S}$) and for the switching of **S** to **C** ($k_{S\rightarrow C}$) at different temperatures, and the equilibrium constant K that represents the ratio of **S**/**C** at equilibrium.

T (°C)	$k_{C\rightarrow S}$ (s^{-1})[a]	$k_{S\rightarrow C}$ (s^{-1})[b,c]	K[b]
25	2.8×10^{-6}	3.7×10^{-7}	7.6
32.5	6.0×10^{-6}	1.0×10^{-6}	5.8
40	1.5×10^{-5}	2.8×10^{-6}	5.3
47.5	3.2×10^{-5}	6.8×10^{-6}	4.7

[a] Estimated error 5%. [b] Estimated error 15%. [c] calculated from $k_{S\rightarrow C} = k_{C\rightarrow S}/K$.

The switching from **C** to **S** was monitored at four different temperatures (Figure 4a) from which, with the help of van 't Hoff and Eyring plots, the entropic (ΔS) and enthalpic (ΔH) contributions to the activation energy ($\Delta G^{\neq}$) and the free energy of binding (ΔG^{o}) could be determined. The resulting energy diagram with all these parameters is presented in Figure 4b. The switching process is unfavorable both in entropy and in enthalpy, but the majority of the free energy of activation ($\Delta G^{\neq}$) is enthalpic of origin (the proposed mechanism will be presented later in this chapter).

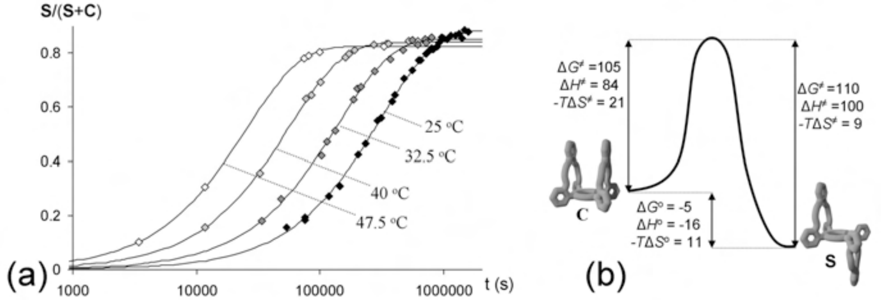

Figure 4. (a) Kinetics of switching from **C** to **S** at different temperatures in $CDCl_3/CD_3CN$ 1/1 (v/v), monitored by ^{1}H-NMR. (b) Energy diagram of the switching process with the entropic and enthalpic parameters (all in $kJ\cdot mol^{-1}$).

The obtained parameters ΔS^{o} and ΔH^{o} (Figure 4b) revealed that the formation of the trans-linked isomer **S** is enthalpically more favorable than the cis-linked isomer **C**, whereas the latter is entropically more likely to form. The value of ΔH^{o} suggests that **S** experiences more stabilizing intramolecular interactions than **C**. These are presumably π-π interactions between the handle phenyl groups and the porphyrin plane, and additional van der Waals interactions. The entropic parameters suggest that **C** has more disorder than **S**, which could be the result of a restricted motion of the handles in **S** as a result of the intramolecular binding interactions (entropy-enthalpy compensation[40]). Another possibility is that **S** needs to organize more solvent molecules in a defined shell than **C**, which would result in the release of solvent to the bulk upon switching from **S** to **C**, thereby accounting for the entropic gain. The observation that **C** dissolves significantly better in the used solvent mixture than **S** could validate this hypothesis, although solubility depends on more factors.

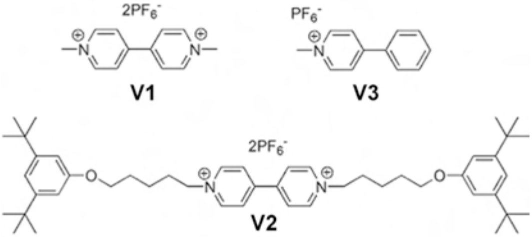

Figure 5. Structure of viologens **V1** and **V2** and pyridinium compound **V3**.

1.4 Binding of viologen derivatives

The binding of viologen derivatives **V1**, **V2**, and **V3** (Figure 5) to isomers **C** and **S** was investigated. As a result of the high kinetic stabilities of **C** and **S**, no detectable isomerisation was observed in the first few hours after their separation, which allowed the study of the binding properties of the individual isomers. A ^{1}H-NMR titration (Figure 6a) between **C** and **V1** revealed that **V1** binds strongly to this receptor in a face-to-face geometry with respect to the porphyrin.[41] The addition of increasing amounts of **V1** to **C** resulted in large downfield complexation induced shifts (CIS) of the crown ether proton resonances (H-3 to H-6), which indicates that their position in the proximity of the porphyrin is replaced by **V1** (Table 2). The inner amine proton resonances of **C** shifted dramatically upfield upon complex formation, indicating their shielding by the aromatic rings of **V1**. Also the signals of **V1** displayed large upfield shifts compared to their original positions (Figure 6a), confirming their position in the proximity of the shielding porphyrin ring current. The addition of one equivalent of **V1** resulted in the full binding to **C**, stressing the strong affinity between the components. To derive an accurate value for the association constant (K_{CV1}), the binding of **V1** to **C** was investigated at lower concentrations (**[C]** ≈ 10^{-6} M) with the help of a fluorescence titration experiment. The addition of increasing amounts of **V1** to a solution of **C** resulted in the quenching of the porphyrin fluorescence of the receptor. The obtained binding curve could be fitted with a 1:1 binding isotherm and the association constant was calculated to be $K_{\mathrm{CV1}} = 3 \times 10^5\ \mathrm{M}^{-1}$ (Table 4).

Molecular modeling revealed that **V1** preferably accommodates its positive charges in between the two ‘handle’ crown ether rings of **C**. The complex adopts a so called suit(2)ane[42] geometry in which the positive charges are wrapped inside the crown ether sleeves of the suit-shaped receptor **C** (see Figure 7a). Since it is impossible to directly derive the exact geometry of the complex with the help of NMR techniques and attempts to obtain an X-ray structure of the complex were unsuccessful, it was decided to compare the binding between **C** and **V1** with that between **C** and **V2**. **V2** can not adopt the proposed suit(2)ane geometry as a result of the presence of 3,5-di-tert.-butyl-phenyl blocking groups, which can impossibly slip through the crown ether rings of **C**. A ^{1}H-NMR titration between **C** and **V2** (Figure 6b) indicated that **V2** adopts a different binding geometry with **C** than **V1**. Although **V2** also binds in a face-to-face orientation with respect to porphyrin plane of **C**, as can be concluded from the observed upfield shift of the inner amine proton resonances of the receptor (Table 2), the CIS values for all the other proton resonances are significantly different for the complex between **C** and **V2** when compared to the complex between **C** and **V1**. Moreover, the association constant for the binding of **V2** to **C** is almost two orders of magnitude lower than that for the binding of **V1** to **C** (Table 3). These combined results strongly suggest that **V1** indeed binds to **C** in the proposed suit(2)ane geometry, whereas **V2** adopts a geometry as indicated in Figure 7b.

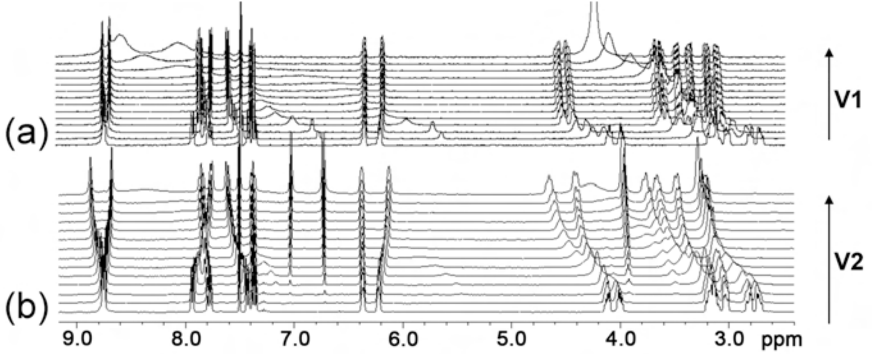

Figure 6. ^{1}H-NMR spectra (400 MHz, 1/1 $CDCl_3$/CD_3CN (v/v) of **C** with (from bottom to top) increasing amounts of (a) **V1** and (b) **V2**. See Scheme 1 for proton numbering.

In addition to the binding to **C**, the binding of **V1** to trans-linked **S** was investigated. A ^{1}H-NMR titration revealed complex formation between **V1** and **S**, which was expressed in large CIS values for the proton resonances of **V1** and **S**. As observed for the binding of **V1** with **C**, the inner amine proton resonances and aromatic viologen signals shifted upfield, whereas the crown ether proton resonances shifted downfield (Table 2), which suggests a binding geometry in which the porphyrin of **S** and the aromatic rings **V1** adopt a face-to-face orientation. The experimentally obtained binding curve could however not be fitted with a 1:1 binding isotherm, which strongly points in the direction of 2:1 complex formation between **V1** and **S**. This was moreover indicated by the CIS value of the inner amine proton signals of **S** (Table 2), which shifts significantly further upfield upon complexation of **V1** than in the complex between **V1** and **C** (and other known face-to-face viologen-porphyrin complexes known in literature[43–45]), which indicates that this is the result of the presence of two viologen molecules that are sandwiching the porphyrin (see Figure 7d). Data analysis of the binding curves with a 2:1 binding isotherm gave a satisfying fit with association constants of 1.3 x 10^4 M^{-1} and 6 x 10^2 M^{-1} for the binding of the first (K_{SV}) and second (K_{VSV}) molecule of **V1** to **S**, respectively. Considering the statistical factor of 4 for the difference in binding of the first and the second identical guest molecule to a bivalent receptor, there is a negative cooperative effect for the binding of the second molecule of **V1** to **S** with a factor of 5.8. This is most probably caused by the repulsive interactions between the positive charges of the two viologen derivatives.[46]

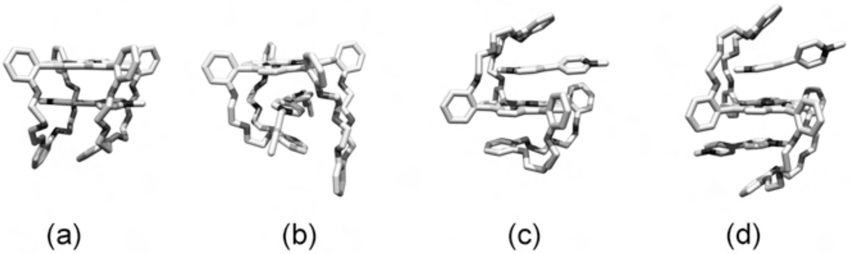

Figure 7. Proposed geometries based on the binding studies of the 1:1 complexes between (a) **C** and **V1**, (b) **C** and **V2** (blocking groups are not shown for clarity), (c) **S** and **V1** and (d) the 2:1 complex between **V1** and **S**.

Table 2. Selected calculated CIS values (ppm) of receptor proton signals upon binding of viologens to **S** and **C**.[a]

	C			**S**		
Proton[b]	**V1**	**V2**	**V3**[d]	**V1**	**V2**[e]	**V3**[d]
H-1	0.00	0.01	0.01	–0.28	–0.06	–0.28
H-2	–0.03	–0.10	–0.03	–0.13	–0.08	–0.06
H-3 to H-5[c]	0.42	0.43	[f]	0.47	[f]	0.50
H-6a	0.51	0.64	[f]	0.25	[f]	0.21
H-6b	0.47	0.29	[f]	0.21	[f]	0.17
N-H	–1.04	–0.98	–0.51	–1.12	–0.33	–0.85

[a] Calculated from ^{1}H-NMR experiments (400 MHz, 298 K, 1/1 $CDCl_3/CD_3CN$ (v/v)) [b] See Scheme 1 for proton numbering. [c] Average shifts of the series of protons. [d] Concentration **V3**: 1 x 10^{-2} M. [e] Concentration **V2**: 3.3 x 10^{-3} M. [f] Resonances were obscured.

Because the guest-induced switching between the conformers, which will be presented in Section 2.5 is performed at elevated temperatures, the effect of temperature on the binding constants of **V1** to **S** and **C**, respectively, was studied with the help of fluorescence titrations. Although **V1** was shown to form 2:1 complexes with **S** at ^{1}H-NMR concentrations (10^{-3} M), at the used experimental concentrations of the fluorescence titrations (10^{-6} M) 2:1 complex formation was so marginal that it could be ignored, and the obtained fluorescence titration curves could therefore be fitted with the use of simple 1:1 binding isotherms. This was emphasized by both the good fits and the calculated value of the association constant that were obtained from the fluorescence titration for the 1:1 complex between **V1** and **S**, which was in very good agreement with the value of K_{SV} obtained from the ^{1}H-NMR titration experiment at the same temperature.[47] With the use of Van het Hoff plots the enthalpic (ΔH^o) and entropic (ΔS^o) contributions to the total free binding energy (ΔG^o) of **V1** with **S** and **C**, respectively, could be determined. Quite surprisingly, the calculated parameters revealed that the differences in binding strength between **V1** and **C** and **V1** and **S**, respectively, are mainly entropic of origin (Table 3). Similar values were obtained for the binding enthalpy (ΔH^o). Complex formation between **C** and **V1** is slightly favorable in entropy whereas complex formation between **S** and **V1** is unfavorable in entropy.

Intuitively, two good reasons why the binding of **V1** to **C** should be enthalpically more favorable than the binding of **V1** to **S** can be envisaged. The first reason is that isomer **C** can provide more stabilizing interactions to **V1** than isomer **S** as a result of the presence of two crown ether handles, which can both interact with the viologen guest, on the same side of the porphyrin plane. The second reason is that within isomer **S** more intramolecular interactions are present than within **C**, which have to be overcome in order to accommodate **V1** (as suggested by the value of ΔH^{o} for the switching process as presented above). The fact that no enthalpic difference is observed between the two binding processes, and that the difference in binding is mainly entropic of origin, therefore suggests that the binding of viologen derivatives to both isomers depends to a crucial extend on the desolvation of the viologen derivatives upon complex formation. Isomer **C** can fully accommodate the positive charges of the viologen, thereby perfectly shielding it from the solvent (Figure 7a). In contrast, isomer **S** is only capable of shielding one of the positive charges of the viologen from the solvent (Figure 7c). As a result, the binding of **V1** to **C** is accompanied by the release of more solvent molecules to the bulk than the binding of **V1** to **S**, which accounts for the observed difference in binding entropy.

Table 3. Association constants (K_a) and binding free energies (ΔG^{o}) at 298 K and the enthalpic (ΔH^{o}) and entropic (ΔS^{o}) contribution to the binding free energy between isomers **C** and **S** and viologen guests.

Receptor isomer	Guest	K_a [c] (M^{-1})	ΔG^{o} (kJ·Mole^{-1})	ΔH^{o} [d] (kJ·mol^{-1})	ΔS^{o} [e] J $M^{-1}K^{-1}$
S	**V1** (K_{SV})	1.3×10^{4} [a,b]	-23.6	–31.3	25.9
	(K_{VSV})	6.0×10^{2} [a]	-15.8		
C	**V1**	3.0×10^{5} [b]	-31.2	–30.1	–3.7
C	**V2**	3.5×10^{3} [a]	-20.2		

[a] Determined in 1/1 $CDCl_3/CD_3CN$ (v/v) by ^{1}H-NMR titrations. [b] Determined In 1/1 $CHCl_3/CH_3CN$ (v/v) by fluorescence titrations. [c] Estimated error 30%. [d] Estimated error 10 kJ·mol^{-1}. [e] Estimated error 10 J $M^{-1}K^{-1}$.

2.5 Guest-induced switching

Thermodynamics. As a result of the higher affinity of **V1** for **C** than for **S** ($\Delta\Delta G^{o}$ = 7.6 kJ/mole), it would be expected that in the presence of the guest the equilibrium should be switched further in the direction of the thermodynamically less favorable isomer **C**. Because **S** is 5 kJ·mol^{-1} more stable than **C** (Figure 4b), it could theoretically result in an equilibrium situation which is maximally 2.6 kJ/mole in the direction of **C**, and which would be translated into a ratio of approximately 74% **C** and 26% **S** at equilibrium, or $[\mathbf{S}]_{tot\text{-}eq}/[\mathbf{C}]_{tot\text{-}eq} = 0.36$). A first isomerisation experiment, in which a mixture of **S** and **V1** was annealed at 80 °C in 1/1 toluene/acetonitrile (v/v) for 12 hours, indeed revealed that the conformational equilibrium had shifted in the direction of **C**. After workup and purification of the reaction mixture, the different isomers were isolated in a ratio of approximately **C**:**S** = 2:1. This ratio is strikingly different from the ratio obtained after annealing isomer **S** under the same experimental conditions but in the absence of **V1**, which amounted to approximately **C**:**S** = 1:5.

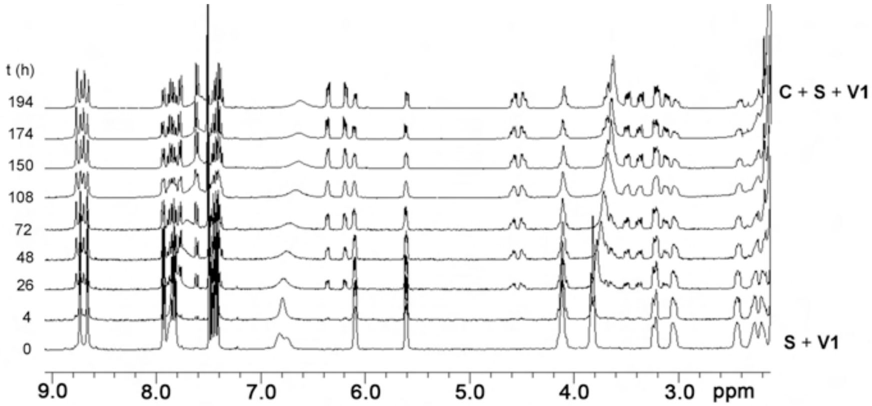

Figure 8. Partial 400 MHz ^{1}H-NMR spectra recorded in time and revealing the decrease in population of isomer **S** at the expense of the population of isomer **C** in the presence of 1.3 equiv. of **V1** at 37.5 °C in $CDCl_3/CD_3CN$ 1/1 (v/v).

In order to gain more detailed information about the guest-induced switching, it was decided to follow the switching from **S** to **C** in the presence of **V1** with the help of ^{1}H-NMR spectroscopy. The ^{1}H-NMR spectra of a mixture of **S** (1 mM) and **V1** (1.3 mM) in $CDCl_3/CD_3CN$ 1/1 (v/v) at 37.5 °C clearly revealed that in time isomer **C** was formed at the expense of isomer **S** (Figure 8), resulting in a final equilibrium ratio of $[\mathrm{S}]_{\text{tot-eq}}/[\mathrm{C}]_{\text{tot-eq}} = 0.56$ (64% **C** and 36% **S**).

In order to further explore the switching effect of **V1**, the isomerisation from **S** to **C** in the presence of different concentrations of this guest was monitored by ^{1}H-NMR spectroscopy. The measurements clearly reveal that there is an optimal concentration of **V1** in which the equilibrium ratio ($[\mathbf{C}]_{\text{tot}}/\{[\mathbf{C}]_{\text{tot}}+[\mathbf{S}]_{\text{tot}}\}$) is shifted furthest in the direction of $[\mathbf{C}]_{\text{tot}}$ (see Figure 10a and Table 4), after which increasing concentrations of **V1** result slowly in the shifting back of the conformational ratio in the direction of $[\mathbf{S}]_{\text{tot}}$. This observation is attributed to the possibility of also forming the 1:2 complex between **S** and **V1**, as presented in Figure 9. At relatively low concentrations of **V1**, the equilibrium will shift towards the 1:1 complex between **V1** and **C** (since $K_{\text{CV}} > K_{\text{SV}}$) and thus in the direction of $[\mathbf{C}]_{\text{tot}}$. At further increasing concentrations of **V1**, however, the formation of the 1:2 complex between **S** and **V1** will become more favorable which results in a shifting back of the equilibrium situation towards $[\mathbf{S}]_{\text{tot}}$. This behavior follows directly from Equation 1, which presents the equilibrium constant (K_{switch}) as a function of free **V1** in solution ($[\mathbf{V}]$) and all the individual equilibrium constants.

$$K_{\text{switch}} = \frac{[\mathbf{S}]_{\text{tot}}}{[\mathbf{C}]_{\text{tot}}} = \frac{[\mathbf{S}]+[\mathbf{SV}]+[\mathbf{VSV}]}{[\mathbf{C}]+[\mathbf{CV}]} = K_{\text{S/C}} \cdot \frac{1+K_{\text{SV}}[\mathbf{V}]+K_{\text{SV}}K_{\text{VSV}}[\mathbf{V}]^2}{1+K_{\text{CV}}[\mathbf{V}]} \qquad (1)$$

In Equation 1, $K_{\text{S/C}}$ is the equilibrium constant between **S** and **C** in the absence of viologen guests, K_{SV} and K_{CV} are the association constants of **V** to **S** and **C**, respectively, for the formation of the 1:1 complexes and K_{VSV} is the association constant for the formation of the 1:2 complex between **S** and **V**. The concentration of free **V** is obviously directly related to the concentration of isomers **C** and **S** in solution, but it is clear from Equation 1 that there will exist a concentration of **V** in which K_{switch} has a minimum value and thus that $[\mathbf{C}]_{\text{tot}}$ will be maximal. The value for K_{switch} as a function of different equilibrium constants and concentrations of **V1** could be determined numerically with the use of Mathematica®. Although the experimental data did not exactly match the theoretical calculations on the basis of all the experimentally derived individual equilibrium constants, as can be seen in Figure 10a (which is not surprising, since 4 equilibrium constants are involved of which some have errors of up to 30% and K_{VSV} had to be estimated), the trend in switching is clearly as would be expected on the basis of the binding model in Figure 9. Moreover, the data could be fitted with the assumed binding model and the calculated equilibrium constants as obtained by the fit did not deviate significantly from the experimentally derived values for the individual equilibrium constant (see Figure 10a).

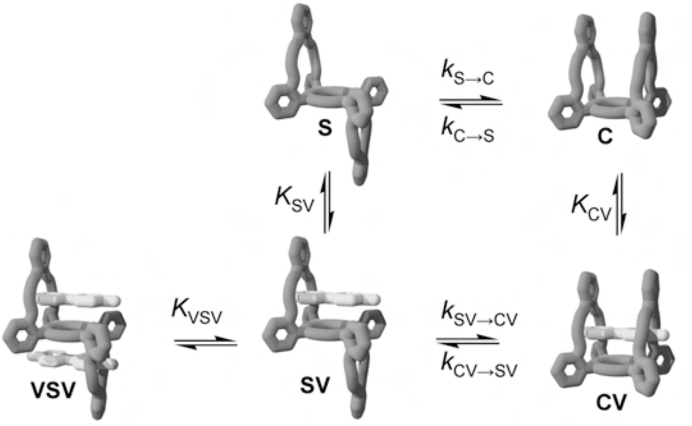

Figure 9. Binding scheme of the isomerisation between **S** and **C** in the presence of **V1**.

Table 4. Calculated rate constants ($k_{\text{S}\rightarrow\text{C-obs}}$) and equilibrium constants (K_{switch}) for the switching of **S** to **C** in solutions with different concentrations of viologen guests **V1**–**V3**.[a]

Guest	Conc (mM)	$k_{\text{S}\rightarrow\text{C-obs}}$[b,d] ($s^{-1}$)	K_{switch}[c,e]
No	0	1.8×10^{-6}	5.5
V1	0.5	2.3×10^{-6}	1.0
V1	1.3	3.0×10^{-6}	0.6
V1	2.6	2.7×10^{-6}	0.6
V1	3.1	2.6×10^{-6}	0.7
V1	6.5	1.9×10^{-6}	1.0
V2	3.3	2.4×10^{-6}	0.9
V3	20	1.1×10^{-6}	10.0

[a] Determined by ^{1}H-NMR experiments in 1/1 $CDCl_3/CD_3CN$ (v/v) at 37.5 °C. [b] Calculated from the initial 25% of the switching curves. [c] Calculated from the ratio $[\mathbf{S}]_{\text{tot}}/[\mathbf{C}]_{\text{tot}}$ at equilibrium. [d] Estimated error 20%. [e] Estimated error 15%.

In addition to switching induced by **V1**, it was also investigated with double blocked **V2** and half-viologen **V3** (1-methyl-4-phenyl-pyridinium hexafluorophosphate). As can be seen in Figure 11, also **V2** is capable of switching the equilibrium in the direction of **C**, which indicates that this guest has a higher affinity for **C** than for **S**. This binding process was further confirmed by the gradually upfield shifting aromatic resonances of the guest in time upon switching from **S** to **C** in the ^{1}H-NMR spectra. Although the binding of **V2** to **S** was not studied in detail, it is obvious that **C** can provide more stabilising interactions (or cause more solvent shielding upon complex formation) to **V2** than **S**.

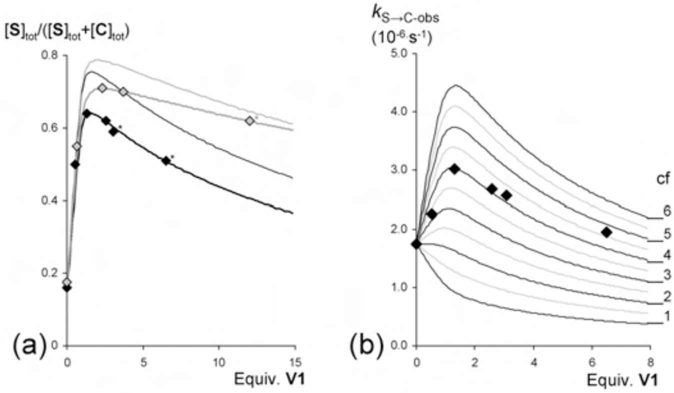

Figure 10. (a) Equilibrium ratios ($[S]_{tot}/([S]_{tot}+[C]_{tot}$}) at 37.5 °C (◆) and 47.5 °C (◇) plotted against the concentration of **V1** present in solution and the expected equilibrium ratios ($[S]_{tot}/([S]_{tot}+[C]_{tot}$}) based on the experimentally derived individual equilibrium constants (thin lines) and the bests fits (thicker lines matching the data points) of the experimental data (37.5 °C: $K_{S/C}$ = 5.5, K_{SV} = 1.5 x 10^{4} M^{-1} , K_{VSV} = 2.0 x 10^{2} M^{-1}, K_{CV} = 1.8 x 10^{5} M^{-1}. 47.5 °C: $K_{S/C}$ = 4.7, K_{SV} = 7.0 x 10^{3} M^{-1} , K_{VSV} = 70 M^{-1}, K_{CV} = 9.5 x 10^{4} M^{-1}). (b) Observed initial rates ($k_{S\rightarrow C\text{-obs}}$) for the switching of **S** to **C** in solutions with different concentrations of **V1** at 37.5 °C. The framework represents the theoretical rates based on different values of the cooperativity factor (*cf*), assuming equilibrium constants K_{SV} = 1.5 x 10^{4} M^{-1} and K_{VSV} = 2.0 x 10^{2} M^{-1}.

The switching experiment in the presence of **V3** (20 equiv.) revealed that this guest is not capable of switching the equilibrium in the direction of $[\mathbf{C}]_{tot}$, but that it causes the opposite effect and equilibrium is reached more in the direction of $[\mathbf{S}]_{tot}$ (Figure 11). This observation suggests that **S** has a higher affinity for **V3** than **C**, which is more or less in line with expectation since only one handle is needed for the accommodation of the single positive charge of **V3**.[48]

Kinetics of switching. In addition to the thermodynamics of the guest-induced switching, the kinetics were investigated. The observed initial rates ($k_{S\rightarrow C\text{-obs}}$) in solutions with different concentrations of **V1** at 37 °C could be calculated from the initial 25% of the switching curves, as obtained by ^{1}H-NMR spectroscopy. The data, which are presented in Figure 10b and Table 4, reveal that the observed initial rates increase upon increasing concentrations of **V1**, and reach a maximum value after which they decrease again. This decrease is fully in line with expectation,

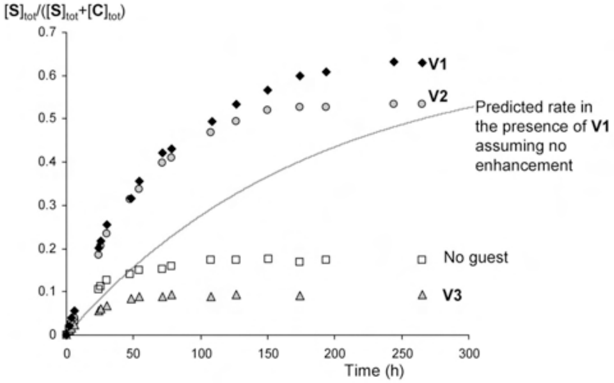

Figure 11. Kinetics of the switching of **S** (1 x 10^{-3} M) to **C** in the absence of guest (□) and in the presence of 1.3 equivalents of **V1** (♦), 3.3 equivalents of **V2** (◎) and 20 equivalents of **V3** (△). The line represents the calculated curve for the switching in the presence of 1.3 equivalents of **V1** assuming no induced switching effect.

since increased concentrations of **V1** shift the initial equilibrium further in the direction of the 2:1 complex **VSV** (Figure 9) in which both handles are restricted from rotation. The initial increase in rate in solutions with lower concentrations of **V1**, on the other hand, is surprising and suggests that the switching is enhanced by the presence of **V1**. Statistically, it was expected that the switching rate from **S** to **C** in the presence of **V1** ($k_{SV\rightarrow CV}$, see Figure 9) should be a factor 2 lower than in the absence of **V1** ($k_{S\rightarrow V}$) as a result of the restricted rotation of one of the handles of **S** upon complex formation with **V1**. In the absence of viologen-induced rate enhancement, the observed switching rates ($k_{S\rightarrow C\text{-obs}}$) should therefore decrease upon complex formation between **V1** and **S**, and drop even further upon a further increase in concentration of **V1**, as a result of 2:1 complex formation. To be able to fit the experimental data, a rate enhancement factor (*cf*) has to be included into the model. The initial rate ($k_{S\rightarrow C\text{-obs}}$) should evolve as a function of [**S**], [**SV**] and [**VSV**] according to Equation 2, in which $k_{SV\rightarrow CV}$ is defined according to Equation 3 in which both the statistical factor of 0.5 and the rate enhancement factor is taken into account.

$$k_{S\rightarrow C\text{-obs}} = k_{S\rightarrow C}\cdot[\mathbf{S}]/[\mathbf{S}]_{tot} + k_{SV\rightarrow CV}\cdot[\mathbf{SV}]/[\mathbf{S}]_{tot} \qquad (2)$$

$$k_{SV\rightarrow CV} = cf\cdot 0.5\cdot k_{S\rightarrow C}. \qquad (3)$$

$$k_{CV\rightarrow SV} = cf\cdot 0.5\cdot k_{C\rightarrow S}\cdot K_{SV}/K_{CV}. \qquad (4)$$

Since the individual constants $k_{S\rightarrow C}$, K_{SV} and K_{VSV} were determined earlier on, the magnitude of the factor *cf* could be calculated. To this end, the expected overall initial rate constants were calculated with the help of Mathematica® as a function of magnitude of *cf* and concentration of **V1** (which determines the ratios of [**S**], [**SV**] and [**VSV**]). The calculated rates as a function of **V1** are presented as the framework in Figure 10b, and from this framework it can be seen that the magnitude of *cf* is approximately 4, hence the switching rate is enhanced by the presence of **V1** by a factor of 4. In order to stress the acceleration of the switching process in the presence of **V1**, the expected kinetic curve of switching from **S** to **C** under the same conditions, assuming $cf = 1$, is presented in Figure 11. In addition to **V1**, also **V2** clearly accelerates the switching process, as can be observed in Figure 11 and Table 4. The observed rate ($k_{S\rightarrow C\text{-obs}}$) in the presence of **V3**, on the other hand, is lower than $k_{S\rightarrow C}$ (Table 4), which indicates that the switching rate is not enhanced by **V3**.

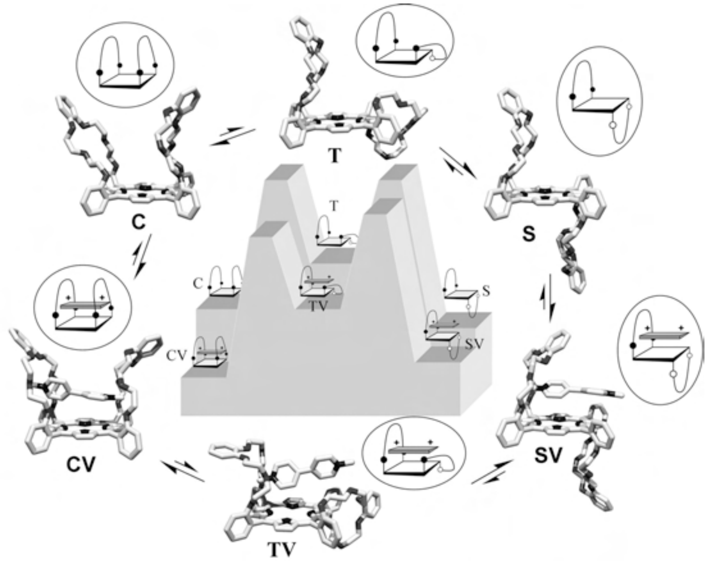

Figure 12. Proposed energy landscape of the switching between **C** and **S** in the presence of **V1**.

Mechanism. The magnitudes of the rate constants and the enthalpic and entropic contributions to the transition state energy for the switching process between the isomers **C** and **S** are all very similar to the values observed for atropisomerisation of *ortho*-*meso*-phenyl-substituted porphyrins, involving rotations around one single bond.[49-55] This suggests that the mechanism of isomerisation between **C** and **S** is not significantly different from other porphyrin atropisomerisation reactions. For this reason, the switching between **S** and **C** occurs most probably not via a simultaneous but via a consecutive rotation around the two phenyl rings. As a result, the switching consists of two steps that have similar activation barriers, with in between them a local energy minimum in which the handle is halfway the switching process (**T** in Figure 12). The energy level of **T** is unfavorable compared to both the energy levels of **S** and **C**. **T** is therefore part of the transition state, and can not be observed experimentally. The presence of **V1** in the switching process is expected to have a significant influence on the relative energy levels. The same interactions that cause that the complex **CV** is energetically more favorable than the complex **SV** (Figure 12) will influence the transition state of the switching process. Transition state intermediate complex **TV** will experience additional stabilizing interactions compared to **T** as a result of the fact that half the handle is switched to the side of the viologen (hence [**T**]/[**S**] > **TV**]/[**SV**]). Also the rotation around the second phenyl ring in the switching process from **T** to **C** is energetically more favorable as a result of these interactions. The viologen guest thus lowers the barriers associated with the switching process and effectively pulls the handle through to the other side of the porphyrin. Note that these same interactions should also cause a similar rate enhancement while switching back from **C** to **S**, in line with the principle of microscopic reversibility. The observation that both **V1** and **V2**, which bind in 90 degrees rotated geometries with respect to the porphyrin, accelerate the switching process is in line with this mechanism, since independent of the geometry of the eventual complexes, both **V1** and **V2** can exert these stabilizing interactions in the transition state. **V3** most probably accommodates its positive charge inside one crown ether handle and is consequently not capable of stabilizing the transition state involving the switching of the other handle, which accounts for the apparent absence of rate enhancement in the presence of **V3**.

3. Conclusion

The study presented in this chapter reveals that the presence of viologen guests has a large influence on the thermodynamics and kinetics of the atropisomerisation between an adjacent-cis-linked and an adjacent-trans-linked 'basket handle' porphyrin. The thermodynamic outcome of the guest-induced switching strongly depends on the relative affinities of the individual isomers for the different viologen guests. In all cases, the switching experiments were in very good agreement with theoretical predictions based on the individual equilibrium constants. The kinetic studies of the switching process revealed that the presence of viologen derivatives actually enhances the rate of the switching process. It is suggested that this enhancement is caused by favorable interactions between the positively charged guest and the crown ethers of the receptor in the process of switching, which stabilize the transition state energies according to a mechanism similar to those proposed by Warshel[56,57] for the stabilization of transition states in enzymatic systems. Although the rate enhancement factor of four observed in this switching is not even close to the rate enhancement in the natural systems, which are generally many orders of magnitude, the cooperative working of many of these stabilizing interactions could well account for a substantial part of the enzyme proficiencies.

4. Experimental section

Materials and methods. All solvents and chemicals were used as received. K_2CO_3 was dried in an oven (150 °C). Chloroform and acetonitrile used in fluorescence titration experiments were distilled from $CaCl_2$. Preparative TLC was performed on Merck silica glass plates (TLC Silica gel 60 F_{254}). Fluorescence experiments were performed on a Perkin-Elmer LS50B luminescent spectrometer equipped with a thermostatted cuvette holder. UV-Vis spectra were recorded on a Cary 100 Conc (Varian, Middelburg) UV-Vis spectrometer. The synthesis of ditosylate **1** is presented in Chapter 2 of this thesis. 5,10,15,20-tetrakis(*meso*-*o*-hydroxyphenyl)porphyrin **2**,[58] **V1**,[43] and **V2**[59] are described in the literature. The synthesis of **V3** is presented in Chapter 3 of this thesis.

‘Basket handle’ isomers X, S and C.

A suspension of **1** (0.90 g, 1.51 mmol), 5,10,15,20-tetrakis(*meso-p*-hydroxyphenyl)-porphyrin **2** (0.50 g, 0.74 mmol) and K_2CO_3 (1 g, 7.2 mmol) in DMF (250 mL) was reacted for 16 h under argon atmosphere at 110 ^{o}C. After filtration of the salts and evaporation of the solvents the product was purified by column chromatography (3% MeOH in $CHCl_3$ (v/v)) yielding 450 mg (52%) of a mixture of isomers **X**, **S** and **C**. The three isomers could be separated by preparative TLC (5:5:1 toluene/ethyl acetate/acetonitrile (v/v/v)) to give the products in a ratio of **X**:**S**:**C** = 4:8:1. (adjacent-trans-linked **S** could also be selectively crystallized out of a mixture of 5:1 acetonitrile/chloroform (v/v) containing isomers **C** and **S**) The separate products were dissolved in a minimal amount of $CHCl_3$ and to this solution *n*-pentane was added. Precipitates were formed which were collected by centrifugation and dried under vacuum at low temperatures yielding the different isomers **X**, **S** and **C** as purple solids (in order to prevent isomerisation between **C** and **S**, both speed and low temperatures are of essential importance in the separation process):

Cross-trans-linked ‘basket handle’ porphyrin isomer X.

^{1}H-NMR ($CDCl_3$ 400 MHz) δ 8.71 (s, 8H), 7.75 (d, 4H, J = 7.2 Hz), 7.69 (t, 4H, J = 7.9 Hz), 7.22 (d, 4H, J = 8.3 Hz), 7.12 (t, 4H, J = 7.4 Hz), 6.83 (m, 4H), 6.60 (m, 4H), 4.00 (M, 8H), 3.00 (M, 8H), 2.25 (t, 8H, J = 4.5 Hz), 1.59 (t, 8H, J = 4.6 Hz), −2.72 (s, 2H) ppm.

^{13}C-NMR ($CDCl_3$ 75 MHz) δ 158.68, 149.16, 135.02, 130.91, 129.69, 122.30, 119.60, 117.65, 115.65, 111.04, 69.65, 69.21, 68.63, 68.42 ppm.

MS (FAB) MALDI TOF *m/z* = 1180 (M + H^{+}).

UV-Vis ($CHCl_3$) λ/nm (log(ε·M^{-1}cm^{-1})) 418.5 (5.6), 513.0 (4.3), 546.5 (3.8), 589.0 (3.8), 643.5 (3.5)

Adjacent-trans-linked ‘basket handle’ porphyrin isomer S.

^{1}H-NMR ($CDCl_3$ 400 MHz) δ 8.69 (s, 4H), 8.68 (s, 4H), 8.00 (dd, 4H, J = 1.7 Hz, J = 7.4 Hz), 7.75 (ddd, 4H, J = 1.7 Hz, J = 7.6 Hz, J = 8.3 Hz), 7.39 (dt, 4H, J = 1.0 Hz, J = 7.5 Hz), 7.28 (dd, 4H, J = 0.8 Hz, J = 8.4 Hz), 6.27 (dd, 4H, J = 3.5 Hz, J = 6.0 Hz), 5.70 (dd, 4H, J = 3.6 Hz, J = 5.9 Hz), 3.94 (m, 8H), 3.08 (m, 4H), 2.88 (m, 4H), 2.27 (m, 4H), 1.94 (t, 8H, J = 3.9 Hz), 1.51 (m, 4H), −2.88 (s, 2H) ppm.

^{13}C-NMR ($CDCl_3$ 75 MHz) δ 158.82, 147.91, 134.91, 131.60, 129.79, 120.89, 119.85, 115.41, 114.67, 112.43, 69.41, 69.01, 68.60, 68.04 ppm.

MALDI TOF *m/z* = 1180 (M + H^{+}).

UV-Vis ($CHCl_3$) λ/nm (log(ε·M^{-1}cm^{-1})) 419.5 (5.6), 513.5 (4.3), 547.0 (3.9), 589.0 (3.9), 645.0 (3.5).

Ajacent-cis-linked ‘basket handle’ porphyrin isomer C.

^{1}H-NMR ($CDCl_3$ 400 MHz) δ 8.74 (s, 4H), 8.74 (s, 4H), 7.95 (dd, 4H, J = 1.7 Hz, J = 7.4 Hz), 7.74 (ddd, 4H, J = 1.8 Hz, J = 7.5 Hz, J = 8.3 Hz), 7.37 (dd, 4H, J = 1.0 Hz, J = 7.1 Hz), 7.34 (m,

4H), 6.36 (dd, 4H, J = 3.6 Hz, J = 6.0 Hz), 6.26 (dd, 4H, J = 3.6 Hz, J = 6.0 Hz), 4.11 (td, 4H, J = 5.6 Hz, J = 11.1 Hz), 4.00 (m, 4H), 3.33 (m, 4H), 3.22 (m, 8H), 2.96 (m, 8H), −2.75 (s, 2H) ppm.
^{13}C-NMR ($CDCl_3$ 75 MHz) δ 158.65, 148.58, 136.03, 131.63, 129.72, 121.22, 119.88, 115.65, 114.89, 112.90, 69.54, 69.28, 69.09, 68.80 ppm.
MALDI TOF m/z = 1180 ($M + H^+$).
UV-Vis ($CHCl_3$) λ/nm ($\log(\varepsilon \cdot M^{-1} cm^{-1})$) 420.0 (5.6), 514.5 (4.3), 550.0 (3.8), 591.0 (3.8), 646.5 (3.4).

Table 5. Crystal data and structure refinement for adjacent-trans-linked isomer **S**.

Identification code	CLIP10
Crystal colour	dark purple
Crystal shape	rough thick platelet
Crystal size	0.21 x 0.20 x 0.05 mm
Empirical formula	C72 H66 N4 O12
Formula weight	1179.29
Temperature	208(2) K
Radiation / Wavelength	MoKalpha (graphite mon.) / 0.71073 A
Crystal system, space group	Monoclinic, P21/a
Unit cell dimensions	a, alp= 12.9808(4) A, 90 deg.
44169 reflections	b, bet= 14.6770(9) A, 105.642(4) deg.
1.900 < theta < 25.000)	c, gam= 16.2856(12) A, 90 deg.
Volume	2987.8(3) A^3
Z, Calculated density	2, 1.311 Mg/m^3
Absorption coefficient	0.090 mm^-1
Diffractometer / scan	Nonius KappaCCD with area detector phi and omega scan
F(000)	1244
Theta range for data collection	1.90 to 25.00 deg.
Index ranges	-15<=h<=15, -17<=k<=17, -19<=l<=19
Reflections collected / unique	44169 / 5264 [R(int) = 0.0597]
Reflections observed	3609 ([Io>2sigma(Io)])
Completeness to 2theta = 25.00	95.7%
Absorption correction	SADABS multiscan correction(Sheldrick,1996)
Refinement method	Full-matrix least-squares on F^2
Computing	SHELXL-97 (Sheldrick, 1997)
Data / restraints / parameters	5264 / 0 / 397
Goodness-of-fit on F^2	1.066
SHELXL-97 weight parameters	0.033600 2.925100
Final R indices [I>2sigma(I)]	R1 = 0.0636, wR2 = 0.1139
R indices (all data)	R1 = 0.1040, wR2 = 0.1281
Largest diff. peak and hole	0.856 and -0.219 e.A^-3

The association constants for the 1:1 complex formation between the different isomers and viologen derivatives were determined according to standard fitting procedures. The association constants for the 2:1 complex formation between **S** and **V1** in the ^{1}H-NMR titration experiment were fitted with the use of Mathematica®, in which the association constant K_{SV} was varied and the fit provided the value of K_{VSV}. In this chapter the values for K_{SV} and K_{VSV} of the optimized fit are given.

The assumption that at lower concentrations the binding of **V1** to **S** can be fitted with the use of a 1:1 binding isotherm can also be shown analytically. In a titration of **S** with a viologen **V** in which 2:1 complex formation is allowed both the 1:1 complex **SV** and the 2:1 complex **VSV** can form. The overall binding process in the titration is therefore: **S** + **V** $\rightleftharpoons$ **SV** + **VSV**. The association constants for the 1:1 (K_{SV}) and the 2:1 complex formation (K_{VSV}) are presented in Equations 5 and 6.

$$K_{SV} = \frac{[SV]}{[S][V]} \tag{5}$$

$$K_{VSV} = \frac{[VSV]}{[SV][V]} \tag{6}$$

$$K_{app} = \frac{[SV]+[VSV]}{[S][V]} = \frac{K_{SV}[S][V]+K_{SV}[S][V]K_{VSV}[V]}{[S][V]} = K_{SV}(1+K_{VSV}[V]) \tag{7}$$

From the apparent association constant, which is given in Equation 7, it becomes clear that this constant, which describes the equilibrium of the combined 1:1 and 2:1 complexes, changes upon increasing concentrations of **V**. There is, however, a certain concentration regime in which the deviations between Equation 5 and 7 are very marginal. As long as $K_{VSV}\cdot[V]$ is small, the overall binding process does not deviate from a 1:1 binding process. At the experimental concentrations, the maximum concentration of **V1** ($[V]_o$) was never higher than 1 x 10^{-4} M and the concentration of **S** ($[S]_o$) was 1 x 10^{-6} M. Because of this excess of **V1** it can be safely stated that $[V]_o \approx [V]$. Assuming an association constant K_{VSV} of 600 M^{-1} as derived from the ^{1}H-NMR titration, it becomes clear that the apparent association constant deviates only 6% from the 1:1 binding behavior at the final point of the titration ($K_{VSV}\cdot[V] = 0.06$), whereas in the initial part of the titration, in which lower concentrations of **V** are present, this deviation will be even smaller. Since this error is by no means larger than the experimental error in the chosen concentration regime of the titration experiment, accurate fits can be obtained with the help of 1:1 binding isotherms.

5. References and notes.

1. Le Gac, S. W.; Marrot, J.; Reinaud, O.; Jabin, I. *Angew. Chem. Int. Ed.* **2006**, *19*, 3123−3126.
2. Specht, A.; Bernard, P.; Goeldner, M.; Peng, L. *Angew. Chem. Int. Ed.* **2002**, *41*, 4706−4708.
3. Schneider, H.-J.; Güttes, D.; Schneider, U. *J. Am. Chem. Soc.* **1988**, *110*, 6449−6451.
4. Cram, D. J.; Choi, H.–J.; Bryant, J. A.; Knober, C. B. *J. Am. Chem. Soc.* **1992**, *114*, 7748−7765.

5. Liu, Y.; Chen, Y. *Acc. Chem. Res.* **2006**, *39*, 681–691.
6. Trabolsi, A.; Urbani, M.; Delgado, J. L.; Ajamaa, F.; Elhabari, M.; Solladié, N.; Nierengarten, J. -F.; Albrecht-Gary, A.-M. *New J. Chem.*, **2008**, *32*, 159–165.
7. Gibson, H. W.; Yamaguchi, N.; Hamilton, L.; Jones, J. W. *J. Am. Chem. Soc.* **2002**, *124*, 4653–4665.
8. Jones, J. W.; Zakharov, L. N.; Gibson, H. W. *J. Am. Chem. Soc.* **2002**, *124*, 13378–13379.
9. Sato, H.; Tashiro, K.; Shinmori, H.; Osuka, A.; Murata, Y.; Komatsu, K.; Aida, T. *J. Am. Chem. Soc.* **2005**, *127*, 13086–13087.
10. Thordarson, P.; Coumans, R. G. E.; Elemans, J. A. A. W.; Thomassen, P. J.; Visser, J.; Rowan, A. E.; Nolte, R. J. M. *Angew. Chem. Int. Ed.* **2004**, *43*, 4755–4759.
11. Houk, K. N.; Leach, A. G.; Kim, S. P.; Zhang, X. *Angew. Chem. Int. Ed.* **2003**, *42*, 4872–4897.
12. Koshland, D. E. Jr. *Proc. Nat. Acad. Sci. USA* **1958**, *44*, 98–104;
13. Steitz, T. A.; Ludwig, M. L.; Quiocho, F. A.; Lipscomb, W. N. *J. Biol. Chem.* **1967**, *242*, 4662–4668.
14. Bennett, W. S.; Huber, R.; *Crit. Rev. Biochem.* **1984**, *15*, 291–384.
15. Koshland, D. E. Jr. *Angew. Chem. Int. Ed. Engl.* **1994**, *33*, 2375–2377.
16. Gerstein, M.; Lesk, A. M.; Chothia, C. *Biochemistry* **1994**, *33*, 6739–6749.
17. Rebek, J. Jr.; Askew, B.; Killoran, M.; Nemeth, D.; Lin, F.-T.; *J. Am. Chem. Soc.* **1987**, *109*, 2426–2431.
18. Vicent, C.; Hirst, S. C.; Garcia-Tellado, F.; Hamilton, A. D. *J. Am. Chem. Soc.* **1991**, *113*, 5466–5467.
19. Sijbesma, R. P.; Nolte, R. J. M. *J. Am. Chem. Soc.* **1991**, *113*, 6695–6696.
20. Hayashi, T.; Asai, T.; Hokazono, H.; Ogoshi, H. *J. Am. Chem. Soc.* **1993**, *115*, 12210–12211.
21. Hayashi, T.; Asai, T.; Borgmeier, F. M.; Hokazono, H.; Ogoshi, H. *Chem. Eur. J.* **1998**, *4*, 1266–1274.
22. Palyulin, V. A.; Emets, S. V.; Chertkov, V. A.; Kasper, C.; Schneider, H.-J. *Eur. J. Org. Chem.* **1999**, 3479–3482.
23. Weinig, H.-G.; Krauss, R.; Seydeck, M.; Bending, J.; Koert, U. *Chem. Eur. J.* **2001**, *7*, 2075–2088.
24. Chong, Y. S.; Smith, M. D.; Shimizu, K. D. *J. Am. Chem. Soc.* **2001**, *123*, 7463–7464.
25. Chong, Y. S.; Shimizu, K. D. *Synthesis* **2002**, 1239–1240.
26. Kacprzak, K.; Gawroçski, J. *Chem. Commun.* **2003**, 1532–1533.
27. Rebek, J. Jr., *Acc. Chem. Res.* **1984**, *17*, 258–264.
28. Takeuchi, M.; Ikeda, M.; Sugasaki, A.; Shinkai, S. *Acc. Chem. Res.* **2001**, *34*, 865–873.
29. Gawroçski, J.; Kacprazak, K. *Chirality* **2002**, *14*, 689–702.
30. Iwasawa, N.; Takahagi, H. *J. Am. Chem. Soc.* **2007**, *129*, 7754–7755.
31. Gottwald, L. K.; Ullman, E. F. *Tetrahedron Lett.* **1969**, *36*, 3071–3074.
32. Walker, F. A. *Tetrahedron Lett.* **1971**, *52*, 4949–4952.
33. Momenteau, M.; Look, B.; Mispelter, J.; Bisagni, E. *Nouv. J. Chim.* **1979**, *3*, 77–79.
34. Momenteau, M.; Look, B. *J. Mol. Catal.* **1980**, *7*, 315–317.
35. Jimenez, H. R. ; Moratal, J. M. ; Faus, J. ; Momenteau, M. *New J.Chem.* **1994**, *18*, 1247–1252.
36. Landergren, M.; Baltzer, L. *J. Chem. Soc., Perkin Trans. 2* **1992**, *2*, 355–359.
37. Weber, E. *Liebigs Ann. Chem.* **1983**, *5*, 770–801.

38. Simonis, U.; Walker, F. A.; Lani Lee, P.; Hanquet, B. J.; Meyerhoff, D. J.; Robert Scheidts, W. *J. Am. Chem. Soc.* **1987**, *109*, 2659–2668.
39. The error obtained via measuring the integrals was significantly higher
40. Experimental uncertainties in van't Hoff plots used to determine the ΔH^{o} and ΔS^{o} values may lead to accidental correlations with no statistical significance.
41. Hunter, C. A.; Sanders, J. K. M. *J. Am. Chem. Soc.* **1990**, *112*, 5525–5534.
42. Williams, A. R.; Northrop, B. H.; Chang, T.; Stoddart, J. F.; White, A. J. P.; Williams, D. J. *Angew. Chem. Int. Ed.* **2006**, *45*, 6665–6669.
43. Elemans, J. A. A. W.; Claase, M. B.; Aarts, P. P. M.; Rowan, A. E.; Schenning, A. P. H. J.; Nolte, R. J. M. *J. Org. Chem.* **1999**, *64*, 7009–7016.
44. Gunter, M. J.; Hockless, D. C. R.; Johnston, R.; Skelton, B. W.; White, A. H. *J. Am. Chem. Soc.* **1994**, *116*, 4810–4823.
45. Gunter, M. J.; Jeynes, T. P.; Johnston, M. R.; Turner, P.; Chen, Z.; *J. Chem. Soc., Perkin Trans. 1* **1998**, 1945–1958.
46. This negative cooperativity is significantly lower than that observed for the binding of two molecules of **V1** to a double cavity-containing porphyrin in an earlier report of this group. As was proposed in the article, the negative cooperative effect of a factor of 350 is a result of structural (allosteric) changes in the receptor upon the binding of the first molecule of **V1**. P. Thordarson. E. J. A. Bijsterveld, J. A. A. W. Elemans, P. Kasák, R. J. M. Nolte, A. E. Rowan, *J. Am. Chem. Soc.* **2003**, *125*, 1186–1187.
47. Unfortunately, the effect of temperature on the binding of the second molecule of **V1** to **S** (K_{VSV}) could therefore not be investigated.
48. Although it could also be a result of significant 2:1 complex formation. Nevertheless, it is clear that **V3** does not show significant stronger binding to **C** than to **S**.
49. Crossley, M. J.; Field, L. D.; Forster, A. J.; Harding, M. M.; Sternhell, S. *J. Am. Chem. Soc.* **1987**, *109*, 341–348.
50. Hatano, K.; Anzai, K.; Kubo, T.; Tamai, S. *Bull. Chem. Soc. Jpn.* **1981**, *54*, 3518–3521.
51. Hatano, K.; Anzai, K.; Nishino, A.; Fujii, K. *Bull. Chem. Soc. Jpn.* **1985**, *58*, 3653–3654.
52. Fujimoto, T.; Umekawa, H.; Nishino, N. *Chem. Lett.* **1992**, 37–40.
53. Spasojevic, I.; Onzeleev, R.; White, P. S.; Fridovich, I. *J. Inorg. Chem.* **2002**, *41*, 5874–5875.
54. Song, R.; Robert, A.; Bernadou, J. ; Meunier, B. *Analysis* **1999**, *27*, 464.
55. Reginato, G.; Di Bari, L.; Salvadori, P.; Guilard, R. *Eur. J. Org. Chem.* **2000**, 1165–1171.
56. A. Warshel, *Computer Modeling of Chemical Reactions in Enzymes and Solutions*, Wiley, New York, **1991**.
57. A. Warshel, *J. Biol. Chem.* **1998**, *273*, 27035–27038.
58. Rothemund, P. *J. Am. Chem. Soc.* **1935**, *75*, 2010–2011.
59. Coumans, R. G. E.; Elemans, J. A. A. W.; Nolte, R. J. E.; Rowan, A. E. *Proc. Nat. Acad. Sci.* **2006**, *103*, 19647–19651.

Summary

Weak and reversible interactions between molecules are of essential importance to facilitate the machinery of life. These so-called supramolecular interactions help assemble molecular building blocks into well-defined superstructures like the cell membrane, DNA, or a protein. These interactions furthermore form the basis of recognition processes between molecular components as found in enzyme-substrate complexes, and play a dominant role in the transfer of information in and between biochemical systems. In the past decades a new discipline that uses these interactions as a construction tool has emerged in chemistry, i.e. supramolecular chemistry. By synthesizing molecules and macromolecules equipped with specific functionalities for surpramolecular binding, and by studying the self-assembling properties of these systems, a number of characteristic features observed in nature could be mimicked and better understood.

Macrocyclic receptor compounds based on porphyrins have been a fruitfull subject of study in the field of supramolecular chemistry, for instance as artificial systems that mimic certain aspects of biomimetic catalysis. At the Department of Organic Chemistry of the Radboud University Nijmegen research has been focused on so-called porphyrin clips, which, in addition to a porphyrin molecule, contain a receptor binding site based on the cage molecule glycoluril. In this thesis, the synthesis and properties of variants of this type of compounds are described as well as applications in processes like host-guest binding and threading onto polymers.

Binding studies between new, slightly larger and more flexible variants of these porphyrin-clips and a variety of small aromatic guest-molecules reveal that also these new receptor molecules, like the previously studied ones, can bind guests tightly inside their cavities; this binding occurs via an induced-fit mechanism. Insertion of a metal (zinc) ion makes the porphyrin receptor molecule bi-valent, allowing for the simultaneous binding of pyridine ligands and viologen derivatives via a cooperative binding mechanism. A detailed protocol on how to accurately measure the cooperative binding effects is described, and an effort was made to map the mechanistic origins of the observed processes. Phenomena as observed in natural cooperative binding systems, such as inhibition, activation, electronic interactions, effect of solvent and conformational changes of receptors upon binding of guests, can to a certain extent all be mimicked by these synthetic host-guest systems.

When the viologen guest molecules are end-capped with bulky blocking groups, complex formation between the macrocyclic receptor molecule and the guest is hampered. In this case complex formation can only occur via a slow slippage process, which allowed us to accurately determine the kinetics of the host-guest binding process. The cooperative slippage of zinc porphyrin clips over these blocking groups in the presence of pyridine ligands was studied and analyzed in detail with regard to the kinetics and thermodynamics of the process.

Previous studies have revealed that porphyrin-clips can thread onto polymer chains of lengths up to 55 nanometer and translocate on it. The question was how this threading proceeds and whether the porphyrin-clip can thread via a mechanism in which a folded chain first binds in the cavity of the clip and then threads through it. Studies with different bifurcated viologen guests revealed that such a mechanism is not possible because the cavity is too small to hold a folded polymer chain. The porphyrin-clip, therefore, can only thread via the open end of the polymer, after which it completely traverses the polymer chain.

The experimental threading kinetics could be accurately described with the help of a consecutive hopping model in which the initial binding involves a so-called entron effect. This study revealed nicely that the observed threading rates are a combination of the initial binding event and the chance that this binding event leads to viologen-receptor complex formation. The translocation speed is not expressed in the experimental observations.

One of the newly synthesized, slightly larger and more flexible porphyrin receptors was observed to display completely different threading kinetics compared to the smaller and more rigid ones studied before. The translocation process was found to be slower, and was expressed in the observed kinetics, argueably as a result of an induced fit binding of the receptor onto the polymer chain, which decelerates the translocation. The process furthermore involved a highly unusual negative activation enthalpy, which most probably is related to the flexible nature of the macrocyclic receptor.

The threading rates of the smallest porphyrin-clip, which is also very rigid, surprisingly were found to increase at intermediate chain lengths (from 8 to 22 carbon atoms). This observation could be explained with the help of a so-called intramolecular looping mechanism, in which the recognition site of the polymeric guest first binds weakly to the outside of the receptor molecule, after which the open chain-end of the guest loops back into the cavity of the macrocycle, thereby templating and accelerating the threading process. The shortest chains were too small to profit from this mechanism, whereas the outside-association was too weak to have a favorable effect on the longer polymer chains. By increasing the affinity between the outside of the receptor and the recognition site of the polymer, the threading of longer chains could also be accelerated, fully in line with the proposed looping mechanism.

The last part of the thesis describes a ‘basket handle’ porphyrin and the effect of binding events on the isomerisation of this receptor compound. It was found that binding of viologen derivatives could switch the isomerisation in the direction of the thermodynamically unfavorable isomer. Moreover, the rate of isomerisation was accelerated as a result of this binding event, which is likely the result of transition state stabilization.

In summary, this thesis provides an overview of the supramolecular interactions that are involved in the host-guest binding of porphyrin receptor molecules to polymeric guests. The effects of cavity size, flexibility of the host, and the coordination of ligands on the thermodynamics and kinetics of the binding events have been mapped in detail and the mechanisms of the binding events have been elucidated. The supramolecular events of binding, slippage, threading and switching were shown to be governed by key-principles such as induced-fit, inhibition, activation, solvent interplay, fractional saturation, transition state stabilisation, microscopic reversibility, Hess’s law, all-or-nothing effects, and entropy-enthalpy compensation effects. All these principles also play dominant roles in the functioning of the biomachinery of life and this study shows that similar processes can be operative and realized in artificial, man-made systems.

Samenvatting

Zwakke en omkeerbare (reversibele) interacties tussen chemische groepen en bouwstenen, zoals voorkomend in levende organismen, zijn van essentieel belang voor het functioneren van het leven. Deze zogenaamde supramoleculaire interacties vormen de basis van belangrijke biochemische structuren en processen, zoals de assemblage van een celmembraan uit fosfolipide moleculen, de synthese en replicatie van DNA en de vorming van eiwitten. Deze interacties zijn ook de drijvende kracht achter de processen, die maken dat moleculen elkaar kunnen herkennen, zoals de vorming van enzym-substraat-complexen. Daarnaast vervullen ze een dominante rol in de informatie-overdracht (signal transduction), die plaats vindt in biochemische systemen. In de laatste decennia is er in de chemie een nieuwe discipline ontstaan, die zich bezig houdt met deze interacties, namelijk de supramoleculaire chemie. Door het synthetiseren van moleculaire systemen, die zijn uitgerust met specifieke functionaliteiten, die onderlinge binding kunnen bevorderen, en door het bestuderen van de zelfassemblerende eigenschappen van deze systemen, is het mogelijk gebleken om een groot aantal chemische verschijnselen uit de natuur na te bootsen en deze beter te begrijpen.

In de supramoleculaire chemie hebben in de afgelopen jaren porfyrines veel aandacht gekregen, bijvoorbeeld als verbindingen die kunnen worden gebruikt om bepaalde aspecten van biometische katalyse na te bootsen. In de afdeling Organische Chemie van de Radboud Universiteit Nijmegen heeft dit onderzoek zich ondermeer toegespitst op zogenaamde ‘porphyrin-clips’. Dit zijn holtevormige receptormoleculen, die zijn opgebouwd uit een porfyrine-kleurstof en de bouwsteen glycoluril. In dit proefschrift worden de synthese en de supramoleculaire eigenschappen van dit type verbinding beschreven, in het bijzonder met betrekking tot processen zoals het binden en rijgen (threading) van deze verbindingen aan polymere ketens. De beschreven studies richten zich ondermeer op de bindingseigenschappen van nieuwe, iets grotere en meer flexibelere varianten van deze porfyrine-clipmoleculen, die aromatische gastmoleculen (viologenen) kunnen binden via een zogenaamd ‘induced fit’-bindingsmechanisme.

Het plaatsen van een zinkmetaalion in de porfyrine geeft de porfyrine-clip een, wat men zou kunnen noemen, bivalent karakter, waardoor het mogelijk wordt om gelijktijdig een pyridine-ligand en een polymere of oligomere viologeengast te binden. Sterke coöperatieve bindingseffecten werden waargenomen, wanneer zowel deze pyridine-liganden als de viologenen aan de verschillende porfyrine-clipmoleculen werden toegevoegd. Een gedetailleerde studie werd uitgevoerd om precies vast te stellen hoe deze bindingseffecten moeten worden gemeten en worden geëvalueerd om de mechanistische herkomst van het coöperatieve gedrag te kunnen achterhalen. In de natuur voorkomende coöperatieve verschijnselen, zoals inhibitie, activering, elektronische interacties tussen chemische groepen, het effect van het oplosmiddel, en verandering van de ruimtelijke structuur van de receptor als gevolg van binding van een gastmolecuul, kunnen tot op zekere hoogte allemaal worden nagebootst en beschreven met deze artificiële porfyrine-clipmoleculen.

Als de polymere viologenen worden voorzien van grote eindgroepen wordt de complexvorming tussen de porfyrine-clipmoleculen en deze gastmoleculen bemoeilijkt. Complexvorming kan alleen geschieden door middel van een traag ‘slippage’-proces, waardoor het echter wel mogelijk wordt om de kinetiek van het bindingsproces nauwkeurig te bepalen. De coöperatieve effecten van de pyridine-liganden op dit 'slippage'-proces zijn in kaart gebracht, waardoor een mooi kinetisch overzicht kon worden verkregen van alle optredende coöperatieve bindingseffecten, dit als aanvulling op de thermodynamische evaluaties van deze effecten.

Eerdere studies in Nijmegen hebben aangetoond dat porfyrine-clips zich kunnen hechten aan polymeerketens met lengtes tot 55 nanometer en zich hierover kunnen verplaatsen. Onderzocht werd of een porfyrine-clip zich kan binden aan een gevouwen polymeerketen en zich vervolgens, net als een draad die door het oog van een naald gaat, kan rijgen aan deze keten. Studies met voor dit doel speciaal gesynthetiseerde dubbele ketens toonden aan dat zo'n proces niet plaatsvindt. De conclusie is derhalve, dat de porfyrine-clip zich moet hechten aan het uiteinde van de polymeerketen en zich daarna over deze keten verplaatst.

De experimentele resultaten, die met betrekking tot het rijg (threading)-proces zijn verkregen, konden nauwkeurig worden beschreven met behulp van een z.g.n. 'consecutive hopping mechanism', d.w.z. een mechanisme van opeenvolgende sprongetjes. Hierbij vindt de initiële binding plaats op basis van een zogenaamd 'entron-effect'. De studies tonen aan dat de experimenteel waargenomen rijg (threading)-snelheden een combinatie zijn van de initiële binding en de kans dat deze binding ook resulteert in complexvorming tussen de receptor en de viologeenbindingsplaats op de polymeerketen. De snelheid van het bewegen over de polymeerketen komt niet tot uitdrukking in de experimenteel waargenomen snelheden..

Eén van de nieuw gesynthetiseerde porfyrine-clips, en wel een iets grotere en wat meer flexibelere verbinding, vertoonde een totaal afwijkende threading-kinetiek, wanneer deze werd vergeleken met de wat kleinere en meer starre porfyrine-clips, die eerder waren bestudeerd. De snelheid van bewegen over de polymeerketen was langzamer en deze snelheid kwam nu wel tot uitdrukking in de kinetiek, waarschijnlijk als gevolg van een 'induced fit'-effect bij de binding aan het polymeer, waardoor de beweging over het polymeer wordt vertraagd.

Een opmerkelijke waarneming was het feit dat de aanrijg (threading)-snelheden van de kleinste en meest starre porfyrine-clip groter werden wanneer de polymeerketens een tussenliggende lengte bezaten (van 8 tot 22 koolstofatomen). Dit experimentele feit kon verklaard worden door een zogenaamd 'intramoleculair looping'-mechanisme aan te nemen, waarin de bindingsplek op het polymere gastmolecuul eerst zwakjes aan de buitenkant van de receptor bindt, waarna vervolgens het uiteinde van de polymeerketen via een loop in de holte van de receptor geplaatst wordt. Polymeerketens met korte lengtes bleken niet lang genoeg te zijn om van dit mechanisme te kunnen profiteren, terwijl de binding aan de buitenkant te zwak was om ook voor de langere ketens van voordeel te kunnen zijn. Door de affiniteit tussen de buitenkant van de porfyrinereceptor en de bindingsplek op het polymeer te vergroten kon het aanrijgen van langere ketens ook versneld worden, hetgeen geheel in overeenstemming was met het gepostuleerde mechanisme.

Het laatste onderdeel van het proefschrift handelt over een z.g.n. 'basket handle' porfyrine en in het bijzonder over de invloed van gastheer-gast (host-guest) interacties op de isomerisatie van deze verbinding. Binding van viologeenmoleculen blijkt het isomerisatie-evenwicht te verschuiven in de richting van het thermodynamisch minst stabiele isomeer. De snelheid van de isomerisatie wordt bovendien door deze binding vergroot, hetgeen waarschijnlijk moet worden toegeschreven aan een stabilisatie van de overgangstoestand ('transition state') van het proces.

Samenvattend geeft dit proefschrift een uitgebreid overzicht van de supramoleculaire fenomenen die ten grondslag liggen aan de binding van (polymere) gastmoleculen in receptormoleculen gebaseerd op porfyrines. De effecten van de grootte van de receptorholte, de flexibiliteit van de verbinding en het effect van coördinerende liganden op de thermodynamica en kinetiek van het bindingsproces zijn in detail in kaart gebracht en de achterliggende mechanismen konden voor een groot deel worden bepaald. De supramoleculaire aspecten van de gastheer-gast-binding, slippage-effecten, het aanrijgen aan polymere draden en het wisselen (switchen) tussen verschillende isomere vormen van een gastheermolecuul blijken gedomineerd te worden door sleutelbegrippen zoals ‘induced fit’, inhibitie, activering, oplosmiddeleffecten, fractionele verzadiging, overgangstoestand-stabilisatie, microscopische reversibiliteit, de wet van Hess, alles-of-niets-effecten en entropie-enthalpie-compensatie effecten. Al deze principes spelen ook een belangrijke rol in de natuur (de ‘biomechanica’ van het leven) en kunnen, zoals in dit proefschrift wordt aangetoond, nagebootst worden en worden begrepen met behulp van artificiële, door de mens ontworpen systemen.

List of Publications

Solution and solid-phase chemoselective synthesis of (1-6)-amino(methoxy) di- and trisaccharide analogues.
Peri, F.; Deutman, A. B. C; La Ferla, B.; Nicotra, F. *Chem. Commun.,* **2002**, *46*,1504-1505.

Processive rotaxane catalysts. Studies on the mechanism of the threading process.
Hidalgo Ramos, P.; Coumans, R.; Deutman, A. B. C.; de Gelder, R.; Smits, J. M. M.; Elemans, J. A. A. W.; Nolte, R. J. M.; Rowan, A. E. *J. Am. Chem. Soc.,* **2007**, *129*, 5699-5702.

Mechanistic aspects of the threading of polymers in processive rotaxane catalysts.
Elemans, J. A. A. W.; Coumans, R. G. E.; Hidalgo Ramos, P.; Deutman, A. B. C.; Rowan, A. E.; Nolte, R. J. M. *PMSE*, **2007**, *97*, 933-934.

Mechanism of threading a polymer through a macrocyclic ring.
Deutman, A. B. C.; Monnereau, C.; Elemans, J. A. A. W.; Ercolani, G.; Nolte, R. J. M.; Rowan, A. E. *Science*, **2008**, *322*, 5908, 1668-1671.

Squaring cooperative binding circles.
Deutman, A. B. C.; Monnereau, C.; Moalin, M.; Coumans, R. G. E.; Veling, N.; Coenen, M.; Smits, J. M. M.; de Gelder, R.; Elemans, J. A. A. W.; Ercolani, G.; Nolte, R. J. M.; Rowan, A. E. . *Proc. Nat. Acad. Sci.* **2009**, *106*, 10471–10476.

Porphyrin macrocyclic catalysts for the processive oxidation of polymer substrates.
Monnereau, C.; Hidalgo Ramos, P.; Deutman, A. B. C.; Elemans, J. A. A. W.; Nolte, R. J. M.; Rowan, A. E. *J. Am. Chem. Soc.*, **2010**, *132*, in press.

Threading of flexible porphyrin macrocycles
Deutman, A. B. C.; Monnereau, C.; Coumans, R. G. A.; Elemans, J. A. A. W.; Nolte, R. J. M.; Rowan, A. E. Manuscript in preparation.

Thermodynamics and kinetics of guest-induced switching between 'basket handle' porphyrin isomers.
Deutman, A. B. C.; Woltinge, T.; Elemans, J. A. A. W.; Nolte, R. J. M.; Rowan, A. E. Manuscript in preparation.

Terugblik en Dankwoord

Het was ergens eind 2003, dat ik een afspraak had gemaakt met Roeland om me van advies te voorzien bij mijn zoektocht naar een nieuwe baan. Hoewel het aanvankelijk niet de intentie was om in Nijmegen te gaan promoveren, leek me dit na ons gesprek toch wel een ontzettend leuke en ook logische optie. Mijn aantrekkingskracht werd niet alleen gevoed door de interessante onderwerpen die in de groep werden bestudeerd, maar vooral ook door de positieve en collegiale sfeer die de gehele vakgroep uitstraalde. Na wat heen en weer bellen, ik geloof een consult bij Jacques van Boom, een ballotage-keuring op het lab en, als belangrijkste, instemming van Floriske om ons prille familieavontuur in Nijmegen voort te zetten, mocht ik op 1 april 2004 op de toen nog Katholieke Universiteit Nijmegen beginnen aan mijn onderzoek. Ik was na wat aandringen van mijn kant ondergebracht op de porfclips (liever niet die wat onoverzichtelijke virusassemblages), bij Alan, met Hans als mijn dagelijkse begeleider. Als geschoold synthetisch chemicus hadden deze verbindingen vanwege hun omvang en symmetrische structuur al een grote aantrekkingskracht en het feit dat deze verbindingen ook nog een groot scala aan functionaliteit (binding en katalyse) met zich meedragen, maakte het extra uitdagend (ik was niet gewend dat je ook nog iets kon dóen met de verbindingen die je synthetiseerde). Aanvankelijk werd ik door Alan opgezadeld met het waanzinnige idee om aan zo’n porfclip vier verschillende enzymen vast te knopen, daar cascadereacties mee uit te voeren en vervolgens het wereldwijde broeikasprobleem mee op te lossen. Gelukkig werd mij veel vrijheid gegeven bij mijn onderzoek. Ik bevond mij wetenschappelijk gezien op de schouders van een aantal reuzen (waaronder Alan, Hans, Palli en Ruud) en in de jaren voorafgaand aan mijn proefschrift was een groot aantal hoge-impact-publicaties gerealiseerd op porfclips. Hoewel hier en daar gefluisterd werd dat de melkkoe wel opgedroogd was, ging ik vlijtig mijn eigen, iets grotere, variant van deze verbinding synthetiseren om er op zijn minst een te maken met mijn handtekening erop. Na een goede oplossing voor het zuiveren van deze verbinding te hebben gevonden (de naam scheikunde; de kunst van het scheiden, geldt meer dan ook voor dit type verbindingen) ging ik mij, aanvankelijk wat aarzelend, doch spoedig met groeiend enthousiasme en verwondering, toespitsen op de supramoleculaire bindingsaspecten. In mijn beleving van voor die tijd waren titraties saai, ik was per slot van rekening met rede geen analytisch chemicus geworden, maar meten aan dit type verbindingen was andere koek. Fantastisch hoe je aan het schuiven van een aantal NMR-signalen heel duidelijk bindingsgedrag van moleculen, waar je nota bene zelf de geestelijke vader van bent, in kaart kan brengen, zoals te zien is in de vele stapelingen van NMR-spectra in dit proefschrift. Al snel kwam ik erachter dat, ondanks het hoge niveau van het werk dat voor mij was gedaan, aan de basis nog wat wetenschappelijke leemtes opgevuld konden worden. In het relatief jonge vakgebied van de supramoleculaire chemie werd toch nog vooral gekeken naar de synthese van verbindingen en de complexen die deze verbindingen vormden, en minder naar de onderliggende mechanismen en wetmatigheden bij het vormen van de complexen.

Ik ging me daarom, met hulp van Ruud, Michiel, Cyrille en de altijd stimulerende Hans, toeleggen op het in kaart brengen van de coöperatieve bindingseffecten, die bij dit soort verbindingen bekend waren. Juist het feit dat ik hierbij af en toe tegen de stroom in moest roeien heeft ervoor gezorgd dat de hoofdstukken 3 en 4 zo omvangrijk zijn geworden. Ik ben twee keer in mijn promotietijd door Roeland erg duidelijk een bepaalde onderzoeksrichting ingestuurd. Dit gebeurde niet met een simpele opdracht om de werkzaamheden te verrichten, maar het ging subtieler. Zo'n drie maanden voor Lunteren kreeg ik simpelweg de opdracht om een praatje te houden over een onderwerp waar ik helemaal niets aan had gedaan. Het resultaat was dat ik als een idioot ging werken aan dit type onderzoek om toch eigen onderzoeksdata te kunnen presenteren. Zo ben ik de kant van het aanrijgen (threaden) opgestuurd en ben ik mij ook zijlings met katalyse, waar voornamelijk Cyrille zijn tanden op stuk aan het bijten was, gaan bezig houden. Ook bij deze onderwerpen hebben we geprobeerd om de achterliggende mechanismen te achterhalen, iets wat bij het threaden tegen de verwachtingen in wonderwel lukte. Ik hoefde mijn theorie alleen nog maar te staven op een aantal verbindingen met 'korte staartjes' en ik zou klaar zijn. Ik was dan aanvankelijk ook 'not amused' dat deze verbindingen een heel ander gedrag vertoonden dan verwacht (mijn model leek niet meer te kloppen). De verwondering over de experimentele observaties kreeg echter al snel de overhand en de vreemde meetresultaten moesten hoe dan ook gefundeerd verklaard kunnen worden, een overduidelijk voorbeeld van hoe serendipity vaak aan de mooiste wetenschappelijke inzichten ten grondslag ligt. Aanvankelijk dachten we aan een vouw in de keten en hoofdstuk 5, dat grotendeels door mijn student Max bij elkaar is gesynthetiseerd en gemeten, is het directe resultaat van deze onjuiste aanname. Uiteindelijk kwamen we toch op het juiste 'intramoleculair looping'-mechanisme, met zeer veel dank aan Gianfranco Ercolani, en moesten we enkel nog de theorie met een experimenteel voorbeeld staven. Ik liep tegen die tijd aan het eind van mijn contract, maar gelukkig waren Alan en Roeland bereid om mij een half jaartje (en later nog wat meer) extra tijd te geven om deze theorie experimenteel te bevestigen. Cynisch genoeg waren de op het laatste moment en met pijn en moeite gesynthetiseerde moleculen niet in staat om de theorie te bevestigen, maar nota bene een verbinding die al jaren op de planken lag, kon het trucje wel. De rest is geschiedenis.

Nu, alweer 2010, ben ik bezig met de laatste woorden van het proefschrift (een PhD eindigt pas op het moment van de verdediging) en rest mij weinig dan een woord van dank uit te spreken.

Roeland, allereerst dank dat je het aandurfde om nog een Leidenaar in je groep op te nemen. Ik heb een enorm respect voor de manier waarop jij al die jaren de groep hebt geleid. Je bezit de gave om mensen aandacht en vertrouwen te geven ondanks je enorm drukke schema. De stapels Science-manuscripten waar je je elk weekend weer, zonder ervoor vergoed te worden, doorheen wist te referee-en tekenen je drive. Je prikkelend enthousiasme voor de wetenschap heeft een enorm positieve uitwerking gehad op mijn werkzaamheden en ik heb bijna 5 jaar lang met ontzettend veel plezier in de groep rondgelopen. Ik wens je alle succes met je tweede start als onderzoeker.

Alan, jij bent de afgelopen vijf jaar voor mij een bron van inspiratie geweest. Je nimmer aflatende creativiteit en enthousiasme voor nieuwe invalshoeken verbaasden mij telkens weer. Je bezit de bijzondere gave om wetenschap voor een breed publiek aantrekkelijk te maken en weet als geen ander mensen te inspireren, of het hoofd op hol te doen brengen met je ideeën. Ik zal nooit vergeten hoe wij gezamenlijk in de speeltuin in aanwezigheid van onze kinderen de laatste hand legden op het threading-manuscript. Het was een voorrecht voor je te kunnen werken. Ik hoop dat het je, naast een sprankelende voortzetting van je wetenschappelijke carrière, ook persoonlijk voor de wind zal gaan.

Heel veel dank ook aan mijn dagelijkse begeleider en copromotor Hans, die een erg belangrijke rol heeft gespeeld in het tot stand komen van mijn proefschrift. Je uiterst secure en snelle nakijkwerk hebben de vaart in mijn proefschrift weten te houden en zonder jou had het geheel er erg anders uitgezien. Ik waardeer de open deur die ik altijd aantrof als ik weer eens met een spectrum of een idee binnen liep (waarschijnlijk tot vervelens toe). Ik ben ervan overtuigd dat je nog vele mooie wetenschappelijke vindingen op je palmares weet te schrijven.

To my personal post-doc Cyrille: I have enjoyed every second of working together on the lab, your sense of humour is hilarious and I am very grateful for the work you have done for this thesis. I am convinced that you will have an excellent carrier within the academia and we'll stay in touch.

Gianfranco Ercolani, getting into contact with you was one of the best moves in my PhD. I have enjoyed your warm welcome in Rome and I am very grateful for the important contributions you have made to this thesis and the two publications. Apart from providing me with a number of crucial insights, you have given me the confidence to analytically handle supramolecular chemistry problems. I'm also very grateful for the warm words that accompanied your approval of this thesis as a member of the manuscript committee.

I would also like to thank Professor David Leigh for taking the time to have a look at my manuscript. I am very much looking forward to have some chats about ratchets and deamons with one of the giants in the field.

Jan van Hest, dank voor je rol als voorzitter van de manuscriptcommissie. Ik heb de vele praatjes in de wandelgangen en het gezamenlijk nakijken van tentamens erg op prijs gesteld.

Ik was in de gelukkige positie om drie studenten bij mij op het lab te mogen begeleiden. Allereerst Tim, in de tien? weken die je stage hebt gelopen, heb je een mooie bijdrage kunnen leveren aan hoofdstuk 9 van mijn proefschrift. Ik heb je zelfstandige manier van werken erg gewaardeerd en weet zeker dat je over een aantal jaar een mooi proefschrift zal afleveren. David, hoewel er uiteindelijk niets van jouw werk in mijn proefschrift is beland, heeft dat niets met de kwaliteit van het geleverde werk te maken (meer pagina's kon ik de manuscriptcommissie gewoon niet aandoen). Jouw afstudeerverslag had allerminst misstaan als hoofdstuk in menig proefschrift. Ik heb erg veel plezier beleefd aan onze samenwerking en waardeer je erg als collega en als vriend. Ik denk dat ik er nooit achter zal komen hoe onze tafeltennis-niveaus zich daadwerkelijk tot elkaar verhouden, maar ik heb je met alle plezier de hoeken van de squashbaan laten zien. Last, but not least, Max; terugkijkend kan ik me voorstellen dat het niet de gemakkelijkste periode was, eerst opgezadeld met een onmogelijke synthese (wel gelukt met een overall yield van 0.02 % in drie stappen) en vervolgens nog een volledige serie gast-moleculen synthetiseren en bindingsstudies uitvoeren. Je positieve houding zal ik niet vergeten, en zonder jou was hoofdstuk 5 er nooit geweest, waarvoor heel veel dank. Ik hoop dat we dat stukje nog eens gaan publiceren. Ook jou wens ik alle succes met je promotie.

Nico, Nikos, Nikos, Heather, Michiel, Ruud, Pilli, Paul, Paul, Friso, Onno, Jan, Renee, Ad, Martin, Desiree, Paula, Jacky, Peter, Pieter, Floris en Floris hebben allen op hun manier een bijdrage geleverd aan het tot stand komen van dit proefschrift, waarvoor veel dank.

Zoals gezegd, ik heb bijna vijf jaar met ontzettend veel plezier op het lab rondgelopen, wat grotendeels te danken is aan de open en relaxte sfeer die er heerst. Omdat ik zeker collega's ga vergeten, ga ik hierbij verder geen namen noemen (ik weet dat ik hierbij de mensen teleurstel die graag willen weten wat er achter hun naam komt te staan in het dankwoord, maar ga er maar vanuit dat het niet negatief was geweest).

Minstens zo belangrijk als een goede werksfeer is het leven daarbuiten. We hebben een heerlijke tijd gehad op de Hertogstraat en denken vaker dan gedacht weemoedig terug aan onze periode daar. Met name Friso, Aurélie en dochters, Lee & Hefziba en zonen, Dennis & Paula en Rafaël, David, Cyrille, Hans & Sandy, Mathijs & Irene, Capo & Nikos, Anneke & Duncan hebben onze periode in Nijmegen erg waardevol gemaakt.

Jelle, Niels, Coen, Fleur, Jasper, Diederik en club-, huis- en LST-genoten. Allen dank voor de vriendschap, de interesse van een afstand die nu weer wat korter is geworden, en ik hoop dat met het afronden van de promotie er ook weer meer tijd komt om vaker leuke dingen te gaan ondernemen.

Ik heb veel familie die me nauw aan het hart gaat. Te beginnen met mijn schoonfamilie. Jan, Frida, Dajo, Bienie & Niels. Het is altijd fijn om in Weesp te zijn. Dank voor de gezelligheid, de betrokkenheid en de vele momenten dat jullie ons uit de brand hielpen door de zorg van de kinderen even op je te nemen.

Carien & Harald, Henriette & Lars, August & Ditri, en alle kinderen. Wat kan ik zeggen….; ik vind dat we een ontzettend leuke familie hebben en geniet altijd enorm van de momenten dat we samen zijn.

Pappa en Mamma. Het is toch altijd gewoon thuiskomen op de Adrianaweg. Ik ben ontzettend dankbaar voor alle mogelijke steun die jullie maar blijven bieden. Ik vind het een heerlijk gevoel dat jullie er altijd voor me zijn.

Ik verwacht niet van mijn paranimfen dat ze het boekje hebben doorgenomen, hun taak is veel belangrijker dan 240 bladzijden wetenschap.

Friso, ik ken je al ruim 13 jaar, maar in de Nijmeegse periode ben je een echte buddy geworden. Je SMS'jes omvatten meestal maar een woord: 'Biertje?', en dat was dan ook precies waar de behoefte lag, waarop dan weer zo'n heerlijke kansloze avond in een kroeg ergens in Nijmegen volgde. Ik vind het prachtig te zien hoe jij en Aurélie aan het leven aan het bouwen zijn en heb onze vriendschap erg hoog zitten.

August, alweer paranimf. Jammer dat we net uit het Oosten weg zijn gegaan nu jullie er zijn gaan wonen, maar verder…. Broers: een band die ons in de schoot geworpen is, en zich steeds meer blijkt te versterken en verdiepen.

Diederik, wat een feest dat jij bij ons bent gekomen. Ik verheug me op alles wat we nog van je gaan zien.

Jannemijn, mijn allerliefste prinsesje. Ik ben ongelooflijk trots zo'n prachtig en talentvol wezentje te hebben voortgebracht.

Flo, ik heb geen woorden voor wat je voor me betekent. Moordwijf? Ja! maar dan veel meer dan dat. Waarschijnlijk is juist het feit dat we niet altijd de makkelijkste weg nemen wel de kracht van onze relatie. Ik vind het heerlijk mijn leven met jou te doen.

Curriculum vitae

Alexander Deutman werd geboren op 9 april 1977 te Nijmegen. Na het behalen van zijn VWO diploma aan het Canisius college in zijn geboortestad in 1995 begon hij, na een korte uitstap rechten te Leiden, in 1996 aan de studie Scheikunde aan de Universiteit Leiden. Tijdens zijn studie liep hij stage op de vakgroep Bio-Organische Synthese van wijlen prof. dr. Jacques H. van Boom. In 2001/2002 heeft Alexander met een Erasmus beurs een half jaar lang onderzoek gedaan bij de groep Organic and Bio-molecular Chemistry van prof. dr. Francesco Nicotra aan de Universiteit van Milano-Bicocca. In 2003 behaalde hij zijn doctoraaldiploma en in 2004 begon hij aan zijn promotieonderzoek op de groep Fysisch Organische en Supramoleculaire Chemie onder leiding van promotores prof. dr. Roeland J. M. Nolte en prof. dr. Alan E. Rowan en copromotor dr. J. (Hans) A. A. W. Elemans aan de Radboud Universiteit te Nijmegen. Een deel van de behaalde resultaten van dit onderzoek ligt voor u. Sinds maart 2009 is Alexander Deutman in dienst van Cerexagri B.V. (UPL) als Head Formulation Chemistry Laboratory. Alexander is getrouwd en vader van twee kinderen.